A model for the nonlinear, time-dependent and strengthening analysis of shear critical frame concrete structures

TESIS DOCTORAL

Doctoral Thesis

Denise Carina Santos Ferreira

Supervisors

Prof. Antonio Ricardo Marí Bernat

Prof. Jesús Miguel Bairán García

Prof. Rui M. Carvalho Marques de Faria

Barcelona, February 2013

Universitat Politècnica de Catalunya, Barcelona Tech
Departament d´Enginyeria de la Construcció

UNIVERSITAT POLITÈCNICA DE CATALUNYA
BARCELONATECH

Departament d'Enginyeria de la Construcció

Doctoral Thesis

A model for the nonlinear, time-dependent and strengthening analysis of shear critical frame concrete structures

Presented by

Denise Carina Santos Ferreira
Civil Engineer, Universidade de Aveiro (Portugal)
M.Sc. Structural Eng., Faculdade de Engenharia da Universidade do Porto (Portugal)

for the degree of Doctor with International Mention

by the Universitat Politècnica de Catalunya

This PhD thesis was financed by the Portuguese Foundation for Science and Technology (FCT) in the ambit of the Social European Found and the POPH program.

FCT Fundação para a Ciência e a Tecnologia
MINISTÉRIO DA CIÊNCIA, TECNOLOGIA E ENSINO SUPERIOR

POPH PROGRAMA OPERACIONAL POTENCIAL HUMANO

QREN QUADRO DE REFERÊNCIA ESTRATÉGICO NACIONAL PORTUGAL 2007.2013

UNIÃO EUROPEIA
Fundo Social Europeu

Supervised by:

Prof. Dr. Antonio Marí — Universitat Politècnica de Catalunya

Co-supervised by:

Assoc. Prof. Dr. Jesús Bairán — Universitat Politècnica de Catalunya

Assoc. Prof. Dr. Rui Faria — Universidade do Porto, Portugal

Departament d'Enginyeria de la Construcció, Universitat Politècnica de Catalunya
C/ Jordi Girona 1-3, Edifici C1- Planta 2, Campus Nord-UPC 08034 – Barcelona. Tel. (93) 401 10 60 - Fax (93) 405 41 35

Aos meus pais, Laurindo e Leonor.

General Index

Acknowledgments

As every big accomplishment in life, finishing my PhD thesis leaves me with a mixed feeling of sweet nostalgia about the past and hopeful excitement about the future. These last years in Barcelona were definitely a wonderful experience regarding my academic, scientific and personal growth. Such a pleasant experience was only possible due to the tutoring, inspiration and friendship from the people with whom I add the opportunity to work, interact and share time along this journey. Hence, here I leave my statement of gratitude towards them.

Firstly, I want to thank Professor Antonio Marí for trusting in my potential, accepting me in his team and guiding me trough my PhD work. I want to recognize his concern about my good adaptation at Universitat Politècnica de Catalunya (UPC) and his efforts for making me feel at home in my early times in Barcelona. I also want to acknowledge his constant support, motivation and friendship during the various stages of development of my PhD. His enthusiasm, his positive and welcoming attitude, his academic excellence and his charisma will be forever an inspiration for my professional and personal life.

Subsequently, I want to thank Professor Jesús Bairán the commitment in tutoring my PhD work. I acknowledge his patience, dedication and seriousness in helping me solving the many problems I had to face during the development of my doctoral studies. His deep knowledge about the thematic of my work and his daily assistance were essential to the accomplishment of my PhD.

I extend my appreciation to Professor Rui Faria. Since my early years as a M.Sc. student, the values of scepticism, rigour and determination in the research activity, that I had learnt from his example, had been present in my work and will certainly continue in my future career. I also want to thank him the prolific support in the development of my doctoral thesis. In addition, I want to acknowledge Prof. Rui Faria for helping me arranging the contact and the scholarship to come to the UPC to get my PhD.

The funding provided by the Portuguese Foundation for Science and Technology (FCT) and the European Social Found through the PhD grant SFRH/BD/43232/2008 is gratefully acknowledged. Without this financial support the development of this work would have been not be possible. I also thank the financial support through the UPC-FPI pre-doctoral scholarship provided by Prof. Antonio Marí during the last months of my PhD.

This doctoral work was developed in the ambit of the Research Project ‘Assessment of deteriorated, repaired and strengthened structures: theoretical model and experimental verification’ (BIA2009-11764), financed by the Spanish Ministry of Science and Innovation. The experimental tests carried out at UPC that are presented in this thesis were

financed by the Spanish Association of Cement and its Applications (IECA). These supports are also recognized.

I want to thank the administration of the Department d'Enginyeria de la Construcció – Montse Santos, Mercè Gonzalez, Carme Congora y Carmen Longas - the promptness in solving the bureaucratic issues during my doctoral studies. I extend my acknowledgments to the personal of the Laboratori de Tecnologia d'Estructures (LTE) for the precious help during an experimental work developed in the doctoral period. I also acknowledge the friendly, positive and caring attitude of my dear colleagues at UPC – Noemi, Anna, Edison, Agnieska, Oriol Arnau, Maria Delia, Rolando, Natxo, Raúl and Eva Oller – that everyday generated a good and belonging working atmosphere. The interesting discussions and exchange of ideas and their constant encouragement were a fundamental piece in this accomplishment. In particular, I want to thank Anna for the patience and competence for standing my daily stresses in leading with paper work; and also Noemi for the revision of my dissertation. Additionally, I want to thank my colleagues of the Laboratory for the Concrete Technology and Structural Behaviour (LABEST) for making my stay period in Faculdade de Engenharia da Universidade do Porto (FEUP) so pleasant.

I want to thank my girl friends' group *nenas* – Noemi, Anna, Marta, Roser and Olga – for the many pleasant hours spent talking and reflecting about general life issues and for being a constant cheery and enthusiastic company. A special word of acknowledgement goes to Noemi and Anna, for their daily friendship and support during this last 4 years. Also, to Marta, for making me feel as part of her family and never alone in this foreign country. I also thank the deep friendship of my *sidewalk family* – Vanessa and Diederik – and for being always there for me, sharing many good and some not-as-good moments, during my last years in Barcelona. All the great time that I had spent here is because of all of you.

I also acknowledge my parents in law, Madalena and Francisco, for the caring support and encouragement during my stay in Barcelona.

I want to thank my parents Leonor and Laurindo, their infinitive care, trust and support essential to all the things I had achieved in life. Their constant presence and unconditional love accompanied all the stages of my life and had always guided me towards the right direction. You are definitely my strongest reference in life and all I am I owe to you. Also, to my brother Rúben, I recognize his caring and amusing attitude, that is always present despite of the physical distance.

Finally, I express my endless gratitude to the backbone of my life: my best friend and beloved partner Nuno. I feel blessed by sharing each of my single days with your cheerful, peaceful and charming way of living. I have no fear about the future to come because I known that, wherever place we end up living, we will certainly be happy.

Barcelona, January 2013
Denise Carina Santos Ferreira

Summary

Nonlinear fibre beam models, due to its intrinsic simplicity and computational efficiency, are often an adequate alternative to the complex nonlinear plane and solid FE models for the assessment of entire frame structures. For the cases in which shear strains are negligible, fibre beam models had reached a high level of accuracy in a wide range of structural applications. Nevertheless, simulations of structural concrete members undergoing relevant shear stresses cannot be performed by these models, as nonlinear shear effects and shear-bending interaction are neglected. In its turn, the presence of shear stresses in cracked reinforced concrete (RC) elements leads to a rather complex resistant mechanism which numerical modelling is neither straightforward nor clearly established.

Within this problematic, the formulation proposed in this thesis is an upgrade version of an existent flexural fibre beam model for the time-dependent analysis of segmentally constructed RC frames by taking into account the shear effects. The model is devised for the analysis of 2D RC and prestressed frame elements under combined axial, bending and shear forces. Shear-bending interaction is taken into account by means of a hybrid kinematic/force-based sectional approach. The key characteristics of the proposed model are: (*i*) at the material level RC is simulated through a smeared cracked approach with rotating cracks; (*ii*) at the fibre level an iterative procedure guarantees equilibrium between concrete and transversal reinforcement, allowing to compute the biaxial stress-strain state of each fibre; (*iii*) at the section level a uniform shear stress flow is assumed in order to estimate the internal shear stress-strain distribution and (*iv*) at the element level, the Timoshenko beam theory takes into account the deformation due to shear. Also, discrete crack representation is performed by means of an external algorithm that prints the cracking development in the elements.

As a result, the relevant attributes of the proposed formulation can be resumed as: (*i*) its capability for considering shear effects in both service and ultimate levels; (ii) the time step-by-step solution procedure enables taking into account the time-dependent response due to creep and shrinkage of concrete, temperature variations and relaxation of prestressing steel considering the multiaxial stress-strain state of the fibres and; (*iii*) the sequential type of analysis allows capturing the strengthening effects, accounting for the state of the structure prior to the intervention.

After the description of the proposed formulation, the model is validated through experimental tests available in the literature, as well as through an experimental campaign carried out by the author. Accordingly, the capacity of the model to efficiently reproduce the behaviour of shear critical beams is demonstrated. Experimental measurements of deflections, principal strains and directions in concrete, distortions, strains the longitudinal and transversal reinforcement and cracking patterns are compared with the results computed by the proposed model. In general, a fairly good fitting is achieved. The importance of including shear-bending interaction in the numerical analysis is underlined by comparing the results with the ones provided by the pure flexural basis model.

The influence of transversal stresses on the time-dependent response of shear and bending dominant beams is also studied with the proposed model. Considering shear effects in modelling the time-dependent response of diagonally cracked RC and prestressed beams is found to be relevant. However, its main influence is related with the instantaneous response; the differed deflection correspondent to distortion is found to be rather insignificant. Also, the influence of restraint strains due to shrinkage in the latter response of shear critical beams is numerically assessed. The previous damage brought by the restraint strains affected the long-term load carrying capacity of the beams failing in shear.

Subsequently, the proposed model is successfully used to predict the experimental results of a shear damaged and subsequently strengthened RC beam, available in the literature. An alternative strengthening solution for the damaged beam based on post-tensioned stirrups is numerically analysed. This technique showed to be effective to avoid brittle shear failure allowing for the development of all the flexural capacity of the repaired beam. In general, the importance of considering shear-bending interaction and previous damage in the numerical assessment of strengthened RC beams is revealed.

Finally, the response of a dismantled prestressed concrete bridge, with deficient shear resistance, submitted to full-scale tests is successfully simulated with the proposed model. In addition, different strengthening proposals based on post-tensioning measures are studied for this bridge. In this manner, the capacity of the model to determine the safety of existent structures and to analyse the performance of strengthening measures is demonstrated.

Contents

Chapter 6

NUMERICAL ASSESSMENT AND STRENGTHENING INTERVENTIONS ON SHEAR CRITICAL CONCRETE STRUCTURES 179

List of Symbols

Latin letters

A	Area of each fibre
A^*	Total area of the shear resistant fibres
A^*_{stren}	Total area of the shear resistant strengthen fibers
$A_{st,k}$	Area of the transversal reinforcement
A_{in}	Hidden state vector for creep computation
a_i	Scale factors of the Dirichlet function for creep computation
$\underline{a}_j$	2D Displacement vector in each node
B_e	Elasticity matrix
B	Strain transformation matrix
b_k	Width of the cross-section
c_1	Parameter of tension stiffness equation
D_{12}	Material stiffness matrix of concrete at the principal directions
D_c	Material stiffness matrix of concrete at the local referential
D_{fibre}	Material stiffness matrix of the fibre at the local referential
dt_1	Damage variable of concrete in tension
E_p	Elasticity modulus of active steel
E_s	Elasticity modulus of longitudinal passive steel
E_{st}	Elasticity modulus of transversal passive steel
E_t	Tangent stiffness of concrete in compression
E_0	Initial elasticity of modulus of concrete
E_1, E_2	Stiffness modulus in principal directions
$f_c^{'}$	Uniaxial compressive strength of concrete
f_{ct}	Maximum tensile strength of concrete
f_p	Compression peak stress in concrete

f_{pu}	Ultimate stress of active steel
f_{py}	Yielding stress of active steel
f_{su}	Ultimate stress of passive steel
f_{sy}	Yielding stress of passive steel
$\underline{F}_{elem}$	Internal force vector of the element
$\underline{F}^{nm}$	Equivalent nodal force vector due to non-mechanical strains
G^*	Transversal stiffness of concrete
G_{12}	Transversal modulus of concrete in principal directions
J	Creep compliance function
k	Counter of stirrups configurations
k_{ci}	Compression strength enhancement factor of concrete
$\underline{k}_{elem}$	Stiffness matrix of the element
$\underline{k}_{fibre}$	Stiffness matrix of the fibre in condensed form
$\underline{k}_{sec}$	Stiffness matrix of the section
$\underline{k}_{sec}^{c+st}$	Contribution of concrete and transversal steel to the sectional stiffness
$\underline{k}_{sec}^{sl}$	Contribution of longitudinal steel to the sectional stiffness
k_2	Parameter of the tension stiffness equation
n_k	Number of stirrups configurations
$\underline{R}^{nm}$	Equivalent nodal load vector due to non-mechanical strains
s_k	Longitudinal spacing between stirrups
s_m	Average crack spacing
$\underline{S}_{fibre}$	Internal force vector of the fibre
$\underline{S}_{sec}$	Internal force vector of the section
$\underline{S}_{sec}^{c+st}$	Contribution of concrete and transversal steel to the sectional internal force vector
$\underline{S}_{sec}^{nm}$	Sectional equivalent force vector due to non-mechanical strains
$\underline{S}_{sec}^{sl}$	Contribution of longitudinal steel to the sectional internal force vector
T	Transformation matrix: generalized sectional strains to strains in the fibre
t	Age
t'	Age of loading
t_n	Time step
T_{sl}	Transformation matrix: generalized sectional strains to strains in steel filament
T_ε	Rotation matrix of the strain tensor
T_σ	Rotation matrix of the stress tensor
u	Axial displacement

$V_{z,ul}$	Residual shear force
w	Transversal displacement
w_m	Average crack width

Greek letters

α	Coefficient of thermal expansion of concrete
β	Compression softening factor of concrete
γ_0	Distortion at the neutral axis of the section
γ_{ul}	Unbalanced shear distortion
$\gamma_{xz,m}$	Average shear strains at the cross-section
Δ	Increment of stress or strain
δ	Unbalanced stress or strain
$\underline{\varepsilon}^c$	Creep strain tensor
$\underline{\varepsilon}^{sh}$	Shrinkage strain tensor
$\underline{\varepsilon}^T$	Temperature variation strain tensor
$\underline{\varepsilon}^0$	Stress independent strain tensor
ε_{cr}	Strain at peak stress in concrete in tension
ε_{cu}	Ultimate strain in concrete in compression
ε_p	Strain at peak stress in concrete in compression
ε_{pu}	Ultimate strain of active steel
ε_{su}	Ultimate strain of passive steel
ε_{sy}	Yielding strain of passive steel
$\underline{\varepsilon}_{xz}$	Average strain tensor in the local referential $[\varepsilon_x, \varepsilon_z, \gamma_{xz}]^T$
ε_0	Axial strain at the section reference axis
$\underline{\varepsilon}_0$	Generalized sectional strain tensor $[\varepsilon_0, \gamma_0, \varphi_y]^T$
ε_1	Maximum principal average strain
ε_2	Minimum principal average strain
ε_2^p	Plastic strain in concrete in compression
$\underline{\varepsilon}_{12}$	Principal strain tensor $[\varepsilon_1, \varepsilon_2, \gamma_{12}]^T$
θ_y	Rotation to respect to the y-axis
λ_i	Parameter that defines the shape of the logarithmically decaying creep curve
$\rho_{st,k}$	Volumetric ratio of transversal steel

$\underline{\sigma}_{xz}$	Average stress tensor in the local referential $[\sigma_x, \sigma_z, \tau_{xz}]^T$
σ_z^c	Stress in concrete in the transversal direction
σ_z^{st}	Stress in the stirrups in the transversal direction
$\sigma_{z,k}^{st}$	Axial stress in transversal steel
σ_1	Maximum principal average strain
σ_2	Minimum principal average stress
$\underline{\sigma}_{12}$	Principal stress tensor $[\sigma_1, \sigma_2, \tau_{12}]^T$
τ^*	Shear stress applied in a fibre
ϕ_y	Curvature to respect to the y-axis

List of Figures

List of Tables

Chapter 1

INTRODUCTION

1.1 Background and motivation

Computer-aided nonlinear analysis procedures for reinforced concrete (RC) structures are very established in both engineering and research fields. In fact, these tools are essential to design complex new projects, perform safety assessment of existing structures and support key decisions of change of use, demolition or strengthening. Researchers continuously aim to enhance the numerical models in order to better approximate the computation to the phenomenology of the response of RC structures.

In one hand, further advances related to the material response and to the structural mechanics are ceaselessly sought after. However, in the other hand, the singular characteristics of RC, such as, non homogeneity and nonlinear behaviour, cracking, force distribution, time-dependent characteristics, bond slip, dowel action, aggregate interlock, etc., which are difficult to understand and to simulate numerically, act as drawbacks in terms of solutions for its computational mechanics.

Due to this intricacy and to the difficulty to link the complex numerical models to the design and assessment of real structures, an alternative research trend seeking to maintain

the numerical tools as simple as possible and accurate enough to assist engineering practice is supported by many researchers. Accordingly, the work developed in the ambit of the present thesis is inserted into this former category of numerical models for the analysis of RC structures.

The need for assessment and strengthening of aged RC infrastructures is becoming a major concern in developed countries due to the deterioration of the materials, the greater loading demand (such as increasing traffic loads in bridges) and the drop of governmental funds for new construction, leading to a new tendency of increasing the life-span of existing infrastructures.

Relating to existing RC structures, the design of strengthening procedures implies, on one hand, the knowledge of the current state of the structure and, on the other hand, an accurate prediction of the efficiency of the repair or retrofit measures. Also, a correct assessment of the state of the structure is of paramount importance in order to take an accurate decision and to carry out a proper intervention. Therefore, numerical models able to perform life-time assessment analysis of entire structures and predict the response of strengthening proposals are required for these purposes. Accurate analyses are only possible if the time-dependent behaviour, the phased construction and the nonlinear behaviour of the structures are considered.

The Finite Element Method (FEM) is nowadays the most used computational tool for the nonlinear analysis of RC structures. One of the key differences between the available models based on the FEM to simulate frame structures is its order, as it is schematically represented in Figure 1.1: solid (3D), plane stress (2D) and linear (1D) finite elements (FE).

In design or assessment of real frame structures, the use of complex nonlinear 2D and 3D FE programs can turn out to be impracticable due to the difficulty to define all the required constitutive input variables, the high computational costs and the huge amount of generated data that makes the handling of results a very time-demanding and complex task. Instead, discrete FE models with distributed non-linearity represent a good compromise between simplicity and accuracy, allowing for complex nonlinear analysis without the need of a great computational cost and permitting a more straightforward results' interpretation and understanding of the structural response.

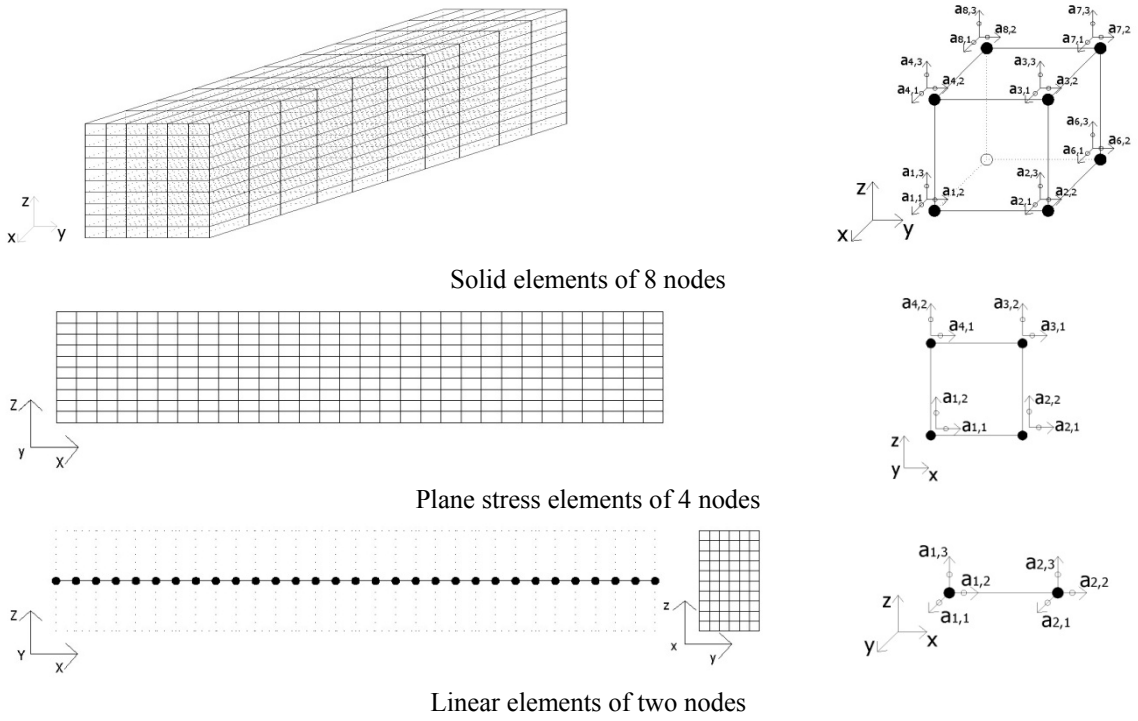

Figure 1.1 – Example of FE models: a) meshes, b) elements

Pertaining to the specific case of fibre beam models, the Navier-Bernoulli plane section theory and the use of a fibre sectional discretization combined with accurate uniaxial constitutive laws, proved to be an accurate and rational solution for the cases where shear strains are negligible. A schematic representation of its general characteristics is given in Figure 1.2. Effectively, nonlinear fibre beam elements had been developed for more than 30 years (Kang and Scordelis 1980; Buckle and Jackson 1981; Chan 1982; Marí 1984; Ulm, Clement et al. 1994, are some examples). This approach allows fairly accurate analyses of flexural dominant RC frames to be obtained. Moreover, its inherent simplicity and computational efficiency contributed to make this approach a particularly advantageous solution.

For these reasons, nonlinear fibre beam models are increasingly seen as an adequate alternative to the complex nonlinear plane and solid FE models to perform nonlinear life-time analyses of entire frame structures. Evidencing this fact is the great research effort to enhance this type of models that has emerged in the last decades, covering aspects such as segmental construction, time-dependent effects, improved constitutive laws, bond slip, joint simulation, etc. Due to this endeavour, fibre beam models had reached a high level of development (Marí 2000).

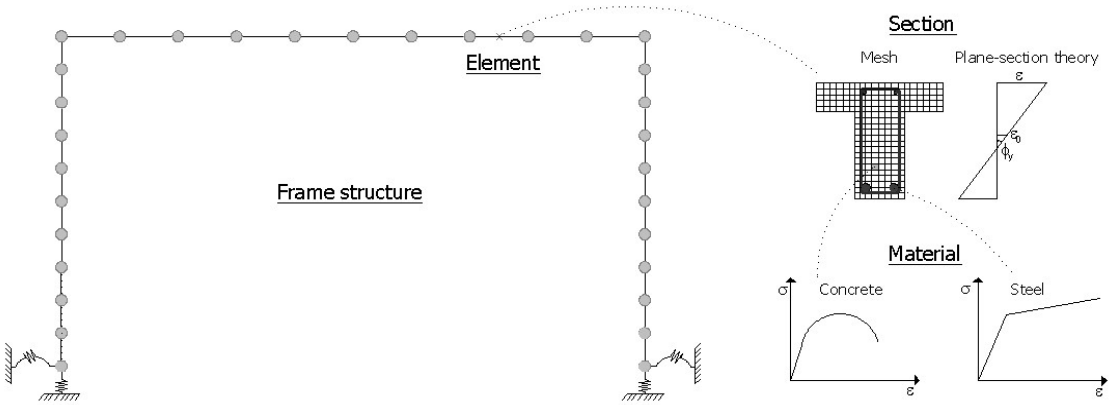

Figure 1.2 – Characteristics of the fibre beam models

Nevertheless, traditional fibre beam models neglect shear effects and its interaction with other internal forces. Consequently, accurate simulation of structural members that are submitted to important shear forces cannot be done by Navier-Bernoulli models. In fact, neglecting shear effects can be critical for some existing structures, designed with old shear provisions, or for those susceptible to fail in shear. In addition, checking safety in shear when a structure is strengthened in bending is fundamental, as the increase of bending load capacity may produce a change of failure mode; this is a task that cannot be performed by pure bending modelling strategies. Also, disregarding shear can lead to unsafe estimations of strength and ductility, which can be particularly dangerous in the assessment of existing structures with low quantities of transversal reinforcement.

Solving this handicap of the fibre beam models is imperative to supply plain and precise nonlinear models to an industry that is opening doors to the use of nonlinear FE analysis in the practical structural activity. In fact, this tendency is present not only for the design of safer and more economical new infrastructures, but especially for the assessment of the older ones.

However, including shear effects in these models is not an easy task. The existent behavioural models for shear, at both kinematic and constitutive levels, are far away from the bending models in terms of rationality and generality. As it is generally accepted among researchers, shear mechanism in RC elements is complex and not straightforward to model numerically (Bairán and Marí 2007). As it is represented in Figure 1.3, this great complexity in relation to the flexure models is mostly due to the multiaxial stress state that is generated along with the strong nonlinear behaviour found in diagonally cracked concrete.

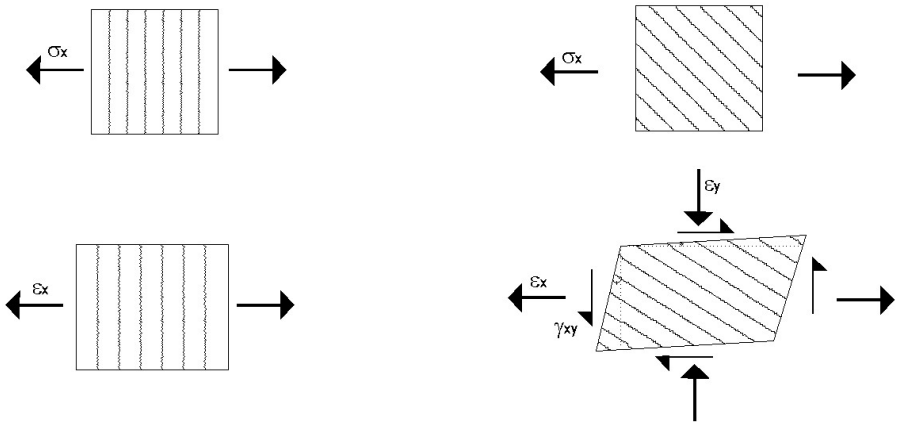

Figure 1.3 – Strain and stress state in cracked concrete: a) uniaxial (bending) and b) multiaxial (bending and shear)

Thereby, in the presence of shear forces the plane section hypothesis is no longer strictly valid due to the appearance of distortion. Also, a sort of different force contributions and interactions to the shear resistant mechanism, such as shear stresses in the uncracked compression zone, remaining tension transferred along the crack plane, aggregate interlock, dowel action at the longitudinal reinforcement and the resisting mechanism of the transversal reinforcement, are not plainly reproduced. In addition, the significant nonlinearities brought by the non-orthogonal cracks and the strain-softening of the concrete make the analyses quite vulnerable to numerical instabilities and convergence problems, which is also a critical handicap of these types of models.

Even though, an extensive research effort on shear in RC elements has emerged in the last years. This exertion was largely motivated by a range of historically episodes of shear failures that took place during the last century. Relating to non-seismic accidents, in 1955 and 1956, in the U.S.A., a series of American Air Force Warehouses failed in shear (Figure 1.4a) and these accidents strongly influenced the following ACI code in 1963 in terms of shear design. Since this code, ACI has required a minimum amount of stirrups area whenever the design shear load exceeds half of the shear strength provided by concrete. In 1991 in Norway, a concrete deep water structure – the Sleipner offshore oil platform (Figure 1.4b) – failed under shear dominant loading conditions, causing an enormous economic lost. The post-accident investigations discovered that the root cause of the failure resulted from inaccurate structural design calculations by means of complex FE analysis: the shear stresses were underestimated by 47%, leading to an insufficient design of transversal reinforcement and thickness of the cell walls; the loss of the structure was due

to the failure of a cell wall under a water head of 65 meters when it was designed to be at 70 meters, leading to a strong crack and leakage. Careful FE analyses of the structure performed after the accident predicted failure to occur at a depth of 62m, which approximately matches what actually happened (Collins, Vecchio et al. 1997). More recently, a highway overpass failed suddenly in Quebec in 2006 (Governement du Québec 2007) right after a structural inspection (Figure 1.4c), causing human losses.

a) American Air Force warehouses 1955-56

b) Sleipner offshore oil platform, Norway 1991

c) Highway overpass, Quebec, 2006

d) Shear failure of the Hanshin expressway, Kobe earthquake 1995

e) Shear failure of the piers of a bridge, Taiwan earthquake 1999

f) Pier shear failure of the bridge crossing Bio Bio River in Chile earthquake in 2010

Figure 1.4 – Structural shear failures

Regarding seismic accidents, the failures observed in concrete structures in the important earthquakes of the last years are mostly related to shear; some noteworthy examples are: Loma Prieta earthquake in 1989, Northridge in 1994, Kobe in 1995 (Figure 1.4d), Taiwan in 1999 (Figure 1.4e) and Chile in 2010 (Figure 1.4f). Disasters like these ones contributed to recognize the current feeble state of knowledge regarding shear design and putted this topic on the agenda of many research groups worldwide.

From this research effort an assortment of different approaches to model the shear resistant mechanism of RC had emerged, with different levels of accuracy and computational costs. However, despite the development of more and more sophisticated models, the gap between the scientific level analysis and the design methods for Civil Engineering practice has increased. In fact, the most used analytical procedure in shear design is the Mörsch truss analogy that was developed more than a century ago. This design methodology is based on the theory of plasticity and, for that reason, is more representative of the ultimate loading stage.

Moreover, even at the present, there is no agreement between different standards concerning the design of RC elements to shear. This disparity leads to important differences in the solutions given by different codes, and in some cases unsafe solutions are reported (Collins, Bentz et al. 2008). This disagreement between standards' procedures and the difficulties to pass new models to the design field are mainly due to the inexistence of a worldwide accepted shear theory.

Hence, it is globally recognised in the civil engineering community that shear mechanisms are not-well understood and more research is needed in this field. Moreover, the development of accurate and simple shear models for the everyday design is a priority. As a matter of fact, several models were developed in the recent years with the goal of extending the fibre beam elements to analysis including shear (Navarro 2009; Saritas and Filippou 2009; Ceresa, Petrini et al. 2010; Mohr, Bairán et al. 2010), but still without reaching consensus. In fact, fibre beam models can accurately simulate the behaviour of RC frames under combined normal and shear forces, by means of multiaxial constitutive equations and suitable kinematic section assumptions (Bairán and Marí 2007).

The response of RC structures under high shear forces may also be influenced by the time-dependent phenomena, the procedures of phased construction, by the deterioration and damage agents and by the repair and retrofit measures. Therefore, this is the overall problematic that moved this thesis. The inclusion of nonlinear shear effects into an existent

enhanced pure flexural fibre beam model able to simulate time-dependent and segmental constructed frame structures was the paramount objective of this thesis. For this purpose, a nonlinear fibre beam model with shear-bending interaction was developed. The outcome of this thesis is a numerical tool that enables a vast type of analyses with affordable computation times and straightforward interpretation of results, being adequate for nonlinear structural analysis in the engineer practice.

1.2 Scope and objectives

The general objective of this thesis is the development of a numerical model for the nonlinear and time-dependent analysis of existing and strengthened RC frame structures by taking into account the axial force-shear-bending interaction. Hence, as already mentioned, the model developed in this thesis intends to broaden the capabilities of an existing basic flexural fibre beam approach, to deal with applications where shear has a dominant role. Therefore, the proposed formulation is based on the numerical model CONS originally developed at University of California (Berkeley) by (Marí 1984) and extended at the Universitat Politècnica de Catalunya - BarcelonaTECH (UPC) (Marí 2000). It is a displacement-based FE model for the material and geometric nonlinear and time-dependent analysis of reinforced, prestressed and composite concrete frames.

Regarding the extension of the flexural filament beam model for the inclusion of shear effects, the present work can be seen as a natural development of the previous experiences in this field, achieved in the Doctoral Thesis of Bairán (Bairán 2005) and Mohr (Mohr 2011), in an attempt to develop a simpler and less time consuming computational model.

Therefore, the model proposed in this thesis is devised for analyses of 2D RC frames under combined axial, bending and shear forces. The features of time-dependent and sequential analysis available in the basic model are exploited in the proposed model by extending its application to the case of RC structures under multiaxial stress states.

To achieve the general objective of this thesis a set of specific goals were considered:

- To organize and adapt the existent basis code in order to meet the requirements for the implementation of the shear model.

- Development of a nonlinear section model for coupling of shear and normal forces, suitable for fibre beam formulations.
- Extension of the shear-flexure section model for the element level, allowing for the consideration of shear flexibility at the structural level.
- Implementation of the shear model into the basic model by maintaining the existent features of time-dependent and segmental construction procedures.
- Validation of the proposed model through benchmarks of shear critical RC frame elements available in literature.
- Struggle for solutions for the numerical instabilities that are typically found on the computation of cracked concrete and brittle failures. Implementation of continuation methods in order to improve the performance of the proposed model in analysing shear-critical problems.
- Adapt the time-dependent analysis model for the case of biaxial stress states, in order to be coherent with the mechanical shear model.
- Study the influence of shear in the long-term response of RC frame structures.
- Extent the shear model to segmentally constructed sections.
- Implementation of numerical features that allow simulating repair of structures to shear: supply of extra stirrups and transversal reinforcement prestressing.
- Evaluate the accuracy of the numerical model to simulate shear damaged and strengthened RC frame structures.
- Perform numerical studies on the assessment of real structures submitted to high shear forces and design strengthening solutions.

1.3 Research significance

The research significance of the work developed in this thesis is the implementation of a nonlinear shear-bending interaction formulation into a fibre beam model. By implementing a shear-analysis procedure in the existent non-linear and time-dependent FE program it is possible to perform time-dependent and evolutive construction analyses of structures under high shear forces. As the formulation is based on the fixed stress approach, the effects of shear reinforcement in the resistant mechanism of shear-critical beams are properly simulated, in contrast with existent proposals.

By these means and motivated by its computational efficiency, it is intended to create an alternative numerical tool to the high complex 2D/3D FE models for the nonlinear assessment of shear critical frame structures, both at service and ultimate limit states. Also, meeting the rising need for repair or strengthening of existent structures, the proposed model aims to be a practical engineering tool to accurately assess the structural behaviour and also serving as a decision tool for repair or demolitions acts. An introduction to the study of the long-term responses of frame structures submitted to important shear stresses is a further contribution of this work.

1.4 Outline and contents of this thesis

The present thesis is divided into 7 chapters. After this first opening chapter that points out the overall context, the most relevant motivations and objectives of the research work, an overall description of the state-of-the art is presented in Chapter 2. This second chapter is focused on the topics that are essentially related with the ambit of the research work carried out in this thesis. Being so, it makes a generally description of the fibre beam models and the very high advanced state they reached for the case of pure bending analysis. Afterwards, the complexity of the phenomenology and modelling of the shear resistant mechanism of RC elements is revised. Existent kinematic and constitutive theories are discussed, as well, as its adaptability to fibre beam models. Subsequently, a general view on the subject of repair and strengthening of existent structures is presented, focussing on the importance of time-dependent models able to assess the actual state of the structures to predict the efficiency of repair or strengthening projects. Finally, a general discussion on the state-of-the-art is presented. The context in which the present research is inserted in, and the gap of knowledge that it pretends to fill, are remarked. Accordingly, the options taken in the development of the numerical model, which were supported by previous findings reported in the literature, are highlighted.

Chapter 3 describes in detail the proposed model – the hybrid beam-column model including shear effects. The explanation of the constitutive equations used for concrete and reinforcement, the state determination procedure at the fibre level and the assumptions taken at both the section and element levels are exhaustively presented. The validation of the model is carried out though different benchmarks of shear critical beams available in the literature and also by own experimental tests. The various validation examples try to

embrace different shear-related characteristics of the RC beams, such as, geometry, reinforcement, loading scheme, cracking patterns, failure modes, etc.

In Chapter 4 the numerical analyses are enlarged for the cases of RC frames. An experimental validation of a RC frame test available in the literature, focused on the shear-related mechanism and on its influence on the overall response of the frame, is presented. Afterwards, a parametric study on the influence of the level of longitudinal restraint on the ultimate response of shear-critical beams that belong to frames is carried out with the proposed model.

Subsequently Chapter 5 presents an overall discussion on the topic of shear effects and time-dependent responses of RC frames. It is noteworthy that this chapter is not the foremost ambition of this thesis. However, it is a natural and logic choice to take profit of the existent features of the basic flexural model and adapt them to the new shear model. Also, including time-dependent capabilities in the proposed shear model is relevant to perform life-time analysis of in-service frame structures with some shear damage. Accordingly, the time-dependent behaviour of concrete available in the basic model for the 1D case is enlarged to the 2D case. The validation of the model is carried out through a typical flexural benchmark and an experimental campaign on diagonally cracked beams under sustained load, both available in the literature. The parametric study presented in Chapter 3 on the response of shear critical beams belonging to frames is enlarged in Chapter 5 by considering the effects of restrained shrinkage and study its influence on the ultimate resistance. A general discussion on the influence of shear effects on the long-term deflection of beams and on its subsequently ultimate load is also sustained through another parametric study. It is important to say that this chapter handles very complex problems and is a first insight, leaving a wide range of questions to be solved in future research.

In Chapter 6 the proposed time-dependent shear model is enlarged in order to considerer the features of segmental construction. By these means, the step-by-step nonlinear sequential type of analysis allows capturing the strengthening effects accounting for the state of the structure prior to intervention. After the description of the new features of the shear model accounting for segmental construction, a validation example based on experimental tests carried out on previously shear damaged and subsequently strengthened beams is presented. Alternative shear strengthening solutions based on vertical prestress are also analysed. Finally, an application of the proposed model to the numerical assessment and study of a possible strengthening solution for a real structure (the Wassnerwald Bridge in Switzerland) is presented. Actually, this chapter represents the

most relevant significance of this thesis, which is, to predict the response of existent shear-critical RC frame structures and study the efficiency of suitable strengthening interventions.

The main conclusions of the research work developed in the ambit of this thesis are drawn in Chapter 7, along with the proposals for future work. The use of the proposed fibre beam model to study structural problems related with shear and strengthening are the main path left open for future research.

Chapter 2

STATE OF THE ART ON FE MODELS FOR FRAME STRUCTURES

2.1 Preamble

Structural analysis can be performed by means of numerical models that simulate the geometry, the materials' properties, the applied loads, the support conditions and the construction sequence in order to obtain the structural response. The characteristics of the models depend on the objective of the analysis. For instance, studying local effects with multiaxial stress states - such as, punching of a slab around a column - requires 3D FE models to obtain a satisfactory response. However, when the purpose of the analysis is to obtain the general response of a frame (without focusing in the local effects, e.g., the joints' behaviour), more global models, based on linear elements, are generally adequate even when considering the nonlinear behaviour of the structure. Actually, many structures can be assimilated to planar or spatial frame members, and their proper simulation can be achieved through 1D FE models. In effect, these models present a good balance between accuracy, simplicity and computational demanding for the analysis of frame structures.

Within 1D FE there are two main categories, depending on how nonlinearities are considered: lumped and distributed (or smeared). Regarding lumped models, the nonlinear behaviour of the frame elements is considered in concentrated points, usually located at the

end of the beams and columns or at their midpoints. These models have been extensively used in the dynamic and seismic analysis of RC multi-storey frames. In fact, the simplicity of such formulation is its major advantage; however, there are some handicaps that limit their application: predefined definition of the inelastic zones; a priori assumptions of the parameters of the model (moment-curvature, moment-rotation, etc.) and the difficulty to calibrate the many parameters involved. Members with extensive damage and plasticity cannot be accurately analysed with this type of models.

Distributed nonlinearity has been proposed by researchers in order to overcome the problems of the lumped models and to be able to reach better correlations with experimental tests and broaden its range of applications. Therefore, in these models the structure is divided into elements interconnected by nodes and the material nonlinearities are introduced at each control section. The element behaviour is determined through the numerical integration of the response of key sections that are monitored throughout the analysis. In the specific case of fibre beam elements, each section is discretized into longitudinal fibres which allows accounting for the axial-bending interaction in a direct and rational manner and also tracing the uniaxial nonlinear response of each fibre.

Two main beam theories are usually used in frame element models: Euler-Bernoulli (EBT) and Timoshenko (TBT). In the EBT it is assumed that plane sections remain plane and normal to the longitudinal deformed axis of the element and thus no shear deformation is considered. In this way, the EBT is capable of capturing the behaviour of beams subjected to normal forces (axial forces and bending moments) but is not able to considerer the influence of shear strains. In turn, the TBT assumes that plane sections remain plane but not necessarily normal to the longitudinal axis, so the shear deformation is considered. As the Timoshenko theory still assumes that the section remains plane, it means that a constant shear strain distribution is considered through the cross section. In Reddy's second and third order beam theories (RBT) (Reddy and Wang 1997) the shear strain distribution is not assumed as constant, since the straightness assumption for the section is no longer considered. In these cases, quadratic or cubic variations of shear strains are assumed, leading to null shear stresses at the top and bottom faces of the beam.

Frame element models are generally formulated either by displacement-based or force-based approaches. On one hand, the displacement-based approach (stiffness method) is related to the classical finite element formulation (Zienkiewicz 1977): predefined shape-functions are used to interpolate the displacements in the element as functions of the nodal displacements; the Virtual Work Principle is used to determine the stiffness matrix and the

load vector for each FE. Since this is an approximate method, a refined mesh is needed in order to achieve a satisfactory accuracy. On the other hand, in the force-based approach (flexibility method) the sectional forces are directly related to element forces through the beam's internal equilibrium equations (Scapone, Filippou and Taucer 1996). Therefore, this method is theoretically *exact*. In the classical fibre beam approach, the stiffness method has demonstrated accurate performances. However, various attempts on the consideration of shear effects on fibre beam models have relied on the flexibility-based approach, as it will be later addressed on this chapter.

The research work on nonlinear shear analysis developed in this thesis is in the ambit of displacement-based, 1D finite element models with distributed non-linearity. For this purpose, a flexural fibre beam model is used as a basis platform for the development of the shear model: the nonlinear and time-dependent model for the analysis of reinforced and prestressed concrete frames CONS (Marí 1984; Marí 2000). This model is founded on the FEM and on the Bernoulli's beam theory for the nonlinear and time-dependent analysis of 3D reinforced, prestressed and composite concrete frames. It allows the consideration of the nonlinear material and geometrical structural behaviour, as well as the non-mechanical strain fields caused by creep, shrinkage, aging and temperature gradients. Also, the time step-by-step analysis allows the simulation of segmental construction.

In this chapter, after a brief description of the existent basic model for axial-bending analysis, the more relevant theories available for modelling RC elements under transversal forces are presented. Specifically, the previous works on complex shear models (Bairán 2005; Mohr 2011) that gave rise to the development of the simplified shear model in this thesis are addressed in more detail. Also, regarding the implementation of shear formulations in fibre beam models, the previous proposals are explained and reviewed, by pondering their main advantages and drawbacks. Accordingly, the fibre beam model with shear effects developed in this thesis is clearly contextualized in relation with the existent proposals.

The main goal of the proposed numerical model developed in this thesis is the simulation of shear damaged structures and the evaluation of the efficiency of different strengthening solutions towards increasing safety. In this ambit, an overview of the repair and strengthening technologies and materials for shear damaged RC structures is presented. Also, the essential characteristics needed in a numerical model in order to accurately simulate interventions in damaged structures are examined.

Finally, after setting the background context of this work, a discussion on the present state of the art is presented, focusing on the contributions that the proposed numerical model aims to reach.

2.2 Nonlinear fibre beam model for bending-axial analysis

The basic flexural fibre beam model CONS is briefly described in the following. Its general characteristics, such as, geometric nonlinearities, prestressing, time-dependent analysis and segmental construction, were maintained in the model developed in this thesis. Exhaustive descriptions of the theoretical background of the basic model can be found in (Marí 1984;Marí 2000).

2.2.1 Finite element formulation

The general characteristics of the basic model CONS are:

- the use of a beam-type linear Hermitian finite element,
- the cross-sections are discretized into concrete fibres and longitudinal steel filaments,
- each fibre and filament are assumed to be in a 1D strain-stress sate,
- the plane section theory is adopted as the sectional kinematic law,
- shear strains are not considered,
- transversal reinforcement is neither considered,
- perfect bond between concrete and steel is assumed,
- both material and geometrical nonlinearities are considered.

2.2.1.1. Hermitian finite element

The FE used is the Hermitian beam element with 13 degrees of freedom (Chan 1982 and Marí 1984). Accordingly to Figure 2.1, in each external node three displacements (u, v, w) and three rotations (θ_x, θ_y, θ_z) are considered and an additional axial displacement node is adopted in the middle length (u_n). This additional node is not located in the element's boundaries; therefore, it is possible to eliminate it by static condensation as it is not needed to maintain displacement continuity along the mesh. However, the internal node is

necessary for internal compatibility and equilibrium within the element's length if the response is nonlinear or a variation of neutral axis position is expected between internal sections.

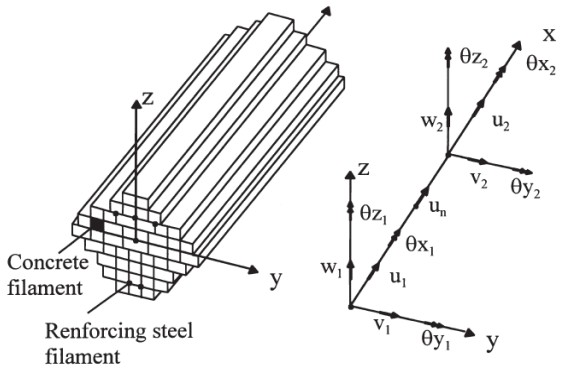

Figure 2.1 – Fibre beam in model CONS (Marí 2000)

The shape functions (N_i) that determine the displacement fields in the local *x*-axis of the beam (u_0, v_0, w_0) from the nodal displacements are (Figure 2.2): linear functions for the axial displacements and torsion twist at the end nodes (N_1 and N_2); cubic polynomials for the transverse displacements ($N_{\phi 1}$ and $N_{\phi 2}$) and rotations ($N_{\phi 3}$ and $N_{\phi 4}$); and a quadratic function for the middle-node axial displacement (N_3) with zero displacement in the boundary nodes and maximum in the inner node (this is also referred as bubble function), given as,

$$u_0 = \left(N_1, N_2, N_3,\right)\begin{bmatrix} u_1 \\ u_2 \\ u_n \end{bmatrix} \tag{2.1}$$

$$v_0 = \left(N_{\phi 1}, N_{\phi 2}, N_{\phi 3}, N_{\phi 4}\right)\begin{bmatrix} v_1 \\ v_2 \\ \theta_{z1} \\ \theta_{z2} \end{bmatrix} \tag{2.2}$$

$$w_0 = \left(N_{\phi 1}, N_{\phi 2}, -N_{\phi 3}, -N_{\phi 4}\right)\begin{bmatrix} w_1 \\ w_2 \\ \theta_{y1} \\ \theta_{y2} \end{bmatrix} \tag{2.3}$$

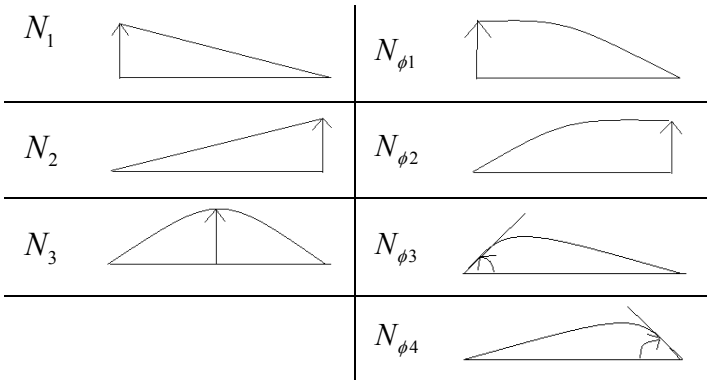

Figure 2.2 – Shape functions in model CONS

The Navier-Bernoulli's plane section theory is the adopted kinematic law, which can accurately reproduce the coupled axial-bending response of the beam element as function of the generalized strains. Accordingly, from the displacements (u_0, v_0, w_0) the axial displacement u_x and the axial strain ε_x in the section are obtained as

$$u_x = u_0 - z\frac{\partial w_0}{\partial x} - y\frac{\partial v_0}{\partial x} \tag{2.4}$$

$$\varepsilon_x = \frac{\partial u_0}{\partial x} - z\frac{\partial^2 w_0}{\partial x^2} - y\frac{\partial^2 v_0}{\partial x^2} \tag{2.5}$$

The dependency between strains ε and nodal displacements d is given by the transformation matrix B as

$$\varepsilon = Bd \tag{2.6}$$

$$B = LN \tag{2.7}$$

where L is the derivate operator of the shape functions N.

The element stiffness matrix K_e is obtained through the application of the Virtual Work Principle resulting in the following expression:

$$K_e = \int_V B^T DB \; dv + \int_L B_x^T GJ B_x^T dx \tag{2.8}$$

where D is the stiffness matrix; torsional stiffness is determined along the element length in a separated manner through a uncoupled constitutive law by means of the axial transformation matrix B_x and the torsional stiffness GJ. The element internal resisting load vector F_e is given by:

$$F_e = \int_V B^T \sigma \, dv + \int_L B_x T_x \, dx \tag{2.9}$$

where σ is the internal stress vector and T_x is the torque force. The numeric integrations are performed by the Gauss Quadrature Method (Zienkiewicz and Taylor 2004) with two Gauss points in each finite element.

2.2.1.2. Plane section theory

RC sections of arbitrary shape are divided into concrete fibres and longitudinal steel filaments, as presented in Figure 2.3a. Consequently, it is possible to assign different materials to different fibres and filaments in a cross-section. Each fibre is assumed to be in an uniaxial strain-stress sate and the Bernoulli's theory is adopted as the kinematic law (Figure 2.3b). Hence, the behaviour under normal and tangential forces is considered uncoupled, and the influence of shear and torsion on the normal deformations is not taken into account. Bond-slip is neglected, as perfect adherence between concrete and steel is considered.

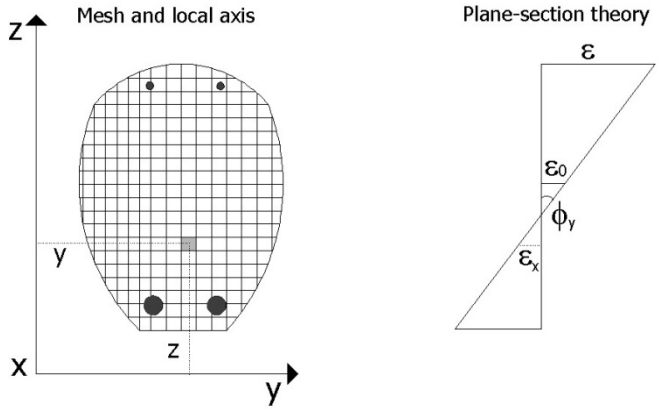

Figure 2.3 – Sectional model: a) fibre discretization and b) plane section theory

Consequently, the increment of axial strain $\Delta\varepsilon$ in each fibre is given by

$$\Delta\varepsilon(y,z) = \Delta\varepsilon_0 + \Delta\phi_y . z - \Delta\phi_z . y \tag{2.10}$$

where (ε_0, ϕ_y, ϕ_z) are the generalized strains in the cross section (respectively, the axial strain, the curvature with respect to the y-axis and the curvature with respect to the z-axis). The correspondent stresses are determined through:

$$\Delta\sigma(y,z) = E_T(\Delta\varepsilon - \Delta\varepsilon^{nm}) \tag{2.11}$$

where E_T is the tangent stiffness and $\Delta\varepsilon^{nm}$ is the non-mechanical strain due to time-dependent phenomena.

Accordingly, the increment of normal forces and bending moments in a cross section (ΔN, ΔM_y, ΔM_z) are given by the stress integration along the area A of the fibres and filaments:

$$\begin{aligned} \Delta N &= \iint_S \Delta\sigma(y,z)\,dA \\ \Delta M_y &= \iint_S \Delta\sigma(y,z).z\,dA \\ \Delta M_z &= -\iint_S \Delta\sigma(y,z).y\,dA \end{aligned} \tag{2.12}$$

The bending stiffness matrix of the cross section is also computed as the integration of the contributions of each fibre and filament along the cross section as,

$$\begin{aligned} EA &= \iint_s E_T\,dA & ESY &= \iint_s E_T.z\,dA & ESZ &= \iint_s E_T.y\,dA \\ EIZ &= \iint_s E_T.y^2\,dA & EIY &= \iint_s E_T.z^2\,dA & EYZ &= \iint_s E_T.y.z\,dA \end{aligned} \tag{2.13}$$

and in this manner, the relationship between generalized normal strains and forces in a cross section can be written as

$$\begin{bmatrix} \Delta N \\ \Delta M_y \\ \Delta M_z \end{bmatrix} = \begin{bmatrix} EA & ESY & ESZ \\ & EIY & EYZ \\ sym & & EIZ \end{bmatrix} \begin{bmatrix} \Delta\varepsilon_0 \\ \Delta\phi_y \\ \Delta\phi_z \end{bmatrix} \tag{2.14}$$

where the coupling between bending and axial forces is considered by the cross terms of the stiffness matrix.

The full sectional stiffness matrices include, in a decoupled manner, the shear forces V_y and V_z and the torsion moment T_x and their corresponding strains γ_y, γ_z and ϕ_x. Consequently, the cross elements of the sectional stiffness matrix associated with coupled shear-bending-torsion forces are null. The shear stiffness GA_y^* and GA_z^* are set as linear throughout the entire analysis and the torsion stiffness GJ is given by a pre-defined torsion-strain law (T_x - ϕ_x).

$$\begin{bmatrix} \Delta N \\ \Delta M_y \\ \Delta M_z \\ \Delta V_y \\ \Delta V_z \\ \Delta T_x \end{bmatrix} = \begin{bmatrix} EA & ESY & ESZ & 0 & 0 & 0 \\ & EIY & EYZ & 0 & 0 & 0 \\ sym & & EIZ & 0 & 0 & 0 \\ & & & GA_y^* & 0 & 0 \\ & & & & GA_z^* & 0 \\ & & & & & G_\alpha J \end{bmatrix} \begin{bmatrix} \Delta\varepsilon_0 \\ \Delta\phi_y \\ \Delta\phi_z \\ \Delta\gamma_y \\ \Delta\gamma_z \\ \Delta\phi_x \end{bmatrix} \tag{2.15}$$

The exact evaluation of the stiffness matrix is not a necessary requirement for the solution of the equilibrium in a nonlinear analysis, as the iterative process allows its continuous correction until reaching the converged solution, as long as the internal forces are evaluated properly.

2.2.1.3. Constitutive laws

The uniaxial stress-strain curve considered for concrete is presented in Figure 2.4a, in which cracking and load reversals are included. Also tension stiffening is considered: after cracking, the tensile stress does not drop to zero, but decreases gradually with the increasing strain according to a hyperbolic law. In what concerns the reinforcement steel, a bilinear stress-strain relationship is assumed with load reversals as presented in Figure 2.4b.

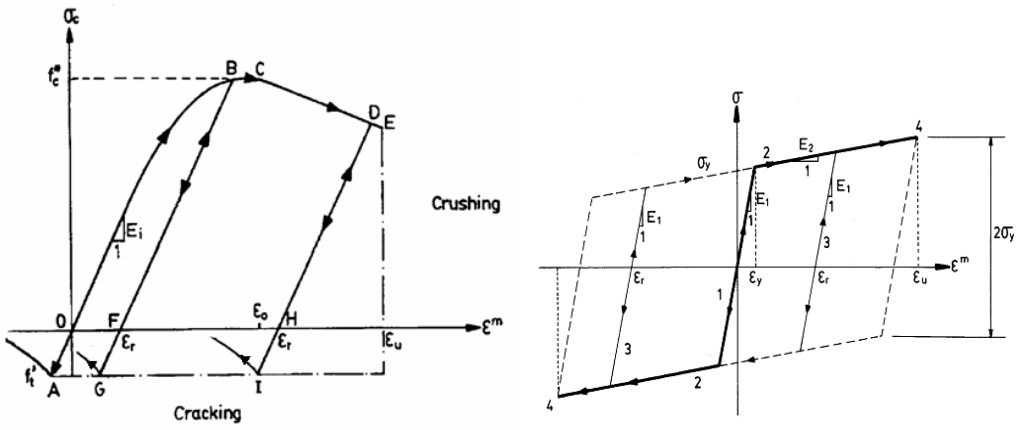

a) b)

Figure 2.4 – Constitutive models in CONS: a) concrete and b) steel (Marí 1984)

A trilinear model proposed by (Chan 1982) is considered to simulate the torsion of the element. This model considers three stages defined by different torque-twist (T_x-ϕ_x) linear

equations: cracking; full yielding of the reinforcement and ultimate failure. The unloading in each phase is assumed to be elastic, considering the initial stiffness.

Pertaining to the time-dependent constitutive laws of concrete, the considered non-mechanical strains $\varepsilon^{nm}(t)$ in the instant of time t are due to creep $\varepsilon^{c}(t)$, shrinkage $\varepsilon^{sh}(t)$, aging $\varepsilon^{a}(t)$ and thermal $\varepsilon^{T}(t)$ effects:

$$\varepsilon_c^{nm} = \varepsilon_c^{c} + \varepsilon_c^{sh} + \varepsilon_c^{T} + \varepsilon_c^{a} \tag{2.16}$$

The total strain $\varepsilon^{t}(t)$ at each time step is given by the direct sum of the mechanical $\varepsilon^{m}(t)$ and non-mechanical $\varepsilon^{nm}(t)$ strains.

Regarding creep phenomenon, the increment of strain with time under sustained stress is determined through an age-dependent integral formulation based on a Dirichlet series (Bazant and Wu 1973). This analytical creep model is fitted, by means of the least squares method, to the empirical expression proposed by the Model Code 1990 (MC-90, CEB-FIP 1992). The linear relationship between stresses and long-term strains is assumed and the superposition principle is considered. Concrete shrinkage is taken as a non-stress and non-thermal influenced volume change caused by water losses from the concrete to the environment. The MC-90 code function is used in the numerical model to compute the shrinkage strain.

In the Model Code 2010 (MC-2010, FIB 2010), new empirical relations for creep determination calibrated on the basis of laboratory tests are proposed, resulting into smaller values of the creep coefficient, comparatively with the MC-90. Pertaining to shrinkage, in the MC-2010, total shrinkage is subdivided into autogenous and drying shrinkage, resulting into higher swelling strains in comparison with the MC-90.

The decrease in the mechanical strain due to aging of concrete is considered through a correction stress factor. This factor is a function of the mechanical strain at each time step (Marí 1984). Lastly, temperature strains occur when the section is subjected to a temperature gradient and is determined through the coefficient of thermal expansion of the material (Marí 1984).

In the basic model, the time-dependent strains are uniaxial. In the proposed model, this time-dependent analysis procedure was maintained. However, due to the presence of shear stresses, the analysis capabilities were enlarged from the 1D to the 2D stress states. For this

reason, a more detailed description of the modelling of the long-term deformations is given in Chapter 5 for the case of 2D stress-strain states.

2.2.1.4. Geometric nonlinearity

To account for the geometric non-linearity, an updated Lagrangian Formulation is used (Chan 1982).The stiffness matrix and the internal forces of each element are determined with reference to local coordinates. Then, before assemblage of the global equilibrium equations, the local coordinate systems are transformed to global coordinates through a transformation matrix. In the analysis considering geometric nonlinearity, this transformation matrix is continuously updated in each increment of nodal displacement to account for the relative displacements between the two ends of the element. Thus, the local system for each element is continuously changing directions as the structure deforms.

The geometric nonlinearity is also considered through the nonlinear form of the strain displacement relationship, as

$$\varepsilon_x = \underbrace{\frac{du}{dx}}_{\text{Linear term}} + \underbrace{\frac{1}{2}\left[\left(\frac{du}{dx}\right)^2 + \left(\frac{dv}{dx}\right)^2 + \left(\frac{dw}{dx}\right)^2\right]}_{\text{Nonlinear term}} \tag{2.17}$$

The geometrical stiffness matrix K_g is obtained by substituting the shape functions of the Hermitian element on the nonlinear term of Eq. (2.17),

$$k_g = \int_V C^T \sigma C \; dv \tag{2.18}$$

where C is the matrix that represents the nonlinear relation between displacements and strains, and is added to the elastic stiffness matrix K_e. Hence, the assemblage of the global matrix is performed with the total element stiffness K_e+K_g, and the equilibrium equations take the form of:

$$F_e = (K_e + K_g).d_e \tag{2.19}$$

which is solved in order to determine the displacements within the iterative scheme of Newton-Raphson.

2.2.2 Prestressing steel

The effect of prestress (in pre- and post-tensioned structures) is considered as an equivalent load vector that is in equilibrium with the forces of the prestressing tendons (Figure 2.5). On one hand, the contribution of prestress to the element end forces is determined by the transformation of the prestress force into equivalent nodal loads and bending moments. On the other hand, the prestress steel contribution to the stiffness of the element is added (after bonding in the case of post-tension) assuming an average eccentricity of the tendon segment; conversely, elastic increments of prestressing forces are also considered after bonding.

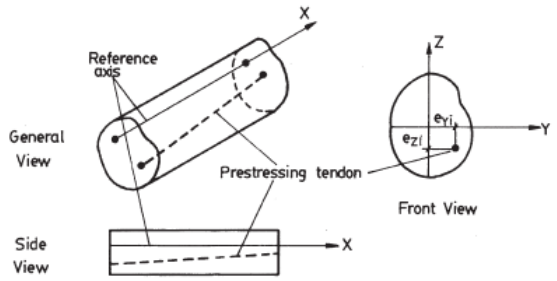

Figure 2.5 – Prestressing consideration in CONS (Marí 1984)

A multilinear stress-strain curve is used for prestressing steel. The prestressing losses due to friction and anchorage slip are considered in the determination of the prestressing forces acting at each time-step (Van Greunen 1979). Stress relaxation is also taken into account through the relaxation curve proposed by (Magura, Sozen et al. 1964).

2.2.3 Time-dependent analysis

The time step-by-step analysis scheme allows accounting for the time-dependent phenomena of creep, shrinkage, aging and temperature variations. A step-forward integration is performed by continuously adding the results obtained at each time step to the previous ones, until reaching the end of the analysis.

The increment of non-mechanical strains $\Delta\varepsilon^{nm}$ occurring during a time interval, from time t_{n-1} to t_n, is evaluated first. Afterwards, the initial strain approach (Kabir 1976) is adopted to compute the structural response during a time-step due to the non-mechanical strains. In this manner, the correspondent equivalent nodal load increment due to non-mechanical strains ΔF^{nm} at time t_n is given by

$$\Delta F^{nm} = \int_V B^T D \Delta \varepsilon^{nm} \, dv \tag{2.20}$$

Thus, the load increment to be applied in the structure ΔF_n at the instant t_n is determined by adding ΔF^{nm} to the increments of external nodal load ΔR^i_n and the unbalanced load vector left over from the previous time step ΔR^u_{n-1}.

2.2.4 Segmental construction features

The phased characteristic of the model CONS allows accounting for modifications occurring during the life-time of a structure. This includes the simulation of segmental construction procedures and subsequent later changes, in which repair and strengthening interventions are included. In a specific manner, in each construction phase, any variation of transversal and longitudinal geometry, structural scheme, connections between elements, boundary conditions, applied loads and materials properties can be reproduced by the numerical model.

Schematic representations of several segmental constructed structures are presented in Figure 2.6: a) segmental constructed bridges requiring continuous changing of the longitudinal scheme and b) segmental constructed cross-sections requiring evolutionary transversal scheme, which encloses changes on the geometry and reinforcement of the cross-section.

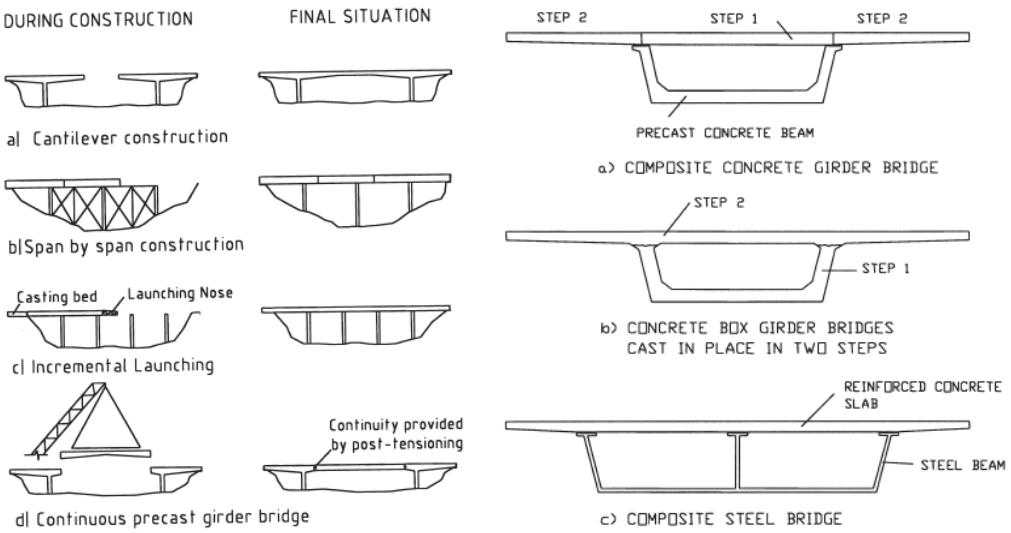

Figure 2.6 – Segmental construction: a) longitudinal and b) cross section (Marí 2000)

Another relevant feature of the model is the fact that each cross section is composed by several filaments that can be made from different concrete and steel types, with different active and removal timings. For this reason, it is possible to simulate deterioration and repair procedures, such as: loss and replacing of concrete and reinforcement, sealing of cracks, enlargement of concrete cross section and adding of reinforcement, external prestressing, repair the cross section with different materials, etc.

2.2.5 Code organization

The computer algorithm that implements CONS was originally written in FORTRAN77 language, and presents a module configuration in a way that can be improved by changing, adding or replacing subroutines. In a general manner, the basic model presents four loops, as it is schematically represented in Figure 2.7: (*i*) constructive phases, (*ii*) time steps, (*iii*) load steps and (*iv*) iterative procedure.

Pertaining to the outer loop, in each construction phase changes on longitudinal and transversal geometry, loading and boundary conditions may take place. Therefore, data about structural geometry, external joint loads, temperature distributions and material constitutive laws have to be compiled at the start of each phase.

Subsequently, the time that passes from one constructive phase to another is divided into time steps. In each time step the materials' properties are updated and the increments of non-mechanical strains and the correspondent equivalent load vector ΔF^{nm} are computed. The load vector F is also updated.

Then, the total load obtained in each time step F is divided into several load steps ΔF. In each load step, the global equilibrium equations, which account for the nonlinear response of the materials at the current stress stage, are solved through the direct stiffness method.

In the inner loop, the iterative Newton-Raphson procedure is performed within each load step until convergence is achieved. The convergence can be controlled either by norms of loads, displacements or sectional strains. In this manner, it is possible to trace the structural load-displacement curve along the different stages of the material behaviour: elastic, inelastic (cracking included) and ultimate ranges.

The basic model was reorganized in the ambit of this work in order to be able to clearly identify the different levels of analysis within a structure, and to be ready to incorporate the

proposed shear formulation. Although, the general loops formerly described were maintained.

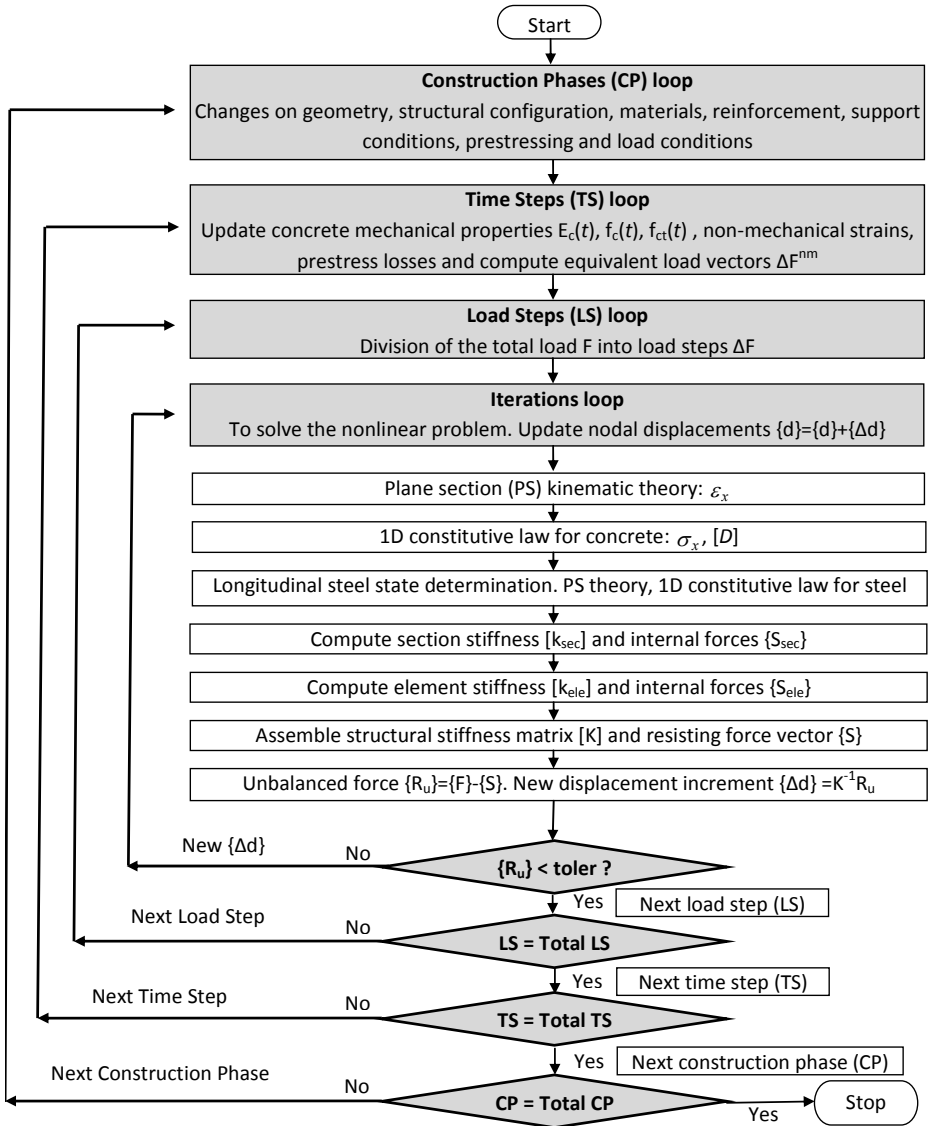

Figure 2.7 – General scheme of the nonlinear and time-dependent model CONS

2.2.6 Applications

The nonlinear model CONS has been extensively validated and used for performing structural analyses of flexural dominant cases, some examples are (Marí 1984; Marí and Valdés 2000; Marí 2000; Marí and Bairán 2008). These analyses comprised theoretical and parametric studies, modelling of laboratorial tests and practical applications regarding

existent structures. From the many conducted applications, four cases are pointed out in the following, representing the type of analyses and results that are possible to accomplish with the model CONS.

For consulting purposes during the design phase, a nonlinear analysis of the 250m span arch bridge Los Tilos (Figure 2.8) was carried out. The bridge was segmentally constructed and the presence of important transversal and longitudinal loads demanded accurate numerical studies to predict structural safety and functionality, both during the constructive process and also along its service life. The nonlinear model allowed ensuring that the dimensions, materials, support conditions and constructive method complied with the functionality and security demands (Marí 2003).

Figure 2.8 – Los Tilos bridge analysed with CONS (Marí 2003)

The experimental tests performed by (Souza and Appleton 1997b) on RC beams previously damaged in flexure and subsequently strengthened were simulated with the model CONS (Figure 2.9). The strengthening measures consisted on the application of extra longitudinal steel and enlargement of the concrete cross-section web (Figure 2.9c). As the model is able to take into account the effects of existing damages previously to the strengthening interventions, a very good fitting between the numerical and experimental results was achieved, as can be observed in Figure 2.10 (Marí and Bairán 2009).

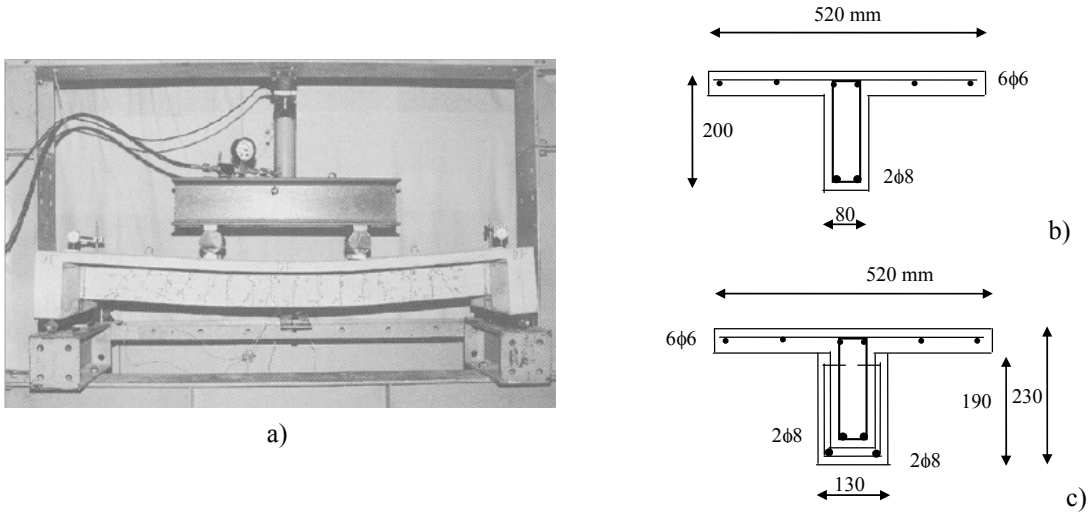

Figure 2.9 – Experimental tests on flexural damaged and subsequently strengthened RC beams by (Souza and Appleton 1997): a) load test, b) cross section of the damaged beam and c) cross-section after strengthening

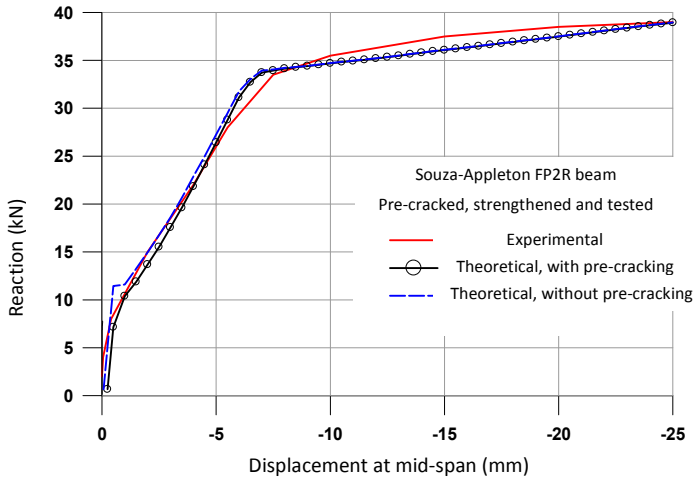

Figure 2.10 – Force-displacement curve of the beam after strengthening (Marí and Bairán 2009)

A theoretical application analysis of a 3-span continuous RC pedestrian bridge affected by corrosion of the upper reinforcement and concrete cover of the top face was also carried out with the nonlinear model CONS (Figure 2.11). The efficiency of a retrofit measure consisting on replacing the degraded concrete by a new and thicker layer was studied, by evaluating its performance during service time and in failure. The predicted reduction of the carrying capacity of the bridge due to the development of corrosion with time is presented in Figure 2.12a. In addition, the computed deflection at the central section of the bridge is depicted in Figure 2.12b, for the cases with and without degradation, and after being retrofitted. It was observed that the retrofit measures avoids the collapse and keeps

the deflection parallel to the curve without degradation, although an increment of the deformations is observed due to the initial damage.

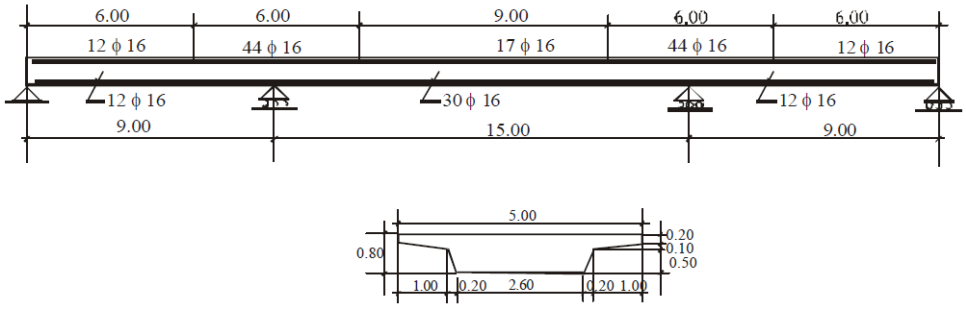

Figure 2.11 – Elevation and cross section of the RC pedestrian bridge (Marí and Bairán 2008)

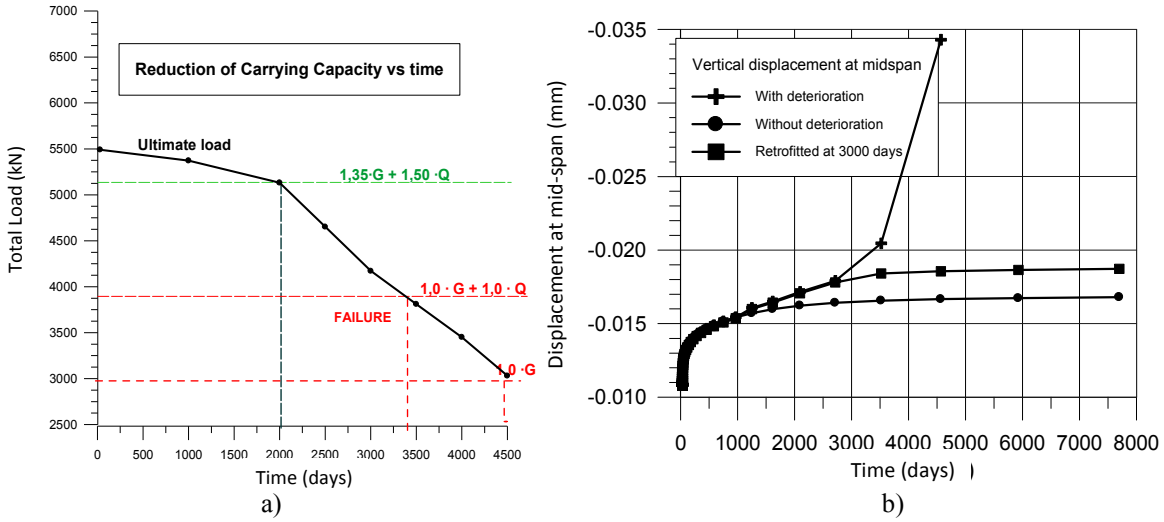

Figure 2.12 – Predicted response of a RC pedestrian bridge with time: a) load carrying capacity and b) displacement at mid-span (Marí and Bairán 2008)

The long-term behaviour under sustained load of a continuous precast concrete girder bridge was studied through a laboratorial test, and it was also simulated with the numerical model CONS (Marí and Valdés 2000). The model consisted on a 24m long post-tensioned continuous box girder bridge beam with two spans and a U-shape cross-section (Figure 2.13a). It was segmentally constructed in laboratory accordingly to the phases presented in Figure 2.13b. The computed results achieved a very good agreement with the experimental data (Figure 2.14), demonstrating its capability to simulate complex time-dependent structural behaviour. The proper simulation of the construction process showed to be essential in the correct prediction of the latter response of the beam.

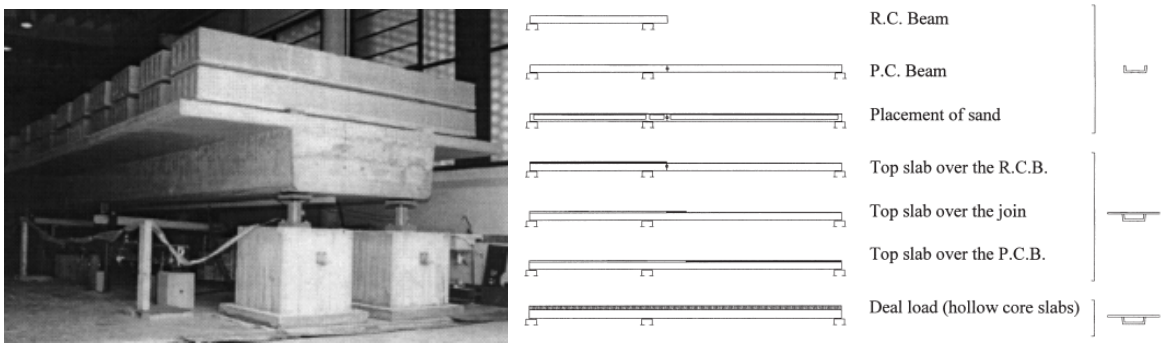

a) b)

Figure 2.13 – Study of the long-term behaviour of a continuous precast concrete beam under sustained load: a) experimental model in the laboratory and b) construction process (Marí and Valdés 2000)

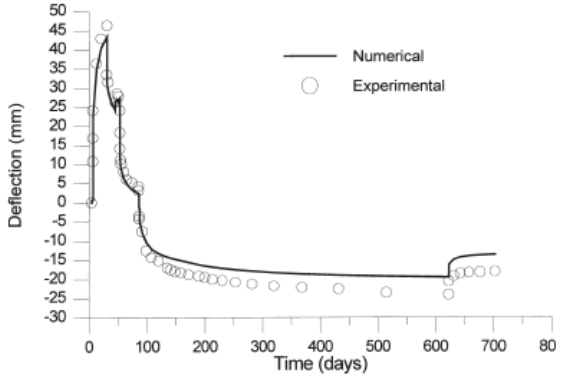

Figure 2.14 – Deflection at the centre of the longest span (Marí 2000)

The presented examples demonstrated that the model CONS is a powerful tool for assessment of structures during design, construction, service and ultimate stages. It is also capable of evaluating the serviceability and durability performance during the life-time of damaged and degraded structures, as well as predicting the efficiency of strengthening and retrofit measures. Moreover, for the cases of dominant bending loading, its accuracy and aptness for a very wide range of structural applications has been demonstrated.

In fact, what motivated most the extension of this numerical model to the cases where shear effects are dominant or cannot be neglected was the good past experience in analyzing and assessing complex structures. Actually, the potential and accuracy of this numerical tool, as well as its range of applications and studies, will increase significantly with the incorporation of a nonlinear element with due account of shear.

2.3 Shear models for RC

2.3.1 Mechanisms of shear resistance

The research on the shear resistance mechanism of RC beams goes back to end of the 19th century with the appearance of steel strips as stirrups in the constructions. It was after the work of Ritter and Mörsch (Figure 2.15a) that a proposal for the determination of the shear behaviour and shear capacity appeared: the truss model. This model explains the shear carrying mechanism of a RC beam through a truss analogy (Figure 2.15b): the flow of stresses is idealized as a series of diagonal concrete struts in compression (shaded concrete strips) and tension ties of reinforcement; the force components in each element are determined through statics. This approach is the basis of the current shear design methods.

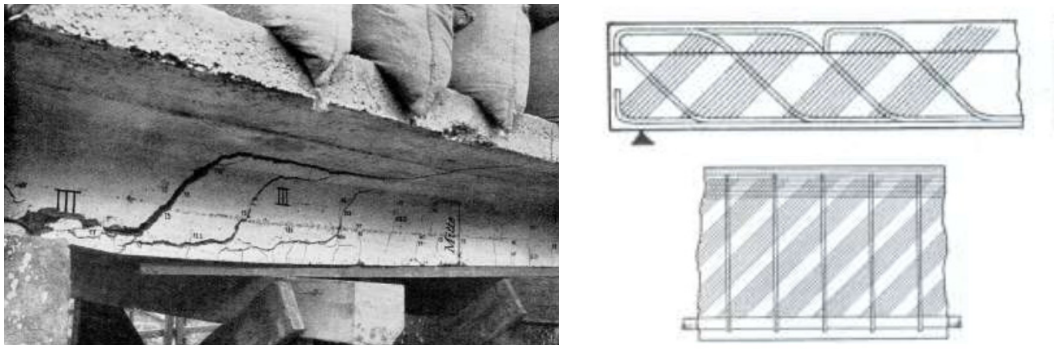

a) b)

Figure 2.15 – Research on shear by Mörsch in 1908: a) shear failure of a T-shape beam without stirrups and b) truss model (adapted from Balázs 2010)

Leonhardt and Walther (1961), through their early experimental tests on shear critical RC beams, stated that the complexity of the shear mechanism is the large number of parameters involved and the difficulty to understand each one in a separate manner and its influence on the other parameters. Accordingly, as conclusions of the experimental campaign, the factors affecting the shear strength of RC beams were settled as: the quality of concrete; the degree of reinforcement; the quality of the bond between the reinforcement and the concrete; the curtailment of flexural reinforcement; the quality of the anchorage of the reinforcement bars; the shape and the effective depth of the cross-section; the type of loading and the moment-shear ratio.

As explained by (Park and Paulay 1994), shear is resisted in a RC element via two mechanisms: the beam-action and the arch-action. As the shear force is the derivative of the bending moment, it consists of two terms: (*i*) variation in the flexural forces acting with

a constant lever arm (beam-action) and (*ii*) constant flexural forces acting with a variable lever arm (arch-action). Pertaining to beam elements, the contribution of the beam-action is usually more important than the arch-action. The former is only important after yielding, when the neutral axis experiments relevant variation or bond-slip of the longitudinal reinforcement occurs.

The load carrying mechanism of a beam involves a system of principal tensile and compressive stresses that continuously change directions and magnitudes along the different cross sections. The resistance mechanism of a cracked RC element subjected to shear is composed by a sort of different contributions of forces (Figure 2.16a): shear stresses in the uncracked compression zone, shear stresses along the crack plane by means of aggregate interlock, dowel action of the longitudinal reinforcements and, residual tension transferred along the crack plane.

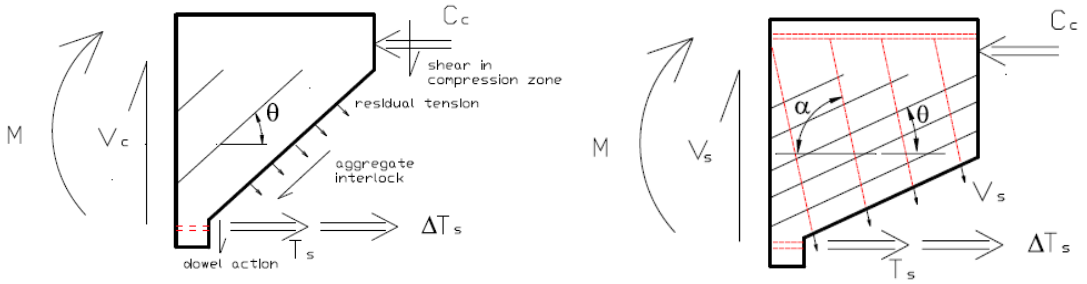

Figure 2.16 – Mechanism of shear resistance: a) concrete and b) transversal reinforcement (Bairán 2005)

The presence of stirrups in RC beams introduces a truss resisting mechanism (Figure 2.16b). Strut-and-tie models, which are based in this mechanism, are the more widely used methods to design RC beams in shear. This design methodology is based on the theory of plasticity and, for that reason, it is more representative of the ultimate loading state. Apart from the truss-action, transversal reinforcement also provides support for the dowel action of the longitudinal steel, contributes to aggregate interlock by limiting the crack width and increases the confinement in the areas under compression and the bonding resistance.

When the principal tensile stresses reach the tensile strength of concrete, cracks perpendicular to these principal stresses appear. In a beam under concentrated or distributed loading, vertical cracks appear in the pure bending areas and diagonal cracks appear in the web in regions with high shear stresses (Figure 2.17a). Shear cracks can also appear as a development of existent vertical cracks. The formation of cracks causes the

transference of the sustained stresses to the transversal reinforcement and the diagonal compression concrete struts. This stress transference is highly dependent on the geometry of the cross-section and on the quantity and direction of the stirrups.

Hence, different shear failures may occur in RC beams: (*i*) 'diagonal tension failure' (Figure 2.17b), which happens when diagonal cracks pass through the transversal reinforcement, the beam is separated in two pieces and the longitudinal steel is pushed to the bottom (this mechanism is also typical of beams without transversal reinforcement, failure occurring suddenly through a main diagonal crack); (*ii*) 'web reinforcement failure', when the transversal reinforcement yields and fails in the truss-mechanism generated in beams with numerous shear cracks, *(iii)* 'web compression failure' (Figure 2.17c), which occurs when the stresses on the diagonal struts reach the compressive strength of concrete and crush before yielding of the stirrups and, *(iv)* 'anchorage failure' (Figure 2.17d), when there is a loss of anchorage of the longitudinal reinforcement in the support, and the compressive struts lose support and the beam fails in shear along the web.

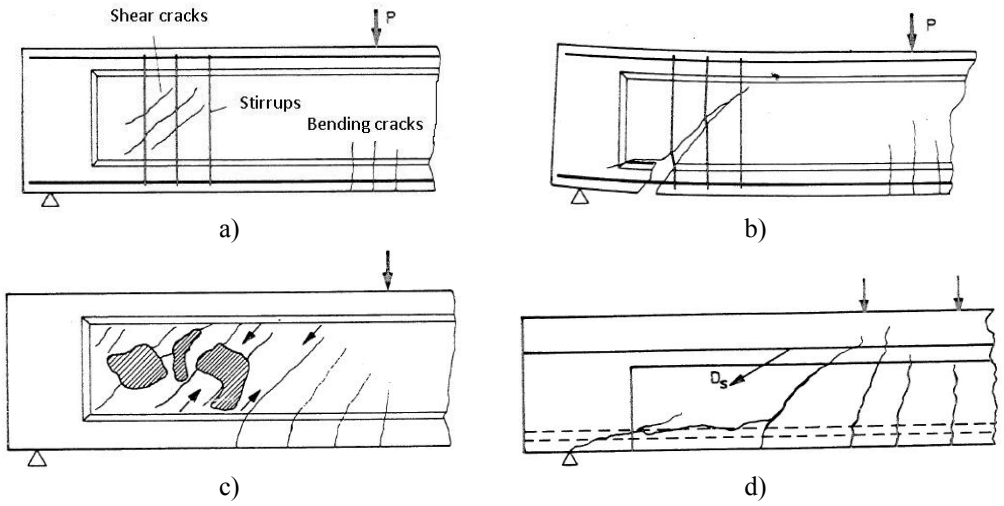

Figure 2.17 – Shear in RC beams: a) cracking, b) diagonal tension failure, c) web crushing failure and d) anchorage failure (Leonhardt 1988)

From the time of Ritter and Mörsch until nowadays, and especially during the last decades, extensive experimental campaigns were carried out, focusing on different aspects of the shear mechanism. From all this experimental research a huge quantity of empirical formulations appeared, and a variety of models for the shear resistance mechanism of RC had been proposed; a general research review on this topic is given in (Collins, Bentz and Sherwood 2008). In that prominent research work, many aspects about the shear resistance mechanism of plain and reinforced concrete were discussed: concrete contribution to shear

resistance; effects of prestressing; size effect; minimum quantity of transversal reinforcement; inclination of the main diagonal cracks; concrete-steel bonding; influence of force's interaction; etc. Even tough, due to complexity of the mechanisms and the large number of parameters involved, diverse cumbersome issues remain unclear and, for this reason, consensus and generality on shear resistance of RC elements has not been accomplished.

The complexity of the phenomenology of shear in RC is reflected on the difficulty to find solutions for its computational modelling. In fact, the development of nonlinear FE models allowed performing shear analyses of RC structures. However, these powerful FE models are still struggling with the accuracy of constitutive models and the very high demands of computational resources, instability and convergence problems (Broo 2008). Pertaining to frame models with inclusion of shear effects, it is aimed to give accurate solutions with low computational time requirements. In this ambit, the existent proposals essentially distinguished from each other in terms of the shear kinematic assumptions taken at the sectional level, and to the type of multiaxial constitutive equations, as it will be discussed in the following.

2.3.2 Constitutive models

In the fibre beam formulations, the nonlinear responses of the element and section are directly determined from the nonlinear behaviour of the fibres. Consequently, the accuracy of the results is directly correlated on the precision of the constitutive models. In the case of the traditional fibre beam elements, since only normal stresses are considered, the constitutive laws are limited to the uniaxial case. When shear is considered, the fibres are no longer under a uniaxial stress-strain state. In this manner, suitable constitutive models able to account for diagonal cracking and multiaxial strain-stress states are essential to incorporate shear effects into fibre beam models.

However, modelling the concrete behaviour under multiaxial strain-stress states is not a straightforward task. Aspects such as cracking for low stresses levels, nonlinear relationships between stresses and strains, the different concrete behaviour under compression and tension, and the softening phenomena, generate a very anisotropic behaviour when concrete is submitted to multiaxial stress states.

There is a wide variety of constitutive models for the analysis of RC structures under multiaxial stress states. Some examples are: (*i*) the microplane models proposed by (Bazant and Ozbolt 1990; Ozbolt and Bazant 1992; Carol, Prat and Bazant 1992; Carol and Bazant 1997); (*ii*) the damage and fracture mechanics models proposed by (Bazant and Oh 1985) and; (*iii*) the plasticity models (Chen 1982). A comprehensive review on this topic can be found in (CEB 1996).

The smeared crack models, in turn, consider cracking as a distributed effect with directionality and cracked concrete is simulated as a continuous medium with anisotropic characteristics (Petrangeli and Ozbolt 1996). This approach is particularly suitable for fibre beam models considering combined loading, as the information about the direction of damage is remitted to a single integration point.

By seeking for a rational and general model for the behaviour of RC in shear, an extensive experimental campaign was carried out in the University of Toronto, involving tests of RC panels subjected to bi-dimensional stress states (Figure 2.18). The Modified Compression Field Theory – MCFT (Vecchio and Collins 1986) was developed by Vecchio and Collins in 1982 in the context of this experimental work, as a smeared-crack model with rotating cracks, considering cracked concrete as a material with their own stress-strain relationships. The main assumptions of the MCFT are (Figure 2.19):

- the reinforcement is considered smeared in concrete,
- cracks are distributed in concrete and are able to rotate continuously,
- loads are applied uniformly in the element,
- equilibrium and compatibility equations are evaluated through the average value of the stresses and strains both in the crack plane and in the concrete between cracks,
- local check of the stress state is performed at the crack plane to account for the possible steel yielding,
- principal directions of the stress and strain tensors coincide,
- MCFT is loading history independent
- it assumes perfect bond between reinforcement and concrete,
- shear stresses in the reinforcement are assumed as null,
- independent constitutive relationships are considered for concrete and steel.

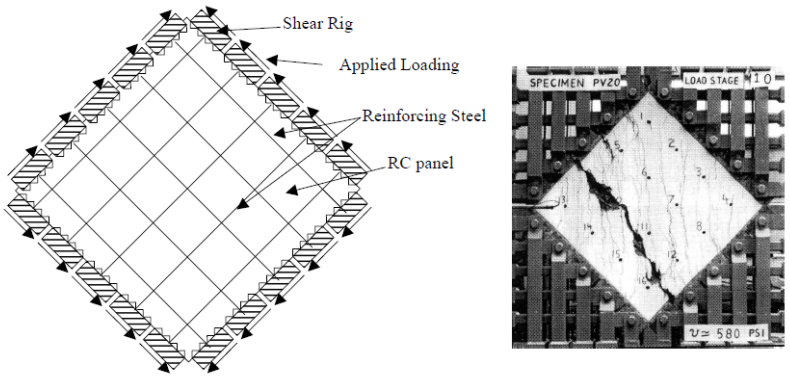

Figure 2.18 – RC panel element tested by (Vecchio and Collins 1986)

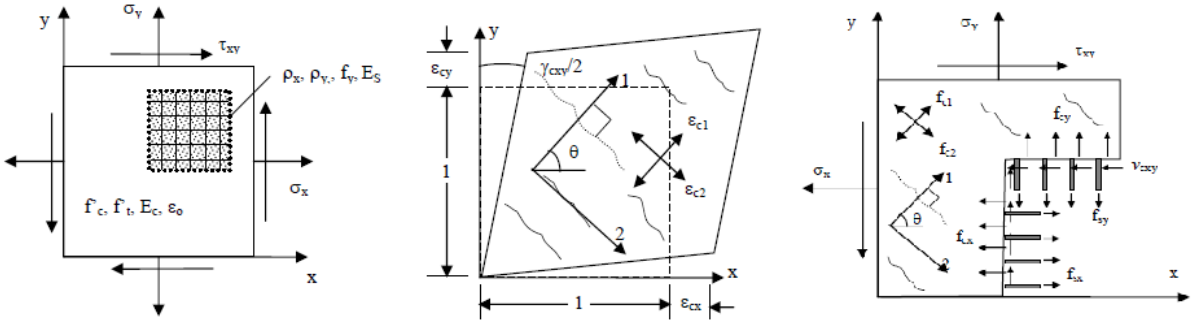

a) b) c)

Figure 2.19 – MCFT: a) RC panel subject to in-plane stresses; b) average concrete strains; and c) free body diagram (Wong and Vecchio 2002)

The Disturbed Stress Field Model – DSFM was presented by (Vecchio 2000) as a further improvement of the MCFT, motivated by the experimental observation of the different principal angles of the stress and strain tensors after cracking and yielding. Thus, DSFM is a mixed formulation of fully rotating-crack and fixed-crack approaches, in which the principal directions of stresses and strains do not coincide; this difference is taken into account as a shear crack-slip through a strain offset.

Parallel to the development of the MCFT, in the University of Houston an experimental campaign on the behaviour of RC membranes was carried out by Hsu and his group. As result, a theory named Rotating-Angle Softened Truss Model - RA-STM (Hsu 1988) was developed, differing from the MCFT on the softening model and stress-strain relationships for concrete in compression and tension. The tension-stiffening model in el MCFT is referred to the concrete and requires checking the crack state (control of the aggregate interlock), whilst in the RA-STM it is referred to the steel. In this manner, safety check at the crack level is not necessary in the RA-STM, as the stress-strain relation for steel

already takes into account the possibility of local yielding at the crack. In addition to this model, the Houston group also proposed the Fixed-Angle Softened Truss Model - FA-STM (Pang and Hsu 1996), which assumes that concrete struts remain with the same inclination as the initial cracks, which can be defined as the principal stress directions in concrete at the onset of cracking.

The constitutive model OU3DC proposed by (Bairán 2005) and used by (Mohr 2011) is based on the rotating-smeared crack approach, dividing the total strains in two components, the mechanical and non-mechanical strains. The mechanical strain component reflect the changes in the stress state and the non-mechanical strain component represent an offset that is not directly related with the state of the material (may include the influence of temperature and time-dependent deformations). In turn, the mechanical strain is decomposed in an elastic (fully recovered after unloading) and a plastic (remaining after unloading) part. The backbone equations for concrete in compression and tension are defined in each principal direction. The current compression strength and cracking stress in the backbone curves are determined through a 3D failure surface of Willam and Warnke (Figure 2.20).The effects of confinement of the transversal steel are accounted for in the model. A model for lateral deformations of concrete under cyclic uniaxial compression developed by (Osorio, Bairán and Marí 2012) is considered. For reinforcement, uniaxial models are used.

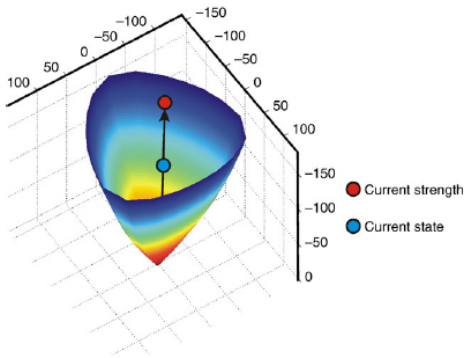

Figure 2.20 – 3D failure surface for the constitutive determination of the concrete state (Bairán and Marí 2007)

The constitutive formulation used in the model proposed in this thesis is based on the MCFT. For this reason, a more comprehensive description of this formulation is presented in the following.

2.3.2.1. Modified Compression Field Theory

The MCFT consists in four sets of relationships: compatibility, equilibrium, constitutive laws and crack check.

Compatibility: Perfect bond between concrete and steel is considered. In this case, the average strain in concrete is equal to the average strain in the reinforcement (Figure 2.21a).

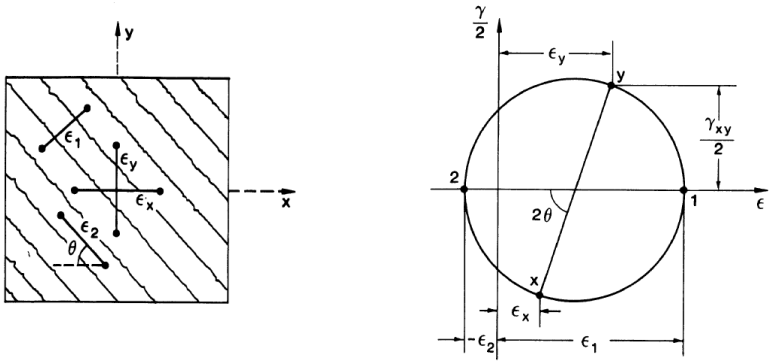

a) b)

Figure 2.21 – Compatibility assumptions in MCFT: a) average concrete strains and b) Mohr´s Circle of average strains (Vecchio and Collins 1986)

Through the 2D strain state of the element (ε_x, ε_y, γ_{xy}), the average concrete principal strains (ε_{c1}, ε_{c2}) and the principal strain direction $\theta_{\varepsilon 1}$ (assumed to be equal to the principal stress direction), can be determined through the Mohr's circle of strains (Figure 2.21b):

$$\varepsilon_{c1} = \frac{\varepsilon_x + \varepsilon_y}{2} + \frac{1}{2}\sqrt{\left(\varepsilon_x + \varepsilon_y\right)^2 + \gamma_{xy}{}^2} \tag{2.21}$$

$$\varepsilon_{c2} = \frac{\varepsilon_x + \varepsilon_y}{2} - \frac{1}{2}\sqrt{\left(\varepsilon_x + \varepsilon_y\right)^2 + \gamma_{xy}{}^2} \tag{2.22}$$

$$\theta_{\varepsilon 1} = \frac{1}{2}\tan^{-1}\left[\frac{\gamma_{xy}}{\varepsilon_x - \varepsilon_y}\right] \tag{2.23}$$

Equilibrium: The resultant applied stresses in the *x*- and *y*-directions are resisted by the average stresses (Figure 2.22), composed by the stresses in concrete (f_{cx}, f_{cy}) and in reinforcement (f_{sx}, f_{sy}). The externally applied shear stress is balanced by the average shear stress in concrete v_{xy}. The reinforcement is considered smeared through the ratios ρ_x, ρ_y in the *x*-and *y*-directions, and average stresses in concrete can be determined by applying the Mohr's circle (Figure 2.22c).

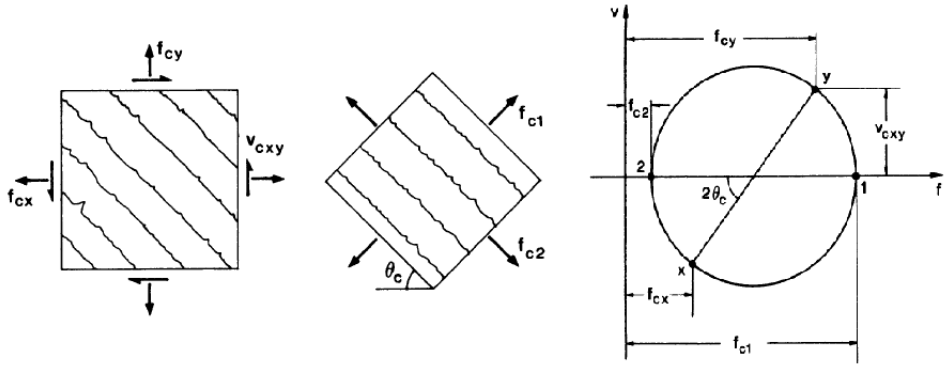

a) b) c)

Figure 2.22 – Equilibrium assumptions in MCFT: a) average concrete stresses; b) average concrete stresses in principal directions and; c) Mohr's circle of average stresses (Vecchio and Collins 1986)

Constitutive laws: The empirical stress-strain curves for the material modelling were derived through the experimental tests performed in the RC panels. Regarding concrete in compression, the constitutive laws relates the principal compressive stress f_{c2} with the principal compressive strain ε_{c2}. During the panel element tests, it was found that the stress-strain relations in cracked RC under 2D stress state are significantly different than the ones obtained in uniaxial element tests. In fact, the compressive strength and stiffness of cracked concrete decreases in the presence of the coexistent principal tensile strain ε_{c1} in the direction normal to compression. This phenomenon led to the development of the so-called 'compression softening formulation' (Figure 2.23a), in which the maximum compression stress in cracked concrete f_p is expressed as function of the principal tensile strain ε_1 (Vecchio and Collins 1986).

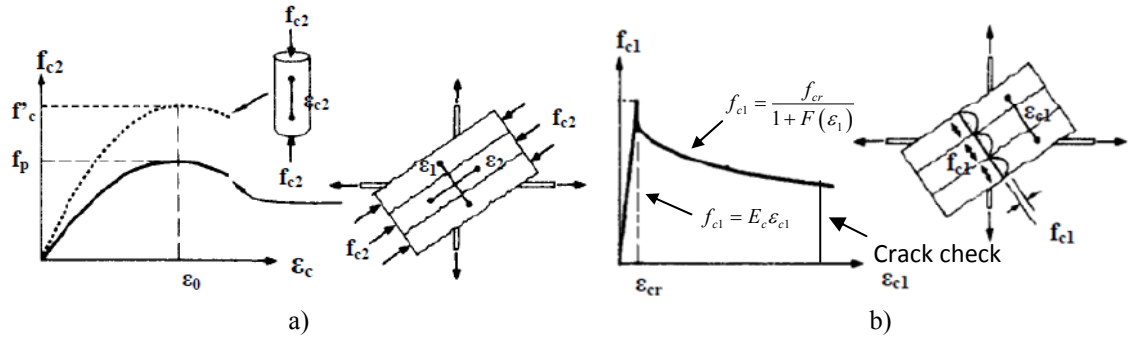

a) b)

Figure 2.23 – Constitutive models for concrete in MCFT: a) compression and b) tension (Vecchio and Collins 1986)

Concerning to concrete in tension (Figure 2.23b), the pre-cracking response is given by a linear function. The cracking strain ε_{cr} is determined as function of the concrete cylinder compressive strength f_c' through the ACI expression (ACI Committee 318 1995) or the

function proposed by (Bentz 2000). After cracking, tensile stresses are resisted by concrete between the cracks until high levels of tensile strains, corresponding to the so-called 'tension stiffening phenomenon', in which the tension stiffening factor $F(\varepsilon_1)$ (see expression in Figure 2.23a) was proposed by (Vecchio and Collins 1986), later modified in (Collins and Mitchell 1987) and more recently by (Bentz 2000).

Steel is simulated through a bilinear relationship, in both the x- and y-directions, between the average stresses (f_{sx}, f_{sy}) and the average strains (ε_{sx}, ε_{sy}).

Crack check: Tension stiffening allows concrete to carry average tensile stresses after cracking (Figure 2.24a). However, in a crack concrete does not carry tensile stresses, so an increment in the reinforcement is generated in order to equilibrate the average tensile stresses (Figure 2.24b). For this reason, the transmission of this stresses along the cracks requires ensuring that the reserve capacity of the reinforcement is not reached. Interface shear stresses v_{ci} in the concrete cracked surface develop as consequence of the local increment of reinforcement stresses. MCFT limits this value through the aggregate interlock mechanism formulation proposed by (Walraven 1981) (Figure 2.24c), which sets a limit to the concrete tensile principal stress, i.e., it limits the tension stiffening effects as:

$$f_{c1} \leq \frac{0.18\sqrt{f_c'}\tan\theta}{0.31+\frac{24w}{a+16}} \tag{2.24}$$

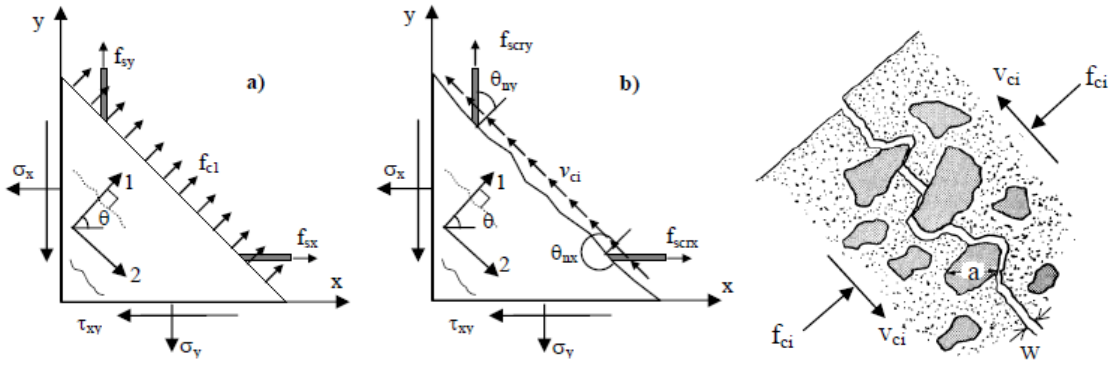

Figure 2.24 – Crack check in MCFT: a) average and b) local stresses at a crack (Wong and Vecchio 2002) and; c) Aggregate interlock (Vecchio and Collins 1986)

This limiting expression is a crucial procedure of the MCFT, as disregarding it can generate unsafe results. Though, crack check expressions are function of the average crack width w, considered as the product of the average concrete stress and the average spacing perpendicular to cracks, whose determination is not simple nor well defined. In conclusion,

the MCFT has proved to be a powerful tool in predicting the structural response of RC beams in shear.

2.3.3 Sectional kinematic approaches considering shear effects

The plane section hypothesis gives an adequate relationship between normal strains and stresses when a cross section is only submitted to normal forces. However, when tangential forces are applied this formulation is no longer valid due to the appearance of distortion. In fact, actual distribution of shear strains and stresses in the cross-section is complex and state-dependent, showing important variations while cracking is developing, and when approaching the ultimate state; in addition, it also depends on the geometry and distribution of the reinforcement.

The presence of shear forces generates a variation of the bending moments along the beam's axis. Due to this bending increment, a fibre in the longitudinal direction is submitted to an increment of axial stresses that are equilibrated by out-of-plane stresses, as deduced by Jourawski in 1856 (Figure 2.25).

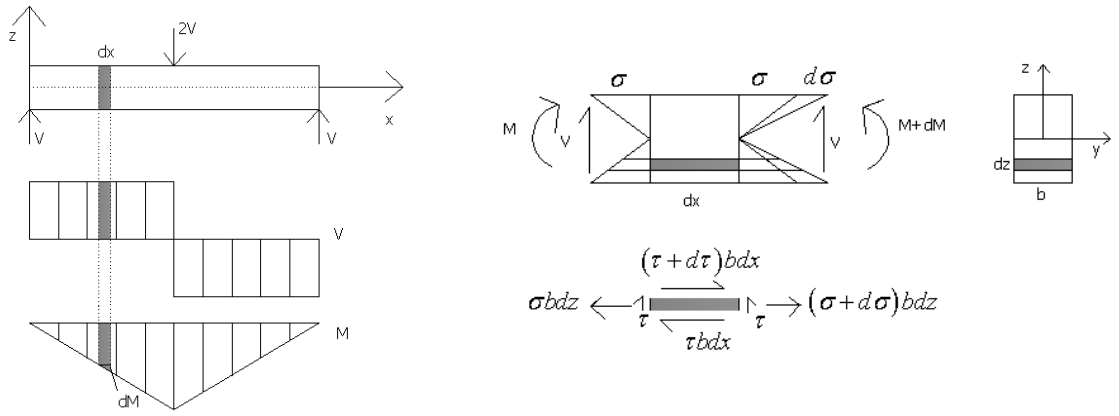

a) b)

Figure 2.25 – In plane shear stresses in a beam deduced by Jourawski in 1856: a) internal forces in a beam and b) equilibrium in a fibre

Hence, the equilibrium equation of the fibre is given by:

$$\frac{\partial \sigma_x}{\partial x} + \frac{\partial \tau_{xz}}{\partial z} = 0 \tag{2.25}$$

and the shear stress at any point of the section $\tau_{xz}(z)$ can be written as:

$$\tau_{xz}(z) = -\frac{1}{b}\int_0^z \frac{\partial \sigma_x}{\partial x} b dz \tag{2.26}$$

In case of isotropic-elastic material, the solution for the former equation is straightforward and well-known:

$$\tau_{xz}(z) = -\frac{1}{b}\int_0^z \frac{Vbz}{I} dz = \frac{VQ(z)}{Ib(z)} \tag{2.27}$$

where Q(z) is the first moment of area integrated from the bottom of the section to point z and $b(z)$ is the width of the cross section at the coordinate z. By means of the elastic tangential modulus G, the shear strain γ_{xz} can be directly written as:

$$\gamma_{xz}(z) = -\frac{1}{Gb}\int_0^z \frac{Vbz}{I} dz = \frac{1}{G}\frac{VQ(z)}{Ib(z)} \tag{2.28}$$

However, due to the different nonlinear responses along compression and tension, cracked concrete presents a strong anisotropic behaviour, in which coupling of normal and tangential stresses and strains appears. In this case, the determination of shear stresses and strains along a cracked cross section becomes a difficult task, as it is dependent on the state of the material and on the sectional geometry. Hence, this problematic is the essence of the difficulty of modelling nonlinear response of RC sections with the presence of shear forces. In this manner, finding a solution or approximation for Eq. (2.27) and Eq. (2.28) is the basis for a kinematic constraint to model shear in cracked RC sections (Bairán and Marí 2007).

In attempting to extend frame models to loading conditions that include shear effects, several theories for the kinematic sectional response under tangential and normal forces were developed. In this manner, sectional kinematic models for RC under coupled loading forces can be divided in two general groups:

(*i*) 'The approaches considering the inter-fibre equilibrium', where shear stress-strain distributions are state-dependent and consequently change during loading. These approaches are equivalent to the force-based sectional model, as internal equilibrium between fibres is satisfied. Models that belong to this group are highly complex, and are able to consider force-interaction in its formulation with high accuracy. However, its high complexity and computational demanding limit their straightforward application in fibre beam models. The models Dual Section Analysis (Vecchio and Collins 1988),

Longitudinal Stiffness Method (Bentz 2000), TINSA (Bairán 2005) and the model of (Mohr 2011) belong to this type and are subsequently described.

(*ii*) 'The fixed pattern approaches', where an *a priori* fixed kinematic constraint is assumed in the cross section. These approaches are equivalent to the displacement-based sectional model, and estimate the internal shear stress-strain distribution in the cross section (τ-γ) by assuming a shear strain or stress pattern constant during the whole loading process (Vecchio and Collins 1988). The inter-fibre equilibrium, in these cases, is not directly verified, as compatibility in the transversal direction is not guaranteed. These proposals are less computational demanding and less accurate than the previous ones.

A comprehensive state of the art report on sectional models for RC elements under tangential and normal forces is offered in (Bairán and Marí 2007). The sectional kinematic models with more relevance to the development of this thesis are presented in the following section.

2.3.3.1. Dual Section analysis

The Dual Section analysis was originally proposed by (Vecchio and Collins 1988), pretending to solve numerically the gradient of normal stresses generated by the presence of shear forces (Figure 2.25), by applying the Finite Difference Method (Figure 2.26a):

$$\frac{\partial \sigma_x}{\partial x} \approx \frac{\sigma_x(x_2) - \sigma_x(x_1)}{s} \tag{2.29}$$

in which it is required the evaluation of the normal stresses in two different sections ($\sigma_x(x_1)$, $\sigma_x(x_2)$), separated by a distance s. From the equilibrium of the two controlled sections, the distribution of shear strains and stresses is determined through an iterative procedure, schematically presented in Figure 2.26b.

It is clear that this proposal is not a sectional model as it needs information outside the section. Also, a special beam element has to be formulated in order to integrate separately shear and bending. Besides being a rigorous analysis approach where inter-fibre equilibrium is accomplished, it is time consuming, has problems of stability and cannot be introduced easily into a FE code as an independent sectional model.

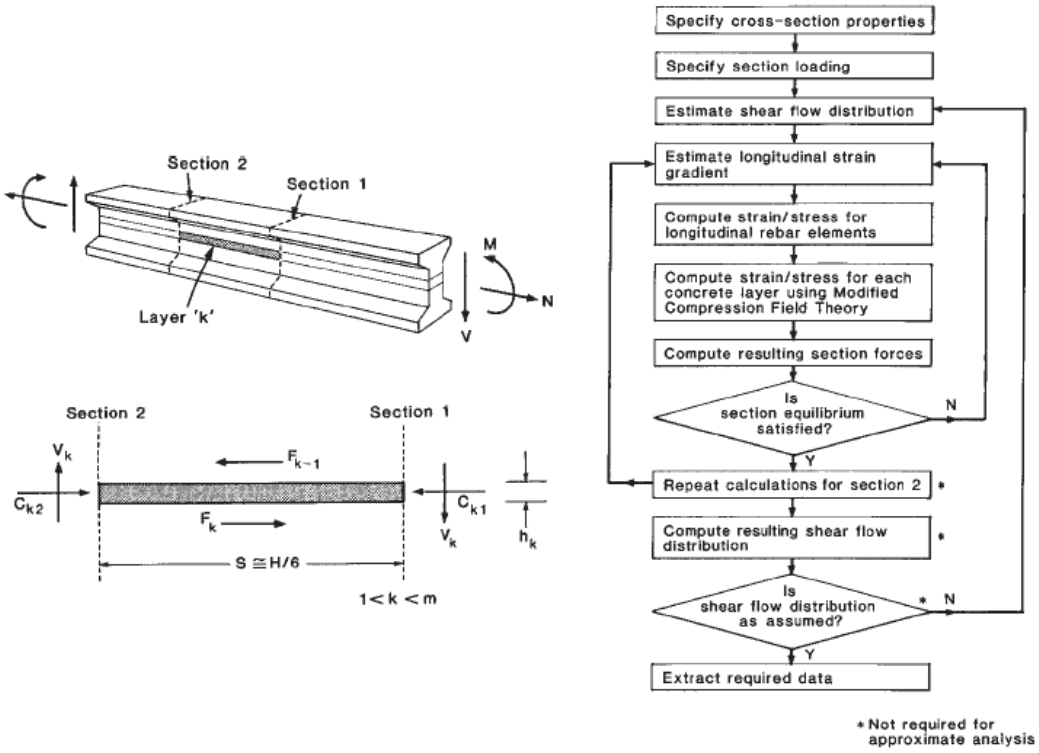

a) b)

Figure 2.26 – Dual section analysis: a) body diagram of a concrete fibre and b) solution procedure (Vecchio and Collins 1988)

2.3.3.2. The Longitudinal Stiffness Method

The Longitudinal Stiffness method is a local sectional model that satisfies inter-fibre equilibrium and was proposed by (Bentz 2000) in order to enhance the accuracy and stability of the Dual Section Analysis method. In this method, the chain-rule is used to determine the gradient of normal stress as the derivative of the stress with respect of the element's axis. It requires an initial shear strain pattern as a function of the average sectional shear deformations (that can be assumed as the Jourawski solution),

$$\gamma_{xz}(z) = F_{\gamma}(x,z)\gamma_m \tag{2.30}$$

$$\gamma_{xz}(z) = \frac{AQ(z)}{Ib(z)}\gamma_m \tag{2.31}$$

where A is the area of cross section. This shear strain profile is used for the further load steps. The Bernoulli's plane section that computes the axial strain is combined with the current strain pattern. In this manner, the strains in each fibre are determined from the axial strain, curvature and average shear strain of the cross section,

$$\begin{bmatrix} \varepsilon_x \\ \gamma_{xz} \end{bmatrix} = \begin{bmatrix} 1 & z & 0 \\ 0 & 0 & F_\gamma(y,z) \end{bmatrix} \begin{bmatrix} \varepsilon_0 \\ \phi_y \\ \gamma_{xz} \end{bmatrix} \tag{2.32}$$

$$\varepsilon(z) = B(z) e_s \tag{2.33}$$

and the differential increment of stress is given by

$$\begin{bmatrix} d\sigma_x \\ d\sigma_z \\ d\tau_{xz} \end{bmatrix} = D_t \begin{bmatrix} d\varepsilon_x \\ d\varepsilon_z \\ d\gamma_{xz} \end{bmatrix} \tag{2.34}$$

where D_t is the tangent stiffness matrix of the fibre. Equilibrium in the transversal direction is achieved through static condensation of the term σ_z. In this manner, the derivative of the normal and shear stresses with respect to the x-axis is computed through the chain-rule and considering Eq. (2.32) and Eq (2.34) as:

$$\frac{\partial \sigma}{\partial x} = \frac{\partial \sigma}{\partial \varepsilon} \frac{\partial \varepsilon}{\partial e_s} \frac{\partial e_s}{\partial x} = D_t B(z) \frac{\partial e_s}{\partial x} \tag{2.35}$$

Hence, in contrast to the Dual Section Analysis, this formulation only requires information from a cross-section of the frame. Only 1D shear flows are considered, and for this reason, its application is limited to in-plane bending and shear.

2.3.3.3. Theory of Bairán-Marí

The model proposed by (Bairán 2005) solves the problem of the total six force interactions at the section level. By applying equations from the theory of continuum solid mechanics, the model considers inter-fibre equilibrium without any assumption about the stress or strain distributions. This implies that the distributions of shear strains and stresses change continuously depending on the state of the section. This theory was implemented in the computer program TINSA - Total Interaction Nonlinear Sectional Analysis. The detailed theoretical formulation and validation examples can be found in (Bairán and Marí 2006; Bairán and Marí 2006; Bairán and Marí 2007a; Bairán and Marí 2007b). The main characteristics of the model are outlined in the following.

The cross section is simulated as a 2D domain under the six internal forces and correspondent strains (Figure 2.27a): axial, shear along *y*- and *z*-axis, bending along *y*- and *z*-axis and torsion. The cross section is discretized into plane elements of concrete, linear

elements for transversal steel and point elements for longitudinal steel. Accordingly, the stresses applied in a fibre are represented in Figure 2.27b.

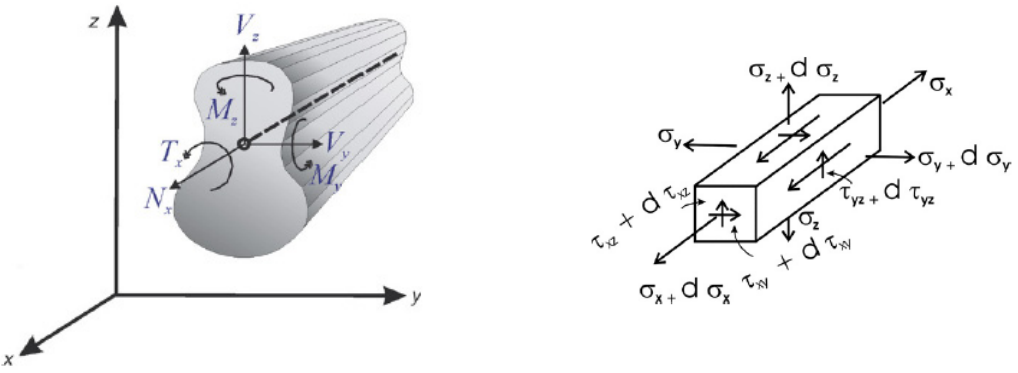

a) b)

Figure 2.27 – Theory of Bairán-Marí: a) sectional problem domain and b) fibre equilibrium (Bairán and Marí 2007a)

The sectional displacement field u is defined by the Bernoulli's plane section theory u^{ps} in addition to a three-dimensional warp-distortion field u^{w}, as schematically represented in Figure 2.28a. In this sense, the additional displacements u^{w} represent an improvement of the plane section approach to approximate the actual displacement of the solid, see Figure 2.28b.

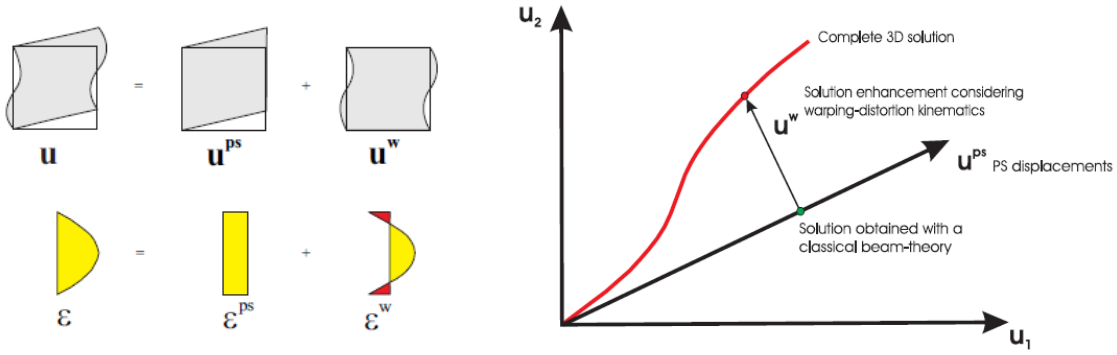

a) b)

Figure 2.28 – Theory of Bairán-Marí: a) displacement field and b) typical solution on the PS-distortion system (Bairán and Marí 2007b)

The sectional warp-distortion field u^{w} is considered as an interpolation through the nodal displacements by a shape function (N_F): $u^{w} \approx N_F d_F$. The nodal warping values d_F are considered as a function of the generalized sectional strains of the beam element (ζ^*): $d_F = A(\zeta^*)$. The considered generalized strain vector in the section ζ^* is composed by

the axial strains, the bending curvatures, the torsion curvature and its derivatives with respect to the *x*-axis

$$\xi^* = \left[\varepsilon_0, \phi_x, \phi_y, \phi_z, \varepsilon_0^{'}, \phi_x^{'}, \phi_y^{'}, \phi_z^{'} \right]^T \tag{2.36}$$

and is obtained from the six-component vector of generalized strains e_s as:

$$\xi^* = \Xi \Omega e_s \tag{2.37}$$

$$e_s = \left[\varepsilon_0, \gamma_{0y}, \gamma_{0z}, \phi_x, \phi_y, \phi_z \right]^T \tag{2.38}$$

where matrix Ω defines the generalized shear strains in the reference axis of the beam element as functions of the bending curvature derivatives and matrix Ξ considers the derivatives of the axial and torsion strains as functions of the correspondent applied loads. *A* is the distortion matrix that relates the generalized strains and its derivatives with the nodal values of the section's distortion strains, and is accomplished by internal equilibrium considerations, strain compatibility equations and energetic balance.

The six strain components of the cross sectional deformation field are obtained as:

$$\varepsilon_s = \varepsilon^{PS} + \varepsilon^w \tag{2.39}$$

$$\varepsilon^{PS} = N^{PS} e_s \tag{2.40}$$

$$\varepsilon^w \approx B_F d_F = B_F A \xi^* \tag{2.41}$$

where N^{PS} is a matrix of shape functions determined from Bernoulli's plane theory and B_F is the distortion interpolation matrix. The differential equations of equilibrium and compatibility among fibres are defined and solved numerically.

This model is independent of the constitutive equation, hence any type of 3D model can be used. In particular, the original work used the orthotropic multiaxial nonlinear equation for concrete OU3DC previously described in Section 2.3.2, which considers cracked induced anisotropy.

Hence, the six-component stress field σ is obtained through the nonlinear 3D constitutive equation with the generalized form

$$\sigma = D\varepsilon = D\left(\varepsilon^{PS} + \varepsilon^w \right) = \sigma^{PS} + \sigma^w \tag{2.42}$$

$$\sigma = [\sigma_x \ \sigma_y \ \sigma_z \ \tau_{xy} \ \tau_{xz} \ \tau_{yz}]^T \tag{2.43}$$

where D is the full material stiffness matrix. Applying the Virtual Work Principle, the sectional stiffness matrix K_s is obtained:

$$\begin{aligned} \sigma_s &= K_s \varepsilon_s \\ K_s &= \Xi^T \Omega^T \iint B^{*T} D B^* dA \Omega \Xi \end{aligned} \tag{2.44}$$

where the matrix B^* evaluates the material 3D strain field as function of the beam element sectional strains. The accomplished stiffness matrix is full, considering all the couplings between the 6 forces.

The model is able to reproduce the force interaction within a cross section, such as coupled normal and tangential forces, for any shape and any reinforcement layout. As this model treats forces and deformations in a single cross section it can be independently implemented in any program of structural analysis with bar elements, regarding any type of beam element formulation.

In Figure 2.29, a result of the model TINSA representative of its capacity to account for force coupling is represented in the predicted curves of moment-curvature of a RC cross section for different levels of shear force. It is notable, that for lower shear-spans and consequently increasing shear forces, there is an important reduction of ductility and ultimate bending moment.

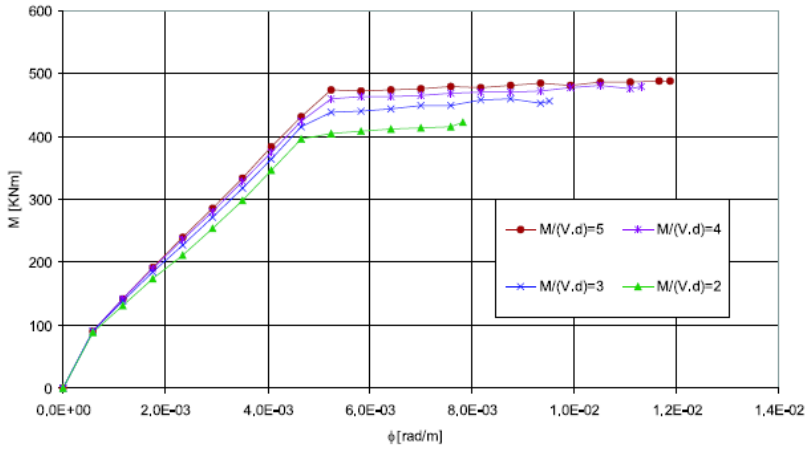

Figure 2.29 – Moment-curvature curves for various shear forces (shear-spans) (Bairán 2005)

The model TINSA proved to be accurate in predicting the sectional response under complex multiaxial loading conditions. However, its high complexity and computational demanding makes implementation in structural programs to be quite challenging.

2.3.3.4. Theory of Mohr-Bairán-Marí

The work of Mohr was motivated by the challenge of extending the model TINSA of (Bairán 2005) from the section to the element level. Due to the high computational complexity and demanding of TINSA, in order to accomplish its initial goal, Mohr had to take some simplicity assumptions. Accordingly, the deviation from the model TINSA consisted on the development of a simpler sectional model where shear deformations are defined through a series of polynomials in order to solve the fibre equilibrium equations. This sectional theory was introduced into a flexibility-based finite element model. In this manner, Mohr *et. al.* (Bairán, Marí and Mohr 2010) proposed a model for the analysis of RC structures submitted to combined normal and tangential forces. A detailed description of this model can be found in (Mohr 2011).

This model was devised for structural analysis of 2D frames and it was developed in two levels. At the section level, the formulation handles the interaction between axial force, bending moment and shear. The cross-section is subdivided in concrete fibres, and longitudinal and transversal reinforcement are discretized as well (Figure 2.30a). At the element level, a flexibility-based approach is considered (Figure 2.30b).

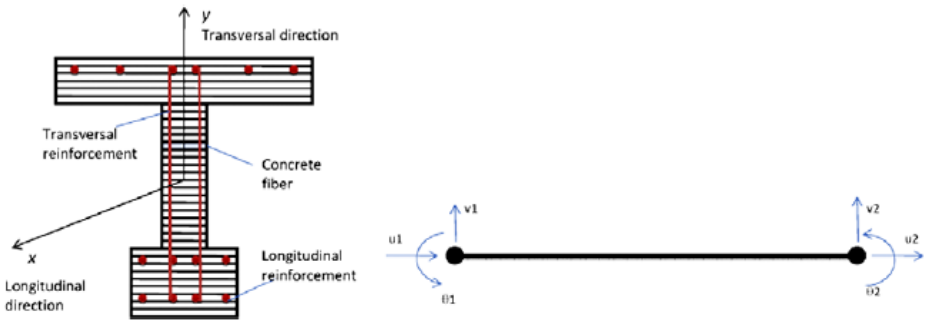

a) b)

Figure 2.30 – Definition of the domain of the model of Mohr: a) section and b) element levels (Mohr, Bairán and Marí 2010)

Based on the TINSA formulation, the displacement in each fibre u is given by the sum of the plane-section displacement u^{PS} with the warp-distortion displacement field u^{w}:

$$u = u^{PS} + u^{w} \tag{2.45}$$

in which the warp and distortion fields are approximated through a series of polynomial shape functions (Figure 2.31). These shape functions, which modulate the distribution of

warping and distortion along the cross-section, are obtained from the generalized strains of the beam element, are state dependent and are determined from internal equilibrium considerations.

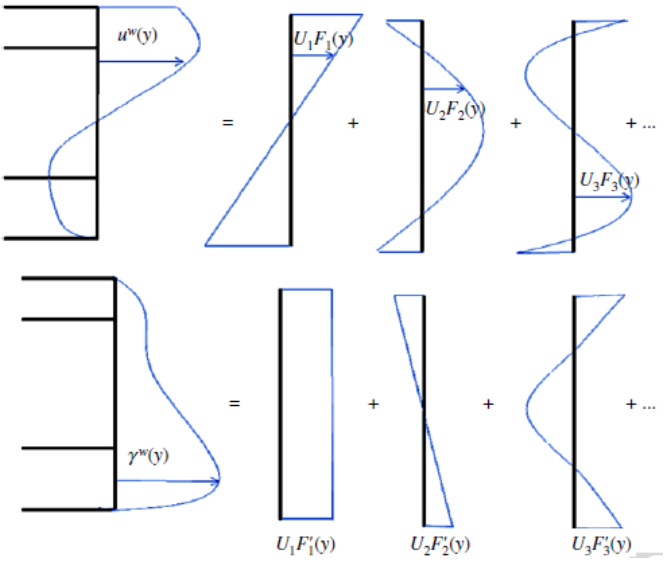

Figure 2.31 – Approximation of the warping and distortion fields by means of series of generalized displacements (Mohr, Bairán and Marí 2010)

In this manner, the multiaxial strain state in a fibre $e = [\varepsilon_x\ \varepsilon_y\ \gamma]^T$ is given by

$$e = B^{PS} e_s + B^w A e_s \tag{2.46}$$

where B^{PS} is the transformation matrix related with the plane section assumption and B^w is the transformation matrix related with the warp-distortion field; $e_s = [\varepsilon_0\ \gamma_0\ \varphi]^T$ are the generalized strains of the beam element and A represent the coefficients that modulate the warp-distortion shape functions.

Multiaxial stresses in a fibre $\sigma = [\sigma_x\ \sigma_y\ \tau]^T$ are computed through an orthotropic uniaxial constitutive model that considers directional damage and crack induced anisotropy through a rotation crack approach. Stresses are also decoupled into a plane-section and a distortion component. Through application of the Principle of Virtual Works, the generalized internal forces in the section $\sigma_s = [N\ V\ M]^T$ are determined by the integration of the generalized internal forces along the fibres:

$$\sigma_s = \int B^{PS} \sigma dA + A^T \int B^{wT} \sigma dA \tag{2.47}$$

and, in turn, the section's stiffness matrix k_s is computed as

$$k_s = \int B^{PS^T} DB^{PS} dA + \int B^{PS^T} DB^{w} dA + A^T \int B^{wT} DB^{PS} dA + A^T \int B^{wT} DB^{w} dA \qquad (2.48)$$

where D is the constitutive matrix of the fibre, that is generally full, and which explicitly reproduces the coupling between axial, bending and shear forces of diagonally cracked sections.

It is noteworthy that different approaches for the sectional model can be achieved by considering different numbers of terms of the series of polynomials N: (*i*) no consideration of shear distortion (N = 0 - *0SD*) leads to the classical Navier Bernoulli beam theory; (*ii*) linear shear-distortion (N = 1 – *1SD*) represents the Timoshenko-based theory as a constant shear distribution is assumed along the section, however, as vertical strains and distortion exists this approach differs from the classical Timoshenko beam and; (*iii*) nonlinear shear-distortion (N = 6 - *NLSD*) is the key proposal of the model and adequately approximates the strains and stresses distributions in the cross section.

In order to illustrate the level of accuracy of these different approaches, the results of the simulation of a shear critical beam are compared in Figure 2.32. It can be observed that, with the presence of important shear loads, both the Timoshenko (*1SD*) and the Bernoulli (*0SD*) theories are incapable of good predictions. In contrast, the nonlinear shear-distortion model (*NLSD*) gives very accurate results accounting for the coupling of normal and shear forces.

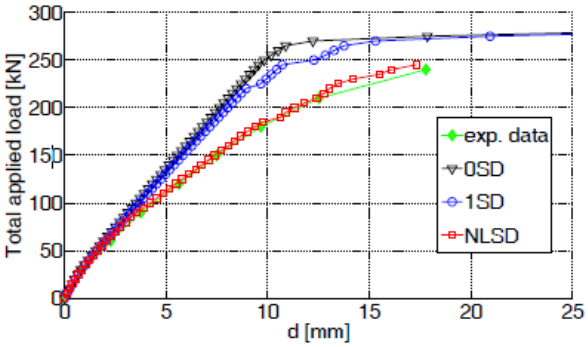

Figure 2.32 – Force-displacement curve of a shear critical beam (Mohr 2011)

In the following, the model TINSA of Bairán and the model of Mohr are compared. The shear force - strain curves for a cross section of a beam tested by (Kani 1977) are depicted in Figure 2.33, along with the predictions computed by both models. The similarity of the responses predicted by both models, and the accuracy levels achieved in relation to the experimental test, are remarkable.

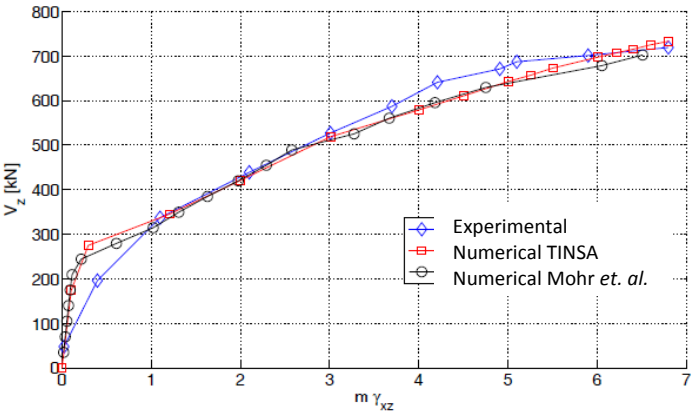

Figure 2.33 – Shear force-strain curve in a cross-section (Mohr 2011)

In spite of the greater simplicity and lesser computational demand of the model of Mohr in comparison with TINSA of Bairán, there are still some drawbacks for its direct implementation in general bar models related with processing time and numerical stability.

2.3.3.5. Fixed pattern approaches

The Fixed Strain Approach proposed by (Vecchio and Collins 1988) determines the shear response of a cross section by assuming an *a priori* fixed pattern for the tangential strain. In this manner, as represented in Figure 2.34a, the normal strains ε_x are determined through the Bernoulli's plane section hypotheses and a kinematic law for the distortion γ_{xz} is assumed. The strains in each fibre (ε_x, γ_{xz}), are determined as functions of the generalized strains in the cross section (ε_0, φ_y, γ_0).

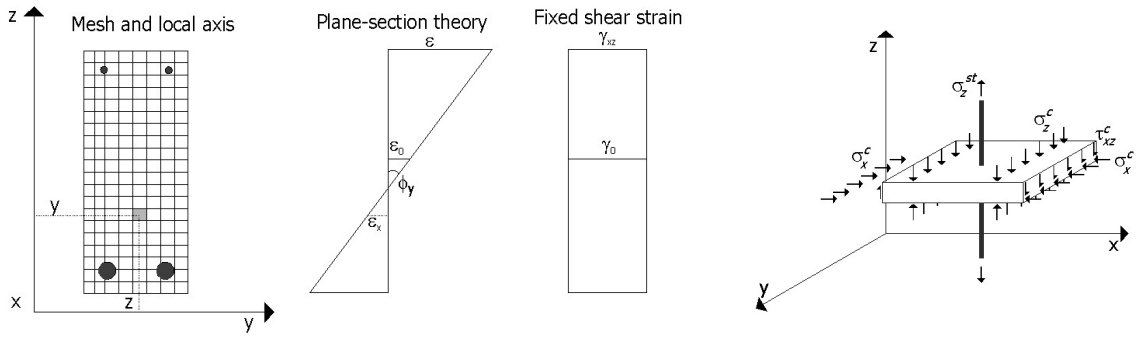

a) b)

Figure 2.34 – Fixed strain approach: a) assumptions and b) stresses applied in a fibre

The stress tensor $\sigma = (\sigma_x, \sigma_z, \tau_{xz})^T$ and the material stiffness D (full matrix of dimensions 3x3) of the fibre are determined through nonlinear uniaxial equivalent constitutive laws for concrete and steel. The stresses applied in a fibre are represented in Figure 2.34b; the

existence of vertical normal stresses σ_z is incompatible with the equilibrium in the transverse direction of each fibre. In this manner, the contribution of steel in tension σ_z^s and concrete in compression σ_z^c must cancel altogether:

$$\sum \sigma_z = \sigma_z^c + \rho_T \sigma_z^s = 0 \tag{2.49}$$

in which

$$\sigma_z^c = D_{21}\varepsilon_x + D_{22}\varepsilon_z + D_{23}\gamma_{xz} \tag{2.50}$$
$$\sigma_z^s = E_s \varepsilon_z$$

E_s is the elasticity modulus of the steel, whose contribution is accounted by means of the percentage quantity of transversal reinforcement ρ_T. Through the former equations, the vertical strain ε_z can be determined as function of the axial strain ε_x, the shear deformation γ_{xz} and the material stiffness matrix D as

$$\varepsilon_z = f\left(\varepsilon_x, \gamma_{xz}, D\right) = -\frac{D_{21}\varepsilon_x + D_{23}\gamma_{xz}}{D_{22} + \rho_T E_s} \tag{2.51}$$

In this equation it is visible that the section's distortion is needed to reach vertical equilibrium, and for this reason a suitable strain kinematic constraint for shear strain must be used. Compatibility and fibre equilibrium along the vertical direction are not explicitly verified. In its turn, shear stress τ_{xz} in a fibre is determined through the constitutive equation:

$$\tau_{xz} = D_{31}\varepsilon_x + D_{32}\varepsilon_z + D_{33}\gamma_{xz} \tag{2.52}$$

This approach has been considered by several authors (Petrangeli, Pinto et al. 1999; Güner 2008 and Ceresa; Petrini et al. 2009) because of its straightforward implementation in a Timoshenko based FE model: the constant distortion of the element is taken as the fixed strain in the cross section. However, this model usually underestimates the vertical strains and, for this reason, predicts lower stresses in the stirrups after the onset of diagonal cracking, as pointed out in (Vecchio and Collins 1988; Bairán and Marí 2007; Navarro 2009; Mohr 2011).

The Fixed Stress Approach was also proposed by (Vecchio and Collins 1988) and considers the plane section theory coupled with a fixed shear stress constraint as represented in Figure 2.35. In this manner, a mixed strain ε_x and stress τ_{xz} input information is generated for each fibre.

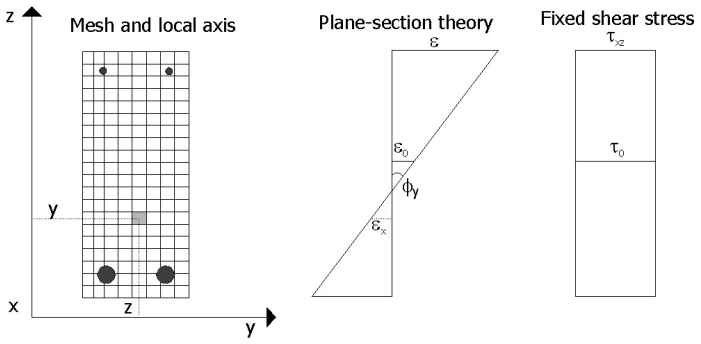

Figure 2.35 – Fixed Stress Approach

As for the case of the Fixed Strain Approach, the equilibrium equation in the vertical direction is established in Eq.(2.49) and the shear stress τ_{xz} for each fibre is set through the constitutive equation in Eq.(2.52). Pertaining to the Fixed Stress Approach, from the consideration of these former equations the vertical strain ε_z and the distortion γ_{xz} are determined as functions of the axial strain ε_z, the shear stress τ_{xz} and the material stiffness matrix D as:

$$\varepsilon_z = f\left(\varepsilon_x, \tau_{xz}, D\right) = \frac{\left(D_{23}D_{31} - D_{33}D_{21}\right)\varepsilon_x - D_{23}\tau_{xz}}{D_{22}^{*}D_{33} - D_{23}D_{32}} \tag{2.53}$$

$$\gamma_{xz} = f\left(\varepsilon_x, \tau_{xz}, D\right) = \frac{\left(D_{23}D_{21} - D_{22}^{*}D_{31}\right)\varepsilon_x + D_{22}^{*}\tau_{xz}}{D_{22}^{*}D_{33} - D_{23}D_{32}} \tag{2.54}$$

where D_{22}^{*} is the equivalent stiffness in the vertical direction that accounts for both concrete and transversal steel. In the same manner as in the Fixed Strain Approach, with this formulation strain compatibility in the transversal direction is not guaranteed and internal fibre equilibrium is not directly established.

In order to compare the accuracy achieved by different models, the results computed by the approximate methods based on the Fixed Pattern Approaches and by the more rigorous Dual Section model are presented in Figure 2.36. In a general way, both approximate approaches give fairly similar results to those obtained with the Dual Section Analysis. However, the Fixed Strain Approach tends to concentrate the shear stresses in the compressive regions of the section, underestimating the strain in the tension side. In its turn, the Fixed Stress Approach slightly overestimates the strains and underestimates the stress. Nevertheless, this last method allows capturing a good prediction of the sectional response whenever an adequate choice of the shear flow is given.

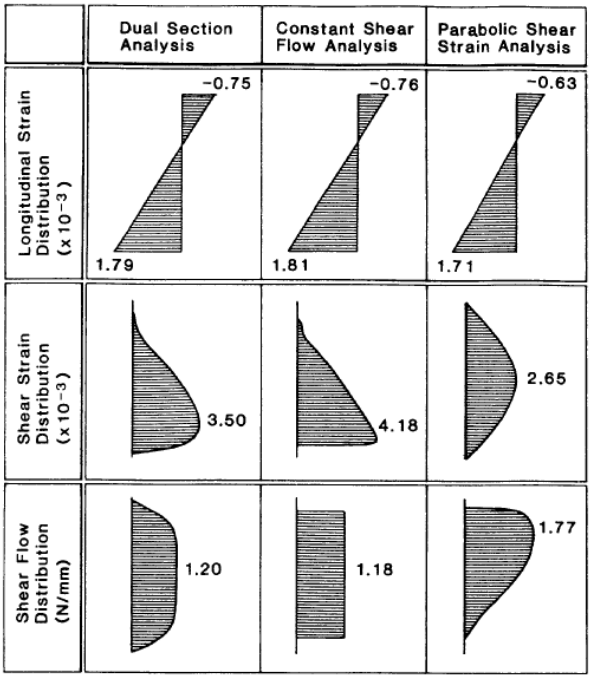

Figure 2.36 – Shear flow and strain distribution determined with dual section analysis and fixed pattern approaches (Vecchio and Collins 1988)

2.3.3.6. Model of Valipour and Foster

Valipour and Foster (2007) developed a flexibility based beam-column element for nonlinear analysis of RC frames under static and cyclic loads. The model was based on the direct integration method. In this approach, the fibre beam element framework is maintained and a network of integration points in the section is used to determine the stiffness matrix.The solution scheme used is the secant stiffness method for increasing computational stability.

The formulation for inclusion of shear effects is based on the Fixed Stress Approach. In fact, the actual shear stress distribution deviates from symmetric predefined forms due to the different nonlinear behaviour of concrete in tension and compression, plastic deformation of steel and concrete cracking. The shear stress flow profiles are dependent on several parameters, such as, quantity of transversal reinforcement, load levels, etc. The contribution of the cracked or crushed zones of concrete to the shear resistance is less than that of the intact zones. Thus, different proposals for shear stress functions were analysed: (*i*) a simple parabolic distribution; (*ii*) a 4th order polynomial function; (*iii*) an exponential-polynomial function and (*iv*) a five point multi-linear function. The three last functions are

state dependent; the parameters that characterize their shapes are defined through the following conditions:

- Null shear stresses at the top and bottom edges of the element

$$\tau_{xy}\left(y=-\frac{h}{2}\right)=0 \tag{2.55}$$

$$\tau_{xy}\left(y=\frac{h}{2}\right)=0 \tag{2.56}$$

- The expansion of the equilibrium equations for a 2D case allows writing the relationship between the gradients of the shear stress and the gradient of the longitudinal and vertical stresses as:

$$\frac{\partial\sigma_{xx}}{\partial x}+\frac{\partial\tau_{xy}}{\partial y}=0 \tag{2.57}$$

$$\frac{\partial\tau_{xy}}{\partial x}+\frac{\partial\sigma_{yy}}{\partial y}=0 \tag{2.58}$$

- The finite difference scheme is used to estimate the longitudinal gradient of stresses along the edge of a segment Δx of the element as:

$$\frac{\partial\sigma_{xx}}{\partial x}=\frac{\sigma_x^{i+1}-\sigma_x^{i}}{\Delta x} \tag{2.59}$$

The multi-linear shear distribution is represented in Figure 2.37: the angles α and β represent the slope of the shear function at the end points; τ_2 and τ_4 are determined by trigonometric rules and τ_3 is determined from the equilibrium equation between shear stresses and the shear force V applied in the section, by adopting a constant shear stress in the section.

As the model does not considers equilibrium in the vertical direction in each fibre, an explicit function for the vertical stress is provided. At the material level, a uniaxial law is considered for modelling the concrete behaviour, disregarding the 2D strain-stress state generated by the presence of the shear forces. The results of the four types of shear stress patterns were compared with the nonlinear 2D displacement-based FE model ATENA (Cervenka, Jendele and L. & Cervenka 2005) in the analysis of a beam under shear forces. Accordingly, the shear stress distributions along a cross-section are presented in Figure 2.38, for different force levels V.

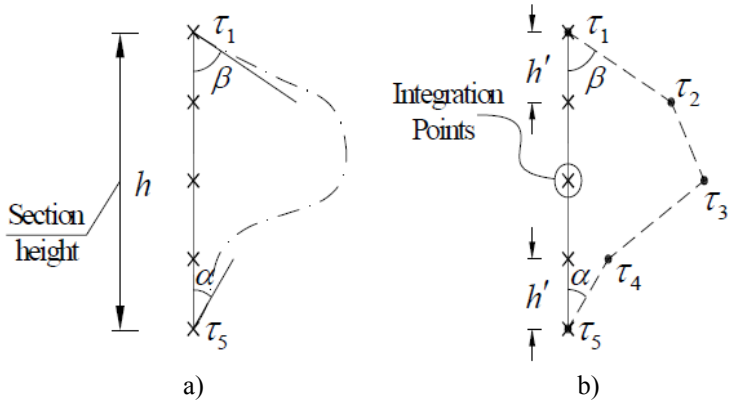

Figure 2.37 – Shear stress distribution over the height of the section: a) continuous and b) multilinear functions (Valipour and Foster 2007)

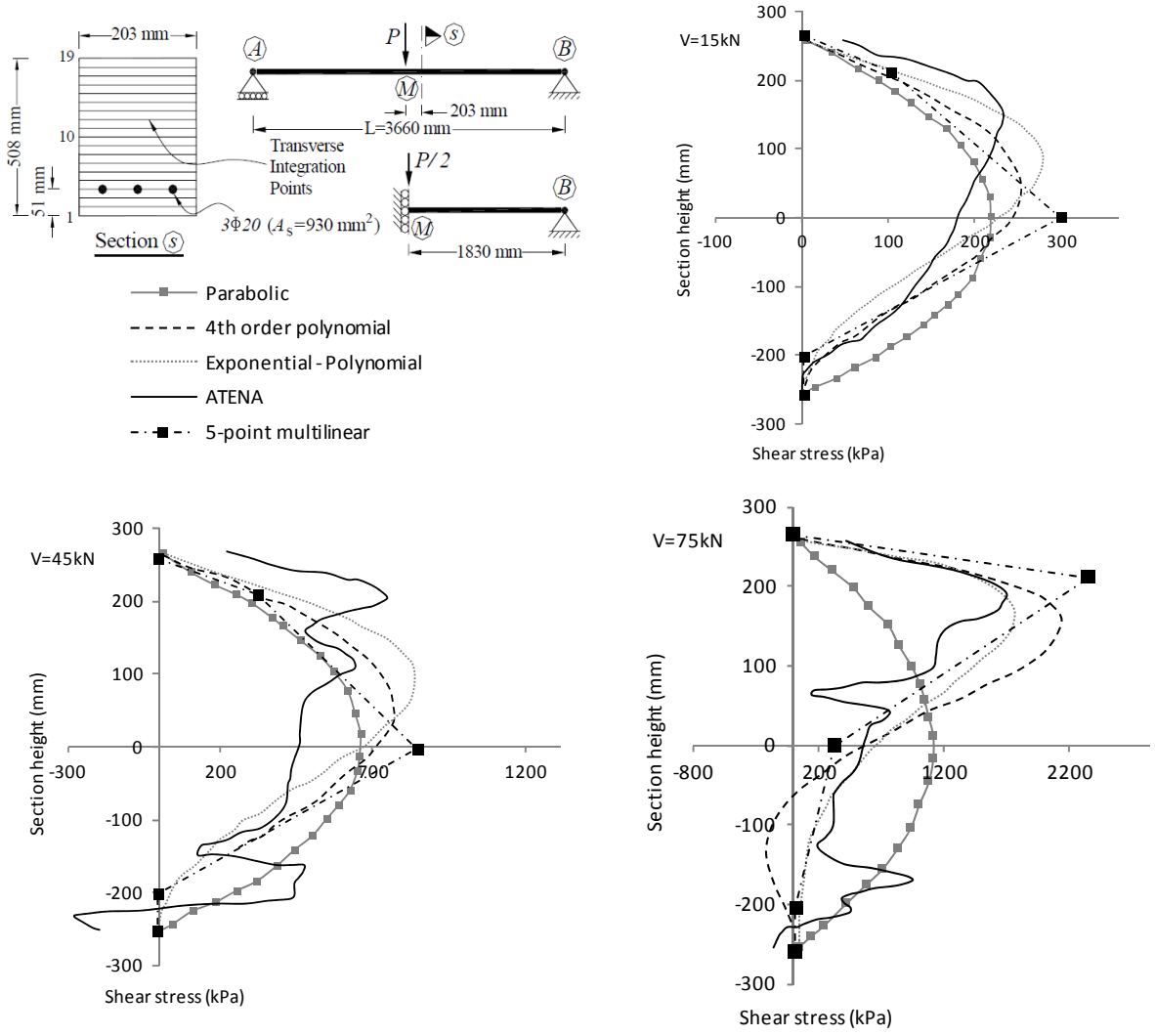

Figure 2.38 – Shear stress distribution along a RC section, adapted from (Valipour and Foster 2007)

It can be observed that, with the increasing of damage, the stress flow is less equally distributed in the cross section, being more concentrated in the uncracked areas. The different shear distributions considered presented diverse results: the exponential-polynomial and the 4^{th} order polynomial give similar results and correlate reasonably with ATENA predictions; instead, the parabolic pattern is the one with more deviation from the other assumptions, being the difference more accentuate for higher load levels. Studies on the shear stress profiles can be also found in (Bairán 2005; Mohr 2011) for different cross-sections and loads.

The model is able to take into account the shear influence on the flexibility and deflection of structures, but is not prepared to catch shear failure modes. Stirrups are only accounted for through the appropriate parameters that define the stress-strain relationship of confined concrete. Also, no interaction between normal and shear forces is considered at the constitutive level.

2.3.4 Proposals for frame structural analysis including shear

Several models were developed in the recent years with the goal of broadening fibre beam models from the classical 1D formulation to analyses considering 2D and 3D strain-stress states. The different models differ from each other in the shear kinematic assumptions taken at the sectional level, in the type of multiaxial constitutive equations and also in the approach of stiffness or flexibility base of the FE formulations. Comprehensive states of the art on this topic can be found in (Bairán and Marí 2007; Ceresa, Petrini and Pinho 2010).

In a general way, fibre beam models with shear effects can be divided in two main groups: (*i*) formulations that consider independent approaches for flexural and shear deformations and (*ii*) models that aim to capture the structural response through rational constitutive laws and adequate sectional kinematics.

In the following, some relevant proposals within the two groups are briefly presented. The main characteristics, advantages and drawbacks are pointed out. Accordingly, it is also commented how the previous proposals influenced the decisions taken for the accomplishment of the model proposed in this thesis.

2.3.4.1. Uncoupled shear effects

Within this first group, there are fibre beam elements that determine the shear components through truss models (strut-and-tie analyses) and add it to the analysis from the flexure beam model (Figure 2.39a). An example of these type of models is the proposal of (Guedes and Pinto 1997). In this manner, shear and normal forces are considered in an uncoupled fashion. Moreover, truss models do not take into account other shear resistance mechanisms, such as, dowel action, aggregate interlock, and concrete contribution to shear resistance.

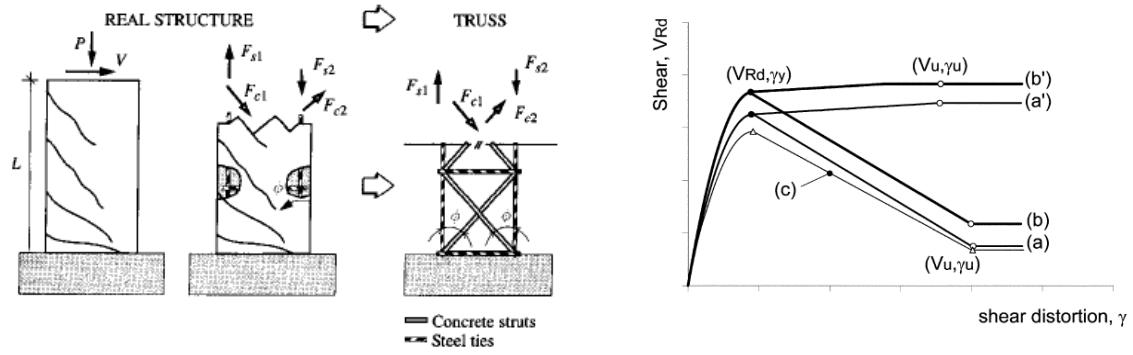

a) b)

Figure 2.39 – Models with uncoupled shear effects: a) truss analogy (Guedes and Pinto 1997) and b) shear force-distortion curves (Marini and Scapone 2006)

Other proposal is to use uncoupled empirical shear stress-strain equations for the consideration of shear effects. In this ambit, (Marini and Scapone 2006) presented a bar model for plane frames under monotonic and cyclic loading that included axial, bending and shear effects. Force-based 2D Timoshenko beam theory was assumed. The classical fibre beam section approach allowed for coupling of axial and bending forces, whilst shear was considered uncoupled through a nonlinear empirical shear force-strain equation (Figure 2.39b).

Despite their simplicity, these models fail to obtain accurate solutions for the behaviour of shear critical RC elements where the interaction between normal and tangential forces is relevant.

2.3.4.2. Coupled normal-shear formulations

The coupling of shear and normal forces on the nonlinear response of a structure is considered by means of sectional and element formulations. These models aim to

accomplish normal-shear interaction by means of rather complex constitutive formulations and kinematic approaches. Consequently, these models are more complex and accurate than the previous ones, although, in turn, they are more computational demanding and susceptible to numerical instabilities and convergence problems. The model developed in the ambit of this thesis is inserted in this type of models that consider normal-shear forces in a coupled manner. In addition to the work of (Bairán, Marí and Mohr 2010) and of (Valipour and Foster 2007) already described, other relevant proposals for modelling shear effects in fibre beam models are listed in the following.

Vecchio and Collins (1988) used the dual section method in the sectional analysis of fibre beam elements to predict the response of RC beams subjected to shear. The numerical program developed in this ambit (Vector5) was based on the MCFT and is able to perform nonlinear frame analyses under monotonic loading, including shear effects. A dual-section analysis was also used by (Ranzo 2000) in a beam element to study the behaviour of RC elements under seismic loading.

Vecchio and Emara (1992) proposed a frame analysis algorithm with force-based layer elements including shear at the sectional level through a fixed stress pattern approach. The MCFT was used as constitutive model at the material level. The algorithm is based on matrix analyses to determine the forces applied in the element, which is a rather simplified approach that does not account for the coupling of normal-shear effects on the stiffness of the element.

Petrangeli, Pinto and Ciampi (1999) developed a flexibility-based fibre beam FE model using the plane section hypothesis in conjunction with predefined functions for the shear strain. The equilibrium in the vertical direction was imposed in each fibre. The biaxial constitutive law used was based on the microplane theory. This was a pioneer proposal in including shear effects into cyclic analysis of RC sections by means of fibre beam models and, for this reason, it is an important reference in this research ambit.

Güner (2008) improved the previously developed program Vector5 (Vecchio and Collins 1988) for cyclic and reverse loading conditions. It consists on a global frame analysis model with a layered sectional approach. Shear at the cross section is considered through different options based on Fixed Pattern Approaches: uniform shear flow, uniform shear strain and parabolic shear strain distributions. A reformulated version of the MCFT to account for cyclic loading was used as the constitutive law for RC. It was concluded that

shear-strain-based approaches are less time consuming, less computationally demanding and more stable into the post-peak regimes then shear-stress-based approaches.

Ceresa, Petrini, Pinho and Sousa (2009) presented a 2D displacement-based Timoshenko beam element. At the sectional level, a plane section assumption is used to determine axial strains, along with the consideration of a constant shear strain distribution along the section. The MCFT is adopted as the constitutive law. 'Bubble functions' were presented as linear shape functions linked to the transversal displacement field, to overcome the shear locking problems of the Timoshenko beam theory. This model was used to simulate the cyclic responses of RC elements.

Navarro (2009) presented a 1D frame FE model for the analysis of reinforced and prestressed concrete sections under combined loading. The model is based on the Timoshenko beam element and the MCFT was used as the constitutive model for RC. The assumption of the constant shear strain of the Timoshenko beam theory was studied along with improved shear strain profiles.

Saritas and Filippou (2009) presented a flexibility based FE model with shear consideration. The nonlinear response of the cross sections accounts for the interaction of axial force, bending moment and shear force. This coupling of forces is achieved through numerical integration of an inelastic multi-axial material model over the cross-section.

Mullapudi and Ayoub (2010) contribution is a 2D force-based model for shear critical RC columns under seismic loading, using the Soft Membrane Model at the constitutive level. Coupling of normal-shear forces were accounted at the section and element levels.

Stramandinoli and La Rovere (2012) presented a FE fibre beam model for the nonlinear analyses of RC beams taking into account the shear deformation. The model was based on the classical Timoshenko beam theory and the MCFT was used as the constitutive model, along with a tension-stiffening equation developed by the authors; a constant shear strain was assumed for all the fibres along the cross-section. The model presented some inaccuracy as far as predicting the behaviour of shear reinforced critical beams was concerned.

From the previously exposed, the models that use simplified approaches to model shear effects, like the constant shear strain assumption have been extensively used due to their computational robustness (Vecchio and Collins 1988; Petrangeli, Pinto and Ciampi 1999; Güner 2008; Ceresa, Petrini, Pinho and Sousa 2009; Mohr, Bairán and Marí 2010).

However, inaccurate results in beams highly reinforced for shear have been reported in (Vecchio and Collins 1988; Mohr, Bairán and Marí 2010), which is explained by the fact that strains and stresses in the stirrups are deficiently simulated through this assumption. Furthermore, in (Stramandinoli and La Rovere 2012) it was stated that the behaviour of beams with low transversal reinforcement ratio was better represented numerically than for beams with high transversal reinforcement ratio. This is highly unexpected, as the concrete shear resistant mechanism is dependent on many random variables of difficult definition (aggregate interlock, tensile strength, etc.) in comparison with the well-defined parameters of the shear resistant mechanism of the stirrups (geometric characteristics and steel material properties).

This fact is evidenced in the stress-strain curves in the stirrups of the beam presented in Figure 2.40. The complex formulations (TINSA and Model of Mohr – PM 6SF) are able to accurately predict the experimental strains in the stirrups, whilst the constant strain assumption (*1SF*) predicts almost no loading of the stirrups. For this reason, in order to validate fibre beam FE models with inclusion of shear effects, the following key aspects of the response of RC elements must be represented: force-displacements curves; failure mechanism and force-strains curves in the stirrups. These results are essential to prove that the numerical simulation is representing well the resistance mechanism of a shear critical element.

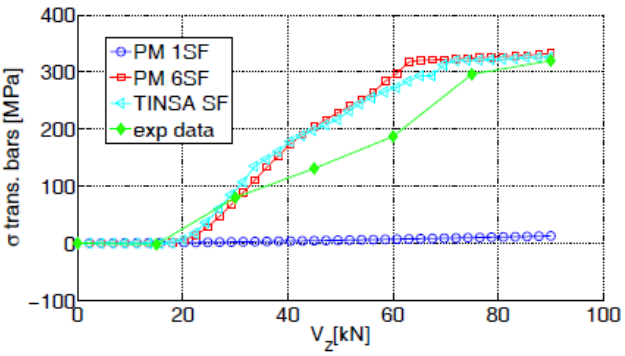

Figure 2.40 – Stresses in the transversal reinforcement (Mohr 2011)

The strategy for inclusion of shear effects in the basic model CONS had to consider several input conditions: the original version of CONS is already a fairly complex model able of comprehensive nonlinear structural analysis by accounting for time-dependent phenomena and segmental construction procedures; the influence of shear effects on these features is not easy to understand nor to consider numerically. Therefore, to guarantee consistency

between shear effects and the original characteristics of CONS, the implemented shear model should be maintained as simple as possible ensuring an adequate accuracy. The previous complex models developed in the same research team (TINSA by Bairán and the Model of Mohr) are highly accurate but lack some computational efficiency and stability. Due to this great complexity, their implementation in CONS was expected to be impracticable. In this manner, the path chosen in this thesis for the implementation of a shear formulation in the model CONS was based on simplified approaches. Assuming a constant shear strain along a cracked reinforced cross-section is an over-simplification that does not reflect its behaviour satisfactorily. Conversely, the assumption of constant shear stress distribution was taken as basis of the proposed sectional shear model.

2.3.5 Algorithm performance

Modelling shear effects in RC elements involves a great computational effort in handling the nonlinearities brought by the diagonal cracks, the strain-softening phenomena and the fragile failure modes. For this reason, these nonlinear models are quite vulnerable to numerical instabilities and convergence problems. Some authors reported these problems in the analysis of RC elements submitted to important tangential stresses; the objectivity of the numerical solutions and the difficulties to obtain converged results for the entire loading path of the structure were also discussed (Borst and Nauta 1985; Borst 1987; Abdollahi 1996).

Concerning to shear critical problems, limit points appear along the analysis (Figure 2.41), brought by a sort of strong material nonlinearities, such as diagonal cracking, softening and stirrups yielding, which need to be surpassed in order to guarantee numerical stability. Hence, it is essential to control and limit these problems in order to ensure robust and efficient analysis. Also, as there is no ductility in the shear failure mode, it is important to guarantee that a fragile shear failure is well captured by the model, and not hindered by a sudden stop of the analysis in non-convergent intermediate limit points (Park, Klingner and Wheat 1995).

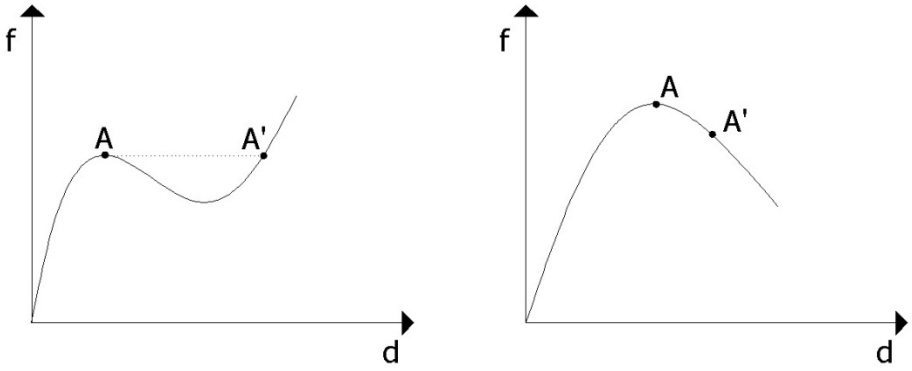

Figure 2.41 – Discontinuity points: a) intermediate limit and b) softening

Accordingly, advanced solution procedures such as line searches and continuation techniques are essential to reach efficient, stable and robust solution algorithms based on Newton-Raphson iterative approaches (Crisfield 1996). Line searches are methods that speed up the convergence by reducing the number of iterations. Continuation methods, such as the arc-length and its variants (Figure 2.42a), consider an additional restrictive constraint in the system of equations for the solution of the problem. These approaches, also named Constrained Methods, lead to a variation on the load step during the iterative loop, so that the representative vector of the iterative solutions lies on the restrictive adopted constraint. This technique enhances the efficiency of complex nonlinear problems by detecting and overpassing limit points in the structural analysis. There are different proposals for the additional constraint condition allowing for different levels of complexity and efficiency. For example, the updated normal plane (Figure 2.42b)), which is a linearized version of the arc-length method, has shown to attain very good results with much less computational effort than the classical arch-length method (Póvoas 1991).

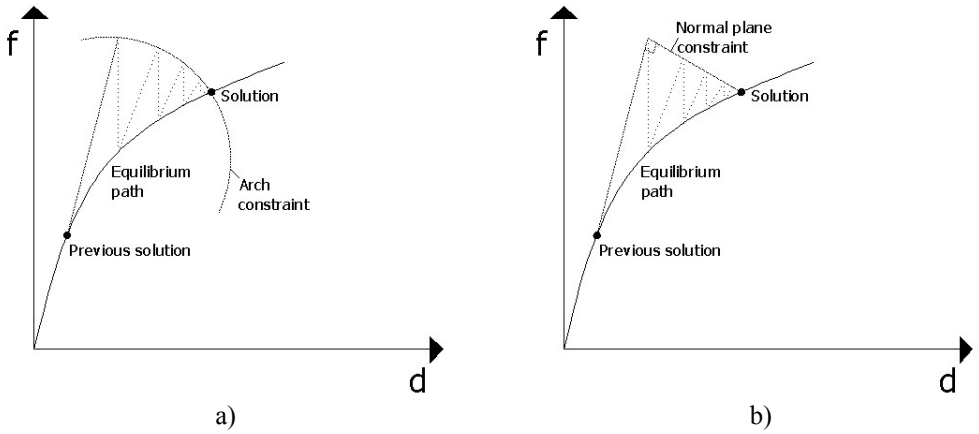

Figure 2.42 – Continuation techniques: a) arch-length and b) updated normal plane methods

The comprehensive description of the theory, implementation and efficiency of these methods can be found in (Crisfield 1996). In the proposed model a continuation technique, the updated normal plane method, was implemented.

2.4 Repair and strengthening of existing structures

The assessment and strengthening of existing RC structures is a topic of great urgency, due to the advanced aging stage reached by many infrastructures in developed countries. Besides being a problem that is on the agenda of many research groups and public administrations worldwide, it is far from being solved. In fact, there is an increasing demand for accurate structural life-time assessment methods able to evaluate the needs of intervention in aging infrastructures and designing efficient strengthening or retrofit measures. Standards and advice committees are clear about the future directions of RC structures: increase their lifespan, rationalize the materials' consumption, improve the strengthening techniques and, therefore, contribute to promote the sustainable development of the construction field.

Deterioration and damage of existing RC structures, due to aggressive environmental conditions and permanent or accident loading, leads to a reduction of structural performance and service life-time. Strengthening or retrofit measures can increase the life-span of existing structures and also improve structural performances. However, understanding and predicting the competence of the strengthening measures is essential to achieve adequate interventions in damaged existing structures. This can only be accomplished by a deep understanding of the strengthening materials and techniques, associated with numerical models able to accurately simulate damaged structures and predict the efficiency of possible strengthening interventions.

Strengthening measures to increase bending capacity of structures, such as longitudinal external prestress, longitudinal fibre reinforced polymers (FRP), the enlargement of concrete cross sections and the application of extra longitudinal reinforcement, have been extensively studied and applied in the past (a general state of the art description focused on FRP strengthening is given in (Bakis, Bank, Brown *et. al.* 2002)). The same cannot be said about shear. In fact, the efficiency of different strengthening techniques in shear critical RC structures is not well known. Actually, in relation to shear critical structures, the resistant mechanism of a strengthened element is even more complicated to understand and

to predict than the original one. For this reason, this topic is currently motivating a vibrant research effort both on experimental and analytical approaches in order to better understand the particularities of shear strengthening and to apply it in practice with adequate safety. Also, numerical models able to accurately take into account these strengthening procedures are needed.

2.4.1 Materials and techniques

Regarding shear strengthening techniques, some common methods for RC beams are represented in Figure 2.43 (Taljsten 2003). Adding extra transversal steel and enlarging the concrete beam web (Figure 2.43a) are, perhaps, the most commonly used methods. Hence, the existing concrete on the top of the slab is removed, new extra stirrups are put around the cross section and new concrete is casted or sprayed to the element. This method is efficient in increasing the shear capacity, as long as the adhesion between new and old concrete is ensured (Souza and Appleton 1997a). However, it is a very intrusive and time-consuming intervention.

For cases demanding for a slight augment of shear resistance, the application of steel reinforced shotcrete (Figure 2.43b) or epoxy bounded steel plates (Figure 2.43c) are some common alternatives. The drawback of these methods is the risk of bonding loss due to the fact that the strengthening material is not anchored to the compressive zone.

The application of steel tendons, as represented in Figure 2.43d and in Figure 2.43e, are efficient methods to increase shear resistance of RC cross-sections. These tendons can either be post-stressed or not. In fact, post-tensioning repair techniques are a well-recognised and widely used retrofitting method for enhancing flexural capacity of RC frame structures, and its application can be expanded to the improvement of shear strength. The use of prestressed transversal reinforcement can provide an active confinement to the concrete section and allow the development of the flexural capacity of beams. Experimental studies on shear critical beams demonstrated that the inducement of transverse compressive forces by means of prestressed transversal reinforcements augmented the shear capacity, increased the ductility and was able to avoid brittle shear failures (Collins and Roper 1990; Aboutaha and Burns 1994; Adhikay and Mutusuyoshi 2006). In this intervention, special attention has to be paid to the position of the existing longitudinal reinforcement, as there is the risk of cutting it off during drilling.

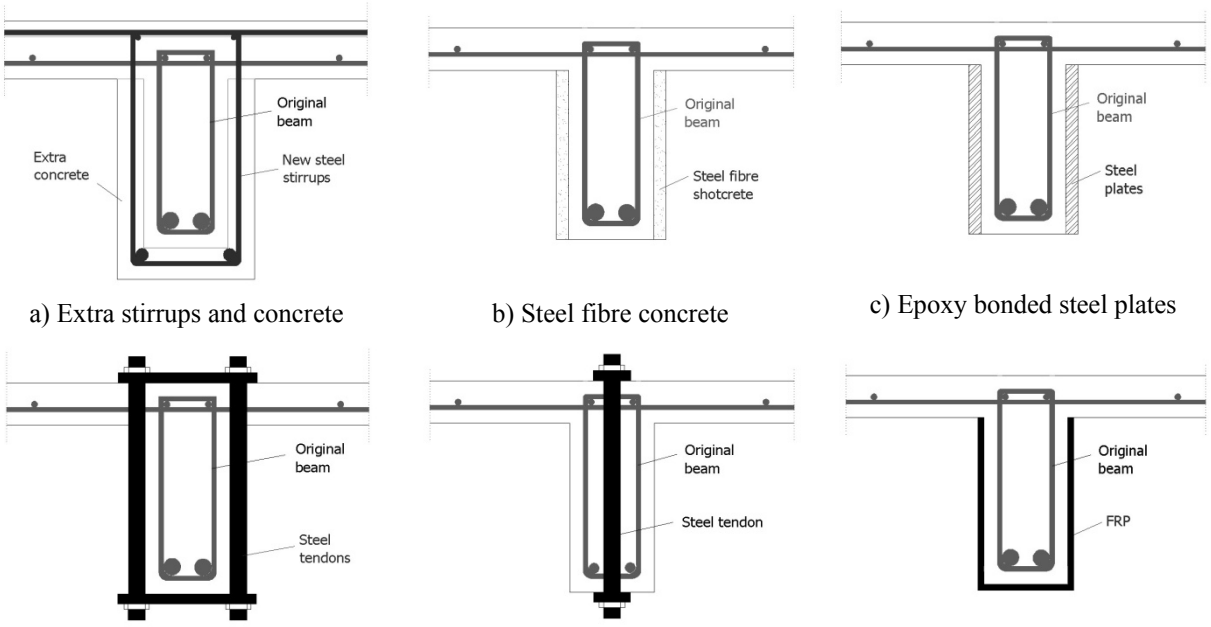

a) Extra stirrups and concrete

b) Steel fibre concrete

c) Epoxy bonded steel plates

d) External steel tendons (with or without transversal prestressing)

e) Internal steel tendons (with or without transversal prestressing)

f) Fibre reinforced polymers (FRP)

Figure 2.43 – Shear strengthening methods for RC beams

The use of externally bounded FRP, represented in Figure 2.43f, has shown to be an efficient technique of strengthening and retrofitting a damaged RC element. The reasons for its popularity are: immunity to corrosion, low weight, very high tensile strength, the stiffness can be adapted to the design requirements, large deformation capacity and practically unlimited availability of dimensions and shapes. Besides the many advantages, some drawbacks also exist, such as, linear elastic failure without plastic deformations, high cost, possible incompatibilities of thermal expansion coefficients with concrete and loss of stiffness when exposed to high temperatures, brittle delamination failures modes, especially if the laminate is not anchored in the concrete compression zone. Concerning to shear strengthening, FRP can be externally bonded with the direction of the fibres coincident to that of maximum principal tensile stresses, or as much parallel as possible. In this manner, the most effective solution is to bond the reinforcement with an angle of approximately 45º, however, in practice, it is more common to bind it vertically. Premature failure through debonding must be avoided, as it is an inefficient usage of the FRP material, brings premature failure and prevents the strengthened member from reaching their full capacity. To avoid anchorage failure FRP must be wrapped around the beam or must be anchored in the compressive zone. (FIB 2006)

The fact that shear resistance mechanism of non-strengthened elements is not totally clarified, acts like a drawback in the analysis of the strengthened elements, as the complexity of the problem increases significantly when a strengthening material is added to the element. In fact, the contribution and efficiency of FRP to shear strengthening is neither well understood nor defined. Aspects such as the determination of the optimal strengthening configuration for each case, the resistance mechanism of the strengthened element, the contribution of FRP to shear resistance, the bonding mechanism and the overall efficiency of this solution is currently motivating many experimental research works; some examples are (Hadi 2003, Mosallam and Banerjee 2007, Bukhari, Vollum, Ahmad and Sagaseta 2010, Kachlakev and McCurry 2000, Khalifa and Nanni 2002 and Taljsten 2003).

2.4.2 Modelling strategies

An existent structure cannot be submitted to safety evaluation on the basis of the same principles as for new structures. Its own singularities, such as the ageing and environmental damaging of the materials, the doubts and unknowns about the design project, the changes on the loading demands and on the geometric characteristics along their service-life require specific assessment strategies. In this ambit, numerical models able to perform life-time analyses that consider all the relevant changes (material properties, geometry, supports and loading conditions, etc.) are needed to ensure an accurate assessment of the state of the structure, and to determine the needs for an intervention. Moreover, in order to predict the efficiency of the strengthening or retrofit measures, the analysis of the strengthened structures has to consider the damaged state previous to intervention. This is only possible if segmental construction features are available in the nonlinear numerical model. Examples of phased and time-dependent nonlinear analyses for the assessment of existing RC structures focused on the shear capacity are (Plos and Gylltoft 2006, Broo 2008, Saether, Kantad, Overli *et. al.* 2010), being accomplished through complex and time-consuming 2D and 3D FE models.

Numerical modelling of RC shear-strengthened members has not been extensively studied, and the existing nonlinear FE models are usually focused on the simulation of FRP techniques; some examples are (Lee, Ha and Afzal 2008, Hoque, Rattanawangcharoen and Shah 2007, Kim and Vecchio 2008). The influence of many parameters in the response of the strengthened structures, such as the amount of steel stirrups, concrete compressive

strength, stiffness of the FRP, amount and direction of FRP and shear span-to-effective depth ratio are of difficult consideration in the numerical models (Godat, Labossière and Neale 2012a). These existent models are mainly struggling with the FRP/concrete interface behaviour, as full strain compatibility between the two materials seems to be quite questionable. Accordingly, failures by loss of bonding between FRP and concrete are difficult to predict numerically (Godat, Labossière, Neale and Chaallal 2012b).

Pertaining to the numerical simulation of strengthened RC structures by means of the various techniques mentioned, fibre beam models can be a proper solution. The possibility of defining different types of materials in the cross section due to the filament discretization makes these models adequate to deal with this problem (Nitereka and Neale 1999). In what concerns to flexural strengthened elements, the nonlinear FE model CONS (Marí 2000) is able to account for the previous damage state of the structure, through the time-step and segmental analysis procedures. In this ambit, the nonlinear fibre beam model with due account of shear-bending interaction developed in this thesis can broaden its applications to shear critical structures.

2.5 Discussion on the state of the art

From the presented state of the art, the following key ideas can be pointed out:

- 1D FE models with distributed nonlinearity, as it is the case of the fibre beam model CONS, allow for complex nonlinear and time-dependent analyses of flexural-dominant RC frame structures with affordable computational costs. However, their incapacity for comprising shear effects in an appropriate manner acts as a handicap towards the range of its application.
- The shear resistance mechanism in RC elements and the interaction between normal and tangential forces are complex, not clearly defined and not straightforward to model numerically.
- Different approaches for the inclusion of shear effects into fibre beam models have been proposed with different levels of accuracy and complexity, differing in the constitutive and kinematic hypothesis assumed.
- Accurate simulations of the shear resistance mechanism and its interaction with other forces are achieved by complex analysis models; however their numerical

instability and very high computational demand difficult their incorporation into fibre beam models.

- Simplified theories for modelling shear in RC (based on the *a priori* assumption of stress and strain distributions) are considered for frame models, being less accurate than the complex models but with higher computational efficiency.
- Regarding the increasing need for assessment and strengthening solutions for aging RC structures, nonlinear and time-dependent fibre beam models can be an efficient option for performing life-time analysis.
- In contrast to bending, shear strengthening in both experimental and numerical fields is still an open issue; aspects such as loss of bonding, optimal configuration of the strengthening measures and the various parameters affecting the resistance mechanism of the strengthened elements are attracting extensive research efforts.

Within the present state of the art, the model proposed in this thesis intends to be an original contribution in the ambit of fibre beam models with the inclusion of shear effects, by taking into account time-dependent behaviour of concrete and the possibility to simulate segmental constructed structures, as well as strengthening procedures. Regarding the basis of the sectional model, the choice of the Fixed Stress Pattern Approach was motivated by its simpler and less computational demanding characteristics, in comparison with the complex models (TINSA of Bairán (2005) and the model proposed by Mohr (2011)) and by being more accurate than the strain-based simplified approach. By choosing a simplified model for shear, expected interferences in the original characteristics of the basic model (time-dependent and segmental analysis) by the consideration of normal and tangential forces are sought to be minimized.

Focusing on the general problematic of assessment and strengthening of existing structures, the relevant characteristics of the model proposed in this thesis are: (*i*) capability for considering shear effects in both service and ultimate levels; (*ii*) considering strengthening procedures accounting for the state of the structure prior to the intervention, and (*iii*) ability to capture possible changes in the failure mode produced by the retrofit measures.

The numerical simulation of shear strengthening and retrofitting of damaged RC structures through fibre beam element procedures, to the author's knowledge, has not been carried out to date. In fact, it can be a suitable alternative to the more complex and computationally demanding 3D models for the determination of structural capacity. Service life modelling and the determination of the efficiency of strengthening measures

can be performed in a deterministic manner. Accordingly, the model can also give support to decisions regarding maintenance planning and optimal intervention solutions that comply with the desired strength capacity of the structures.

Chapter 3

A HYBRID FIBRE BEAM-COLUMN MODEL INCLUDING SHEAR EFFECTS

3.1 Introduction

Traditionally, nonlinear fibre beam models do not consider shear stresses, or simply treat it as linear elastic without interaction with normal stresses. Therefore, simulations of structural RC members undergoing relevant shear effects cannot be performed directly by these models.

Hence, the model to be presented in this chapter intends to broaden the fibre beam approach to applications where shear has a dominant role. It is based on the Timoshenko theory, being devised for analyses of 2D RC frames under combined axial, bending and shear forces. One key feature of the novel model is that a hybrid sectional formulation is used: along with the plane section theory, a constant shear stress flow is assumed to simulate the shear resistant mechanism. A smeared crack approach with full rotating cracks is used to model the constitutive behaviour of concrete under tension. Tension-stiffening and softening effects are included. Transversal reinforcement is considered smeared in concrete, while longitudinal rebars are simulated through the use of steel filaments.

The option of using the fixed shear stress rather than the fixed shear strain approach was motivated by the significant limitations of the former assumption, reported in literature (presented in the Section 2.3.4.2). In turn, as concluded in (Bairán and Marí 2007) the fixed stress approach used in the novel model, although not guaranteeing compatibility between the fibres, gives satisfactory results in the simulation of the shear-resistant mechanism of reinforced cracked concrete cross-sections. By these means, a simplified sectional formulation is developed, based on a hybrid approach in which the input variables take into account the curvature, the axial beam's strain and the applied shear force.

The model proposed in this chapter will be used to perform numerical simulations of a set of experimental tests of beams submitted to important shear stresses. The comparison of the experimental observations with the numerical predictions in terms of failure loads, collapse mechanisms, displacements, strains and crack patterns will deserve a particular attention in the validation of the model.

3.2 Proposed model

3.2.1 Material level

3.2.1.1. Constitutive model for concrete

A smeared cracked approach is assumed to model the constitutive behavior of the cracked concrete, treated as a material with orthotropic average stress-strain curves. The adopted concrete 2D constitutive model is formulated in terms of average principal strains $\underline{\varepsilon}_{12}=[\varepsilon_1\ \varepsilon_2]^T$ and average principal stresses $\underline{\sigma}_{12}=[\ \sigma_1\ \sigma_2]^T$, in which the principal directions of the strain and stress tensors are assumed to be coincident (average in this context means that an average behaviour between the uncracked and cracked areas of concrete is considered). According to Figure 3.1 there are three possible stress states: biaxial compression, tension-compression and biaxial tension. In this formulation subscripts '*1*' and '*2*' represent maximum and minimum principal strains and stresses, respectively. Tensile principal strains and stresses are assumed as positive.

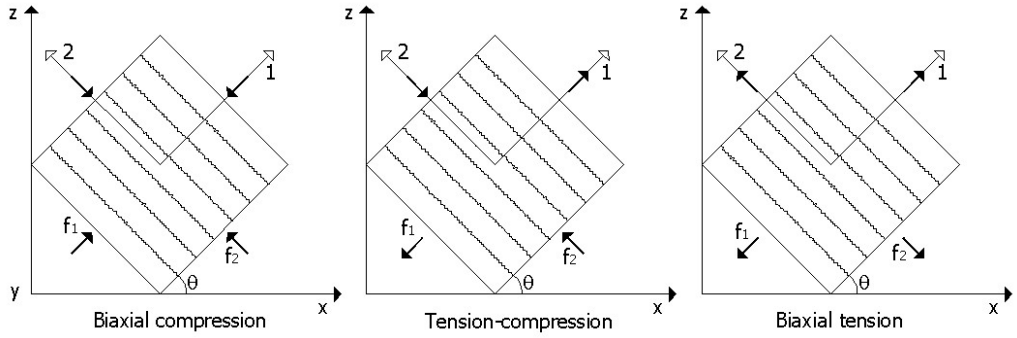

Figure 3.1 – Concrete stress states: a) biaxial compression; b) tension-compression; c) biaxial tension

The backbone 1D equation for concrete in compression is the Hognestad parabola (Hognestad, Hanson and McHenry 1955)

$$\sigma_2 = f_p \left(2\left(\frac{\varepsilon_2}{\varepsilon_p}\right) - \left(\frac{\varepsilon_2}{\varepsilon_p}\right)^2 \right) \tag{3.1}$$

where ε_p is the strain at the peak stress f_p, and the latter depends on the 1D compressive strength of concrete $f_c^{'}$

$$f_p = \beta k_{ci} f_c^{'} \tag{3.2}$$

Factor β accounts for the compressive weakening of concrete that takes place when a tensile strain ε_1 occurs perpendicularly to the actual compressive strain ε_2 (in a tension-compression state), and is given by the equation proposed by (Vecchio and Collins 1986):

$$\beta = \frac{1}{0.85 - 0.27\dfrac{\varepsilon_1}{\varepsilon_2}} \leq 1.0 \tag{3.3}$$

Factor k_{c2} is the one proposed by (Kupfer, Hilsdorf and Rusch 1969), to take into account the compression strength enhancement in direction '2' due to a compressive stress σ_1 applied along direction '1' (biaxial compression state, ε_1<0 and ε_2<0):

$$k_{c2} = 1 + 0.92\left(\frac{-\sigma_1}{f_c^{'}}\right) - 0.76\left(\frac{-\sigma_1}{f_c^{'}}\right)^2 \geq 1.0 \tag{3.4}$$

E_2 is taken as the tangent elasticity modulus which is determined through the derivation of the backbone curve for concrete in compression, neglecting the variations of both softening

and strength enhancement factors as shown in Eq. (3.5). According to the previous material formulation this is a simplification; however, it allows a symmetric constitutive matrix for the cracked concrete.

$$E_2 = 2f_c^{'}\left[\left(\frac{1}{\varepsilon_0}\right) - \varepsilon_2\left(\frac{1}{\varepsilon_0}\right)^2\right] \tag{3.5}$$

Plastic behaviour of concrete that develops during compressive loading is accounted for through the plastic strain ε_2^p

$$\varepsilon_2^p = \varepsilon_2 - \frac{\sigma_2}{E_0} \tag{3.6}$$

As depicted in Figure 3.2a, phases of unloading and partial reloading in compression are considered through straight lines, in accordance to the elasticity modulus of concrete E_0.

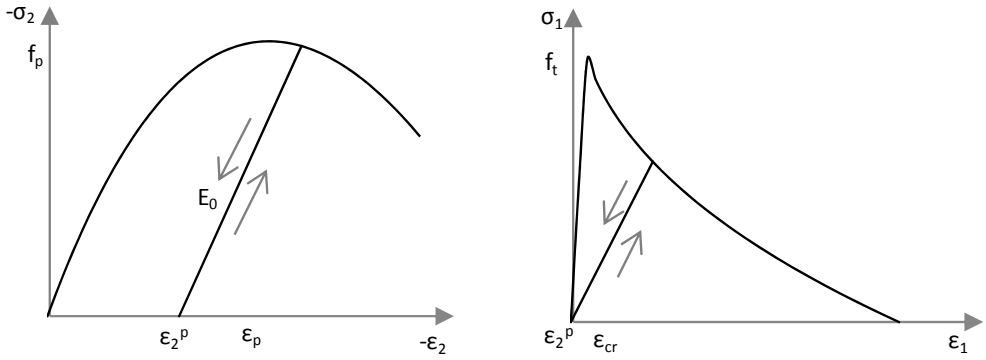

a) b)

Figure 3.2 – Constitutive behaviour of concrete: a) compression, b) tension

According to Figure 3.2b, before onset of cracking concrete in tension performs with a linear-elastic behaviour, where ε_{cr} is the strain that corresponds to the peak tensile stress f_t:

$$\sigma_1 = \begin{cases} E_0\left(\varepsilon_1 - \varepsilon_2^p\right) & 0 \le \varepsilon_1 \le \varepsilon_{cr} \\ f_t\left[1 - \left(\frac{\varepsilon_1}{c}\right)^{k_2}\right] & \varepsilon_1 \ge \varepsilon_{cr} \end{cases} \tag{3.7}$$

If the material has not been in compression before, the plastic strain ε_2^p is null, otherwise it acts like a strain offset. After cracking tension softening is represented by the curve (Cervenka 1985); following recommendations of previous studies (Mohr, Bairán and Marí 2010), the parameters of the Cervenka curve have been considered as c=ε_{sy} and k_2=0.5,

where ε_{sy} is the yielding strain of reinforcement, which implies that tension stiffening vanishes upon yielding of reinforcement.

After cracking the tensile stiffness of concrete is reduced, and softening is included in the model by using a damage variable dt_1:

$$dt_1 = \begin{cases} 0 & 0 \le \varepsilon_1 \le \varepsilon_{cr} \\ 1 - \dfrac{\sigma_1}{E_0\left(\varepsilon_1 - \varepsilon_2^p\right)} \le 1 & \varepsilon_1 \ge \varepsilon_{cr} \end{cases} \tag{3.8}$$

The secant elasticity modulus E_1 is determined through the use of the damage variable as

$$E_1 = (1 - dt_1)E_0 \tag{3.9}$$

Unloading and partial reloading performs by the straight line function (Figure 3.2b):

$$\sigma_1 = \left(1 - dt_1\right) E_0 \left(\varepsilon_1 - \varepsilon_2^p\right) \tag{3.10}$$

with the damage variable dt_1 remaining constant during these phases.

In the principal referential axes, the 2D stress-strain state of the concrete can be written as follows

$$\begin{Bmatrix} \sigma_1 \\ \sigma_2 \\ \tau_{12} \end{Bmatrix} = D_{12} \begin{Bmatrix} \varepsilon_1 \\ \varepsilon_2 \\ \gamma_{12} \end{Bmatrix} \; ; \; D_{12} = \begin{pmatrix} E_1 & 0 & 0 \\ 0 & E_2 & 0 \\ 0 & 0 & G_{12} \end{pmatrix} \tag{3.11}$$

where E_1 and E_2 are the stiffness modulus in each principal direction (secant modulus for the case of tension (Eq. (3.9)) and tangent modulus for the case of compression (Eq.(3.5))) and G_{12} is the transversal modulus determined by the expression that follows (which imposes that the angles of the principal directions of the stresses and strains are the same (Bazant 1983)):

$$G_{12} = \frac{\sigma_1 - \sigma_2}{2\left(\varepsilon_1 - \varepsilon_2\right)} \tag{3.12}$$

At the material level, the 2D average concrete strains at the *x-z* coordinate system (defined in Figure 3.1) are denoted by $\underline{\varepsilon}_{xz}=[\varepsilon_x \; \varepsilon_z \; \gamma_{xz}]^T$. As according to the concrete constitutive law the principal stresses $\underline{\sigma}_{12}=[\sigma_1 \; \sigma_2]^T$ are computed as a function of the principal strains $\underline{\varepsilon}_{12}=[\varepsilon_1 \; \varepsilon_2]^T$, the strain tensor $\underline{\varepsilon}_{xz}$ has to be rotated so as to get $\underline{\varepsilon}_{12}$. Then, the principal stresses $\underline{\sigma}_{12}$ are rotated back to the *x-z* referential, resulting into the average stress tensor

$\underline{\sigma}_{xz}=[\sigma_x\ \sigma_z\ \tau_{xz}]^T$. In the same manner, the material stiffness matrix D_{12} that is defined at the principal directions should be rotated onto the *x-z* referential, to render D_c.

These referential transformations can be performed by the use of the following rotation matrices T_ε and T_σ:

$$\underline{\varepsilon}_{xz} = T_\sigma^T \underline{\varepsilon}_{12} \quad ; \quad \underline{\varepsilon}_{12} = T_\varepsilon \underline{\varepsilon}_{xz} \tag{3.13}$$

$$\underline{\sigma}_{xz} = T_\varepsilon^T \underline{\sigma}_{12} \quad ; \quad \underline{\sigma}_{12} = T_\sigma \underline{\sigma}_{xz} \tag{3.14}$$

$$D_c = T_\varepsilon^T D_{12} T_\varepsilon \tag{3.15}$$

$$T_\varepsilon = \begin{pmatrix} l_1^2 & m_1^2 & l_1 m_1 \\ l_2^2 & m_2^2 & l_2 m_2 \\ 2l_1 l_2 & 2m_1 m_2 & l_1 m_2 + l_2 m_1 \end{pmatrix} ; T_\varepsilon^{-1} = T_\sigma{}^T ; \begin{bmatrix} l_1 = \cos\theta \\ m_1 = sen\theta \end{bmatrix} \begin{bmatrix} l_2 = sen\theta \\ m_2 = \cos\theta \end{bmatrix} \tag{3.16}$$

where θ is the angle between the principal tensile strain and the *x*-axis.

Principal strains and stresses vary in each load step, and consequently the principal directions also change. The state variables of the material - the plastic strain in compression ε_2^p and the tensile damage dt_1 - cannot be incremented in its principal values, because the principal referential is continuously rotating. For this reason, the history state variables have to be accumulated in a fixed referential. Therefore, state variables are computed in an incremental fashion in the current principal system, and are subsequently rotated to the fixed local *x-z* coordinate system and accumulated, and stored to be used in the next load step. The state update numerical procedure used in the model is based on the formulation proposed by (Vecchio 1999), summarily described in the flowchart of Figure 3.3.

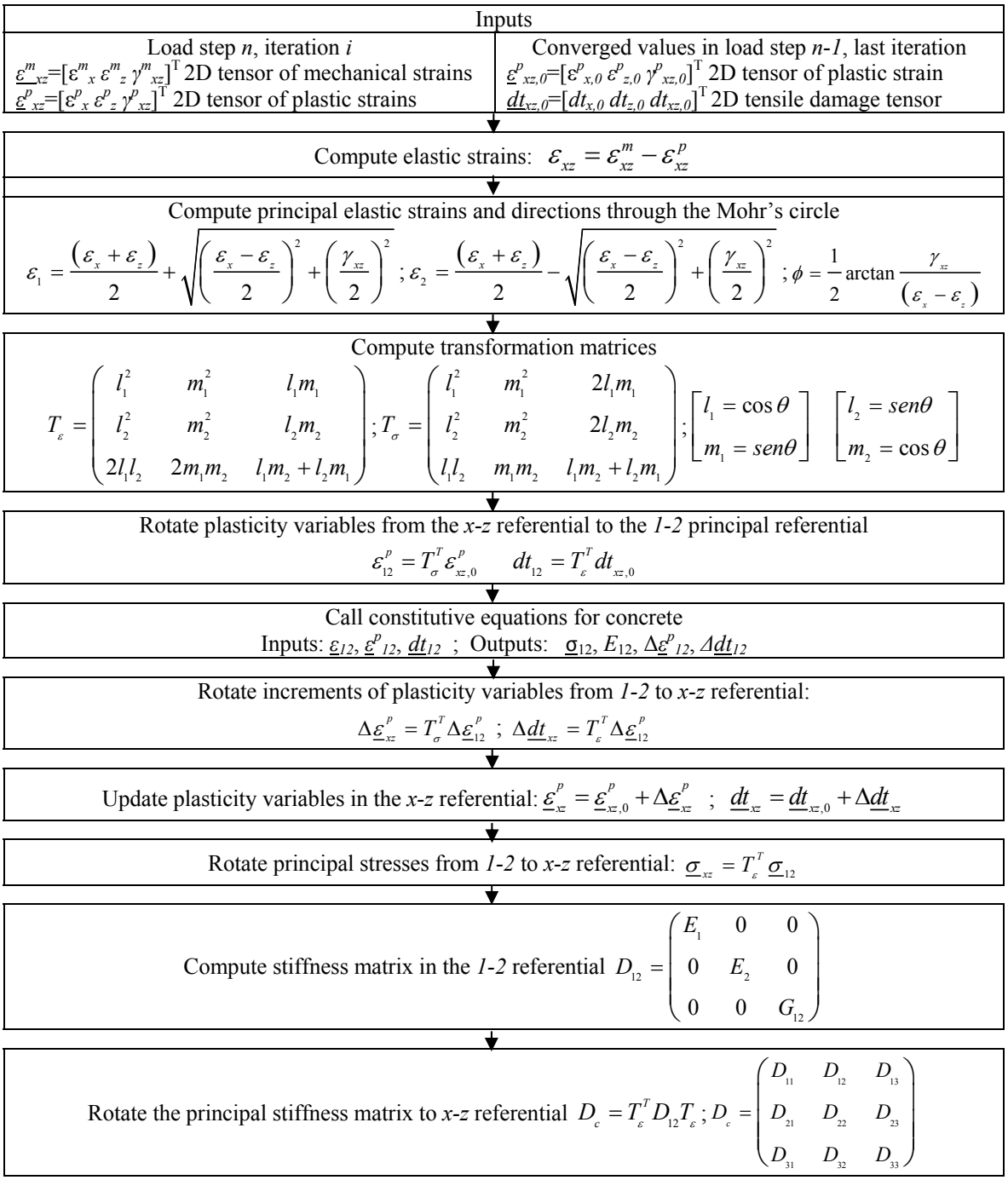

Figure 3.3 – Flowchart of the state update algorithm of concrete

3.2.1.2. Constitutive model for the reinforcement

Steel reinforcement is modelled with the bilinear 1D constitutive relationship depicted in Figure 3.4, where f_{sy} and ε_{sy} are the yielding stress and strain and f_{su} and ε_{su} are the ultimate

stress and strain, respectively. Unloading and partial reloading are performed along straight lines parallel to the initial elastic branch given by the elasticity modulus E_s.

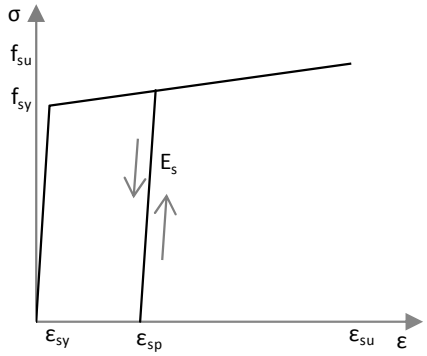

Figure 3.4 – Constitutive behaviour of steel

3.2.2 Fibre state determination

The cross section is discretized into two types of fibres, as presented in Figure 3.5: (*i*) the non shear resistant ones, submitted only to 1D axial stresses, and (*ii*) the shear resistant fibres, submitted to a multiaxial stress-strain state. Since no compatibility of lateral strains between fibres is considered in the formulation, the model is not capable of automatically provide the level of contribution of each fibre to the shear strength resistance as a function of the fibre position. This division is performed considering the following criteria: (*i*) for traditional cross section geometries, such as rectangular or I-shaped, it is considered that the fibers that pertain to the web (disregarding the cover area) are 2D fibers; (*ii*) particularly for the I-shaped cross sections, an effective area of the compressive flanges can be considered to contribute to the shear resistant mechanism and assigned as 2D fibers - the effective width of the flange can be determined accordingly to (Zararis, Karaveziroglou and Zararis 2006); (*iii*) for complex geometries a more sophisticated analysis with the model TINSA (Bairán and Marí 2006a; Bairán and Marí 2006b) is required, in order to determine the portion of section that is preponderant for resisting shear forces (recommendations from design codes like the EC2 (CEN 2004) can be used as well, as simplified criteria). In the validation examples presented in this chapter, options (*i*) and (*ii*) are considered.

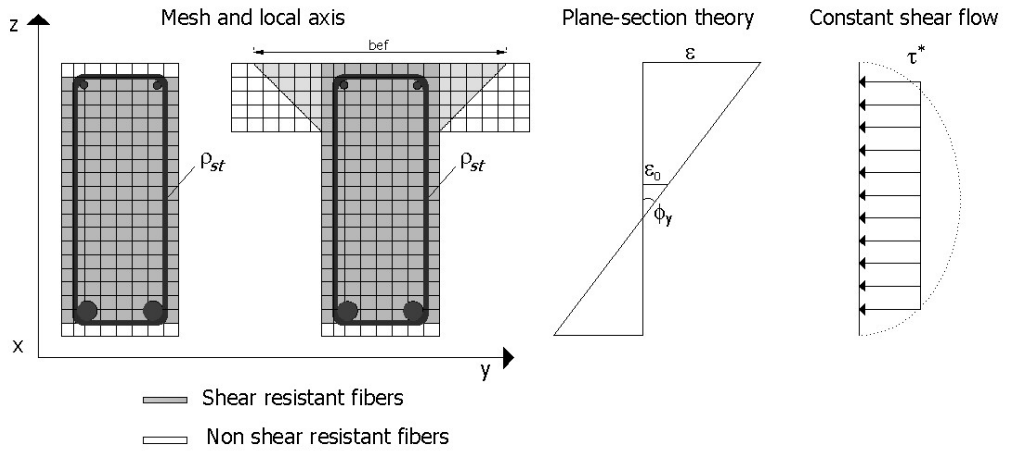

Figure 3.5 – Assumptions of the model at the section level

As represented in Figure 3.5, along with the plane section theory that computes the axial strain ε_x as

$$\varepsilon_x(z) = \varepsilon_0 + \phi_y . z \tag{3.17}$$

(where ε_0 is the axial strain at the section reference axis and ϕ_y is the curvature with respect to the *y*-axis), the adopted model assumes a shear stress τ^* along the section defined as

$$\tau^* = \begin{cases} G^* A^* \gamma_0 & \text{shear resistant fibres} \\ 0 & \text{non shear resistant fibres} \end{cases} \tag{3.18}$$

where G^* is the transversal modulus, γ_0 is the distortion at the neutral axis and A^* is the summation of the areas of the shear resistant fibres. In this manner the plane section theory is coupled with a shear stress constraint, and the determination of the fibre state is performed using a hybrid stress-strain input information.

For each fibre, given the axial strain in concrete ε_x and the assumed shear stress τ^*, and using the equilibrium, compatibility and constitutive equations, the strain and stress states and the stiffness matrix of the fibre are determined, as it will be explained with the following equations. As the non shear resistant fibres have null shear stresses they are under uniaxial stress-strain state only (Figure 3.6a), whereas the shear resistant fibres are submitted to a 2D stress-strain state (Figure 3.6b).

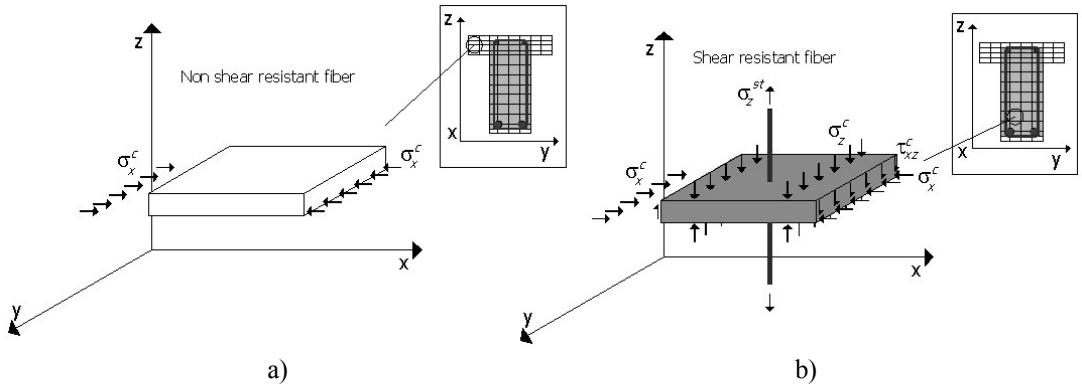

Figure 3.6 – Stresses applied in a fibre

Considering the 2D stress-strain state of the concrete part of the shear resistant fibre, upon rotation of the principal stiffness matrix D_{12} (Eq. (3.11)) to the local x-z referential, a 3×3 stiffness matrix D_c is obtained:

$$\begin{pmatrix} \Delta\sigma_x \\ \Delta\sigma_z \\ \Delta\tau_{xz} \end{pmatrix}^c = D_c \begin{pmatrix} \Delta\varepsilon_x \\ \Delta\varepsilon_z \\ \Delta\gamma_{xz} \end{pmatrix} \qquad D_c = \begin{pmatrix} D_{11} & D_{12} & D_{13} \\ D_{21} & D_{22} & D_{23} \\ D_{31} & D_{32} & D_{33} \end{pmatrix} \tag{3.19}$$

A shear resistant concrete fibre can have different n_k configurations of transversal steel (different dispositions of stirrups), which are accounted for in the model through its volumetric ratio $\rho_{st,k}$ and are submitted to axial stresses σ_z^{st} (along direction z). The increment of axial stresses in the transversal reinforcement $\Delta\sigma_z^{st}$ (along the z-direction) are computed according to

$$\begin{pmatrix} 0 \\ \Delta\sigma_z \\ 0 \end{pmatrix}^{st} = D_{st} \begin{pmatrix} 0 \\ \Delta\varepsilon_z \\ 0 \end{pmatrix}; \qquad D_{st} = \begin{pmatrix} 0 & 0 & 0 \\ 0 & \rho_{st}E_{st} & 0 \\ 0 & 0 & 0 \end{pmatrix}; \quad \rho_{st}E_{st} = \sum_{k=1}^{n_k} \left(\frac{A_{st,k}}{s_k b_k} E_{st,k} \right) \tag{3.20}$$

The total transversal steel is taken into account by summing the contributions of the different stirrups configurations ($A_{st,k}$ is the area of transversal steel, b_k is the width of the cross-section and s_k is the longitudinal spacing of each configuration of stirrups k). Compatibility requirements impose that the vertical strain in concrete and the strain in the transversal reinforcement are equal, being denoted as ε_z. No bond slip is considered.

Along direction z the incremental tensile stresses in the transversal steel $\Delta\sigma_z^{st}$ must equilibrate the incremental compression stresses in concrete $\Delta\sigma_z^c$, that is:

$$\Delta\sigma_z^c + \rho_{st}\Delta\sigma_z^{st} = 0\,; \quad \rho_{st}\Delta\sigma_z^{st} = \sum_{k=1}^{n_k}\left(\frac{A_{st,k}}{s_k b_k}\Delta\sigma_{z,k}^{st}\right) \tag{3.21}$$

From Eq. (3.19) the concrete stress along direction z is computed as

$$\Delta\sigma_z^c = D_{21}\Delta\varepsilon_x + D_{22}\Delta\varepsilon_z + D_{23}\Delta\gamma_{xz} \tag{3.22}$$

Replacing Eq. (3.22) into Eq. (3.21) and making use of Eq. (3.20), the equilibrium in the vertical direction becomes:

$$D_{21}\Delta\varepsilon_x + D_{22}\Delta\varepsilon_z + D_{23}\Delta\gamma_{xz} + \rho_{st}E_{st}\Delta\varepsilon_z = 0 \tag{3.23}$$

In addition to this equilibrium requirement, another condition needs to be fulfilled in order to determine the fibre state: the computed increment of shear stress $\Delta\tau_{xz}$ must equate the imposed increment of shear stress given by the fixed stress constraint $\Delta\tau^*$:

$$\Delta\tau^* - \Delta\tau_{xz} = 0 \tag{3.24}$$

By solving the system of the two Eqs. (3.23) and (3.24), the 2D stress-strain of the fibre (composed by concrete and smeared transversal reinforcement) is obtained, and the complete stiffness matrix of the fibre D_{fibre} is computed as the summation of both contributions (concrete and transversal reinforcement):

$$\begin{pmatrix}\Delta\sigma_x\\ \Delta\sigma_z\\ \Delta\tau_{xz}\end{pmatrix} = D_{fibre}\begin{pmatrix}\Delta\varepsilon_x\\ \Delta\varepsilon_z\\ \Delta\gamma_{xz}\end{pmatrix};\; D_{fibre} = \begin{pmatrix}D_{11} & D_{12} & D_{13}\\ D_{21} & \overline{D}_{22} & D_{23}\\ D_{31} & D_{32} & D_{33}\end{pmatrix};\; \overline{D}_{22} = D_{22} + \rho_{st}E_{st} \tag{3.25}$$

The unknown increments of the vertical axial strain $\Delta\varepsilon_z$ and shear strain $\Delta\gamma_{xz}$ can be determined as functions of the increments of $\Delta\varepsilon_x$ and $\Delta\tau^*$ according to:

$$\Delta\varepsilon_z = f\left(\Delta\varepsilon_x, \Delta\tau^*, D_{fibre}\right) = \frac{\left(D_{23}D_{31} - D_{33}D_{21}\right)\Delta\varepsilon_x - D_{23}\Delta\tau^*}{\overline{D}_{22}D_{33} - D_{23}D_{32}} \tag{3.26}$$

$$\Delta\gamma_{xz} = f\left(\Delta\varepsilon_x, \Delta\tau^*, D_{fibre}\right) = \frac{\left(D_{23}D_{21} - \overline{D}_{22}D_{31}\right)\Delta\varepsilon_x + \overline{D}_{22}\Delta\tau^*}{\overline{D}_{22}D_{33} - D_{23}D_{32}} \tag{3.27}$$

The complete mathematic derivations of Eq. (3.26) and (3.27) are presented in Annex A.

3.2.2.1. Innermost iterative procedure

In order to achieve both requirements – equilibrium of stresses along the vertical direction (Eq. (3.21)) and the fixed stress constraint in the transversal direction (Eq. (3.24)) -, an innermost iterative procedure within the fibre level is needed. After computation of the 2D fibre strain and stress states, Eqs. (3.23) and (3.24) are checked and the unbalanced vertical $\delta\sigma_z$ and tangential $\delta\tau_{xz}$ stresses are respectively computed as

$$\delta\sigma_z = -\rho_{st}\Delta\sigma_z^{st} + \Delta\sigma_z^{c} \tag{3.28}$$

$$\delta\tau_{xz} = \Delta\tau^{*} - \Delta\tau_{xz} \tag{3.29}$$

The longitudinal axial strain increment $\Delta\varepsilon_x$ is kept fixed and the iterative loop goes through the correction of the vertical $\delta\varepsilon_z$ and transversal $\delta\gamma_{xz}$ strains, which are computed through the following expressions as functions of the unbalanced stresses $\delta\sigma_z$ and $\delta\tau_{xz}$:

$$\delta\varepsilon_z = f\left(\delta\tau_{xz}, \delta\sigma_z, D_{fibre}\right) = \frac{\delta\sigma_z D_{33} - D_{23}\delta\tau_{xz}}{\overline{D}_{22}D_{33} - D_{32}D_{23}} \tag{3.30}$$

$$\delta\gamma_{xz} = f\left(\delta\tau_{xz}, \delta\sigma_z, D_{fibre}\right) = \frac{\delta\tau\overline{D}_{22} - D_{32}\delta\sigma_z}{\overline{D}_{22}D_{33} - D_{32}D_{23}} \tag{3.31}$$

The complete mathematic derivations of Eq. (3.30) and Eq. (3.31) are presented as well in Annex A. The strain corrections ($\Delta\varepsilon_z^{it}$, $\Delta\gamma_{xz}^{it}$) are introduced in the next iteration, until both the unbalanced vertical $\delta\varepsilon_z$ and tangential stresses $\delta\tau_{xz}$ almost vanish:

$$\Delta\varepsilon_z^{it} = \Delta\varepsilon_z + \delta\varepsilon_z \tag{3.32}$$

$$\Delta\gamma_{xz}^{it} = \Delta\gamma_{xz} + \delta\gamma_{xz} \tag{3.33}$$

Once convergence is achieved (i.e., $\delta\varepsilon_z \approx 0$ and $\delta\tau_{xz} \approx 0$), the state determination of the fibre is accomplished. As stress σ_z is null and the section model does not include ε_z, a static condensation must be applied

$$\begin{pmatrix} \sigma_x \\ 0 \\ \tau_{xz} \end{pmatrix} = \begin{pmatrix} D_{11} & D_{12} & D_{13} \\ D_{21} & \overline{D}_{22} & D_{23} \\ D_{31} & D_{32} & D_{33} \end{pmatrix} \begin{pmatrix} \varepsilon_x \\ \varepsilon_z \\ \gamma_{xz} \end{pmatrix} \tag{3.34}$$

and thus

$$\begin{pmatrix}\sigma_x\\ \tau_{xz}\end{pmatrix} = K_{fibre}\begin{Bmatrix}\varepsilon_x\\ \gamma_{xz}\end{Bmatrix} \;\; ; \; K_{fibre} = \begin{pmatrix} D_{11} - \dfrac{D_{12}D_{21}}{\overline{D}_{22}} & D_{13} - \dfrac{D_{12}D_{23}}{\overline{D}_{22}} \\ D_{31} - \dfrac{D_{32}D_{21}}{\overline{D}_{22}} & D_{33} - \dfrac{D_{32}D_{23}}{\overline{D}_{22}} \end{pmatrix} \tag{3.35}$$

where K_{fibre} is the condensed stiffness matrix of the fibre. The transversal modulus used in Eq. (3.18) to estimate the constant shear stress applied to the section is given by

$$G^* = D_{33} - \frac{D_{32}D_{23}}{\overline{D}_{22}} \tag{3.36}$$

and its initial value is considered as $E_0/2$.

3.2.3 Element and section models

A schematic representation of the main characteristics of the filament beam model is presented in Figure 3.7. A 2-noded Timoshenko FE with linear shape functions N_1 and N_2 was implemented in accordance to the formulation presented in (Oñate 1995). For the 2D case, the displacement field is a function of two displacements, axial u and vertical w, and a rotation θ_y. In the Timoshenko beam theory it is assumed that undeformed plane sections perpendicular to the beam axis remain plane, but not necessarily normal to the longitudinal axis after deformation. An average rotation of the section due to distortion is considered in order to maintain valid the plane section assumption. The total rotation θ_y of the cross section is then

$$\theta_y = \frac{\partial w}{\partial x} + \gamma_0 \tag{3.37}$$

where γ_0 is the additional rotation due to shear.

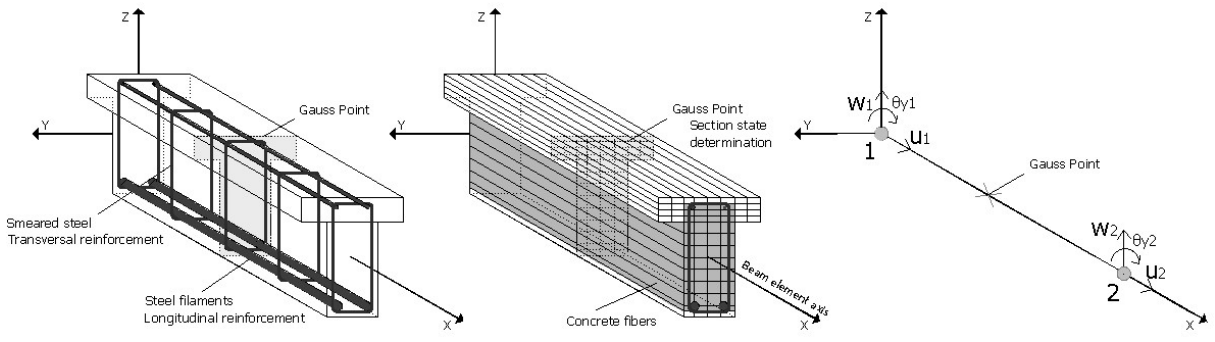

Figure 3.7 – Fibre beam element

The generalized strains in the cross section are the axial strain ε_0, the shear rotation γ_0 and the curvature ϕ_y:

$$\varepsilon_0 = \frac{\partial u}{\partial x} \tag{3.38}$$

$$\gamma_0 = \frac{\partial w}{\partial x} + \frac{\partial u}{\partial z} = \frac{\partial w}{\partial x} + \theta_y \tag{3.39}$$

$$\phi_y = \frac{\partial \theta_y}{\partial x} \tag{3.40}$$

Thus, the kinematic equations that relate the nodal displacements $a_j=[u_j\ w_j\ \theta_{yj}]^T$ of each node j to the generalized sectional strains $\underline{\varepsilon_0}=[\varepsilon_0\ \gamma_0\ \phi_y]^T$ at the Gauss points are given by the transformation matrix B as:

$$\begin{pmatrix} \varepsilon_0 \\ \gamma_0 \\ \phi_y \end{pmatrix} = \begin{bmatrix} B_1 & B_2 \end{bmatrix} \begin{pmatrix} a_1 \\ a_2 \end{pmatrix} \quad ; \quad [B_i] = \begin{pmatrix} \frac{\partial N_i}{\partial x} & 0 & 0 \\ 0 & \frac{\partial N_i}{\partial x} & N_i \\ 0 & 0 & \frac{\partial N_i}{\partial x} \end{pmatrix} \tag{3.41}$$

At the sectional level the relationship between the generalized strains $\underline{\varepsilon_0}$ determined on the axis of the FE and the strains on each fibre $\underline{\varepsilon_{fibre}}=[\varepsilon_x\ \gamma_{xz}]^T$ is given by the transformation matrix T as:

$$\begin{pmatrix} \varepsilon_x \\ \gamma_{xz} \end{pmatrix}_{fibre} = T \begin{pmatrix} \varepsilon_0 \\ \gamma_0 \\ \phi_y \end{pmatrix} \quad ; \quad T = \begin{bmatrix} 1 & 0 & z \\ 0 & 1 & 0 \end{bmatrix} \tag{3.42}$$

After the fibre state determination, contributions of the concrete (denoted as '*c*') and transversal reinforcement (denoted as '*st*') to the stiffness matrix K_{sec} and to the internal load vector $\underline{S_{sec}}$ of the section can be computed by accounting for the contributions of the stiffness matrices K_{fibre} and forces $\underline{S_{fibre}}$ of all the fibres (shear resistant and non-shear resistant):

$$K_{\sec}^{c+st} = \int T^T\ K_{fibre}\ T\ dA \tag{3.43}$$

$$\underline{S}_{\sec}^{c+st} = \int T^T\ \underline{S}_{fibre}\ dA \tag{3.44}$$

where A represents the area of each fibre. Filaments of longitudinal reinforcement are assumed to be submitted only to axial strains as

$$\left(\varepsilon_x\right)_{sl} = T_{sl}\begin{pmatrix}\varepsilon_0\\ \gamma_0\\ \phi_y\end{pmatrix} \quad ; \quad T_{sl} = \begin{bmatrix}1 & 0 & z\\ 0 & 0 & 0\end{bmatrix} \tag{3.45}$$

Bond slip is neglected, and the steel stress state is determined through the 1D constitutive law represented in Figure 3.4. The steel contribution to the sectional stiffness and internal load vector (denoted as '*sl*') is also given by the summation of the stiffness and the forces of each filament:

$$K_{\text{sec}}^{sl} = \int T_{sl}^{\ T}\ E^{sl}\ T_{sl}\ dA \tag{3.46}$$

$$\underline{S}_{\text{sec}}^{sl} = \int T_{sl}^{\ T}\ \sigma_x^{sl}\ dA \tag{3.47}$$

Accordingly, the sectional stiffness matrix K_{sec} and the internal load vector $\underline{S}_{sec}$ are obtained by adding the contributions of the concrete, of the transversal reinforcement fibres and of the longitudinal steel filaments:

$$K_{\text{sec}} = K_{\text{sec}}^{c+st} + K_{\text{sec}}^{sl} \tag{3.48}$$

$$\underline{S}_{\text{sec}} = \underline{S}_{\text{sec}}^{c+st} + \underline{S}_{\text{sec}}^{sl} \tag{3.49}$$

Shear deformation at the FE level is considered as an average rotation constant along the cross-section, resulting into an important simplification of the sectional behaviour. Taking advantage of the hybrid nature of the sectional formulation, which implies both kinematic (axial strains ε_0 and curvatures ϕ_y) and force (shear stresses τ^*) entities, a shear deformation correction can be performed. In fact, there is a difference between the average distortion γ_0 of the Timoshenko FE (determined in Eq. (3.39) and used in Eq. (3.42)) and the average of the shear strains γ_{xz} on each fibre (determined in Eq. (3.27)). Consequently, to accomplish compatibility between the two types of distortions, a residual force $V_{z,ul}$ is determined as

$$\begin{Bmatrix}0\\ V_{z,ul}\\ 0\end{Bmatrix} = K_{\text{sec}}\begin{Bmatrix}0\\ \gamma_{ul}\\ 0\end{Bmatrix} \tag{3.50}$$

$$V_{z,ul} = \left(K_{\text{sec}}\left(1,2\right) + K_{\text{sec}}\left(2,2\right) + K_{\text{sec}}\left(3,2\right)\right)\gamma_{ul} \tag{3.51}$$

where the unbalanced shear strain is given by

$$\gamma_{ul} = \gamma_0 - \gamma_{xz,m} \tag{3.52}$$

and $\gamma_{xz,m}$ is the average of the shear strains in a cross-section considering each fibre weighted by its area A. The residual shear force is included in the internal force vector of the section as

$$\underline{S}_{\text{sec}} = \begin{bmatrix} N \\ V_z + V_{z,ul} \\ M_y \end{bmatrix} \tag{3.53}$$

Making use of the sectional concept presented in this model, the classical FEM definitions (Zienkiewicz and Taylor 2004) of the element stiffness matrix K_{elem} and of the internal load vector $\underline{F}_{elem}$ can be written as

$$K_{elem} = \int B\, K_{\text{sec}}\, B\, dx \tag{3.54}$$

$$\underline{F}_{elem} = \int B^T\, \underline{S}_{\text{sec}}\, dx \tag{3.55}$$

Each element has one Gauss Point located at its mid length. Reduced integration is used in order to avoid shear locking.

3.2.4 Procedure for nonlinear analysis

The implementation of the proposed model is illustrated by the flowchart of Figure 3.8, where two iterative loops are marked: (*i*) an outermost one, which corresponds to the standard Newton-Raphson (NR) procedure for determination of the displacement increments through the global equilibrium equations, and (*ii*) the innermost iteration loop, which corresponds to the state determination of the shear resistant fibres.

Considering the outermost iterative procedure, and in order to overcome intermediate limit points, an arc-length based on the Updated Normal Plane (Crisfield 1996) was implemented in the code. The stop of the outermost iterative procedure is caused by material failure and not by convergence problems or numerical instabilities, as demonstrated in the subsequent examples of validation of the model. Hence, it is possible to determine the structural response along the different stages of the material behaviour: elastic, cracked, yielded and ultimate ranges. In its turn, the innermost iteration procedure at the fibre level is often not able to continue the computation beyond material failure.

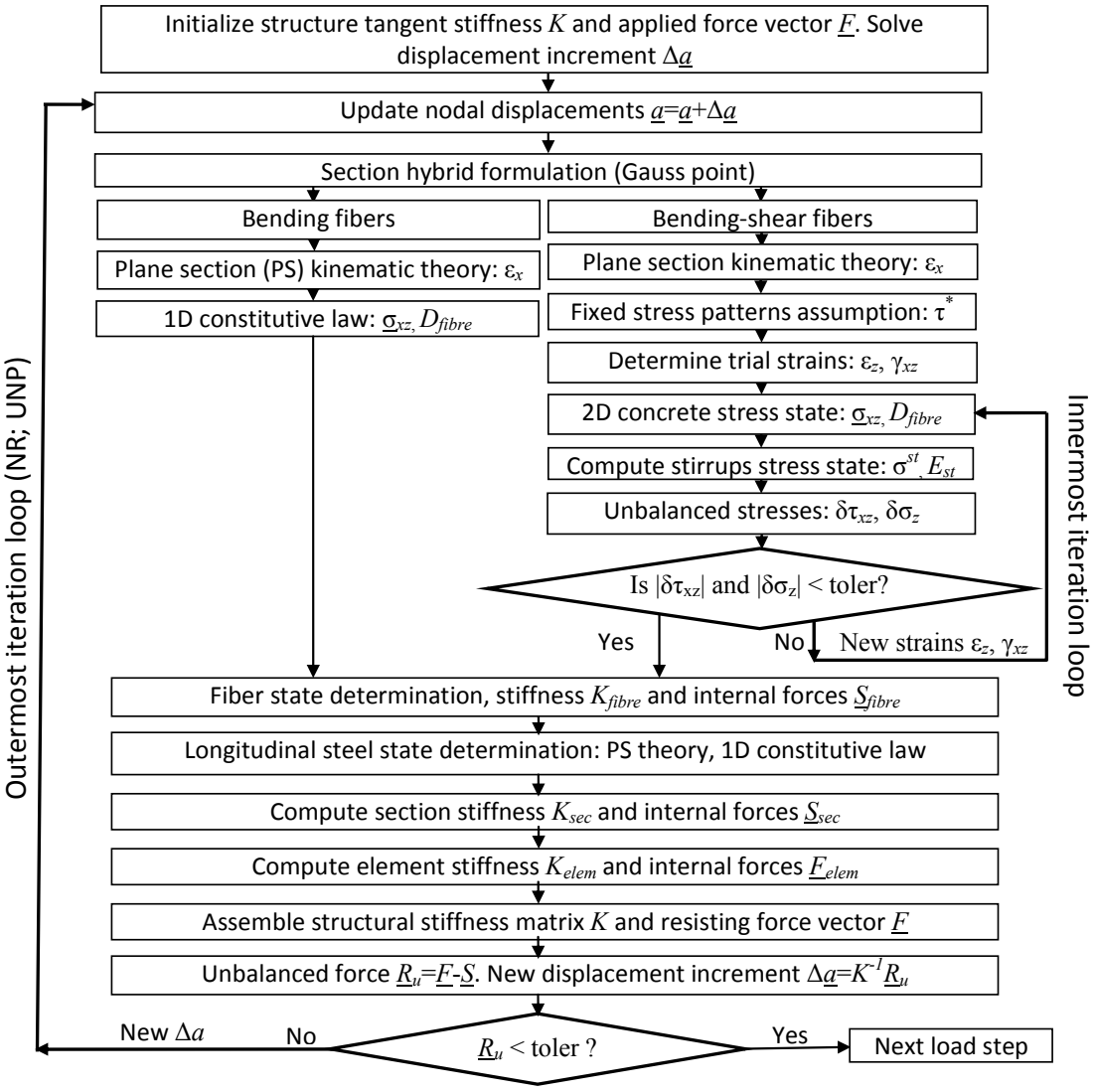

Figure 3.8 – Flow chart of the proposed model

3.2.5 Representation of concrete cracking

Although the constitutive equation for concrete is based on the smeared crack approach, discrete cracking patterns are graphically represented after a post-processing of the multiaxial strain tensor, by means of an external algorithm. As at each Gauss point the principal strains and directions are known (they are outputs of the numerical model), when the principle tensile strain in each fibre reaches the critical strain ($\varepsilon_1 > \varepsilon_{cr}$), an orthogonal line with the inclination of the correspondent principal direction is printed.

Due to the non-verticality of the cracks, the information of the strain state in the location of the crack path does not correspond to a single Gauss point. Consequently, as schematically represented in Figure 3.9, the strain state corresponding to the location of a crack is obtained using a linear interpolation between the strain states of the two close-most Gauss points. In summary, for a given load step in which cracking has started the following procedure is pursued: (*i*) determination of the *x*-*z* coordinates of the crack-tip settled in the previous load step; (*ii*) evaluation of the strain state in this point through interpolation; (*iii*) check the development of the crack by comparing the principle tensile strain with the critical strain.

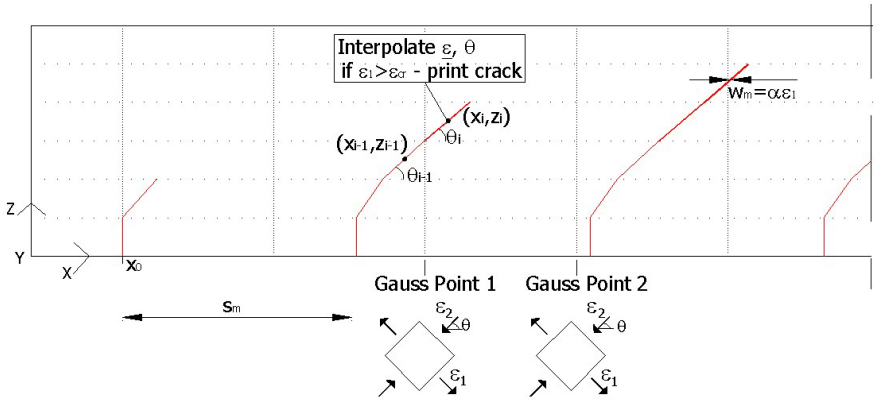

Figure 3.9 – Scheme of the post-processing method for the representation of the cracks

Along with the strain state of each fibre, the *x*-coordinate were the first crack appears (which is randomly assumed) and the crack spacing are the necessary input information to this external algorithm. The average crack spacing s_m is determined according to the Spanish Structural Concrete Code – EHE (CPH 2008) or to the EC2 (CEN 2004), limited by a maximum value correspondent to the stirrups spacing (that are usually the weakest points were vertical cracking starts). The option to represent the lines with the thickness proportional to the average crack width w_m determined as

$$w_m = s_m \varepsilon_1 \tag{3.56}$$

is available in this post-process algorithm, where ε_1 is the principal tensile strain determined by the numerical model for each fibre at each Gauss point. The formation and development of the cracks are not related to the size of elements, as long as a mesh-independent simulation is ensured.

3.3 Validation of the model

3.3.1 Overview

The experimental tests that were simulated with the proposed model for validation purposes will be presented in the following. Different beam tests were chosen in order to embrace diverse types of cross-sections and reinforcement, loading schemes and failure modes.

(*i*) The Stuttgart shear tests

The first test simulated with the model proposed in this thesis is taken from the wide experimental campaign performed by (Leonhardt and Walther 1961), selecting the case of T-beams specimens with light stirrup reinforcement under concentrated loads until shear failure. The goal of this test is to examine the influence of the web width on the shear strength of the beams. A deep validation is carried out considering displacements, strains in reinforcement and in the concrete struts and cracking patterns. The sectional response given by the proposed model is compared with more complex and accurate numerical models. Numerical sensitivity analyses are carried out in order to assess the influence of the mesh on the response of the model (longitudinal and transversal discretization and division between 1D and 2D fibres). The key conclusions about the mesh sensitivity are taken into account in the subsequent examples of validations.

(*ii*) The Vecchio and Shim tests

The classical series of beams tested by (Bresler and Scordelis 1963) were recreated in (Vecchio and Shim 2004) to determine the repeatability of the results. From this experimental campaign that consisted in a total of four series of three beams, each with a rectangular cross section, two beams are simulated with the model proposed in this thesis: one with shear failure and the other with flexural failure. Validation is carried out through load-displacement curves. The numerical results are used to demonstrate the efficiency of the proposed model to capture the increment of stresses in the longitudinal reinforcement due to shear, and the development of stresses in the stirrups along the beam. Also, the predicted response of a shear-span section for different load levels is presented.

(*iii*) The Kaufmann's beams

The VN series of experiments carried out by Kaufmann and Marti in the 'Beam Element Tester' (BET) in Zurich (Kaufmann and Marti 1996) consisted in I-shaped specimens loaded in shear until failure, with a null bending moment at mid-span. The two specimens simulated with the proposed model differ in the load scheme: one beam has a null axial force, whilst the other is subjected to a constant compressive axial force of 1MN. The experimental data available to compare with the numerical predictions consists of principal strains and angles, strains in stirrups and cracking patterns. The influence of confinement brought by axial force on the response of the beams is evaluated.

(*iv*) The experimental tests at UPC

A series of shear beams were tested at the Laboratory of Structural Technology at UPC in May of 2010, in the ambit of a research project for the study of the influence of high quantity of fine aggregate in the shear resistance of RC beams. In this work, only the case of beams with conventional concrete is presented. This experimental campaign consisted in four shear critical beam specimens with different quantities of longitudinal and transversal reinforcement. The validation of the proposed model is carried out by means of displacements and vertical, horizontal and diagonal strains measured in concrete.

All the presented experimental tests were performed under monotonic loading. Parallel to the analysis with the proposed model, numerical simulations with the flexural fibre beam basis model CONS (Marí 2000) (described in Section 2.2) are also performed. The same meshes and material properties are used in both simulations. Thus, by comparing the results computed by both the basis and the proposed models it is possible to evaluate the importance of considering shear effects in the analyses.

3.3.2 The Stuttgart shear tests

3.3.2.1. Description

The benchmark simulated with the proposed model belongs to the classical shear beam tests carried out in Stuttgart and reported in (Leonhardt and Walther 1961). The series of test under study relate to one rectangular and three T-shaped cross section beams, with light stirrup reinforcement and tested till failure under concentrated loading. The goal of this test was to examine the influence of the web width on the shear strength of the beams.

The dimensions and reinforcement of the four beams (ET1, ET2, ET3, and ET4), with varying web widths (b=0.3m, 0.15m, 0.10m and 0.05m, respectively), are presented in Figure 3.10. The location of the sensors related to the most significant experimental information used for validation of the model is also indicated in this figure; experimental results presented for the stresses in the stirrups are average values given by the four strain gauges located in the transversal reinforcement multiplied by its Young's modulus. In a analogue manner, diagonal compressive stresses in concrete where calculated with the aid of the stress-strain curve determined experimentally in concrete specimens by means of the shortening strains measured at 45º in the web. The beams were designed to fail in shear; all beams have the same tensile reinforcement (four 20mm diameter rebars) and vertical two-leg stirrups (6mm diameter rebars) with a constant spacing of 0.11m at the shear region. The ratio of transversal reinforcement ρ_{st} varied from 0.17% of the beam with wider web (ET1) to 1.03% of the beam of narrower web (ET4). The measured material properties for the beams were: $f_c^{'}$ = 28.5MPa and E_0 = 23.8GPa for concrete, f_{sy} = 420MPa and E_s = 210 GPa for longitudinal reinforcement, f_{sy} = 320MPa and E_{st} = 210GPa for transversal reinforcement; the tensile strength of concrete was taken in the present analysis as $f_t = 0.3(f_c^{'})^{0.666}$ = 2.8 MPa.

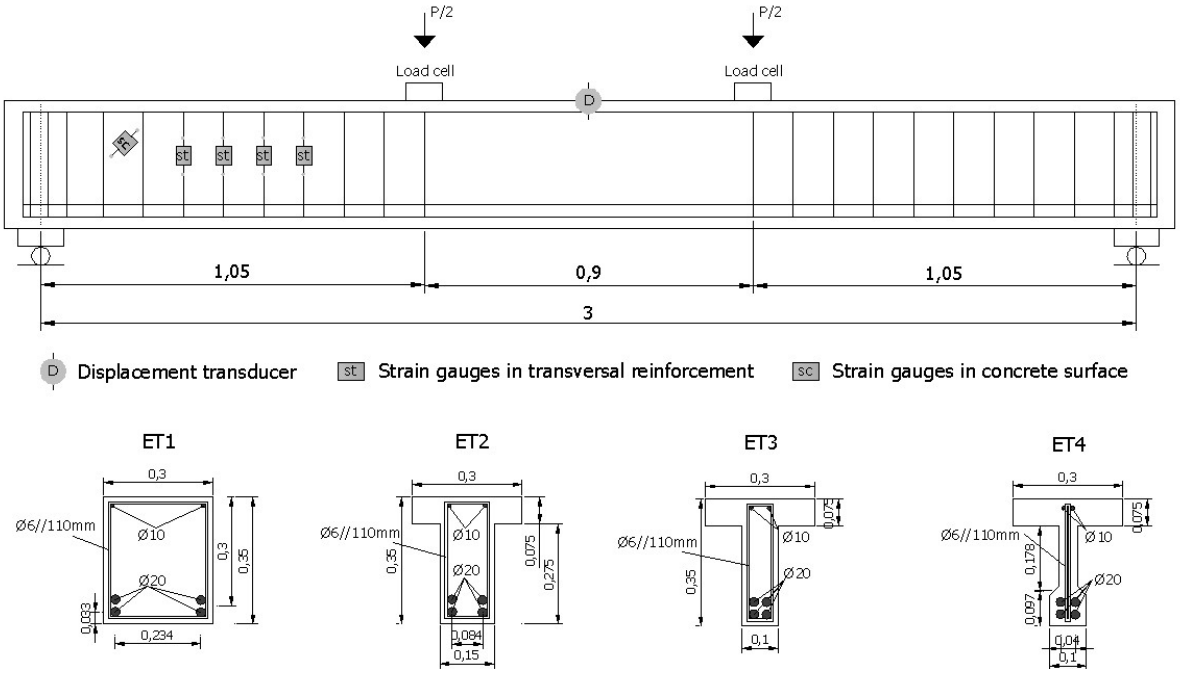

Figure 3.10 – Characteristics of the Stuttgart shear tests

The meshes of the numerical models are represented in the Figure 3.11. The specimens were simulated with 20 beam FEs with the same length, and the cross section was

discretized into fibres 5mm thick. The fibres of the web that do not belong to the concrete cover area are considered the ones that contribute to the shear resistance. No shear resistant fibres were considered in the flanges. Load (P) was applied as nodal forces in an incremental form until failure.

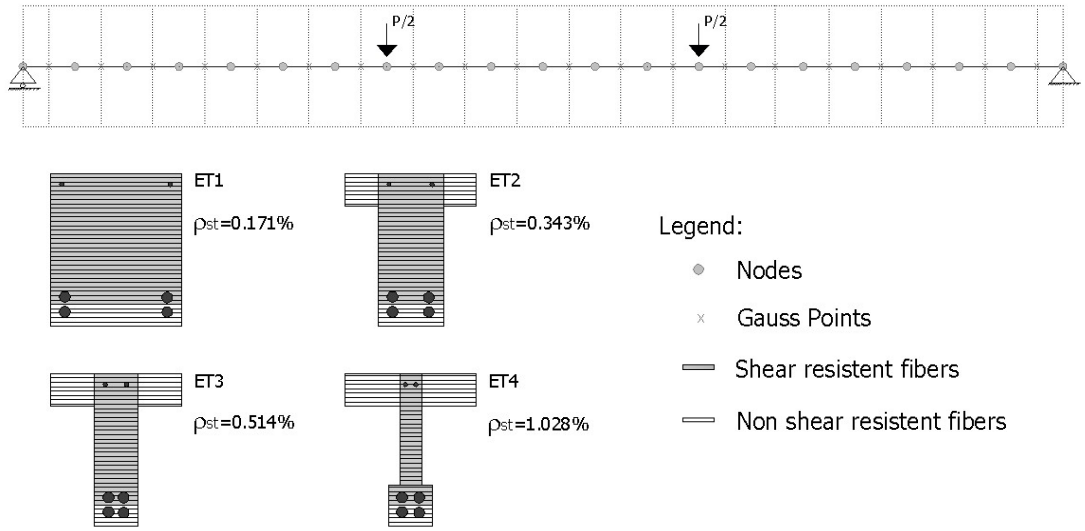

Figure 3.11 – Model of the Stuttgart shear tests

3.3.2.2. Results and discussion

In accordance with the reported observations, with the exception of ET1 all the other beams failed in shear: ET2 showed a shearing failure with crushing of the flexural compressive zone at the end of the main shear crack; ET3 showed crushing of concrete in addition to web failure, as a result of yielding of the stirrups and crushing of the diagonal concrete struts; ET4 failed by concrete crushing of the web after general yielding of the stirrups. Even though ET1 specimen had failed by crushing of the concrete in the bending region, there were vast diagonal cracks in the shear region. Accordingly to the numerical simulations, all beams failed by crushing of concrete in the web after extensive yielding of stirrups, with the exception of ET1 in which failure of longitudinal reinforcement was achieved. As summarized in Table 3.1, failure mechanisms and load carrying capacities were satisfactorily predicted by the proposed numerical model. In contrast, the flexural model provided predictions quite far from the experimental data, due to its intrinsic limitations.

Table 3.1 Summary of experimental and computed results at failure

Beam	Experimental		Proposed shear-bending model		Basic flexural model	
	P_u (kN)	Failure mode	P_u (kN)	Failure mode	P^u (kN)	Failure mode
ET1	241	Bending [a]	240	Shear/Bending [*]	290	Bending [***]
ET2	240	Shear/Bending [b]	238	Shear [**]	283	Bending [***]
ET3	240	Shear [b,c]	234	Shear [**]	282	Bending [***]
ET4	179	Shear [c]	179	Shear [**]	280	Bending [***]

[a] Crushing of concrete in bending region.
[b] Crushing of the flexural compressive zone at the end of the main shear crack.
c Web failure of the diagonal compressive due to yielding of stirrups.
[*] Failure of longitudinal reinforcement, crushing of concrete and extensive yielding of stirrups.
[**] Extensive yielding of stirrups and crushing of the concrete web.
[***] Failure of longitudinal reinforcement.

Computed and measured displacements at mid-span are compared in Figure 3.12. In general, a very good agreement between experimental data and numerical results computed by the proposed model is observed. Regarding the results from the flexural model, it is clear that it is not suitable to analyse this type of structural elements where shear is of relevance, as it results in non-safe predictions. Significance of shear deformation in the total displacements is visible by comparing the results from the shear model with the pure bending model. Specimens ET1, ET2 and ET3 reached approximately the same failure load, however, the ultimate displacements were different. The beams with narrower webs were more flexible and presented higher ultimate displacements. Beam ET4 reached a less load level than the other specimens. This influence of the web width on the response of the beams was well capture by the proposed model. Also, the differences between predictions of the flexural and shear models increased for the beams width narrower web widths, as shear effects become more relevant. The deflection of the beams for an applied load of 120kN are depicted in Figure 3.13, where the same conclusions can be drawn: the proposed model reproduces the experimental behaviour, capturing the effects of the varying web widths on the flexibility of the beam; the basic flexural model underestimates the deflections and does not accounts for the web width influence, as similar predictions are given for the 4 specimens.

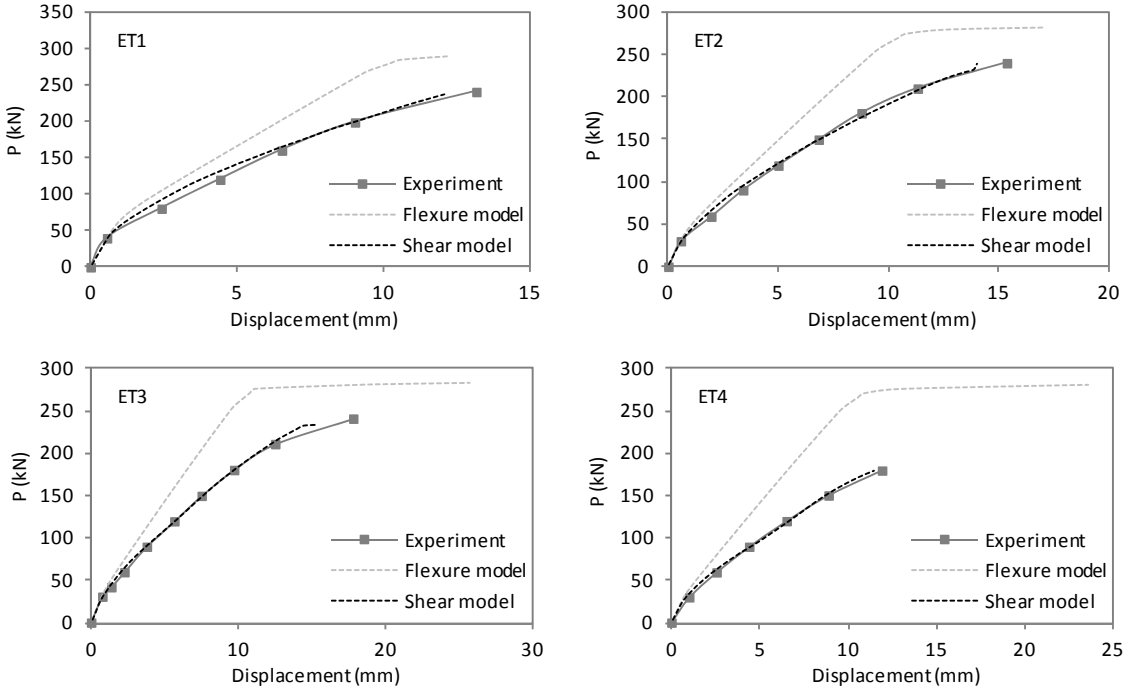

Figure 3.12 – Mid-span displacements of the Stuttgart shear tests

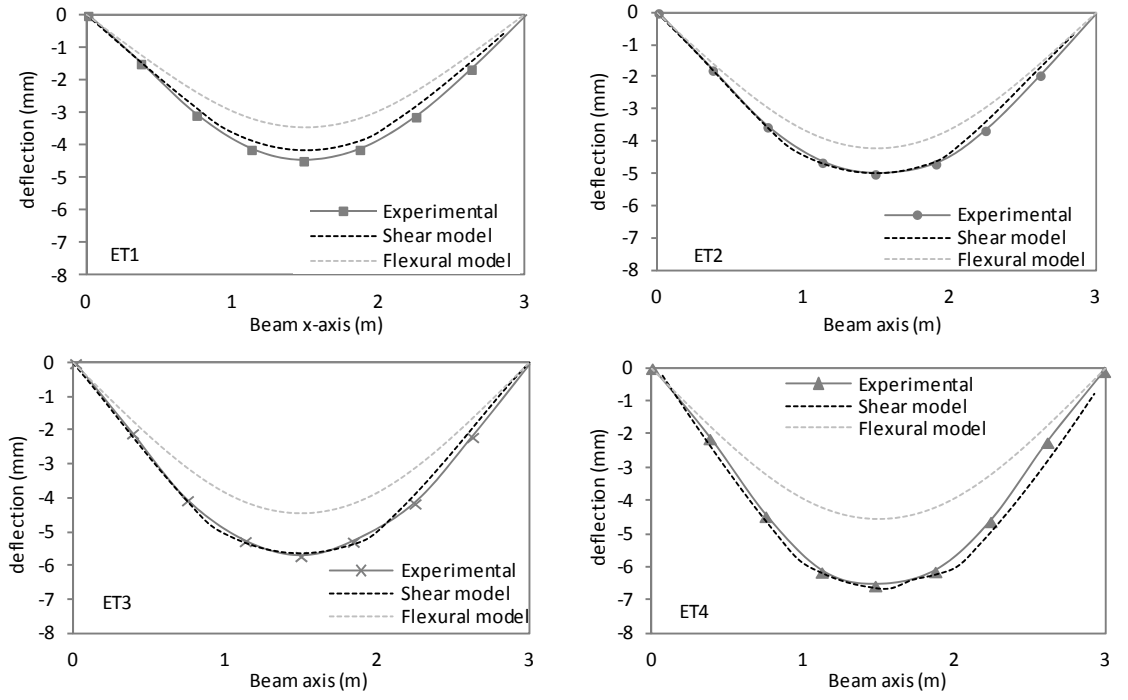

Figure 3.13 – Deflection of the beams for an applied load of 120kN

Average normal stresses in the stirrups are presented in Figure 3.14 for the 4 beam tests. In general a quite good fitting is achieved between the numerical and experimental results, especially in the case of the beams with thinner webs (ET2 and ET3). According to the

graphics, the diagonal cracking load that coincides with the moment where the stirrups start to work, is very well reproduced by the model: in thick webs (beams ET1 and ET2) the stirrups start to take up load only for high loads (circa P=150kN and P=100kN, respectively); on the other hand, in thinner webs (beams ET3 and ET4) the diagonal cracking starts earlier (circa P=75kN and P=50kN, respectively). For the beams with thicker webs (ET1 and ET2) the model tends to overestimate the stirrup stresses. It must be highlighted that the experimental measurements are extremely dependent on the crack locations, as if the crack does not cross the scanned zone the strain data will be less than the real average strain in the stirrups. For the beams with thinner webs (ET3 and ET4) the load for which the stirrups reach yielding is quite accurately predicted by the numerical model. In this case, there are no results from the basic flexural model, as it does not consider shear reinforcement.

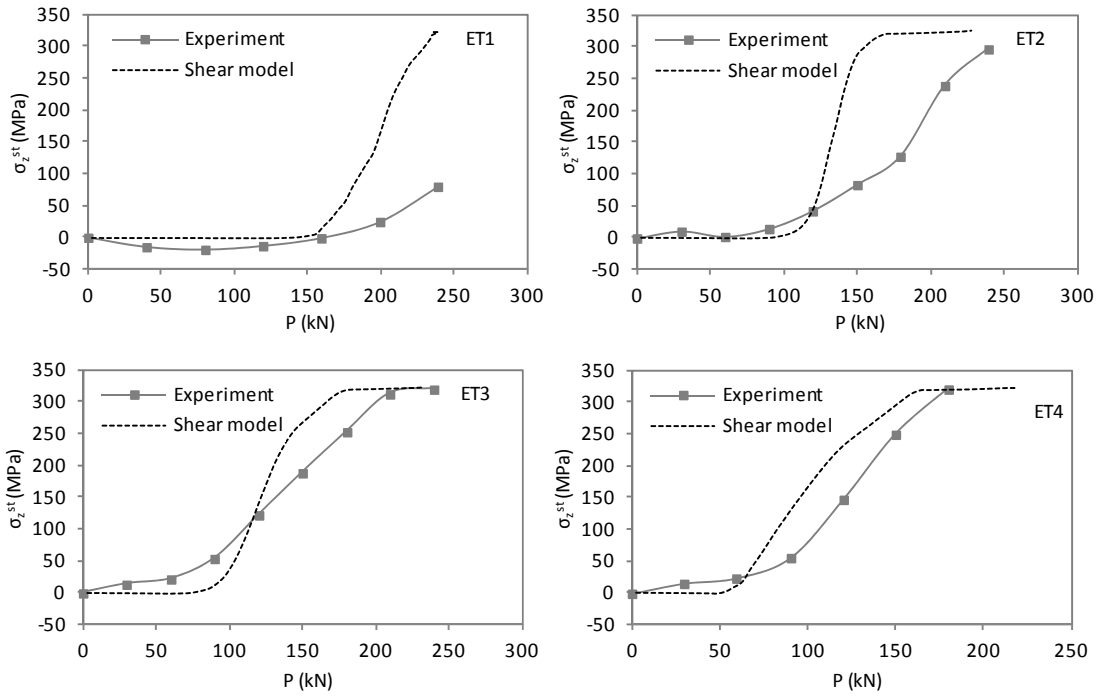

Figure 3.14 – Average normal stresses in the stirrups in the Stuttgart shear tests

The variation of the stirrup stresses along the shear-span of the beams is presented in Figure 3.15 for two load levels: P=120kN and P=180kN. The experimental data consists on the average of several measured points, in which considerable variations depending on the position and length of the shear cracks are reported (Leonhardt and Walther 1961). The overestimation of the stirrup stresses by the model is again perceived in this graphics. Even though, given the limitations of the experimental measurements used for comparison, the

development of the stirrup stresses with the load is acceptably reproduced by the proposed model. Moreover, it is noticed in the experimental data that the stresses in the stirrups increase with the decreasing of the web width. This influence is also present in the predicted numerical results, especially for the lower load level.

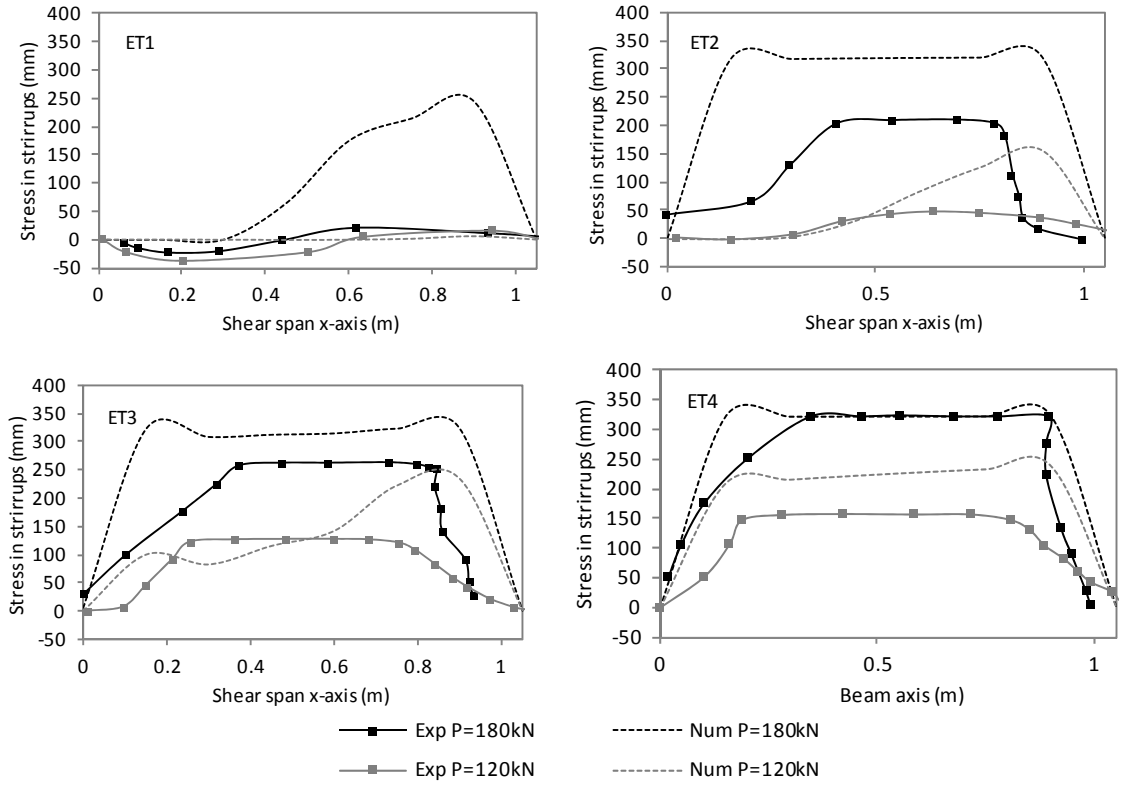

Figure 3.15 – Stresses in the stirrups at various sections along the shear span of the beams for the loads 120kN and 180kN

The experimental diagonal stresses in concrete are compared in Figure 3.16 with the computed results for the three T-shaped beams. The numerical values correspond to the average of the stresses in the fibres corresponding to the location and length of the sensor *sc* represented in Figure 3.10. The experimental measures were taken at an angle of 45º and the computed principal angles took values around 50º and 60º. Hence, in order to perform a direct comparison between numerical and experimental data, the presented computed results correspond to the stresses at the angle of 45º. Although the tendency of the numerical predictions is quite similar to the measured one, it is evident that the model generally underestimated the diagonal concrete stresses. In fact, the numerical prediction of concrete stresses is a non-straightforward task, as it is totally reliant on the constitutive equations, which in turn depend on many random aspects that characterize concrete

behaviour. Even tough, the influence of the thickness of the web in the diagonal compressive stresses in concrete is captured by the numerical model.

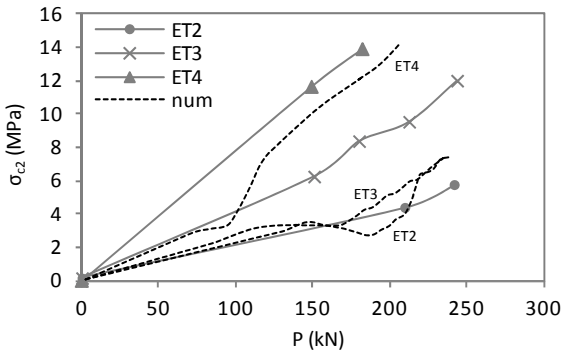

Figure 3.16 – Diagonal stresses in concrete in the Stuttgart shear tests

Contour levels of the tensile stresses in the stirrups σ_z^{st} and of the concrete longitudinal compressive stresses σ_z^{c} along the ET3 beam are depicted in the maps of Figure 3.17 for the last converged load step. By analysing both colour maps, it is noticed an extensive yielding of the stirrups, and very high concrete compressive stresses in the web, the latter reaching values very close to the concrete strength (including compression softening effects), meaning that the beam is near collapse. Thus, the non-convergence of the subsequent load increment was caused by the vast material damages, and not by other sorts of numerical instabilities.

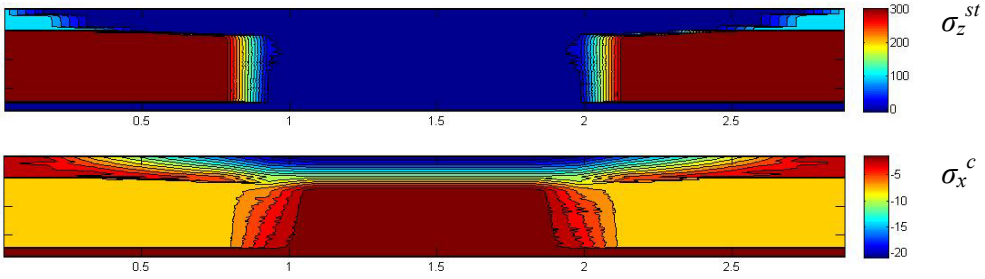

Figure 3.17 – Computed results for the last converged load step of the ET3 specimen: stresses σ_z^{st} in the shear reinforcement and concrete longitudinal stresses σ_x^{c} (MPa)

In relation to the prediction of crack patterns, Figure 3.18 allows comparing the experimental and the computed crack patterns for the beams ET1 and ET3 at failure, in which a correct correlation is observed. In beam ET1 the flexural vertical cracks reached approximately the same length as the diagonal cracks in the shear span. In contrast, beam ET3 presented longer shear cracks, reaching the compressive flange in comparison with bending cracks. Also, higher inclinations of cracks in the shear span were observed for beam ET3 in comparison with beam ET1. These differences on the crack patterns of the

beams were well caught by the numerical model, which evidences the higher influence of shear effects on the narrower web beam (ET3).

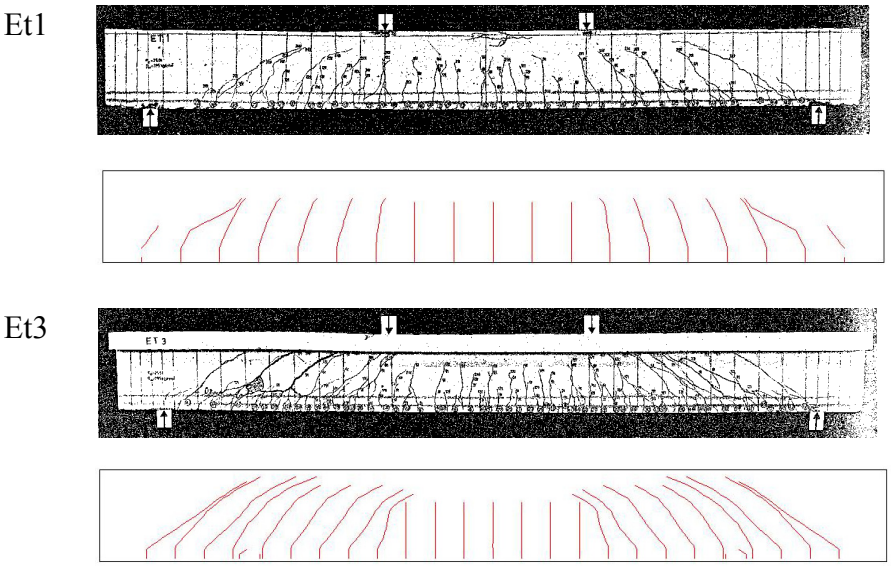

Figure 3.18 – Crack-patterns for the ET1 and ET3 specimens at failure

In the following, the distributions of strains and stresses in concrete and reinforcement along a cross-section located at the shear-span of beam ET1 (x=0.675m) are presented in Figure 3.19 for a load level near failure (240kN). The results computed by the proposed model are compared with more accurate and complex formulations – the TINSA model (Bairán 2005) and the model of Mohr (Mohr 2011) described in Sections 2.3.3.3 and 2.3.3.4, respectively. Predictions from the flexural model are also included.

The prediction of the proposed shear model for the longitudinal concrete strain distribution (Figure 3.19a) nearly matches the ones from the more complex models of Mohr and TINSA; in contrast, the flexural model predicts lower neutral axis positions and lower sectional rotations. The distributions of longitudinal stresses in concrete (Figure 3.19c) computed by the shear-sensitive models are particularly different from the flexural model predictions, especially in the area below the neutral axis. In the case of the flexural model, concrete tensile stresses due to tension stiffening appear in this zone. Instead, due to the shear-bending resistant mechanism, compressive stresses in this area, which correspond to the longitudinal component of the diagonal compressive struts, are obtained in a very similar way by the proposed shear model and by the model of Mohr and TINSA. As the equilibrium of forces and moments in the cross-section has to be fulfilled, these compressive stresses in the tensile zone of the cross-section must be balanced through an increment of tensile stresses in the longitudinal reinforcement. This is the reason for the

existence of the so-called 'tension-shift effect', noticed in Figure 3.19e, where higher stresses in the tensile reinforcement are predicted by the shear related models in comparison to the flexural model.

The distribution of vertical strains in concrete (Figure 3.19b) presents maximum values in the tensile area of the section. The proposed shear model gives a triangular shaped distribution of strains, which approximates quite well the predictions from the more complex models. Although, due to the simplified fixed concrete stress assumption taken in the shear model formulation, an overestimation of concrete strains in the bottom of the tensile area is noticed. Transversal reinforcement is yielded in this area (Figure 3.19f), where the steel stresses are similarly predicted by the three models that include shear effects. Pertaining to the vertical stresses in concrete (Figure 3.19d), the more complex shear models (model of Mohr and TINSA) provide rather discontinuous patterns; even though the proposed model fits adequately these distributions.

The constant shear stress along the cross-section assumed in the proposed shear model is represented in the Figure 3.19h. Considering the parabolic-shape distribution predicted by the more accurate model TINSA, it can be observed that such simplified assumption is very representative of the state of the section. As a consequence of that hypothesis, the shear strains (represented in Figure 3.19g) in the bottom part of the tensile zone of the section are overestimated by the proposed shear model when compared to the results from the model of Mohr and TINSA. Nevertheless, the overall shape of the shear strain distribution given by the proposed shear model is in good accordance with the more complex formulations.

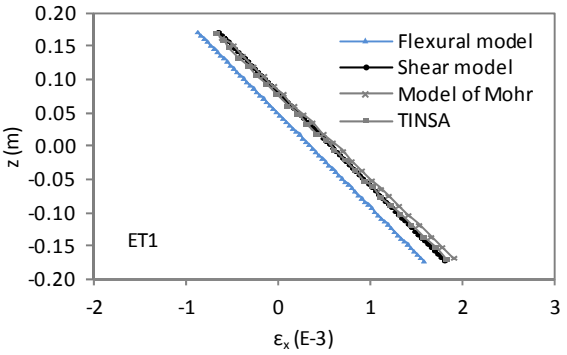

a) Longitudinal strains in concrete

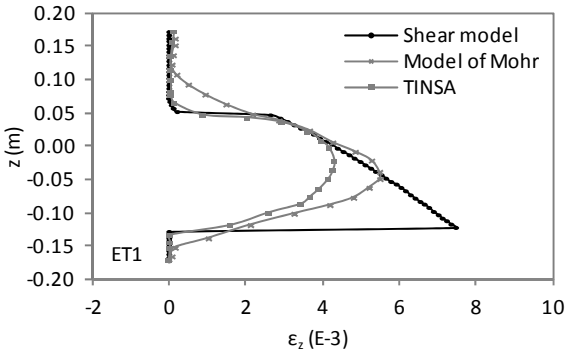

b) Vertical strains in concrete

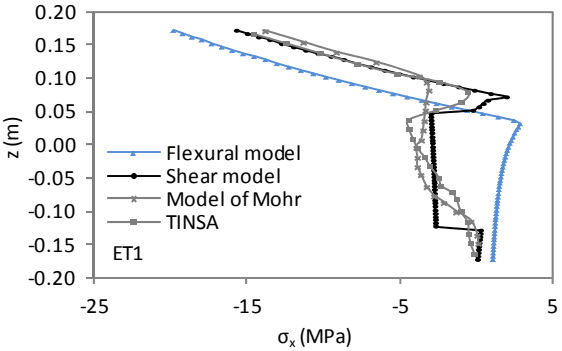

c) Longitudinal stresses in concrete

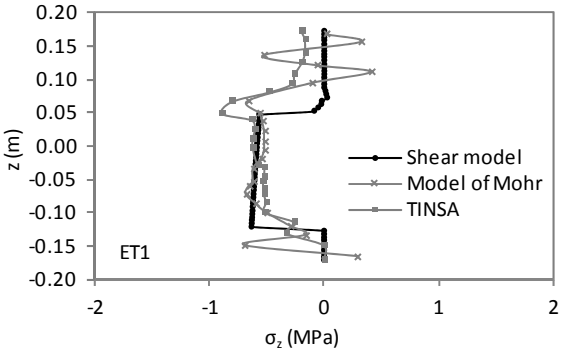

d) Vertical stresses in concrete

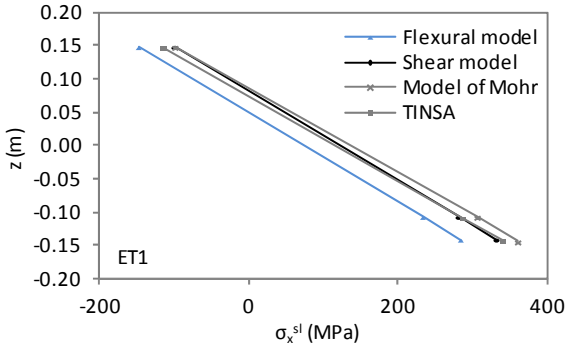

e) Stresses in longitudinal reinforcement

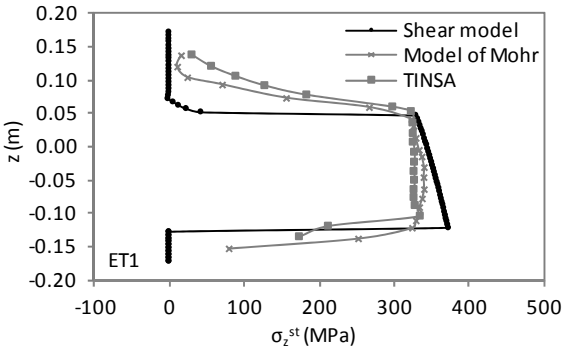

f) Stresses in transversal reinforcement

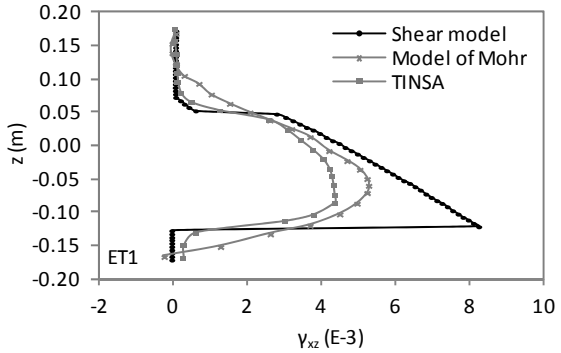

g) Shear strains in concrete

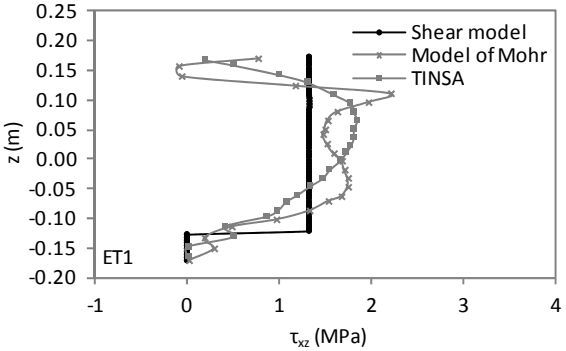

h) Shear stresses in concrete

Figure 3.19 – Strain and stress states at the section x=0.675m of ET1 beam for P=240kN

3.3.2.3. Influence of mesh refinement

A mesh sensitivity analysis was carried out in order to check the influence of the size of the FEs and fibres in the accuracy of the results. For this purpose, considering the original model of beam ET3, other simulations were carried out varying the length of the FEs (0.075m, 0.15m and 0.3m) and varying the width of the fibres (0.003m, 0.005m, 0.01m, 0.015m and 0.025m). The mid-span displacements computed by the models with different meshes are presented in Figure 3.20. The original simulation, which corresponds to FEs with 0.15m of length and fibres with 0.005m of width, and the experimental data are also included in these graphics. A small influence of both the varying length of the FEs (see Figure 3.20a) and of the fibre widths (Figure 3.20b) can be observed. In general, FE lengths of 0.1m to 0.2 m and fibre widths of 0.005m to 0.01m are found to guarantee mesh-independent results. Relatively tighter meshes gave very similar results. These key conclusions about the dimensions of the meshes will be taken into account in the following simulations with the proposed model.

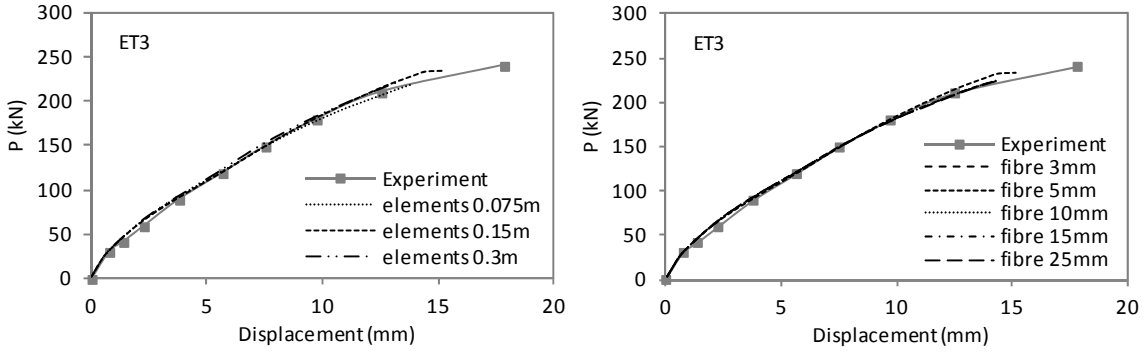

Figure 3.20 – Mesh dependency analysis: a) influence of the length of the FEs and b) influence of the width of the fibres

In order to demonstrate the importance of a correct division of the cross section into 1D (non shear resistant) and 2D (shear resistant) fibres, additional simulations of beam ET3 were carried out: (*i*) considering all fibres in a cross section as shear resistant (only 2D fibres) and (*ii*) taking only part of the flanges as shear resistant fibres (effective width determined according to the proposal of (Zararis, Karaveziroglou and Zararis 2006)). In the original simulation only the fibres that belong to the web were considered shear resistant. In these additional simulations, the original mesh was used (FEs with a length of 0.15m and fibres with a width of 0.005m). The predictions of the mid-span displacement under the applied load provided by these various simulations are depicted in Figure 3.21 along with the experimental data.

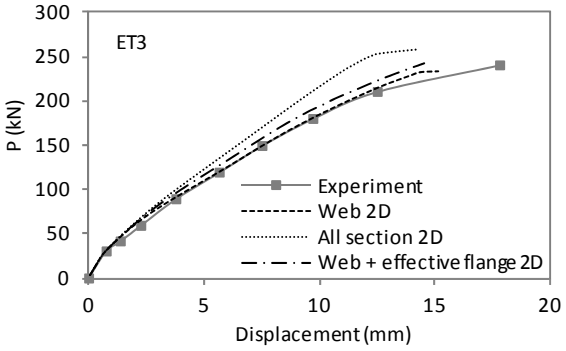

Figure 3.21 – Mesh dependency: influence of division into 1D and 2D fibres

It can be observed that the ultimate shear resistance slightly increases, and the response of the model becomes stiffer, when all the cross-section is considered shear resistant. In this case, the difference between the shear model prediction and the experimental behaviour would increase if all fibres were considered shear resistant. Similar response to the original model is obtained when the effective width of the web is considered.

3.3.3 Vecchio and Shim tests

3.3.3.1. Description

The series of beams tested by (Vecchio and Shim 2004) in Toronto were a reproduction of the experiments by (Bresler and Scordelis 1963). In total, four series of three beams with rectangular cross sections subjected to point loads were tested. They differed from each other in the amount of shear reinforcement, span length, cross-section dimensions and concrete compressive strength. The measured experimental data were the applied load and the displacement at mid-span. From this set of beams, specimens VSA1 and VSA3 were analysed in order to demonstrate the capabilities of the model to capture different failure mechanisms: shear-compression failure (VSA1) and flexure-compression failure (VSA3). The characteristics of the beams in terms of geometry, reinforcement and instrumentation are presented in Figure 3.22. The material properties of concrete, longitudinal and transversal steel are listed in Table 3.2.

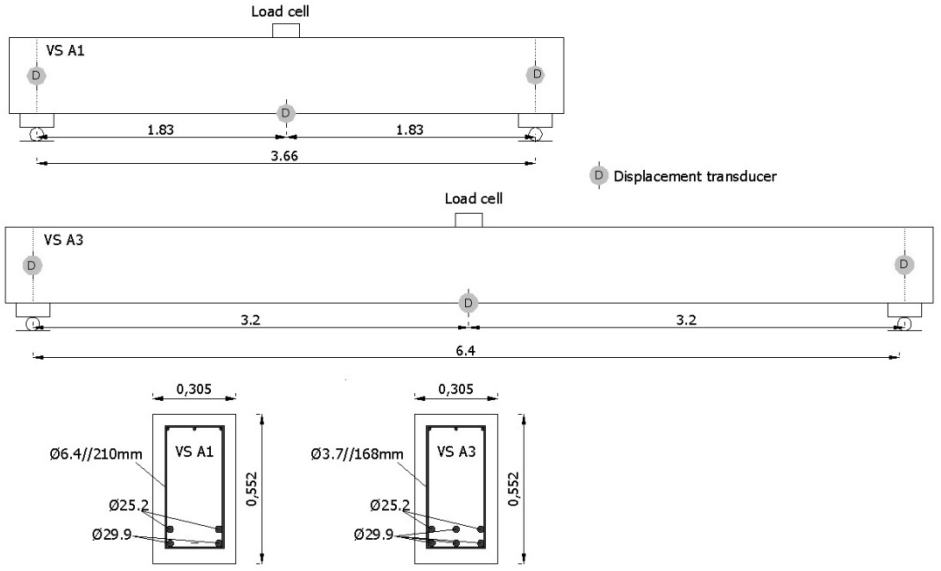

Figure 3.22 – Geometry, reinforcement and instrumentation of the Vecchio and Shim beams

Table 3.2 Material properties of the Vecchio and Shim beams

Beams	Concrete	Longitudinal steel	Transversal steel
VSA1	f_c = 22.6 MPa f_{ct} = 2.37 MPa E_c = 36.5 GPa	Ø25.2mm: f_{sy} = 440 MPa E_s = 210 GPa Ø29.9mm: f_{sy} = 436 MPa E_s = 200 GPa	f_{sy} = 600 MPa f_{su} = 649 MPa E_s = 200 GPa
VSA3	f_c = 43.5 MPa f_{ct} = 3.13 MPa E_c = 34.3 GPa		f_{sy} = 600 MPa f_{su} = 651 MPa E_s = 200 GPa

In what concerns the numerical simulation, the FE meshes of the models are represented in Figure 3.23: VSA1 was discretized into 20 FEs and VSA3 into 32 FEs; the cross section was divided into fibres with approximately 0.016m of width; steel filaments were simulated according to their positions in the beam, and shear reinforcement was considered smeared in the shear resistant fibres. Apart from the concrete cover, all the fibres were considered shear resistant. Load (P) was applied as nodal forces, in an incremental form until failure.

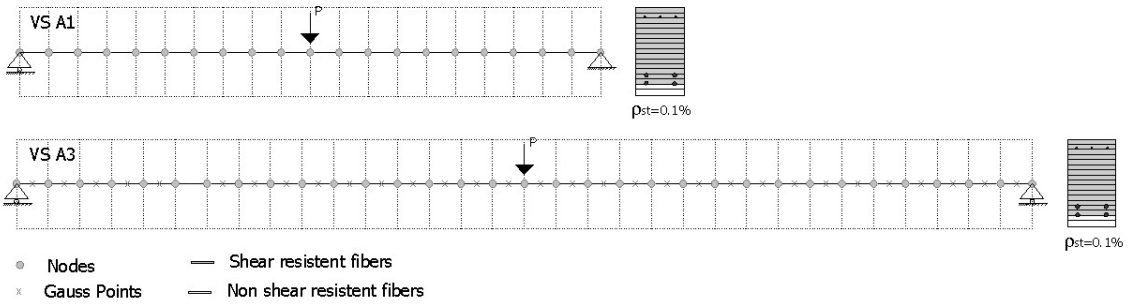

Figure 3.23 – Model of the Vecchio and Shim beams

3.3.3.2. Results and discussion

According to the experimental data (Vecchio and Shim 2004), beam VSA1 failed in shear-compression under two simultaneous effects: crushing of the concrete in compression near the point of application of the load, and crushing of the diagonal concrete struts. Severe diagonal-tension cracks were developed in the later load stages. As the shear-span ratio of this specimen is 3.75, shear effects are important. In contrast, beam VSA3 exhibited a flexure-compression failure, with crushing of concrete in the compression zone, starting from the de zone under the loading plate. Unlike the VSA1 specimen, diagonal tension cracking was minor and flexural cracks were dominant. The shear-span ratio of beam VSA3 is 6.56, so the influence of shear must be of minor importance.

As far as the ultimate loads is concerned, a summary of the experimental results and of the numerical predictions from the proposed shear model and the basic flexural model are presented in Table 3.3. In general the proposed shear model provides better estimations of the ultimate load and displacement than the basic model; however, the difference is more significant for the case of beam VSA1, where shear plays a key role in the resistant mechanism.

Table 3.3 Summary of experimental and computed results at failure

Beam	Experimental	Proposed model[1]	Basic model[2]	Exp / Num[1]	Exp / Num[2]
	Ultimate load P_u (kN)				
	$P_{u,exp}$ (kN)	$P_{u,shear}$	$P_{u,flex}$	$P_{u,exp}/P_{u,shear}$	$P_{u,exp}/P_{u,flex}$
VSA1	459	445	483	1.03	0.95
VSA3	420	431	445	0.97	0.94
	Ultimate mid span deflection δ (mm)				
	$\delta_{u,exp}$	$\delta_{u,shear}$	$\delta_{u,flex}$	$\delta_{u,exp}/\delta_{u,shear}$	$\delta_{u,exp}/\delta_{u,flex}$
VSA1	18.8	15.3	9.8	1.23	1.92
VSA3	51.0	56.7	34.4	0.90	1.48
	Failure mode				
VSA1	Shear-Compression	Shear	Bending	√	x
VSA3	Bending	Bending	Bending	√	√

The experimental deflections at mid-span are compared with the numerical results in Figure 3.24. Concerning to the shear model, a good fitting with the experimental results is achieved for the two specimens. In the case of beam VSA1, a fragile failure is predicted by the model and the more accentuated influence of shear is noticed. In fact, the results of the flexural model deviate more from the experimental data in the case of beam VSA1. For

beam VSA3 the difference between the flexural and the shear models is not as significant as in the case of the VSA1, as shear influence is small. Even though, a better fitting to the VSA3 experimental curve is achieved with the shear model.

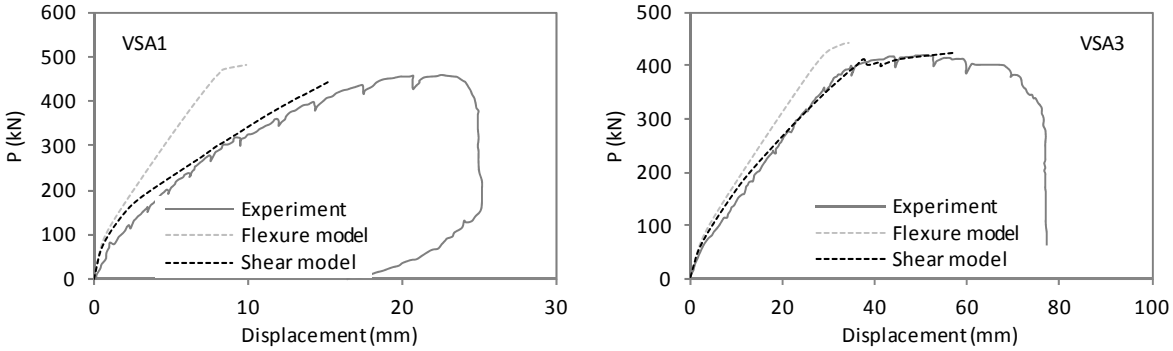

Figure 3.24 – Load-displacement curves at mid span: a) beam VSA1 and b) beam VSA3

Regarding the computed stresses in the reinforcement, in Figure 3.25 the longitudinal σ_x^{sl} and transversal σ_x^{st} stresses along the beam VSA1 are presented for different levels of the applied load (P). Concerning the longitudinal stress distribution in Figure 3.25a, a comparison between the shear and flexural models is presented: the increment of stresses due to the shear resistant mechanism is captured by the proposed model, being more accentuated for higher levels of loading. Stresses in shear reinforcement (Figure 3.25b) can only be computed by the proposed shear model, which predicted the development of yielding and the generally yielded state along the entire beam at the ultimate load.

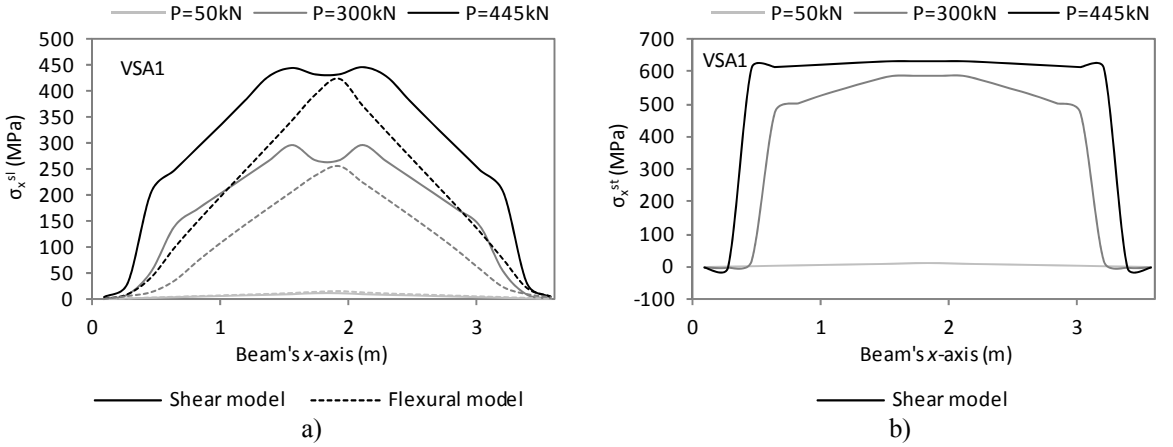

Figure 3.25 – Stresses in reinforcement along x-axis of beam VSA1: a) longitudinal and b) transversal steel

Pertaining to the section level, computed stress and strain distributions along the quarter-span section of beam VSA1 are presented in Figure 3.26 for three load levels: (*i*) P = 50kN, the limit of the linear elastic state, (*ii*) P = 300kN, the onset of the diagonal cracked state and (*iii*) P = 445kN, the failure stage. The graphics represent the typical development of the sectional response determined by the proposed shear model.

The distribution of the axial stresses σ_x in concrete is presented in Figure 3.26*a*: the linear behaviour of the first load stage changes to the nonlinear one for the latter load stages; higher compression forces appear at the top of cross section and low compression forces develop in the cracked area to equilibrate the shear related 'tension-shift effect' in the longitudinal reinforcement. At failure, the neutral axis rises and the concrete compression stresses in the top of the cross section increases.

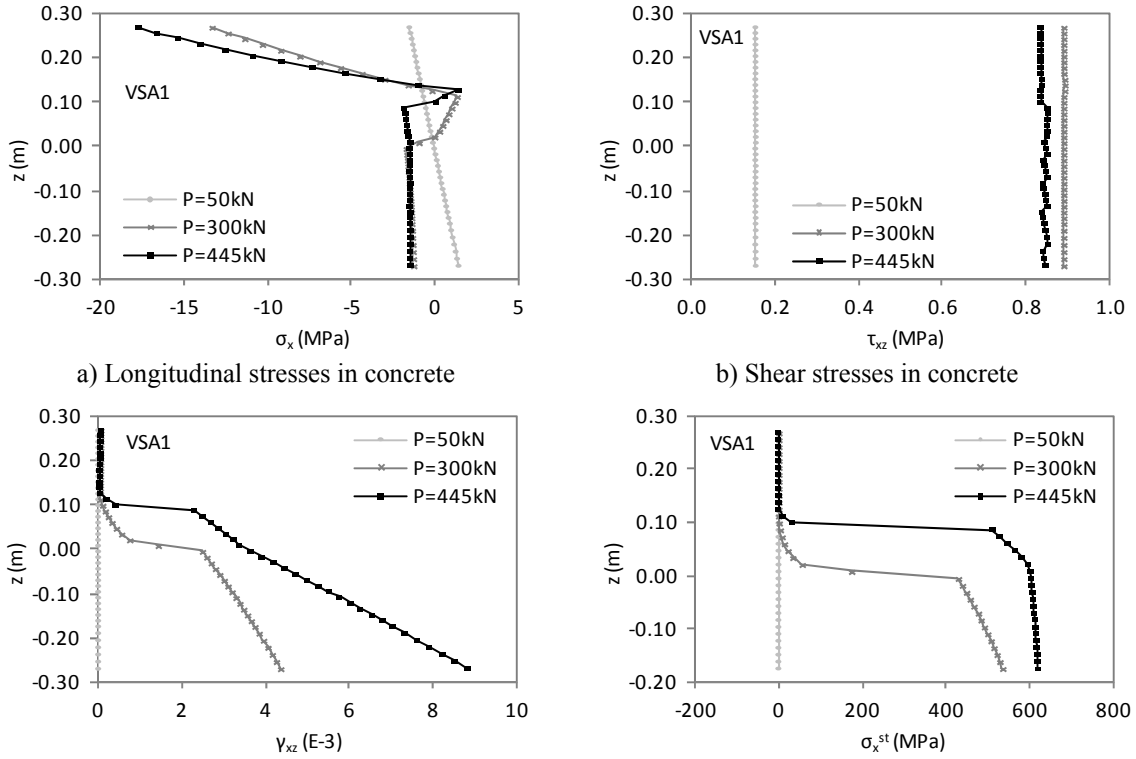

a) Longitudinal stresses in concrete

b) Shear stresses in concrete

c) Shear strains in concrete

d) Axial stresses in transversal reinforcement

Figure 3.26 – Strains and stresses computed in the quarter-span section of beam VSA1

The assumption of a constant shear stress τ_{xz} flow adopted in the sectional analysis is illustrated in Figure 3.26*b*. As a consequence of this assumption, the shear strain distribution γ_{xz} takes the shape presented in Figure 3.26*c*: nearly triangular, with approximately null values in the uncracked top area and higher values in the bottom of the cracked area of the cross section. For the linear state, transversal strains and stresses take

very small values; it is only after diagonal cracking that shear stresses and distortions rise significantly. Figure 3.26*d* presents the computed stress distribution for the transversal reinforcement σ_z^{st}, where null stresses are presented in the linear state and the development of yielding is noticed for the two higher load levels.

3.3.4 Kaufmann's beams

3.3.4.1. Description

The benchmark to be presented next belongs to the VN series of experiments carried out by Kaufmann and Marti in the 'Beam Element Tester' (BET) (Kaufmann and Marti 1996). The testing device was designed to reproduce the behaviour of typical B-regions on beam elements, and to apply sectional forces corresponding to the ultimate resistances of large-sized RC girders. The VN series is composed by identical specimens monotonically loaded in shear until failure, with a null bending moment at mid-span, as schematically represented in Figure 3.27. The analyzed specimens are the beams VN2 and VN4, whose geometry, reinforcement and material properties are presented in Figure 3.28. Beam specimen VN2 has a null axial force, whilst beam VN4 is subjected to a constant compressive axial force of 1MN. The beam specimens are 5.84m long, with an I-shaped 0.78m high cross-section. The width of the web is 0.15m, presenting an enlargement near the supports to increase the shear resistance at these locations. Shear reinforcement content is relatively low (ρ_{st}=0.335%), and the longitudinal reinforcement was designed so as to remain elastic until failure.

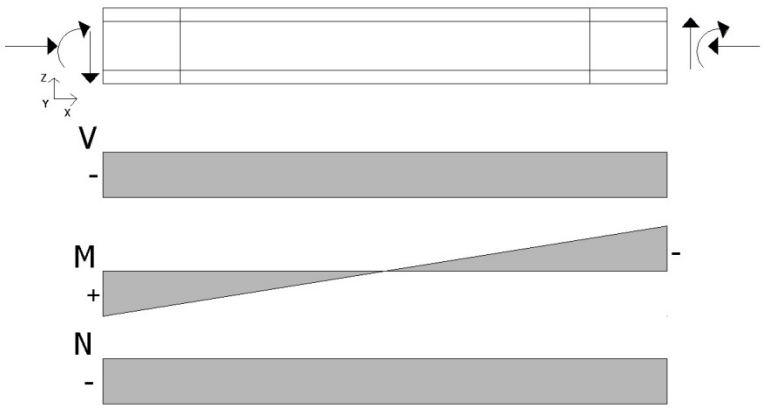

Figure 3.27 – Internal forces in the beam specimens VN2 (N=0) and VN4 (N=1MN) by Kaufmann and Marti

The experimental results to be presented, concerning to concrete strains and crack angles, correspond to average values measured in the web in a segment 1.60m long at the centre of the beam, and using a 0.40m grid of strain sensors placed as a rosette (see Figure 3.28). Both beams VN2 and VN4 were simulated via the proposed shear model, with 38 FEs with the same length and discretizing the cross-section into 59 fibres, as shown in Figure 3.29. Longitudinal rebars were modelled in their positions in the cross section. Concerning to the load application, in the case of VN4 the axial force was applied in the first loading step. Shear force was imposed, for both beams, in an incremental form until failure.

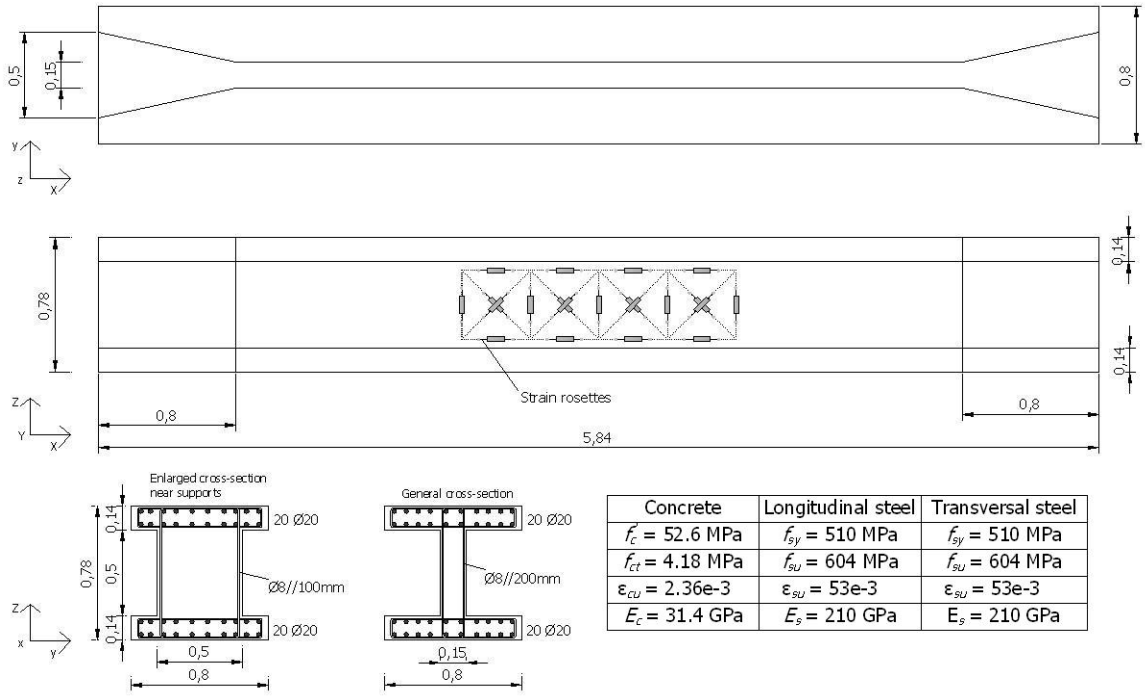

Concrete	Longitudinal steel	Transversal steel
f_c = 52.6 MPa	f_{sy} = 510 MPa	f_{sy} = 510 MPa
f_{ct} = 4.18 MPa	f_{su} = 604 MPa	f_{su} = 604 MPa
ε_{cu} = 2.36e-3	ε_{su} = 53e-3	ε_{su} = 53e-3
E_c = 31.4 GPa	E_s = 210 GPa	E_s = 210 GPa

Figure 3.28 – Geometry, reinforcement and material properties of beams VN2 and VN4

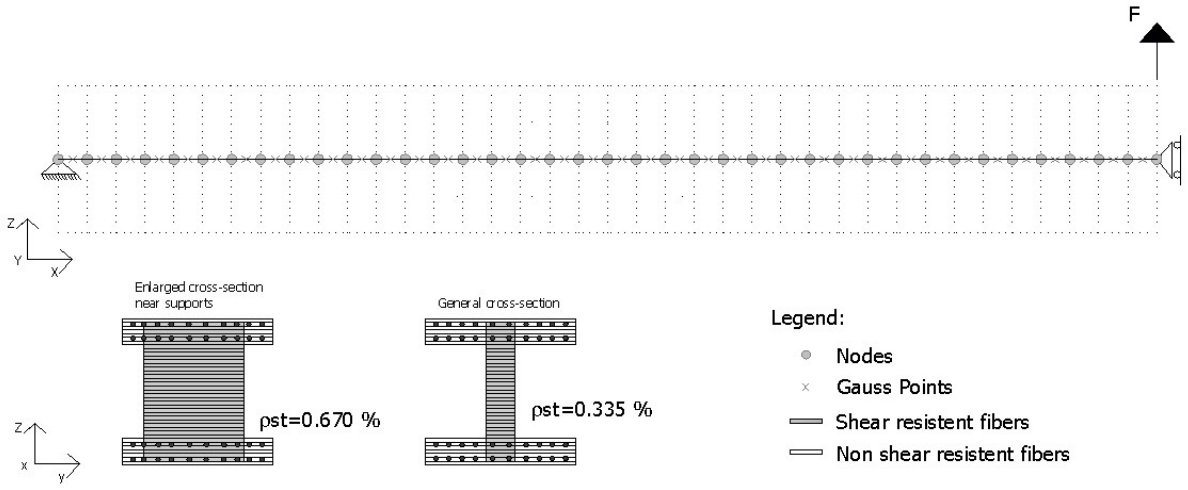

Figure 3.29 – Longitudinal and transversal mesh of the numerical model

3.3.4.2. Results and discussion

In accordance with the reported observations (Kaufmann and Marti 1996), collapse was due to failure of the web in the central part of the specimens for all the tests. In specimen VN2 (results in Table 3.4) collapse was governed by stirrup failure, after some minor spalling of the web concrete cover. Specimen VN4 (results in Table 3.5) failed due to concrete crushing in the web.

Table 3.4 Summary of experimental/calculated and computed results of VN2 specimen in failure

VN2	Experimental / determined*	Shear model	Flexural model
Vu (kN)	548	545	1400
Failure mode	Shear failure: stirrup failure	Shear failure: crushing of concrete after extensive yielding of stirrups	Bending failure: failure of longitudinal reinforcement
$\sigma_{u,z}^{st}$ (MPa)	565*	538	-

* Determined according to (Kaufmann 1998)

Table 3.5 Summary of experimental/calculated and computed results of VN4 specimen in failure

VN4	Experimental / determined*	Shear model	Flexural model
Vu (kN)	564	545	1400
Failure mode	Shear failure: web crushing	Shear failure: crushing of concrete after extensive yielding of stirrups	Bending failure: failure of longitudinal reinforcement
$\sigma_{u,z}^{st}$ (MPa)	568*	539	-

* Determined according to (Kaufmann 1998)

According to the numerical simulations, both tests failed by crushing of concrete in the web after extensive yielding of stirrups. In the case of VN2 failure mode, it seems that a less pronounced effect of the compression softening (due to confinement of the compressive chords) would bring slightly higher values of the compressive strength, and stirrup rupture could be predicted. Besides this, the load capacities of the girders were satisfactorily predicted, as well as the fragile shear failure modes, as summarized in Table 3.4 for VN2 and in Table 3.5 for VN4. Also in these tables, the ultimate values for the stresses in the stirrups ($\sigma_{u,z}^{st}$) determined in the test (Kaufmann 1998) are compared with the predictions from the proposed shear model: a general good accordance between the two is perceived. In addition, results from the pure flexural fibre beam model CONS (Marí 2000) are included in these tables, showing that this approach is not suitable to analyze this type of structural problem.

The confinement effect of the compression force applied to the VN4 specimen was not perceived in the ultimate resistance of the shear model, as the same failure load was predicted for the two beams. However, this effect was noticed in the later development of cracks in beam VN4, when compared with VN2, as to be showed afterwards.

Contour levels of the tensile stresses in the stirrups and of the compressive stresses in the concrete along the beam's length are depicted in Figure 3.30 for the last converged load step. By analyzing both colour maps, it is noticed an extensive yielding of the stirrups, and high compressive stresses in the web, reaching values very close to the concrete strength (including compression softening effects), meaning that the girder is near collapse. Thus, the non-convergence of the next load increment is caused by the vast materials' damages, and not by other sorts of numerical instabilities.

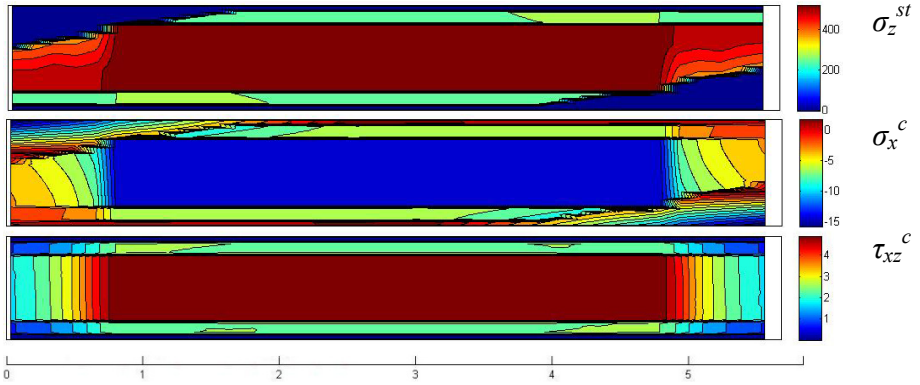

Figure 3.30 – Results at the last converged load step for the VN2 specimen: stresses in shear reinforcement σ_z^{st}, axial stresses in concrete σ_x^c and shear stresses τ_{xz}^c in concrete (MPa)

The measured and numerically computed average concrete strains in the beam segments 1.60m long, at the location of the rosettes of sensors, are compared as well for specimens VN2 and VN4. The average principal tensile and compressive strains are depicted in Figure 3.31 and Figure 3.32, respectively, and the angle θ of the average principal compressive strain with the longitudinal axis of the beam is presented in Figure 3.33. In general, an acceptable concordance between numerical and experimental results is observed. Cracking takes place earlier in the experiments than in the numerical model, as large increments of ε_1 are observed in a gradual manner. For this reason, overall stiffness is slightly overestimated by the numerical model before the yielding of the stirrups. For higher load stages, after yielding of stirrups, principal compressive strains in the experiments are lesser than the ones predicted numerically, inducing to a less pronounced effect of compression softening in concrete. Again, confinement brought by the stirrups must have had greater effect than the one taken into account in the numerical model. In

what concerns to the principal directions, the numerically predicted angles present evolutions similar to the experimentally measured ones. However, for VN2 specimen the compressive struts presented a delayed rotation, motivated by the higher cracking load. At failure, the angle of approximately 15º for both specimens is well predicted by the numerical model. This flat inclination of the compressive struts at failure is due to the low shear reinforcement ratio in these beams.

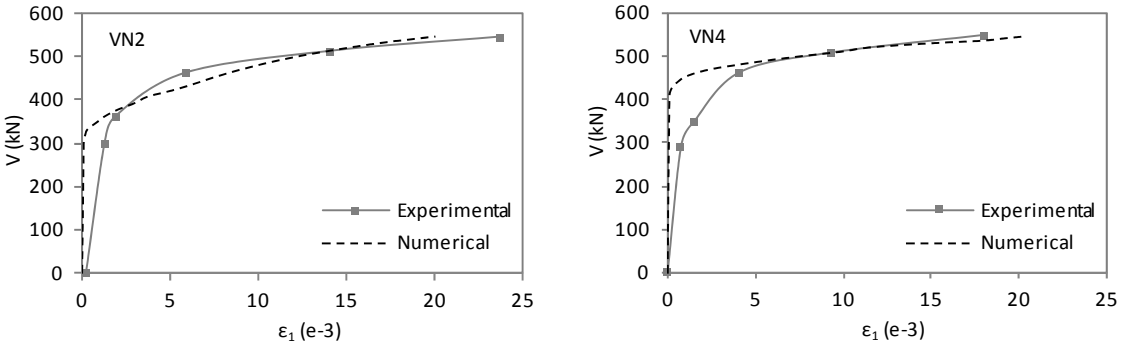

Figure 3.31 – Average principal concrete tensile strain ε_1

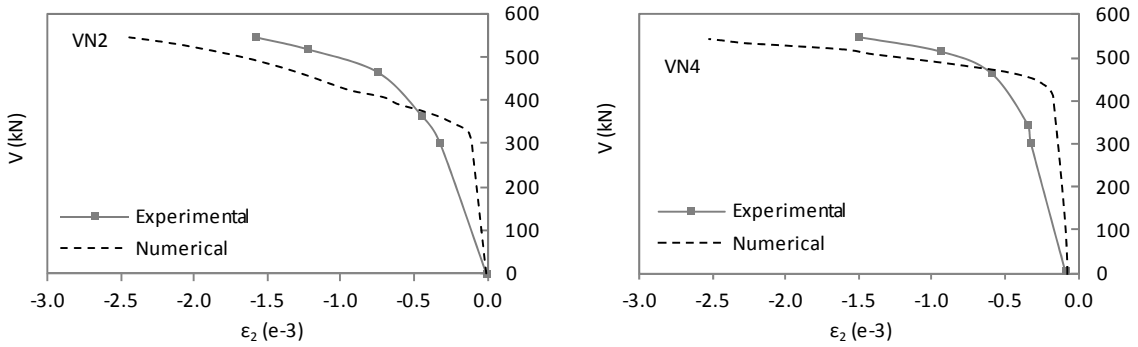

Figure 3.32 – Average principal concrete compressive strain ε_2

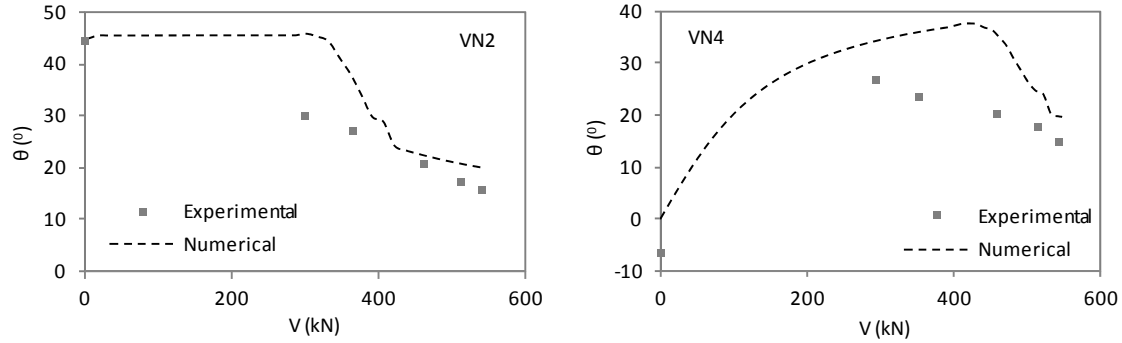

Figure 3.33 – Average principal angle θ

Test and numerically computed average vertical strains ε_z in concrete in the measuring area are compared in Figure 3.34 for both specimens, with good agreements being found. Also, the computed average stresses in the shear reinforcement are presented in Figure 3.35. The sudden increase in the stress evolutions happens when crack of concrete occurs, and the stirrups start to work to equilibrate the forces released by the concrete. According to these graphics, estimation values for the so-called concrete contribution to shear resistance V_c can be made (approximately 360kN for VN2 and 410kN for VN4). Also, in the former figure the ultimate stress state of the stirrups determined by the model proposed by (Kaufmann 1998) showed good conformity with the numerical predictions.

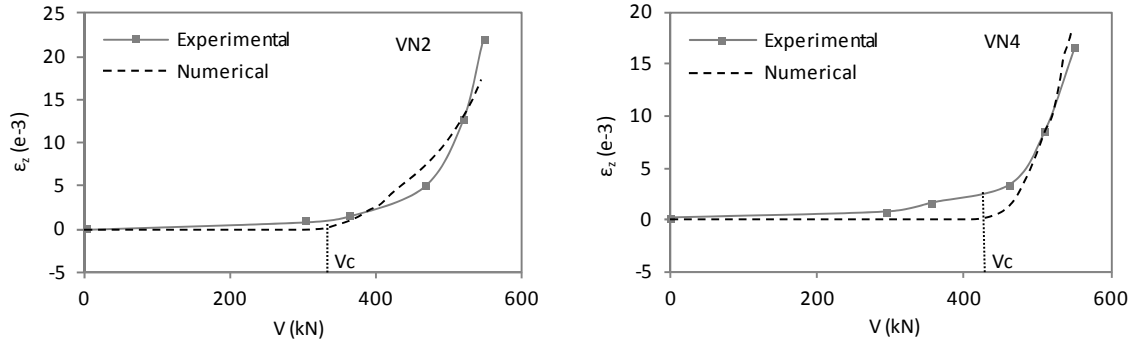

Figure 3.34 – Average vertical concrete strains ε_z

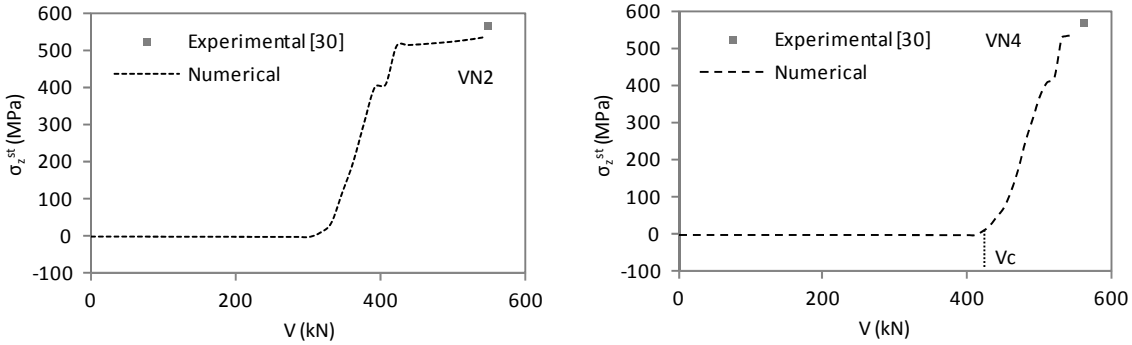

Figure 3.35 – Average stresses σ_z^{st} in the stirrups

Finally, crack development on the two beams was numerically predicted by the use of the discrete representation algorithm. Figure 3.36 and Figure 3.37 allow comparing the experimental (Kaufmann and Marti 1996) and the computed crack patterns for three load levels for beams VN2 and VN4, respectively.

Numerical predictions of the crack propagation and of the variation of the crack inclination show a fairly good agreement with the experimental evidence. The effect of confinement in

beam VN4 (brought by the applied compression force) is perceived in the later development of the experimental observed cracks in contrast to the VN2 specimen (without compression force). This difference is well captured by the numerical model, as can be observed by comparing the predicted cracking patterns previous to failure of Figure 3.36 and Figure 3.37.

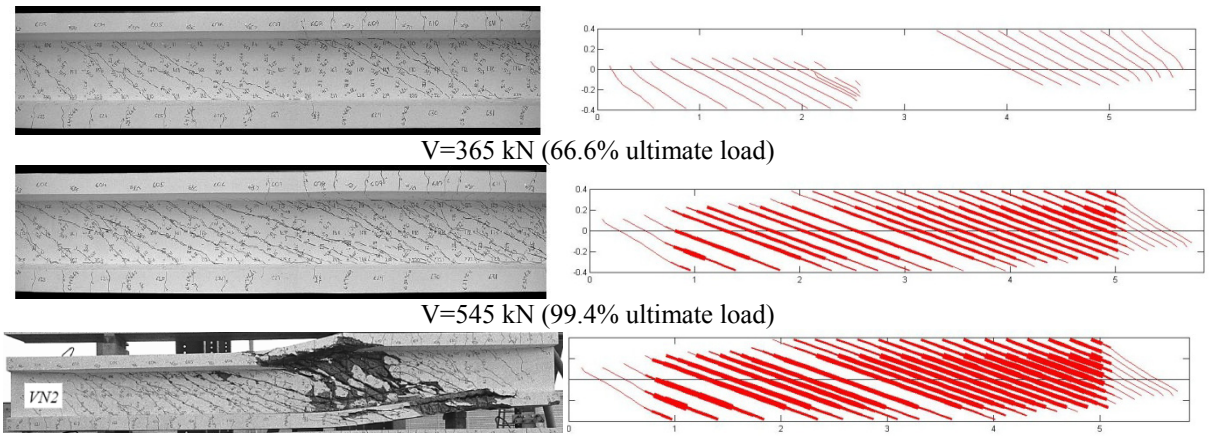

Figure 3.36 – Cracking patterns at different load levels for beam VN2

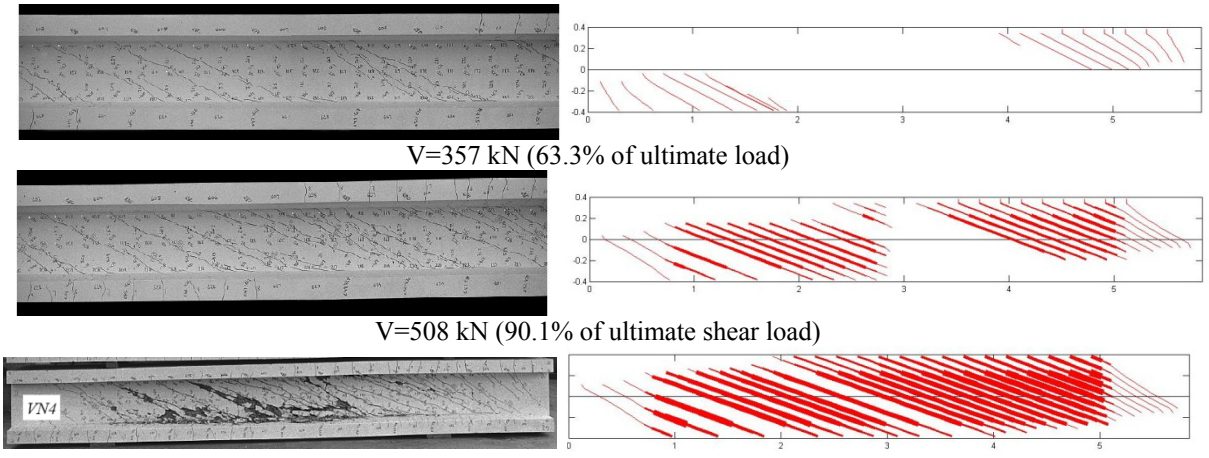

Figure 3.37 – Cracking patterns at different load levels for beam VN4

3.3.5 Experimental tests at UPC

3.3.5.1. Description

The experimental set-up built in the Laboratory of Structural Technology of the Technical University of Catalonia (UPC) is represented in Figure 3.38. The experimental campaign

consisted of 4 beams: 2 made with conventional concrete and other 2 made with concrete with high quantity of fine aggregates. Only the two beams made with conventional concrete are considered, one with and the other without transversal reinforcement in the shear span. Each side of the beams presented different quantities of longitudinal reinforcement. From these two beams two experimental tests were performed in each side, resulting into a total of four experimental tests (CSM, CSM, CTM and CTA). The geometry, reinforcement and material properties of the beams are represented in Figure 3.39 and the main characteristics of the experimental tests are resumed in Table 3.6.

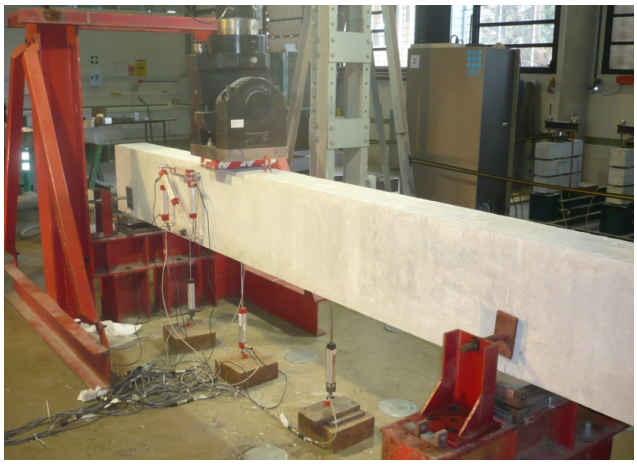

Figure 3.38 – Experimental set-up

The first two tests were performed with the supports LS1 and RS1, with a 3.0m span between them, and a cantilever of 2.25m from the support RS1 and the load applied at 1.2m from support LS1. Afterwards, the beam was turned around and the two subsequent tests were carried out with the supports RS2 and LS2, with the same span and cantilever dimensions, and the load applied at 1.2m from support RS2.

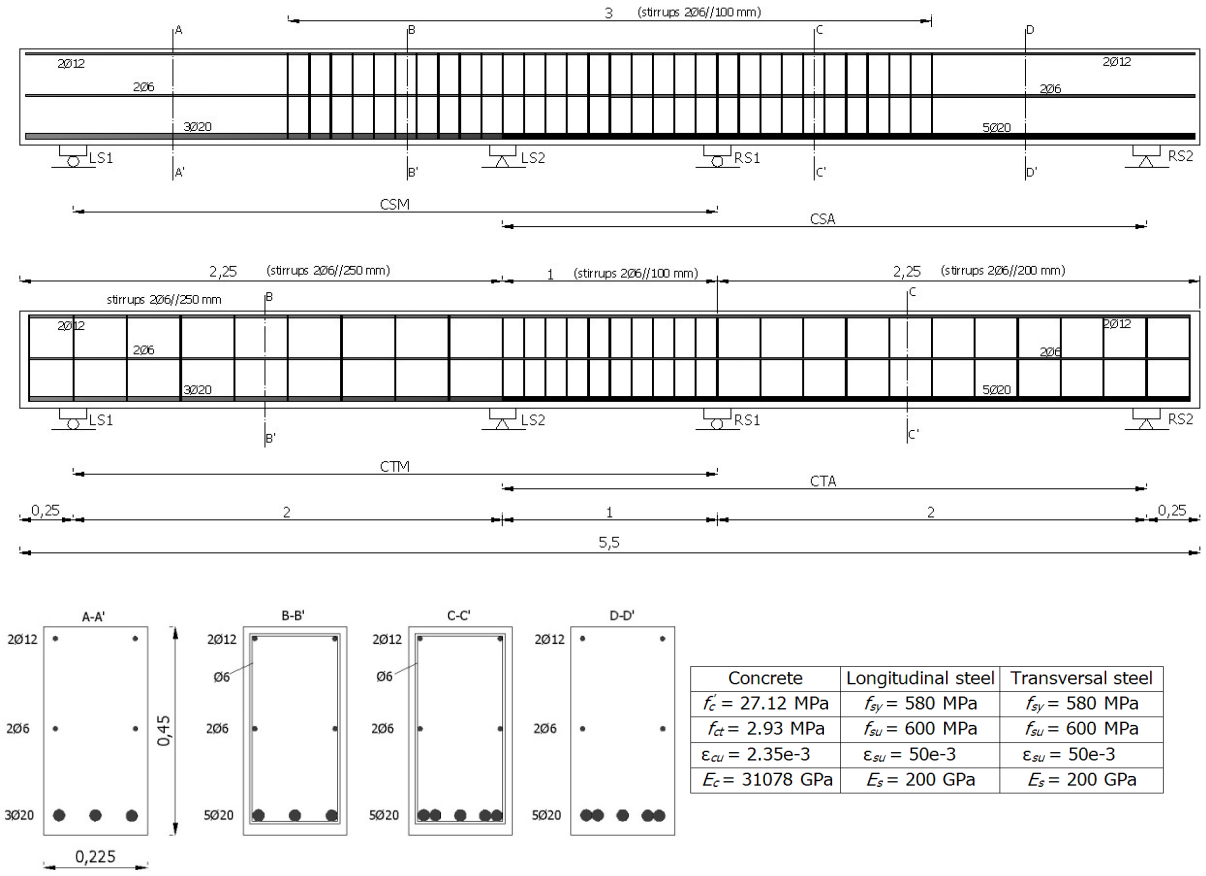

Concrete	Longitudinal steel	Transversal steel
f_c' = 27.12 MPa	f_{sy} = 580 MPa	f_{sy} = 580 MPa
f_{ct} = 2.93 MPa	f_{su} = 600 MPa	f_{su} = 600 MPa
ε_{cu} = 2.35e-3	ε_{su} = 50e-3	ε_{su} = 50e-3
E_c = 31078 GPa	E_s = 200 GPa	E_s = 200 GPa

Figure 3.39 – Geometry, reinforcement and material properties of the beams tested at UPC

Table 3.6 Summary of the characteristics of the shear tests

Beam	Test	Supports	Load distance (to support, m)	h(m)	b(m)	d(m)	Tensile longitudinal reinforcement		Transversal reinforcement	
							Bars	A_{sl}(mm^2)	Bars	ρ_{st} (%)
I	CSM	LS1 / RS1	1.20 (LS1)	0.45	0.225	0.40	3Ø20	942	-	-
	CSA	LS2 / RS2	1.20 (RS2)	0.45	0.225	0.40	5Ø20	1571	-	-
II	CTM	LS1 / RS1	1.20 (LS1)	0.45	0.225	0.40	3Ø20	942	Ø6//0.25	0.13
	CTA	LS2 / RS2	1.20 (RS2)	0.45	0.225	0.40	5Ø20	1571	Ø6//0.20	0.10

The beams where loaded until failure under displacement controlled conditions. The response of the beams was monitored as schematically represented in Figure 3.40: deflection displacements were taken at three points, 0.6m, 1.2m and 2.1m from the left support; a rosette was placed in the concrete face at 0.6m from the left support, and it was composed by two longitudinal, two vertical and one diagonal strain gauges. From the strain rosette, besides measuring the longitudinal and vertical strains in concrete, it was possible to determine the average concrete distortion and the compressive principal angle.

Regarding the numerical simulation, the FE mesh is presented in Figure 3.41. Load was incrementally applied in the model until failure.

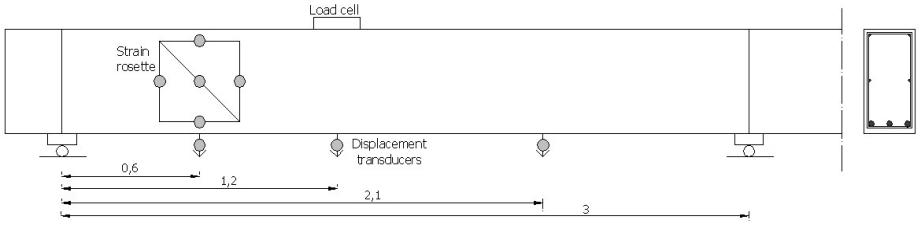

Figure 3.40 – Scheme of the experimental setup

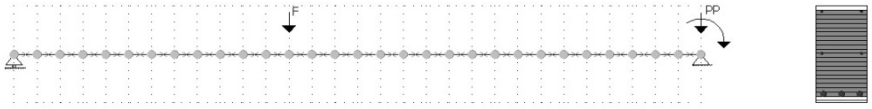

Figure 3.41 – Model of beam tests

3.3.5.2. Results and discussion

Shear failure was observed in the four experimental tests. For the beams without stirrups (CSM and CSA) a fragile shear mode occurred through the sudden opening of the main shear crack, combined with the loss of anchorage of the longitudinal reinforcement. The beams with transversal reinforcement presented less brittle failures, with higher anchorage lengths of the longitudinal reinforcement and overall yielding of the stirrups.

The experimental and computed values of failure loads are presented in Table 3.7. Shear reinforcement increased significantly the shear resistance of the beams: 75kN for the case of the beams with low longitudinal reinforcement (CSM and CTM) and 186kN for the beams with larger longitudinal reinforcement (CSA and CTA). The increment of longitudinal reinforcement had a considerable influence only on the tests with stirrups, as shear resistance of beam CTA was significantly higher than that of beam CTM (approximately 147kN). In the case of the beams without transversal reinforcement, shear resistance is less influenced by the amount of longitudinal steel (the difference between CSA and CSM was around 36kN), as the concrete strength is the mainly variable that rules the resistance mechanism.

Good predictions of failure loads and mechanisms were obtained by the proposed shear model for all the tests. Also, the role of the two types of reinforcement in the shear resistance of the beams was well captured. As expected, the purely flexural-based model

gave unrealistic predictions of failure, with very high ultimate loads for bending failure modes.

Table 3.7 Summary of the experimental and computed results of the beams tested in UPC

Shear test	Experimental		Proposed model		Flexural model	
	P_u (kN)	Failure mode	P_u (kN)	Failure mode	P_u (kN)	Failure mode
CSM	145.4	Shear	138.1	Shear	308.3	Bending
CSA	181.1	Shear	165.7	Shear	448.3	Bending
CTM	220.1	Shear	224.3	Shear	308.3	Bending
CTA	367.3	Shear	336.31	Shear	448.3	Bending

The load-displacement curves of the 4 tested beams are presented in Figure 3.42, along with the computed results. An initial stiffness discrepancy is observed in both the basic flexural and the shear models, which can be attributed to uncertainties in the support displacements and existence of pre-cracking. The proposed shear model presents and acceptable fitting with the experimental results, whereas inadequacy of the purely flexural model to simulate these tests is evident.

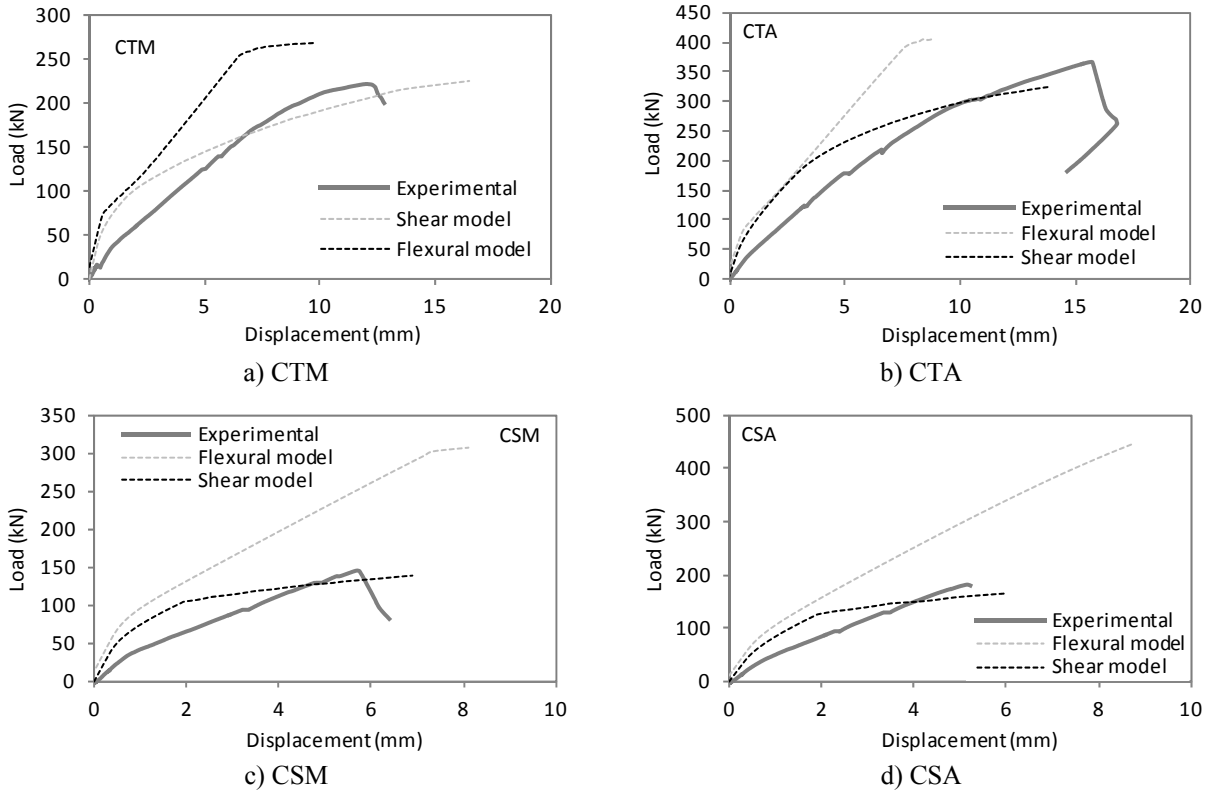

Figure 3.42 – Load-displacement curves

The horizontal strains at the top and bottom of the rosette (see positions of the sensors in Figure 3.40) are compared in Figure 3.43 with the numerical results computed by the proposed shear model. In general, a relatively accurate prediction is accomplished by the model. However, the model is stiffer than the experimental test, especially in the case of the tensile fibres (bottom). In the compression zone (top) a better fitting is achieved with the experimental strain curve.

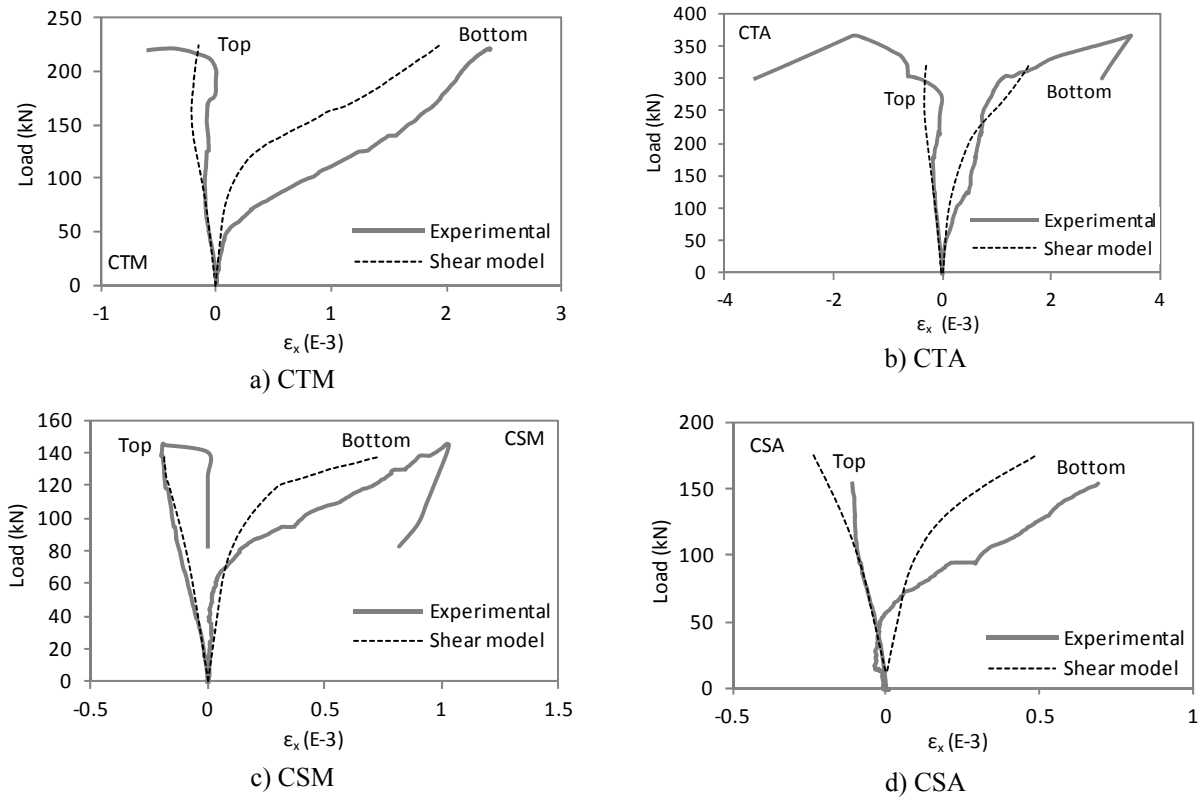

Figure 3.43 – Longitudinal concrete strains in the shear span

The average concrete strains measured in the vertical direction are depicted in Figure 3.44 along with the numerical predictions. For the case of the beam with stirrups (CTA and CTM tests represented in Figure 3.44a and Figure 3.44b, respectively) the agreement between the experimental observations and the numerical predictions is good. In fact, the load level for which the stirrups start to work, as well as the ultimate strain, are well reproduced by the numerical model. As this experimental data is very dependent on the positions of the cracks, the fitting can be considered satisfactory. For the cases of no shear reinforcement (CSA and CSM tests represented in Figure 3.44c and Figure 3.44d, respectively) the developed strains are very low, because of the very brittle failure that happens for the first opened crack. Even though, the shear model is able to capture the end

of the concrete shear contribution that corresponds to the sudden increase of strains. When this stage is reached, as there is no shear reinforcement to absorb the vertical stresses, the beam collapses suddenly. Regarding the specimens with shear reinforcement, the proposed model predicts the yielding of the stirrups in the entire shear span at failure (observed in the contour colour map of Figure 3.45 for test CTA), which is in accordance with the experimental evidence.

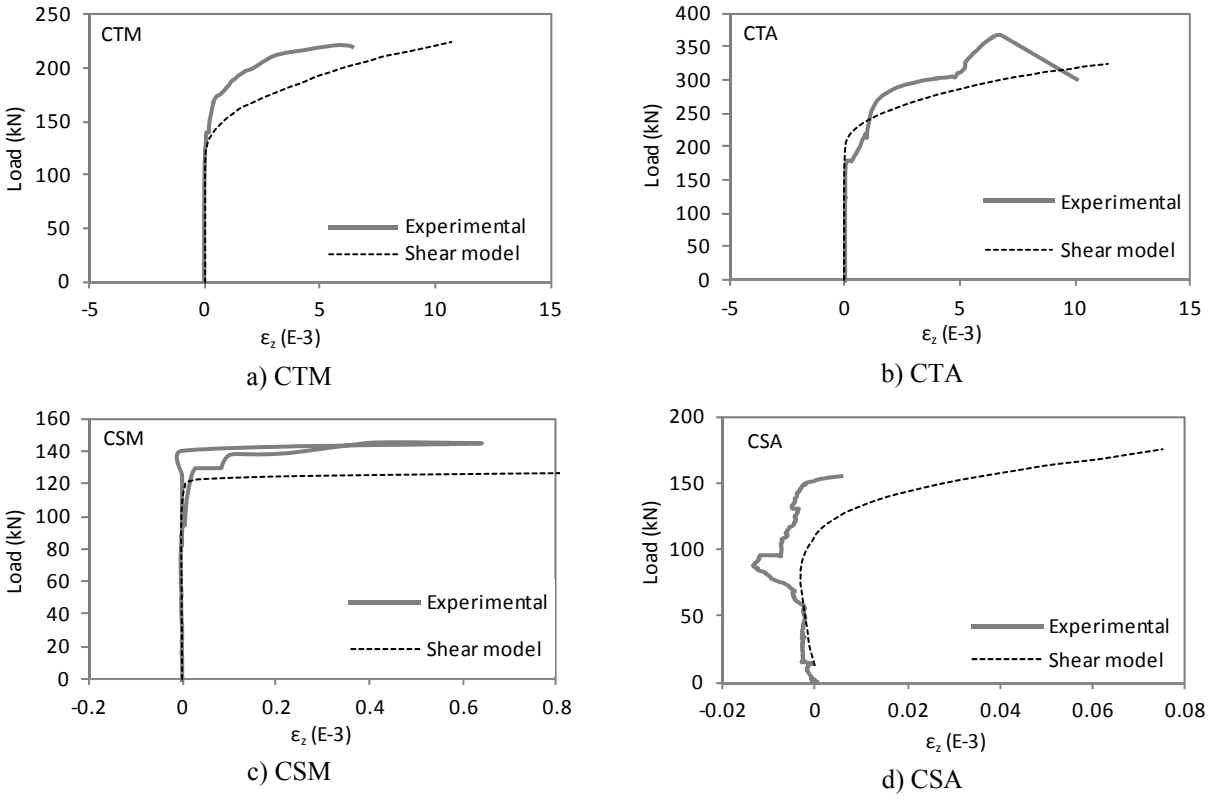

Figure 3.44 – Vertical concrete strains in the shear span

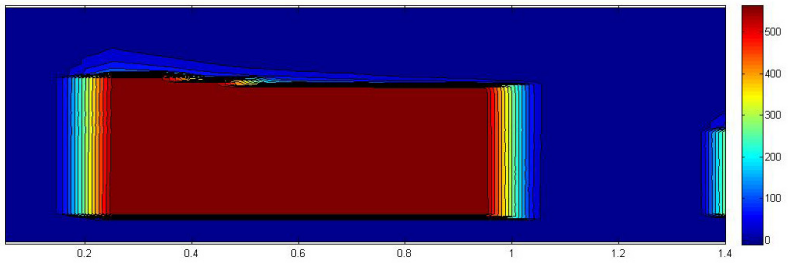

Figure 3.45 – Stirrup stresses σ_z^{st} at failure in the shear span of beam test CTA, x=[0-1.4m] (MPa)

Average distortions in concrete determined with the data provided by the strain rosette are compared with the numerical predictions in Figure 3.46, where a reasonable fitting is observed. The start of diagonal cracking correspondents to a sudden increase of distortions

in the presented curves: the beams with stirrups still developed larger distortions and carried extra load (Figure 3.46a and Figure 3.46b), whilst the beams without stirrups reached failure right after this stage (Figure 3.46c and Figure 3.46d), presenting very low values of distortion.

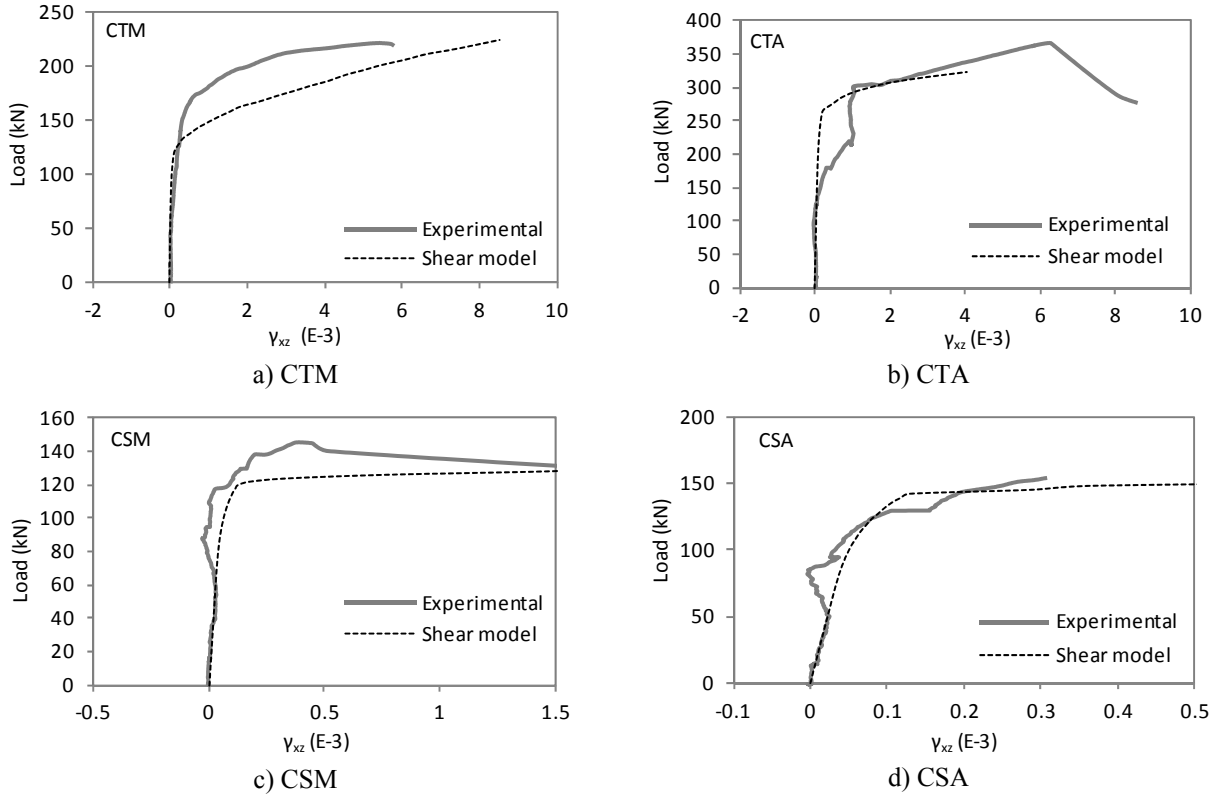

Figure 3.46 – Concrete distortions in the shear span

Also, the average principal compressive angles are compared in Figure 3.47 with the predictions of the proposed model for the 4 beam tests (the average inclinations of the cracks observed in the experiments are included in the graphics as dots). The noise observed in the experimental data is due to the high sensitiveness of the measurements to the presence of the cracks. Regarding the principal strain angles, it can be observed that the computed results captured satisfactorily the experimental tendencies.

Distortions and principal compressive angles represented in Figure 3.46 and Figure 3.47 are determined by means of the average values correspondent to the fibres located in the strain rosette.

According to the observation of the experimental tests, cracking starts vertically due to bending, and then shear cracks appear with an inclination angle of approximately 45º.

Then, with the increment of shear loading these cracks rotate, being influenced by the amount of transversal and longitudinal reinforcement. For the beams without shear reinforcement (CSM and CSA tests) there are less formation of cracks and failure happens due to the opening of a main diagonal crack. In turn, the existence of shear reinforcement (CTM and CTA tests) allows the propagation of more cracks that rotate with the increment of load, reaching inclinations greater than 45º.

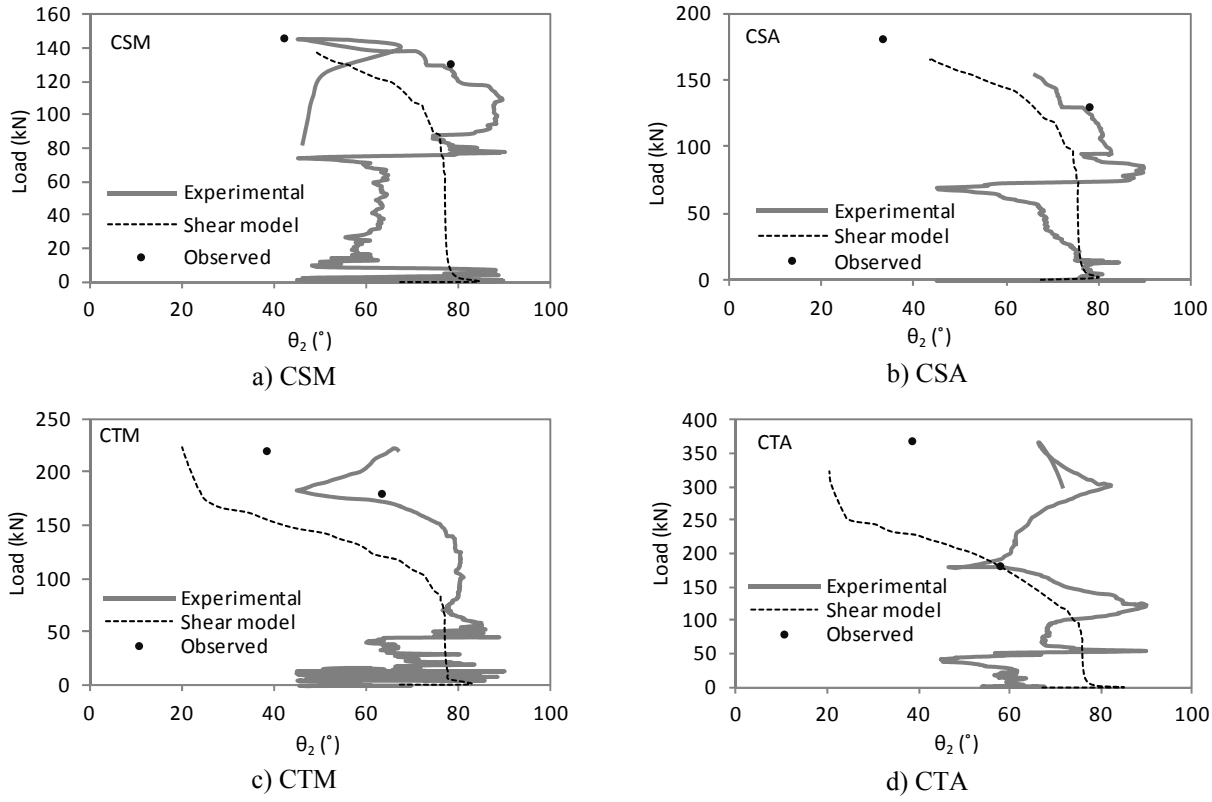

Figure 3.47 – Principal angle in concrete in the shear span

The experimental cracking patterns at failure are presented in Figure 3.48 and Figure 3.49. In this figures, comparisons between the effects of the types of reinforcement on the cracking patterns are presented: (*i*) in Figure 3.48 the beams with stirrups are compared with the beams without stirrups, for the same longitudinal reinforcement ratios (CSM versus CTM and CSA versus CTA); (*ii*) in Figure 3.49 the beams with low and high longitudinal reinforcement ratios are compared for the cases of non-existence and existence of stirrups (CSA versus CSM and CTA versus CTM). According to Figure 3.48 the existence of shear reinforcement increases the number of cracks and higher angles between the cracks and the beam axis are achieved. Conversely, according to Figure 3.49 there is no relevant influence of the quantity of longitudinal reinforcement on the ultimate

crack patterns of the tests, as both the quantity and inclination of the cracks are very similar.

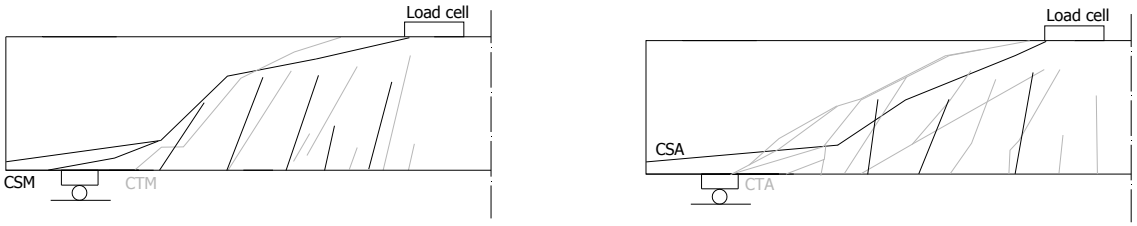

a) b)

Figure 3.48 – Influence of stirrups on the cracking patterns at failure: a) tests with low quantity of longitudinal reinforcement and b) tests with high quantity of longitudinal reinforcement

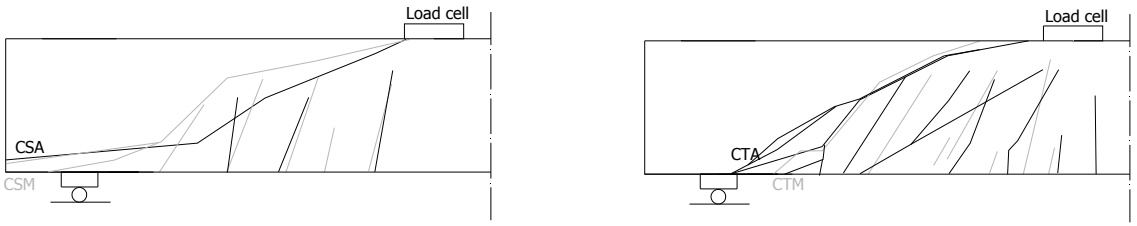

a) b)

Figure 3.49 – Influence of the quantity of longitudinal steel on the cracking patterns at failure: a) tests without stirrups and b) tests with stirrups

Observed and computed cracking patterns at failure are represented in Figure 3.50. For the case of the beams without stirrups (CSM and CSA) the numerical model is not able to predict the main diagonal crack at failure; only the secondary cracks are relatively well reproduced. On the other hand, for beams with stirrups (CTM and CTA) the computed cracking patterns are representative of the observed ones, as there is a good correspondence of the crack propagation and inclinations.

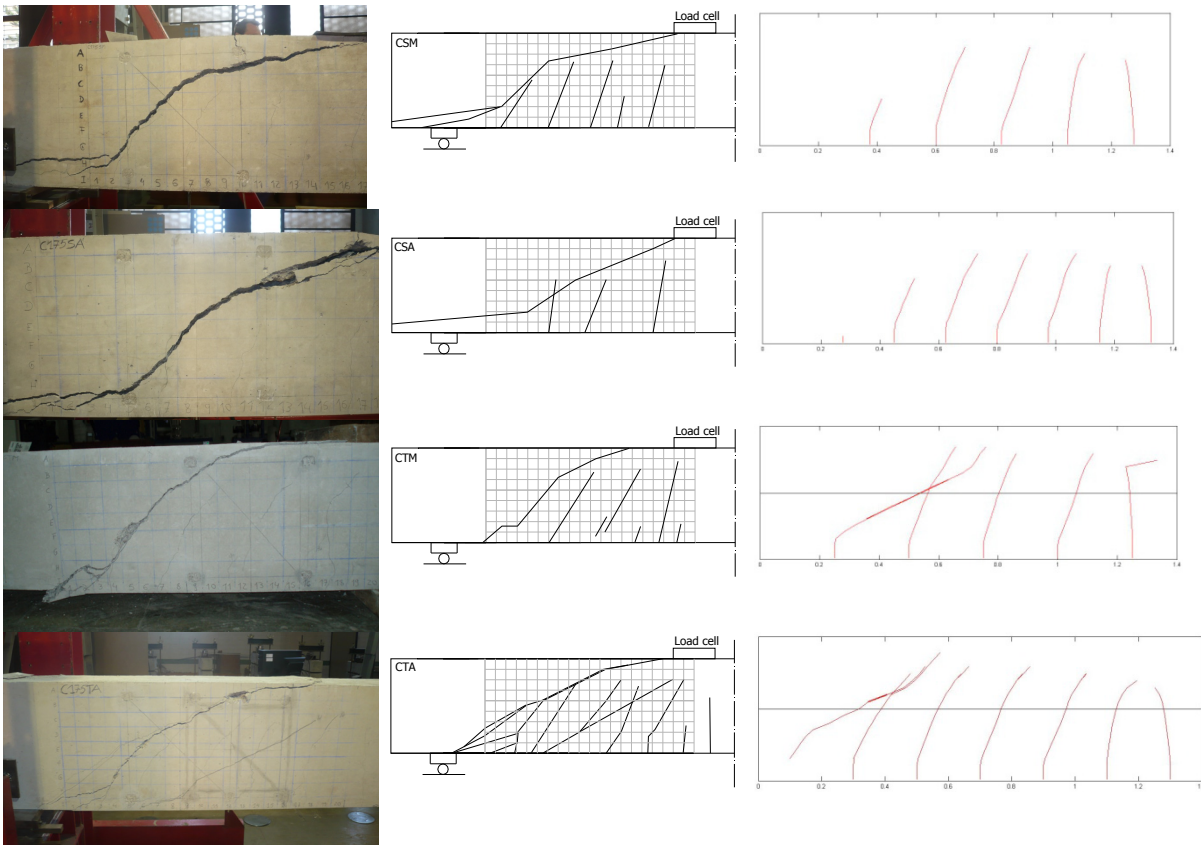

a) b)

Figure 3.50 – Cracking patterns at failure: a) experimental observation (photograph and graphic scheme) and b) computed results

3.4 Conclusions

A fibre FE beam model for the study of RC frame elements subjected to shear, bending and axial forces was presented in this chapter. At the element level, the Timoshenko beam's theory is used to take into account the shear deformation. A hybrid kinematic/force-based formulation is used at the section level, comprising the plane section theory with a fixed shear stress constraint. The non-orthogonal and full-rotating smeared crack concept is adopted for concrete at the constitutive level, to account for shear-bending-axial interaction effects. Biaxial constitutive laws are used to simulate the RC behaviour. For the steel reinforcement, a uniaxial bilinear stress-strain curve is assumed. Longitudinal reinforcement is simulated by the use of filaments, and transversal reinforcement is considered smeared in the concrete fibres. Discrete crack representation is performed by means of an external algorithm that prints the development of the crack

patterns in the elements. Pertaining to numerical efficiency, the model is robust enough to treat problems with vast cracking patterns and fragile failures, such as the typical shear critical cases.

With the objective of validating the proposed numerical model three benchmarks available in the literature were analysed, aiming to embrace different aspects of the shear-related response of beams:

(*i*) The Stuttgart shear tests consisting into T-shaped beams failing in shear demonstrated that the model is able to reproduce the failure load and mechanism of shear critical beams. Longitudinal stresses in stirrups, diagonal concrete stresses and the concrete contribution for shear resistance were well determined by the proposed model.

(*ii*) From the classical experimental campaign of Bresler and Scordelis, recreated by Vecchio and Shim, two beams were analysed: one with a shear critical failure and the other with a ductile flexural failure mechanism. The model load-displacement curves showed a good accordance with the experimental results. The capacity of the model to capture the increment of stresses in the longitudinal reinforcement due to the shear resistant mechanism was demonstrated.

(iii) The Kaufmann's test, consisting in two-large scale shear critical beams monotonically loaded in shear until failure with null bending moment at mid-span, were numerically simulated. Measured web principal strains and directions in concrete, strains in the stirrups and cracking patterns were compared with the ones from the numerical model, with fairly good results.

Moreover, the experimental campaign carried out at UPC consisting on four shear critical beam specimens with different quantities of longitudinal and transversal reinforcement was presented. The numerical and experimental results were compared in terms of displacements, strains and cracking patterns. In a general way, a good fitting of the model predictions to the experimental observations was perceived in the different parameters analysed. In particular, the capability of the model to properly account for the contribution of the stirrups in the shear resistance of the beams was highlighted.

The experimental tests were also simulated with the flexural basic model CONS (Marí 2000), to assess the importance of including shear effects in fibre beam models for this type of analysis. Also, distributions of strains and stresses determined along a shear-

critical cross section were compared with the results of two other rather more complex models - the TINSA model (Bairán 2005) and the model of (Mohr 2011).

Finally, from all the analyses performed the following general conclusions regarding the proposed model for shear-bending interaction can be drawn:

- For the cases of beams submitted to high shear stresses the ultimate load and failure mechanism are fairly well reproduced by the proposed model.
- Shear critical beams cannot be simulated through pure flexural fibre beam models as extremely unsafe predictions are obtained by continuing the analysis until reaching bending failure.
- In addition to the accuracy in predicting the failure load, the proposed shear model is able to reproduce the deflection of the beams, including shear deformations.
- The fixed stress approach considered in the proposed formulation enables to accurately predict the development of stresses in the stirrups, and by these means, ensure proper simulations of beams with and without transversal reinforcement.
- Sectional shear-related results computed by the proposed model revealed a reasonably agreement with the more complex and accurate force-interaction models, in terms of distribution of strains and stresses along the cross section.

It can also be concluded that fibre beam models, as the one proposed in this thesis, may accurately simulate the structural response of beams under combined normal and shear forces, provided that multiaxial constitutive equations are used for concrete and appropriate kinematic assumptions are taken into account at fibre and sectional levels.

In view of its relative simplicity and computational efficiency, the fibre beam models can be seen as an alternative to complex 2D and 3D FE approaches for nonlinear analyses of entire structures. In the next chapter, the numerical simulations are extended to the cases of RC frames.

Chapter 4

SHEAR RESPONSE OF RC FRAMES

4.1 Introduction

In the previous chapter, the fibre beam model including shear-bending interaction developed in this thesis was presented and validated with experimental tests on shear critical beams. In this chapter the analyses are extended to RC frames, with the goal of evaluating the influence of shear related parameters in their structural response.

Firstly, an experimental test of a RC frame available in literature is simulated with the numerical model. The key objective of this study is to verify the accuracy of the proposed model in predicting the behaviour of RC frames. The shear related response of the frame and the capability of the numerical model to take it into account are underlined.

Afterwards, a parametric study on the influence of the restraint brought by the columns in the ultimate resistance of a shear critical beam belonging to a frame is carried out with the proposed model.

4.2 Experimental validation

4.2.1 Description

The experimental test performed by (Vecchio and Emara 1992) on a large-scale, single bay and two-storey RC frame is simulated with the proposed numerical model. Although this frame actually failed in bending, an insight investigation into the shear related parameters and their influence in the frame behaviour was the focus of the experimental test.

The geometry and loading of the frame are presented in Figure 4.1. A constant axial load of 700kN was firstly applied to the columns, and then a lateral load Q in the 2nd storey beam was incrementally applied until failure. The frame was based in a heavily RC foundation, which in turn was fixed onto the lab strong floor. Deflections, longitudinal and transversal strains in concrete and strains in longitudinal reinforcement were monitored. The following material properties were adopted in the numerical model: $f_c' = 30$MPa, $E_0 = 28.6$GPa and $f_t = 1.8$MPa for concrete; $f_{sy} = 418$MPa and $E_s = 192.6$GPa for the longitudinal reinforcement; $f_{sy} = 454$MPa and $E_s = 210$GPa for the transversal reinforcement.

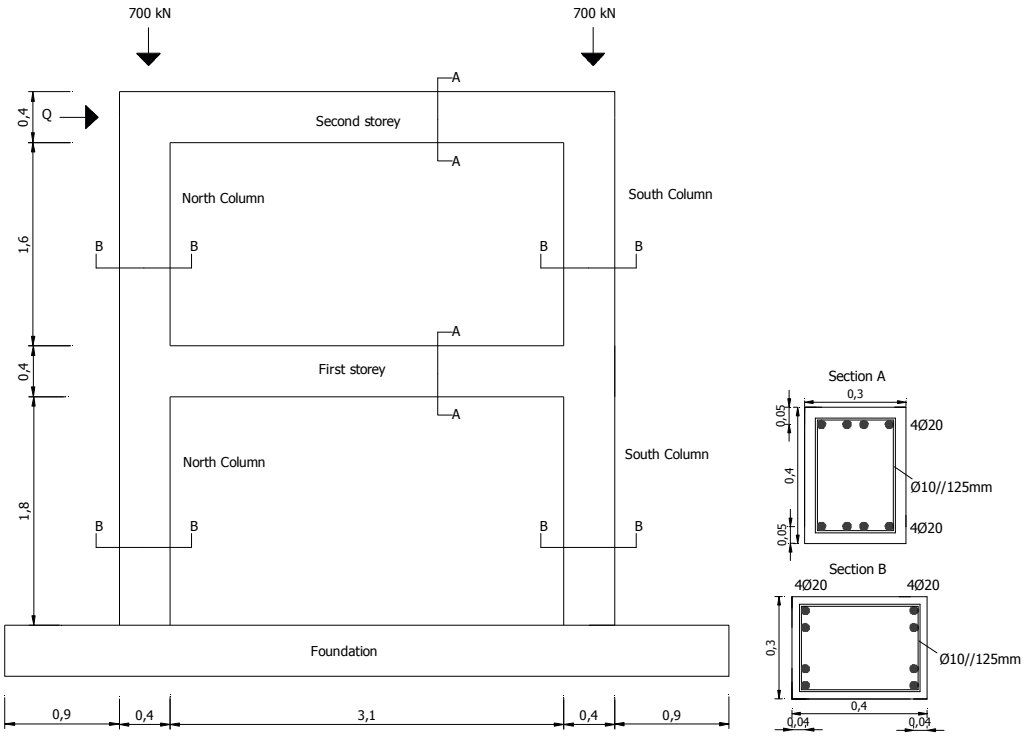

Figure 4.1 – Frame tested by Vecchio and Emara

The FE mesh used to simulate the frame is represented in Figure 4.2. Both cross sections of the columns and beams were discretized into fibres 10mm thick. Filaments of longitudinal reinforcement were placed in their actual positions, and transversal steel taken as smeared in the concrete fibres. With respect to the extra stiffness of the overlapping sections located at the column-beam joints and at the end of the columns, FEs with linear-elastic shear stiffness were considered in these locations as signalized in Figure 4.2 by N1B, S1B, N2B, S2B, BNC and BSC, to prevent unrealistic shear failures in these regions (letters N and S stand for 'north' and 'south' locations). In relation to the support conditions, the following elastic springs taking into account the restraining effects of the foundation were used: K_V = 343349kN/m and $K_{\theta y}$ = 180663kNm.

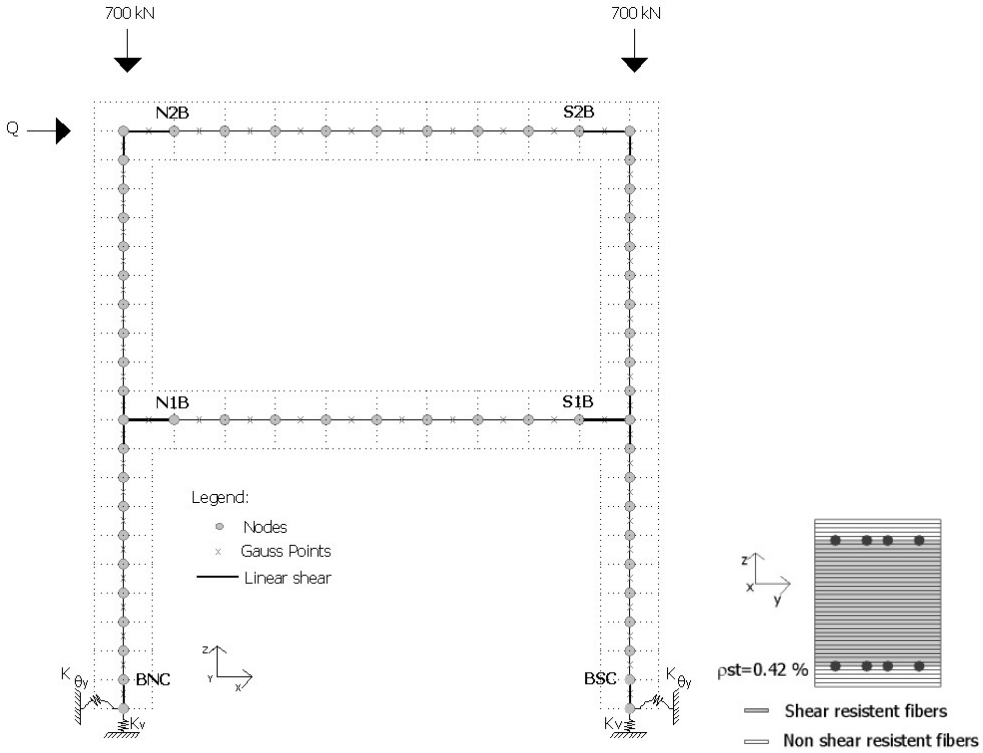

Figure 4.2 – Discretization of the test RC frame

4.2.2 Results and discussion

Numerical predictions are compared with the experimental measurements on the frame, as it can be seen in Figure 4.3 for the lateral displacements at the 2nd storey, in Figure 4.4 for the rotation at the 2nd storey north-joint and in Figure 4.5 for the axial strain in the longitudinal reinforcement in the north-column bottom end. The overall behaviour of the frame under increasing load is accurately predicted by the proposed model, as a general

acceptable fitting between experimental and numerical results is observed. In relation to the lateral displacement and rotation (Figure 4.3 and Figure 4.4), the shear model slightly overestimates the real stiffness of the structure. As the local strain measurements were correctly reproduced, this small differences observed at the global deformations of the frame can be attributed to the difficult definition of the real stiffnesses at the base column supports. The stop of the innermost iterative procedure at the fibre level that occurs at the ultimate load stage does not allow the computation to proceed along the ductile post-failure path. Hence, even though the linearized arc-length is used, the stop of the analysis occurred due to the non-convergence of the iterative procedure of the fibres in which concrete is crushed.

To evaluate the influence of the shear effects on the overall response of the frame, the results correspondent to the flexural model CONS (Marí 2000) are included in these graphics. Pertaining to the lateral displacements at the top storey in Figure 4.3, although the load capacity of the frame was similarly predicted by both models, influence of shear is evidenced by allowing a load-deflection evolution more close to the real performance of the structure. In fact, for loading stages near failure, an average of 17% of the lateral displacement is related to shear effects. However, influence of shear is not perceived in the rotation at the top-north joint (Figure 4.4) and strain in the longitudinal reinforcement (Figure 4.5), as both shear and flexural models presented similar predictions.

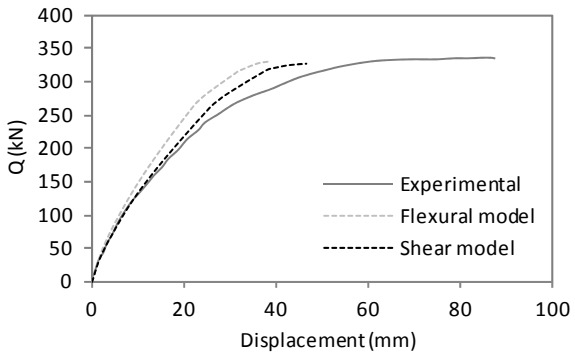

Figure 4.3 – Lateral displacements at the top storey

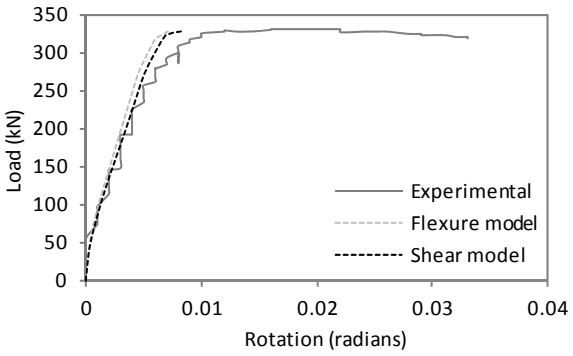

Figure 4.4 – Rotation at the top-north joint

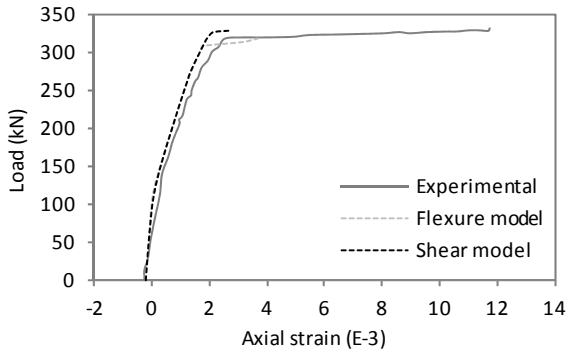

Figure 4.5 – Strain in the longitudinal reinforcement in the north column bottom end

In Table 4.1 a summary of the main experimental observations of the frame response are listed, together with the development of material damages computed by the proposed shear model. This comparison is divided into three stages: cracking propagation, yielding of reinforcement and failure. In general, a strong correlation between the overall model predictions and the experimental observations is visible at all stages. In particular, lateral loads causing first yielding of longitudinal reinforcement and its subsequent propagation were quite accurately predicted by the shear model. Experimental failure of the frame involved the formation of plastic hinges at all the extremities of the beams and columns bases, due to yielding of both the tensile and compressive longitudinal reinforcement, as well as limited concrete crushing. The computed damages at failure were mainly due to the formation of plastic hinging at the column bases BNC and BSC, as well as to yielding of the transversal reinforcement and failure of the longitudinal reinforcement at BNC. Also, the 1st and 2nd storey beams were predicted to be extensively cracked, as experimentally observed.

Table 4.1 Analytical and experimental results for the behaviour of the two-story frame

Experimental Observations		Numerical results (proposed shear model)	
Stage1: Cracking propagation			
Q=52.5 kN	Flexural cracking at the bottom face of the N1B and at the top face of the S1B	Q=41 kN	Flexural cracking at the N1B and S1B
Q=145 kN	Flexural cracking at the BNC and BSC; Web shear cracks in the first story beam	Q=101 kN	Flexural cracking at BNC and BSC
Q>145 kN	Propagation of cracking throughout all members; Response of structure becomes progressively softer	Q=121 kN	Web shear cracks in the N1B and S1B
Stage 2: Yielding of reinforcement			
Q=264 kN	First yielding of the longitudinal bottom reinforcement at N1B	Q=266 kN	First yielding of longitudinal reinforcement at S1B
Q=287 kN	Yielding of the longitudinal top reinforcement at S1B	Q=276 kN	Yielding of longitudinal reinforcement at N1B
Q=323 kN	Yielding at the BNC and BSC; Hinging at N1B and S1B	Q=313 kN	Yielding of longitudinal reinforcement at BSC
		Q=322 kN	Yielding of longitudinal reinforcement at N2B and S2B
		Q=324 kN	Yielding of the longitudinal reinforcement at the BNC
Stage3: Hinging formation and failure			
Q=329 kN	Concrete crushing and hinging at the BNC and BSC; hinging at N2B and S2B	Q=326 kN	Concrete crushing at the BNC and BSC; yielding of transversal reinforcement at BNC
Q=332 kN	Failure; ductile hinging at the ends of the beams and at the bases of the columns	Q=327 kN	Failure of longitudinal reinforcement

Concerning to sectional responses, the experimentally observed and numerically predicted strains at the base of the north column are compared in Figure 4.6. The numerical results refer to the average of the three first FEs starting from the column base. It can be seen that the shear model was able to reproduce accurately the curvature, axial strain and shear strain of the section. By comparing the results predicted by the flexural and shear models, it can be noticed that the influence of shear in the sectional curvature (Figure 4.6a) and axial strain (Figure 4.6b) is not significant.

Although the failure mechanism was mostly flexural, shear strains in the columns reached important values, especially for later loading stages, as it is correctly predicted by the shear model (Figure 4.6c). Accordingly to the description of the experimental test (Vecchio and Emara 1992), large diagonal cracks were observed in the 2nd storey north beam-column joint and in the base of the columns. Maximum shear stresses were also numerically determined at these locations for the ultimate load.

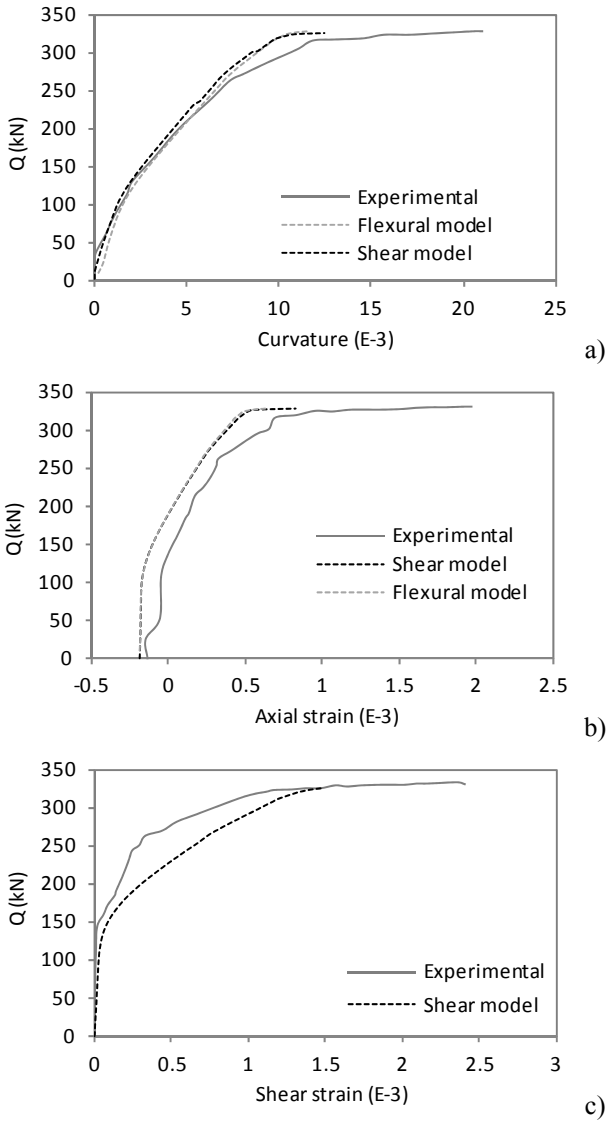

Figure 4.6 – Sectional deformations in the north column bottom: a) curvature, b) axial strain and c) shear strain

Relating to the importance of considering shear effects in the analysis, normal-shear interaction effects cause a reduction of the flexural stiffness of the members, and consequently a decrease of the lateral stiffness of the frame. Relative proportions of total shear in the base of the north and south columns computed by different strategies of analysis are presented in Figure 4.7: nonlinear analyses (obtained with flexural and shear models) are able to reproduce the significant shear redistribution caused by the axial deformation of the beams, as well as by the faster stiffness degradation that occurs in the north column; linear analysis gives the unrealistic result that 50% of the shear force is carried by each column at all loading stages.

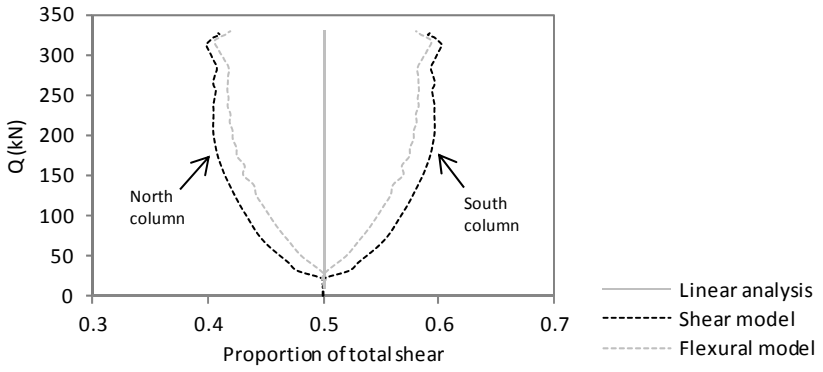

Figure 4.7 – Base shear distribution between the north and south columns

Concerning the two nonlinear analyses, higher shear force distribution among the two columns (north and south) is predicted by the shear model in comparison to the flexural model, due to the greater deterioration of the north column stiffness brought by the interaction of shear-bending forces.

4.3 Parametric study: influence of frame restraint on the response of a RC shear critical beam

The present parametric study has the objective of evaluating the effects of restraint due to the columns on the ultimate response of a shear critical beam. The effects of the generated compression struts in the load carrying capacity of shear critical beams belonging to frames are determined by the proposed model. Additionally, the importance of considering shear effects on this type of simulations is discussed.

The shear critical beam VSA1 analyzed in the Section 3.3.3 is used in the numerical simulations as part of a RC frame. The FE mesh (Figure 3.24) and material properties (Table 3.2) of the beam used in the validation example are kept unchanged. Thereby, the parametric study includes various geometries of the columns, which generate different restraints, in order to evaluate its influence in the beam response. The restraint effects of the columns were simulated through elastic supports at both extremities of the beam. The translation and rotation stiffnesses, K_x and $K_{\theta y}$, were determined in accordance to the geometric characteristics of the columns, as represented in Figure 4.8, where E_c is the elasticity modulus of the concrete, I is the second moment of area of the cross section and L is the beam length.

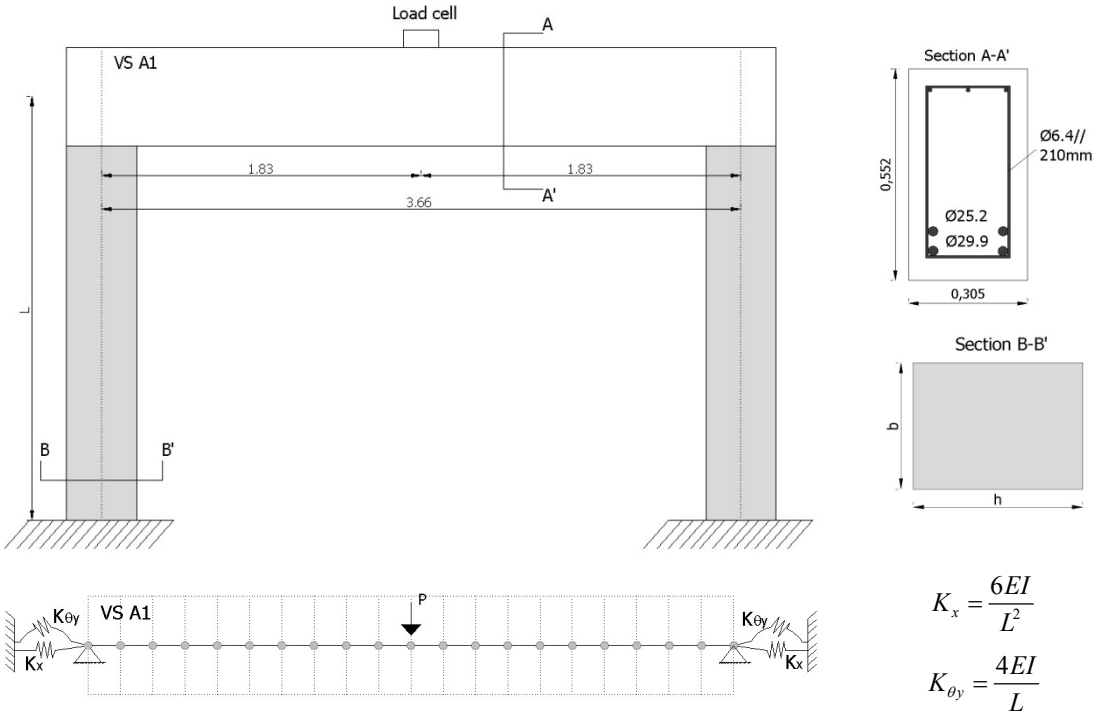

Figure 4.8 – Parametric study on the influence of frame effects on the response of a shear-critical beam

Firstly, the two extreme support conditions were considered: (*i*) simply supported beam VSA1 (K_x=0 and $K_{\theta y}$=0) and (*ii*) fully clamped at both ends VSA1_0 (K_x=∞ and $K_{\theta y}$=∞). Computations with the proposed shear and flexural models were carried out. The corresponding numerical predictions are presented in Figure 4.9, in terms of the mid-span force-displacements curves. Pertaining to the simply supported beam, both models give similar predictions for the ultimate load; however, the consideration of shear effects is determinant to achieve a correct deflection, as also mentioned in Section 3.3.3. The double fixed-ended beam (VSA1_0) presents an increase of the load carrying capacity, with a higher difference between the predictions of the shear and flexural models in terms of ultimate load. Shear failure is predicted for a lower load in comparison with the flexural model, and this difference is more prominent in the case of the double-fixed ended beam. In terms of displacements, this beam (VSA1_0) is less influenced by the shear deformation in its deflection, as the difference between the deflections predicted by the shear and flexural models are less pronounced then in the case of the simple supported beam (VSA1).

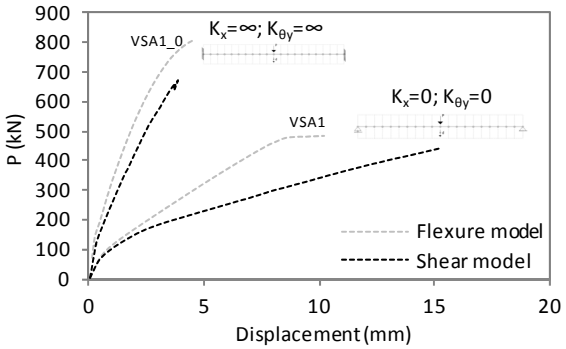

Figure 4.9 – Force-displacement curves for VSA1 and VSA1_0 beams: simple supported and double fixed-ended

Along with the consideration of the two extreme support situations, intermediate values of restraint representing different columns of the frame were analyzed. The considered variable parameters were the length L and the height h of the column's cross section (see Figure 4.8) and the concrete Young's modulus E_c, as listed in Table 4.2. A summary of the results computed by the proposed shear model at the ultimate load stage are presented in Table 4.2, and the mid-span force-displacement curves are depicted in Figure 4.10.

Table 4.2 Summary of the variables considered on the parametric study and the results correspondent to the ultimate response of the shear-critical beams

Beam in frame	Columns				Supports		Results at failure load		
	L (m)	h (m)	b (m)	E_c (MPa)	K_x (kN/m)	$K_{\theta y}$ (kNm)	Failure mode	P_u (kN)	δ_u (mm)
VSA1	0	0	0	0	0	0	Shear	444.8	15.3
VSA1_0	∞	∞	∞	∞	∞	∞	Shear	653.0	3.7
VSA1_1	3	0.3	0.3	30	13500	27000	Shear	470.0	7.9
VSA1_2	3	0.4	0.3	30	32000	64000	Shear	552.4	9.0
VSA1_3	3	0.5	0.3	30	62500	125000	Shear	580.7	8.8
VSA1_4	4	0.3	0.3	30	7594	20250	Shear	490.7	8.6
VSA1_5	4	0.4	0.3	30	18000	48000	Shear	577.6	10.0
VSA1_6	4	0.5	0.3	30	35156	93750	Shear	575.7	9.1
VSA1_7	3	0.3	0.3	35	15750	31500	Shear	481.9	7.8
VSA1_8	3	0.4	0.3	35	37333	74667	Shear	581.3	9.3
VSA1_9	3	0.5	0.3	35	72917	145833	Shear	580.0	8.5
VSA1_10	4	0.3	0.3	35	8859	23625	Shear	532.4	9.4
VSA1_11	4	0.4	0.3	35	21000	56000	Shear	456.9	7.2
VSA1_12	4	0.5	0.3	35	41016	109375	Shear	561.7	8.7

In general, the increase of the column stiffness (associated to higher values of K_x and $K_{\theta y}$) induces an increment of the load carrying capacity and a decrease of the ultimate deflection

of the beam. In fact, the combination of lower bending moments acting concomitantly with the shear forces delays the shear failure for higher load levels. This can be observed in Figure 4.11, where the ultimate load is depicted as a function of K_x and $K_{\theta y}$ for all the situations studied. Shear failure mechanism was predicted in all the analyses.

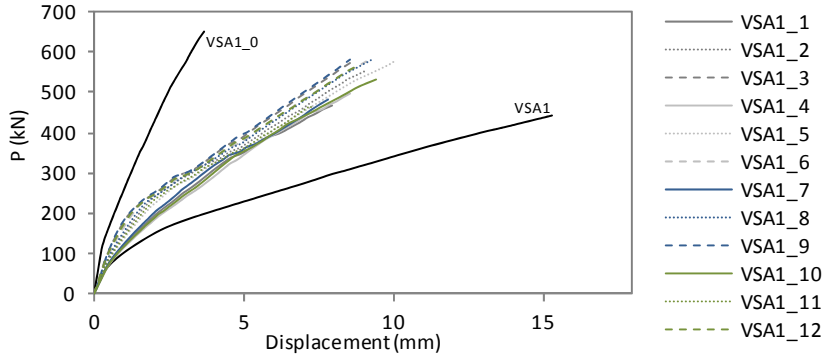

Figure 4.10 – Force-displacement of the beam with different levels of support restraint

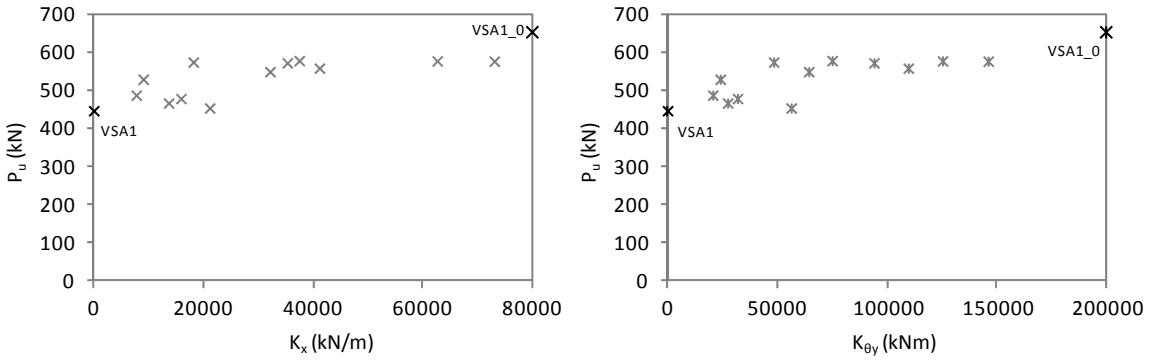

Figure 4.11 – Ultimate load of the beam vs level of restraint of the columns: a) longitudinal stiffness and b) rotational stiffness

Also, due to the restraint at the supports, the stresses acting on the compressive struts can reach higher values and contribute to the increment of the load carrying capacity of the beams. The distribution of the compressive principal stresses is represented in the maps of Figure 4.12, starting from the simple supported case, and increasing the level of restraint due to the columns until the double clamped condition at both extremities is reached. It is observed that as the level of restraint increases there are higher compressive stresses along the web of the section in the shear-span, and the flow of principal compression stresses inclines towards the direction of the supports.

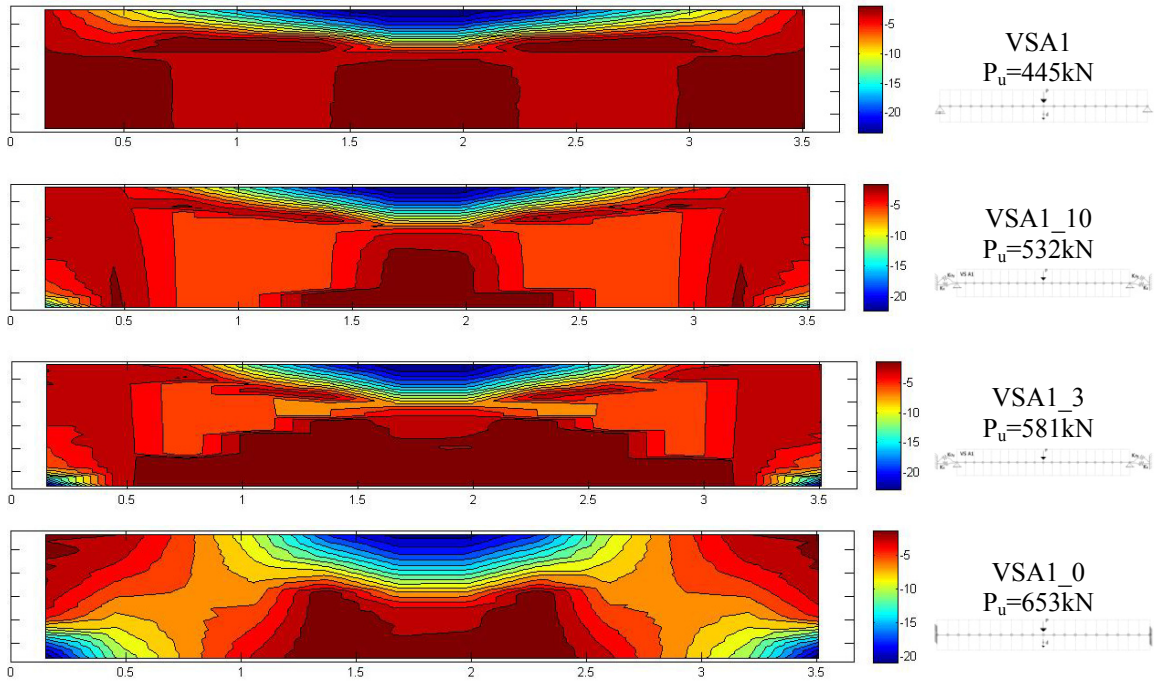

Figure 4.12 – Distribution of the computed minimum principal stress (compression) along the beams for the ultimate load

This example, despite showing rather expected results, is relevant to demonstrate how a 1D fibre beam model can actually simulate the performance of shear critical beams that belong to frames, capturing its multiaxial response. Also, it is an introduction to the problem of how restraint influences the response of beams that are critical to shear. This study will be continued in the next chapter by including time-dependent effects, namely shrinkage strains.

4.4 Conclusions

In this chapter, the examples analyzed with the proposed fibre beam model that accounts for shear-bending interaction were extended to the simulation of entire RC framed structures.

At first, an experimental test consisting of a two-storey frame under monotonic load until failure was presented. The aim of this validation example was to assess the accuracy of the model in predicting the response of RC frames and to determine the importance of including shear effects in the analysis. A good fitting was achieved between the numerical and the experimental results, in terms of both global and local responses. Also, computed

shear strains were in good conformity with the experiments. In general, an accurate simulation of the response of the frame under lateral load was determined by the model, not only in the ultimate load stage but also through the flexural and shearing crack formation and subsequent propagation. The inclusion of shear effects in the analysis revealed to be important in the prediction of the deformation of the frame.

The parametric study presented subsequently aimed to evaluate the influence of the column restraint in the shear-related mechanisms of the beam, namely, its influence on the deflection response with increasing load and the ultimate load capacity. Another goal was to assess the accuracy of the numerical model in capturing the restraint frame effects in the response of a RC shear critical beam. The proposed model predicted a general augment of the load carrying capacity of the beams with the increase of restraint brought by stiffer columns. The compression stresses generated in the web of the cross section by the restraint of the columns increases the shear resistance of the beam. As the ratio of stiffness between the column and the beam increases, the shear resistance of the beam also increases.

Chapter 5

SHEAR EFFECTS AND TIME-DEPENDENT RESPONSE OF CONCRETE BEAMS

5.1 Introduction

In this chapter the fibre beam model for shear-bending interaction is enlarged in order to include the time-dependent features of creep and shrinkage in concrete, temperature gradients and relaxation of prestressed steel. In this manner, the original algorithm for the time step-by-step analysis available in the basic model CONS (Marí 2000) is adapted to the case of multiaxial stress states. The time-dependent model presented in (Van Greunen 1979) for the nonlinear analysis of reinforced and prestressed concrete slabs and panels by means of 2D plane elements is adapted to the case of the 1D fibre beam elements with consideration of a 2D stress-strain state in the fibres.

The inclusion of the time-dependent behaviour in the proposed fibre beam model with inclusion of shear effects is a natural and logic choice, in order to take advantage of these potentialities already available in the basic model. For a matter of coherence, as the shear model considers multiaxial stress-strain state in the fibres, the non-mechanical time-dependent strains must be considered multiaxial as well.

In the regular cases the level of damage and specifically diagonal cracking in RC frame structures under service life conditions must not be very high. However, in service structures with shear damage due to insufficient transversal reinforcement may also exist. In the assessment of the structural safety of these structures and in the design of a repair intervention, life-time structural analysis must account for the shear effects and for the materials' time-dependent responses. The purpose of this chapter is to perform a preliminary study on the significance of considering the multiaxial time-dependent behaviour of concrete beams and, in this manner, to open a possible theme for future work.

Firstly, in this chapter the adopted models to simulate the time-dependent phenomena of concrete creep and shrinkage, temperature variations and relaxation of prestressing steel under multiaxial stress states are described. Afterwards, a benchmark typically used to calibrate the time-dependent analysis of reinforced and prestressed beams under sustained load is simulated with the proposed model. These tests are flexural-dominant and the purpose of this validation is to guarantee the accuracy of the model for the case of bending. Subsequently, experimental tests on diagonally pre-cracked beams under sustained load are simulated with both the shear and flexural models. The importance of considering shear effects and multiaxial time-dependent strains in predicting the response of these beams is pursuit with this example.

Numerical studies on the shear-related time-dependent behaviour of RC beams are carried out subsequently in this chapter. Assessing the importance and understanding the phenomena of shear in the time-dependent response of RC frame elements in both service and ultimate load stages is the main goal of these analyses. In fact, pertinent questions can be raised on this subject:

- *'may high shear stresses affect the time-dependent response of shear-critical beams?'*
- *'may time-dependent phenomena such as creep and shrinkage influence the ultimate resistance of shear critical beams?'*
- '*what happens to the response of a shear critical beams when shrinkage pre-cracking exists?*'

Based on numerical analysis, this chapter provides a general discussion on these issues.

It is noteworthy that the experimental data available on the time-dependent response of shear critical RC beams is very scarce and limited. For this reason, a deep validation and

quantification of the long-term development of the shear related parameters was not possible to be accomplished and is left as an open issue for the future.

5.2 Implementation of time-dependent features in the RC frame model

5.2.1 Overview

Shear-bending interaction is taken into account in the proposed model at different levels: element, section and fibre. As the shear resistant fibres are submitted to 2D stress-strain states (in contrast with the 1D strain-stress state of the pure flexural fibres), the 1D time-dependent analysis originally presented in the basic model CONS (Marí 2000) is extrapolated to the 2D case, as described in the following. Time-dependent effects are taken into account through a biaxial formulation within a time-step procedure based on the work of (Van Greunen 1979).

In order to simulate the nonlinear response influenced by the phenomena of creep, shrinkage, relaxation of prestressing steel and temperature changes of reinforced and prestressed concrete structures, two key features are needed: (*i*) a time-dependent material model and the strategy to its numerical implementation and (*ii*) a solution procedure for the time-dependent analysis within the scheme of FEM.

Both of these topics will be presented in the following, relating to the solution scheme adopted for the consideration of time-dependent analysis in the proposed fibre beam model with inclusion of shear effects.

5.2.2 Material model for concrete

Creep of concrete is the increase in strain under sustained load after the instantaneous elastic deformation at the time of loading. This phenomenon affects the serviceability of RC elements and causes prestress losses. A great quantity of factors influence the creep properties of concrete, such as: strength, age at loading, volume and elasticity modulus of the aggregate, relative humidity of the environment, temperature, thickness of the element, stress state, load duration, etc. Some of these factors are of difficult quantification and can

take values with high levels of variation, which makes the modelling of concrete creep a difficult task. Even though structures are subjected to multiaxial stress states, research on creep under multiaxial load conditions is scarce and many times not conclusive. In fact, extensive experimental research and development of numerical models were conducted to the uniaxial case (Bazant and Carol 1993; Bazant and Guang-Hua 2008). Deterministic models for creep as the ones proposed by (ACI Committee 209 1970; CEB-FIP 1992) establish correlations between analytical formulations and experimental data from tests undertaken in laboratory, providing relatively simple equations to predict this time-dependent concrete phenomenon.

Concrete shrinkage can be defined as the volume change that occurs with time due to loss of water and the chemical reaction of hydration. This phenomenon is typically assumed as stress and temperature independent, and is influenced by many factors, such as, age of concrete when finishing curing, water-to-cement ratio, environmental relative humidity, size of the element and fine aggregate and air contents. Model Code 1990 (CEB-FIP 1992) also suggests an equation to approximately determine the shrinkage strain to be used in numerical modelling.

Creep and shrinkage are known as coupled phenomena, however, as it is generally accepted, they are treated separately in the model of the present thesis. The effects of temperature variations are also considered in an independent fashion. Within a time-step of the analysis, an incremental method is used to compute the non-mechanical strains. By these means, each component of strain - stress-dependent (creep) and stress-independent (shrinkage and thermal) - is determined separately, and afterwards, by assuming the principle of superposition, all the strain components are summed.

Hence, the 2D non-mechanical strain vector $\underline{\varepsilon}^{nm}$ depends on time t and is divided into two types of strains: the stress-dependent $\underline{\varepsilon}^{c}$ and the stress-independent $\underline{\varepsilon}^{0}$:

$$\underline{\varepsilon}^{nm}(t) = \underline{\varepsilon}^{c}(t) + \underline{\varepsilon}^{0}(t) \tag{5.1}$$

The biaxial stress-dependent strains $\underline{\varepsilon}^{c}$ depend on the level of stress that the material is subjected to, and in this model only creep deformations are treated as such:

$$\underline{\varepsilon}^{c}(t) = \begin{Bmatrix} \varepsilon_x^c \\ \varepsilon_z^c \\ \gamma_{xz}^c \end{Bmatrix} \tag{5.2}$$

Strains due to shrinkage and temperature variations are considered stress-independent and are treated as volume changes $\underline{\varepsilon}^{0}$, and for this reason, do not contemplate shear deformations:

$$\underline{\varepsilon}^{0}(t)=\begin{Bmatrix}\varepsilon_x^0\\ \varepsilon_z^0\\ 0\end{Bmatrix}=\begin{Bmatrix}\varepsilon_x^{sh}\\ \varepsilon_z^{sh}\\ 0\end{Bmatrix}+\begin{Bmatrix}\varepsilon_x^{T}\\ \varepsilon_z^{T}\\ 0\end{Bmatrix} \tag{5.3}$$

The format of the biaxial shrinkage strain vector in this equation was also used in (Chong, Foster and Gilbert 2008).

5.2.2.1. Creep

The principle of superposition of creep strains, which states that the strain at a given time is the sum of the strains caused by the loads applied during their respective durations, is considered in this model. It is inherent to this assumption that during each time step the stress state is kept constant. Fulfilment of this hypothesis is ensured by a correct choice of the size of the time steps during the analysis. Creep responses in compression and tension are assumed to be equal before cracking, but after concrete cracking no creep strain is considered under tension.

Concerning to the range of typical service stress levels applied to concrete in actual structures, experimental data on biaxial creep supports the feasibility of adding the various creep strains due to multiaxial stresses (Bazant 1988), by considering that the principles of isotropy, linearity and superposition are valid. By these means, according to (Bazant 1988) the strain tensor in concrete due to creep $\underline{\varepsilon}^{c}$ is given by the following constitutive relationship for an aging material under a multiaxial stress for a given time t

$$\underline{\varepsilon}^{c}(t)=\int_0^t B_e\, J\left(t',t-t',T\right)\frac{\partial\underline{\sigma}(t')}{\partial t'}dt' \tag{5.4}$$

where for the 2D case

$$\underline{\varepsilon}^{c}(t)=\left(\varepsilon_x^c,\varepsilon_z^c,\gamma_{xz}^c\right)^T \tag{5.5}$$

$$\underline{\sigma}(t)=\left(\sigma_x,\sigma_z,\sigma_{xz}\right)^T \tag{5.6}$$

$$B_e = \begin{pmatrix} 1 & -\upsilon_c & 0 \\ -\upsilon_c & 1 & 0 \\ 0 & 0 & 2(1+\upsilon_c) \end{pmatrix} \tag{5.7}$$

where $\underline{\sigma}$ is the stress tensor and B_e is an elastic-like matrix for an isotropic material with a unit elastic modulus for isotropic materials. Creep compliance $J(t', t-t', T)$ is a function of the age of concrete and of the stress tensor $\underline{\sigma}(t')$ applied at the instant of loading t', as well of the temperature T. The ratio between the lateral creep strain and the creep strain in the direction of the applied load is given by the Poisson's ratio υ_c.

It is worth mentioning that the superposition principle and the Poisson's ratio resulting from creep of concrete under multiaxial stress states is rather controversial, not only by difficulties of measurement and because of the variability on the experimental devices, but also due to the many parameters influencing concrete creep. Non validity of the superposition principle for the cases of biaxial stresses is supported by some authors (Gopalakrishnan, Neville and Ghali 1969; Gopalakrishnan, Neville and Ghali 1970), by founding through experimental tests that the effective creep Poisson's ratio under multiaxial compression can be lesser than the one under uniaxial compression, and dependent on the level of principal stresses. Some other authors argue that the multiaxial creep Poisson's ratio varies with time and does not depend on the stress states (Kim, Kwon and Kim 2006). Conversely, the conclusion that concrete creep under multiaxial states of stresses can be satisfactorily predicted in practice by assuming a constant Poisson's ratio equal to the static elastic value, along with a theoretical model for creep under uniaxial stresses, is also sustained by many authors (Illston and Jordaan 1972; Bazant 1988; Kim, Kwon and Kim 2005; Kim, Kwon and Kim 2006). In the present model, as it was considered by (Kabir 1976; Van Greunen 1979), the creep Poisson ratio υ_c under biaxial stresses will be taken as constant and equal to the elastic value for concrete. This simplification assumption along with the superposition principle is seen as accurate enough for structural analyses.

Regarding these assumptions, and starting from the creep model implemented in CONS (Marí 1984) for the 1D case, its generalization to the biaxial state is straightforward. Therefore, regarding the formulation derived by (Bazant and Wu 1973), the biaxial creep strain tensor given by the integral of Eq. (5.4) can be determined through a Dirichlet series

$$J(t', t-t', T) = \sum_{i=1}^{m} a_i(t') \left[1 - e^{-\lambda_i \varphi(T)(t-t')} \right] \tag{5.8}$$

in which a_i are scale factors dependent on the age of loading t', λ_i are retardation times that govern the shape of the logarithmic decaying creep curve, $\varphi(T)$ is the shift function that depends on the temperature, t is the considered time and m are the number of the Dirichlet terms used to approximate the compliance function. The many parameters involved in this equation are determined by applying the minimum square method to an experimentally obtained creep characterization curve.

Algorithmic implementation of the Dirichlet series is performed by means of the hidden variables formulation (Bazant and Wu 1973), which does not require the storage of all previous stress states for the determination of the creep strain increment in a time integration algorithm. Consequently, the demand of computation time and storage for a creep analysis is considerably reduced. By these means, and relating to the computational solution procedure, the time domain is divided into time steps Δt_n that go from t_n to t_{n+1}

$$\Delta t_n = t_{n+1} - t_n \tag{5.9}$$

and the integral of Eq. (5.4) is solved through the following expression

$$B_e \Delta \underline{\varepsilon}_n^c = J\left(t', t-t', T\right) \Delta \underline{\sigma}_n \tag{5.10}$$

In the approximation through the Dirichlet series it comes

$$J\left(t', t-t', T\right) \Delta \underline{\sigma}_n \approx \sum_{i=1}^{m} \underline{A}_{in} \left[1 - e^{-\lambda_i \varphi(T) \Delta t_n}\right] \tag{5.11}$$

and the increment of creep strain $\Delta \underline{\varepsilon}_n^c$ is determined as

$$\Delta \underline{\varepsilon}_n^c = B_e \sum_{i=1}^{m} \underline{A}_{in} \left[1 - e^{-\lambda_i \varphi(T) \Delta t_n}\right] \tag{5.12}$$

where $\underline{A}_{in}$ is the hidden state variable vector, given by

$$\underline{A}_{in} = \underline{A}_{in-1} e^{-\lambda_i \varphi(T) \Delta t_{n-1}} + \Delta \underline{\sigma}_n a_{in} \tag{5.13}$$

Therefore, in the extended format for the biaxial stress-strain state determination of the strain increment vector due to creep involves the following expressions (considering m=3):

$$\begin{pmatrix} \Delta \varepsilon_{n,x}^c \\ \Delta \varepsilon_{n,z}^c \\ \Delta \gamma_{n,xz}^c \end{pmatrix} = B_e J\left(t', t-t', T\right) \begin{pmatrix} \Delta \sigma_{n,x} \\ \Delta \sigma_{n,z} \\ \Delta \tau_{n,xz} \end{pmatrix} \tag{5.14}$$

$$\begin{pmatrix} \Delta\varepsilon_{n,x}^{c} \\ \Delta\varepsilon_{n,z}^{c} \\ \Delta\gamma_{n,xz}^{c} \end{pmatrix} = \begin{pmatrix} 1 & -\upsilon_c & 0 \\ -\upsilon_c & 1 & 0 \\ 0 & 0 & 2(1+\upsilon_c) \end{pmatrix} \begin{pmatrix} \sum_{i=1}^{m} \underline{A}_{in,x} \left(1 - e^{-\lambda_i \varphi(T) \Delta t_n}\right) \\ \sum_{i=1}^{m} \underline{A}_{in,z} \left(1 - e^{-\lambda_i \varphi(T) \Delta t_n}\right) \\ \sum_{i=1}^{m} \underline{A}_{in,xz} \left(1 - e^{-\lambda_i \varphi(T) \Delta t_n}\right) \end{pmatrix} \tag{5.15}$$

$$\underline{A}_{in} = \begin{pmatrix} A_{in,x} \\ A_{in,z} \\ A_{in,xz} \end{pmatrix} = \begin{pmatrix} \underline{A}_{in-1,x} \left(1 - e^{-\lambda_i \varphi(T) \Delta t_{n-1}}\right) + \Delta\sigma_{n,x} a_{i,n} \\ \underline{A}_{in-1,z} \left(1 - e^{-\lambda_i \varphi(T) \Delta t_{n-1}}\right) + \Delta\sigma_{n,z} a_{i,n} \\ \underline{A}_{in-1,xz} \left(1 - e^{-\lambda_i \varphi(T) \Delta t_{n-1}}\right) + \Delta\tau_{n,xz} a_{i,n} \end{pmatrix} \tag{5.16}$$

In order to start the analysis (n=1) the first hidden variable vector A_{i1} is given as

$$\underline{A}_{i1} = \begin{pmatrix} A_{i1,x} \\ A_{i1,z} \\ A_{i1,xz} \end{pmatrix} = \begin{pmatrix} \Delta\sigma_{1,x} a_{i,1} \\ \Delta\sigma_{1,z} a_{i,1} \\ \Delta\tau_{1,xz} a_{i,1} \end{pmatrix} \tag{5.17}$$

The empirical expression adopted for the 1D creep deformation is the one proposed in the Model Code 1990 (CEB-FIP 1992)

$$\varepsilon_c(t,t') = \frac{\sigma_c(t')}{E_c} \phi(t,t') \tag{5.18}$$

where t' is the age of concrete loading and t is the actual time. Creep coefficient ϕ_0 is determined as

$$\phi(t,t') = \phi_0 \beta_c(t-t') \tag{5.19}$$

where the basic creep coefficient ϕ_o depends on the compressive strength of concrete, on the environmental relativity humidity and on the element cross-section dimensions. β_c is the coefficient that describes the development of creep with time, and is a function of the age of loading, of the environmental relativity humidity and on the element cross-section dimensions.

Determination of the creep compliance function is accomplished by fitting, through the least square method, its aging scale parameters a_i to the empirical expression considered. Constants λ_i are set as 10^{-i} (λ_1=0.1, λ_2=0.01; λ_3=0.001) and three terms on the Dirichlet series are considered (m=3). In this manner, regarding Eq. (5.8) the following system of simultaneous equations is obtained

$$\begin{pmatrix} 1-e^{-\lambda_i \Delta t_n} & 1-e^{-\lambda_i \Delta t_n} & 1-e^{-\lambda_i \Delta t_n} \\ 1-e^{-\lambda_i \Delta t_n} & 1-e^{-\lambda_i \Delta t_n} & 1-e^{-\lambda_i \Delta t_n} \\ 1-e^{-\lambda_i \Delta t_n} & 1-e^{-\lambda_i \Delta t_n} & 1-e^{-\lambda_i \Delta t_n} \end{pmatrix}_{n\times m} \begin{pmatrix} a_{1n} \\ a_{2n} \\ a_{3n} \end{pmatrix}_{m\times 1} = \begin{bmatrix} J(t', t_1 - t') \\ J(t', t_2 - t') \\ J(t', t_3 - t') \end{bmatrix}_{n\times 1} \tag{5.20}$$

which is solved to determine the values of a_i that better fit the empirical curve. Typical values for a_i are around 1×10^{-7} and 2×10^{-7}.

In this thesis it is assumed that linear creep occurs. For 1D stress states this approximation is considered valid whenever the compressive stress is less than 45% of the concrete strength. This value can be considered as the threshold for which no damage due to compressive stresses occurs. For multiaxial stress states this threshold level depends on whether the concrete is compressed in multiple directions or subjected to compression-tension states. This is a topic that requires further basic research and is out of the ambit of this thesis.

5.2.2.2. Stress-independent strains

Biaxial shrinkage strain $\underline{\varepsilon}^{sh}$ is given by the vector of stress-independent volume changes:

$$\underline{\varepsilon}^{sh}(t) = \left(\varepsilon_x^{sh}, \varepsilon_z^{sh}, 0\right)^T \tag{5.21}$$

The expression proposed in the Model Code 1990 (CEB-FIP 1992) is applied to compute the increment of shrinkage strain as

$$\Delta\varepsilon_x^{sh} = \varepsilon_{cs0}\beta_s(t - t_s); \quad \Delta\varepsilon_z^{sh} = \varepsilon_{cs0}\beta_s(t - t_s) \tag{5.22}$$

in which t_s is the age of concrete at the start of shrinkage. The coefficient of basis shrinkage ε_{cs0} is a function of the compressive strength of concrete, of the cement type and of the environmental relative humidity; β_s is the coefficient that describes the development of shrinkage with time and depends on the dimensions of the element cross-section.

Effects of the temperature variations are accounted for by means of the stress independent strain vector $\underline{\varepsilon}^T$

$$\underline{\varepsilon}^T(t) = \left(\varepsilon_x^T, \varepsilon_z^T, 0\right)^T \tag{5.23}$$

and the increment of strain is determined by

$$\Delta\varepsilon_x^T(t) = \alpha\Delta T = \alpha\left(T_n - T_{n-1}\right); \quad \Delta\varepsilon_z^T(t) = \alpha\Delta T = \alpha\left(T_n - T_{n-1}\right) \tag{5.24}$$

through the coefficient of thermal dilatation of concrete α and the differences of temperature T between the time steps n and n-1.

The stress independent strain vectors $\underline{\varepsilon}^{sh}$ and $\underline{\varepsilon}^{T}$ are used in Eq. (5.3) as part of the 2D non-mechanical strain vector $\underline{\varepsilon}^{nm}$.

5.2.3 Material model for the active reinforcement

As reinforcement is considered under a 1D stress-strain state, the methodology adopted in the basic model CONS for the consideration of time-dependent losses of prestress are maintained here, and for this reason it will not be detailed further. In brief terms, the loss of prestress that occurs with time is due to the effects of shrinkage and creep of concrete, to the relaxation of the prestressing steel and to the interaction between all them. Its implementation in the numerical model is performed through the fictitious initial stress concept proposed by (Hernández and Gamble 1975) and also used in (Kang 1977; Van Greunen 1979). In this method, in order to take into account losses due to creep and shrinkage, a fictitious initial stress, lower than the actual one, is defined, so that a pure relaxation curve is used for computing the relaxation losses. The stress relaxation during a time interval is given by the formulation proposed by (Magura, Sozen and C.P 1964), which was calibrated with large number of experimental data.

5.2.4 Solution procedure

5.2.4.1. Initial strain approach

The response of a structure accounting for the time-dependent effects is determined during a time step through the initial strain approach derived by (Zienkiewicz 1977) and also used by (Kabir 1976; Van Greunen 1979; Marí 1984). Load is applied at time t_n and is kept constant along the time step Δt_n, and it is assumed that during the latter the stress state of the structure is constant. At each instant t the total strain vector in a fibre $\underline{\varepsilon}^{t}(t)$ is given by the sum of the mechanical $\underline{\varepsilon}^{m}(t)$ and non-mechanical $\underline{\varepsilon}^{nm}(t)$ strain vectors:

$$\underline{\varepsilon}^{t}(t) = \underline{\varepsilon}^{m}(t) + \underline{\varepsilon}^{nm}(t) \tag{5.25}$$

The non-mechanical strain vector in each fibre is given by the summation of the different contributions due to creep $\underline{\varepsilon}^{c}$, shrinkage $\underline{\varepsilon}^{sh}$ and thermal gradients $\underline{\varepsilon}^{T}$

$$\underline{\varepsilon}^{nm}(t) = \underline{\varepsilon}^{c}(t) + \underline{\varepsilon}^{sh}(t) + \underline{\varepsilon}^{T}(t) \tag{5.26}$$

which in the 2D strain state correspond to

$$\underline{\varepsilon}^{t}(t) = \begin{Bmatrix} \varepsilon_x^t \\ \varepsilon_z^t \\ \gamma_{xz}^t \end{Bmatrix} \quad ; \quad \underline{\varepsilon}^{m}(t) = \begin{Bmatrix} \varepsilon_x^m \\ \varepsilon_z^m \\ \gamma_{xz}^m \end{Bmatrix} \quad ; \quad \underline{\varepsilon}^{nm}(t) = \begin{Bmatrix} \varepsilon_x^{nm} \\ \varepsilon_z^{nm} \\ \gamma_{xz}^{nm} \end{Bmatrix} \tag{5.27}$$

The incremental form of the equivalent nodal force vector in the FE due to non-mechanical strains, $\underline{F}_{elem}^{nm}$, is given by:

$$\underline{\Delta F}_{elem}^{nm} = \int_V B^T D \underline{\Delta \varepsilon}^{nm} dV \tag{5.28}$$

However, according to the proposed model for shear-bending interaction described in Chapter 3, the element equivalent force vector due to non-mechanical strains is computed in incremental form by the following expression, making use of the concept of sectional equivalent force vector increment $\underline{\Delta S}_{sec}^{nm}$:

$$\underline{\Delta F}_{elem}^{nm} = \int B^T \, \underline{\Delta S}_{\sec}^{nm} \, dx \tag{5.29}$$

where B is the FEM transformation matrix (see Eq. (3.41)). The increments of the equivalent load force and of the non-mechanical strain vectors for the 2D case are

$$\underline{\Delta S}_{\sec}^{nm} = \begin{bmatrix} \Delta N \\ \Delta V_z \\ \Delta M_y \end{bmatrix}^{nm} \quad ; \quad \underline{\Delta \varepsilon}^{nm} = \begin{bmatrix} \Delta \varepsilon_x \\ \Delta \gamma_{xz} \\ \Delta \phi_y \end{bmatrix}^{nm} \tag{5.30}$$

In turn, the sectional equivalent force vector due to non-mechanical strains, $\underline{S}_{elem}^{nm}$, which includes concrete and the smeared transversal reinforcement, is determined in incremental form by

$$\underline{\Delta S}_{\sec}^{nm} = \int T^T \, \underline{\Delta S}_{fiber}^{nm} \, dA \tag{5.31}$$

where the transformation matrix T relates the generalized strains in the section with the strains in the fibre as described in Eq. (3.42). In each fibre, as the concrete and stirrups are in equilibrium in the vertical direction, and consequently the resultant vertical stresses are

null, the equivalent internal load vector due to initial strains $\underline{S}_{fibre}^{nm}$ is computed incrementally as

$$\Delta \underline{S}_{fibre}^{nm} = K_{fibre} \Delta \underline{\varepsilon}^{nm}$$
$$\Delta S_{fibre}^{nm} = \begin{pmatrix} \Delta \sigma_x^{nm} \\ \Delta \tau_{xz}^{nm} \end{pmatrix}; K_{fibre} = \begin{bmatrix} D_{11}^* & D_{13}^* \\ D_{31}^* & D_{33}^* \end{bmatrix}; \Delta \underline{\varepsilon}^{nm} = \begin{Bmatrix} \Delta \varepsilon_x^{nm} \\ \Delta \gamma_{xz}^{nm} \end{Bmatrix} \tag{5.32}$$

by means of the condensed constitutive matrix of the fibre, whose terms assume the following values:

$$\begin{bmatrix} D_{11}^* = D_{11} - \dfrac{D_{12} D_{21}}{\overline{\overline{D}}_{22}} & D_{13}^* = D_{13} - \dfrac{D_{12} D_{23}}{\overline{\overline{D}}_{22}} \\ D_{31}^* = D_{31} - \dfrac{D_{32} D_{21}}{\overline{\overline{D}}_{22}} & D_{33}^* = D_{33} - \dfrac{D_{32} D_{23}}{\overline{\overline{D}}_{22}} \end{bmatrix} \tag{5.33}$$

in accordance to the determination of the stiffness matrix of the fibre presented in Eq. (3.35).

The input variables needed to perform the fibre state determination are the mechanical longitudinal strain (see Eq. (3.17)) and the shear stress (Eq. (3.18)) applied in each fibre. In the presence of non-mechanical strains, the input equations are rewritten as:

$$\begin{cases} \Delta \varepsilon_x^t(z) = \Delta \varepsilon_0 + \Delta \phi_y . z \\ \Delta \tau^* = G^* A^* \gamma_0 \end{cases} ; \quad \begin{cases} \varepsilon_x^m(z) = \Delta \varepsilon_x^t - \Delta \varepsilon_x^{nm} \\ \Delta \tau^* = G^* A^* \gamma_0 \end{cases} \tag{5.34}$$

It is to be remarked that in these assumptions non-mechanical strains are taken into account only in the longitudinal direction: in fact, as a consequence of the hypothesis assumed by the shear-bending interaction model, neither the vertical nor the transversal non-mechanical strains are accounted for in this stage.

On the other hand, the output mechanical strains (vertical and distortion) resultants of the fibre state determination (Eq. (3.26) and Eq. (3.27)) are computed as functions of the mechanical longitudinal strain, of the imposed tangential stress and of the current damage state of the fibre as

$$\begin{cases} \varepsilon_z^m = f\left(\varepsilon_x^m, \tau^*, state\right) \\ \gamma_{xz}^m = f\left(\varepsilon_x^m, \tau^*, state\right) \end{cases} \tag{5.35}$$

In this manner, in order to accomplish the total strains the non-mechanical strains are added to the correspondent computed mechanical strains as

$$\begin{cases} \varepsilon_z^t = \varepsilon_z^m + \varepsilon_z^{nm*} \\ \gamma_{xz}^t = \gamma_{xz}^m + \gamma_{xz}^{nm} \end{cases} \tag{5.36}$$

Note that in the z-direction ε_z^{nm*} is not directly given by the non-mechanical strain ε_z^{nm}. Actually, the presence of stirrups in the fibres do not allow for the free deformation of the concrete in the z-direction. In order to take into account the restraining effects to the imposed deformations brought by the presence of stirrups, the equilibrium in the z-direction, originally written in Eq. (3.21), is rewritten for the case of non-mechanical strain as

$$\Delta\sigma_z^c + \rho_{st}\Delta\sigma_z^{st} = D^*\varepsilon_z^{nm} \tag{5.37}$$

or, in terms of strains, as

$$D_c\varepsilon_z + \rho_{st}E_{st}\varepsilon_z = D^*\varepsilon_z^{nm} \tag{5.38}$$

resulting into the following expression for the non-mechanical strains in the vertical direction, including the restraining effects of the stirrups in the fibre:

$$\varepsilon_z^{nm*} = \frac{D_c}{D_c + \rho_{st}E_{st}}\varepsilon_z^{nm} = \frac{1}{1+n\rho_{st}}\varepsilon_z^{nm} \quad with \;\; n = \frac{E_{st}}{D_c} \tag{5.39}$$

The stiffness of concrete present in this expression (D_c) corresponds to the element D_{22} of the stiffness matrix of the concrete fibre determined in Eq. (3.19), and E_{st} and ρ_{st} correspond to the Young's modulus and the volume ratio of the transversal steel.

5.2.4.2. Finite element implementation

In order to compute the time-dependent response of structures the period of analysis is divided into time steps, and the non-mechanical strains are continuously updated. In terms of strains, a step-forward integration scheme in the time domain is performed by continuously adding the results obtained at each previous time step. In its turn, the response of a structure during a time step is determined through the initial strain approach previously described.

The general modular format of the numerical solution procedure available in the model for performing time-dependent analysis is presented in the flowchart of Figure 5.1. It is worth mentioning that this flowchart is an extension of the analogous one previously showed in Chapter 3, Figure 3.8, for the case of the fibre beam model for shear-bending interaction, by adding the loop correspondent to the time step analysis.

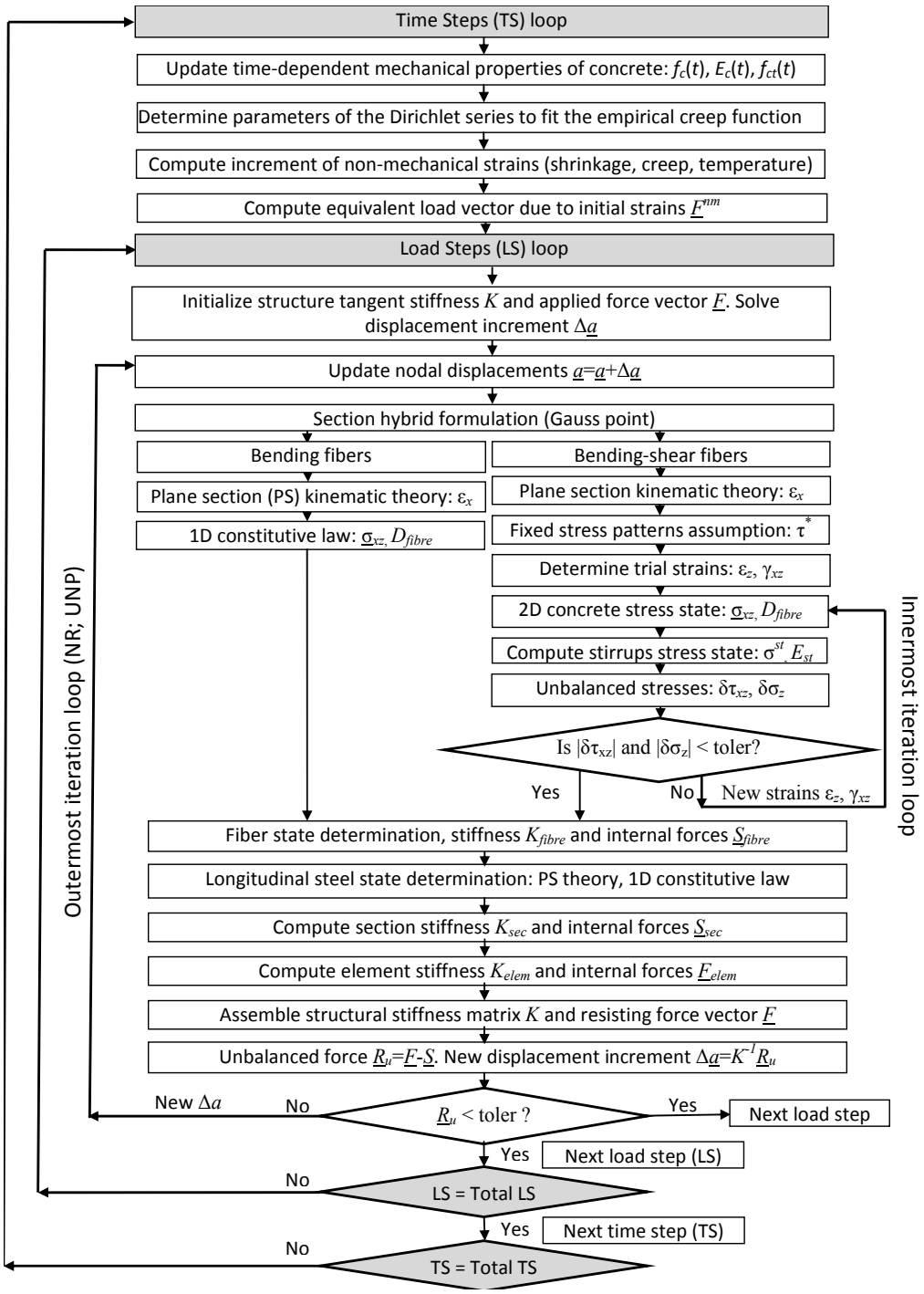

Figure 5.1 – Flowchart of the proposed model for time-dependent analysis

Accordingly, the increment of non-mechanical strains $\Delta\underline{\varepsilon}^{nm}$ that occurs during the time interval Δt_n is given by the summation of the different contributions (creep $\underline{\varepsilon}^{c}$, shrinkage $\underline{\varepsilon}^{sh}$ and thermal gradients $\underline{\varepsilon}^{T}$). Then, the equivalent nodal force vector in the element due to the non-mechanical strains $\underline{F}_{elem}{}^{nm}$ is determined in incremental form. Afterwards, this load vector is assembled into the structural equivalent load vector and, in case it exists, the relaxation load vector of prestressing steel is added. Load is then applied at time t_n and then is kept constant for the time step Δt_n. Then the resultant nodal displacement increments and the strain increments in the sections are determined. The fibre state determination is afterwards performed. Subsequently, the determination of the current internal loads is made, and convergence is checked. The residual forces are computed and the correspondent structural displacements are updated within the Newton-Raphson iteration loop. Once convergence is accomplished, the analysis proceeds to the next time step and continues until the last time step is reached.

5.3 Validation of the model for time-dependent analyses

5.3.1 Overview

In contrast to the case of bending, experimental campaigns focused on shear-related time-dependent response of RC frames are not profuse in the scientific literature. Therefore, firstly the validation of the model is carried out through the simulation of a bending creep benchmark: the partially prestressed flexural beams tested under sustained load by (Espion and Halleux 1991). In this example, due to the relatively low cracking level and non-existence of diagonal cracks, the importance of shear in the analysis is expected to be rather irrelevant. Even though, this validation is important to ensure that the enlargement of the time-dependent model from the 1D to the 2D case was successfully accomplished.

Subsequently, experimental tests focused on the shear related influence on the long-term deflection of beams carried out by (Nie and Cai 2000) are simulated. The tested specimens were pre-cracked with diagonal cracks and submitted to sustained load. The importance of considering shear effects in the time-dependent analysis of these beams should be of great importance. However, to the author's knowledge, there is no other experimental campaign focused on shear related creep parameters and the measurement of the influence of distortion on the long-term deflection of the beams was not performed.

5.3.2 Partially prestressed flexural beams

A series of partially prestressed concrete beams were tested in the University of Brussels between 1981 and 1986 by (Espion and Halleux 1991). These tests are a recognized benchmark (Espion 1993) usually used to validate FE models for the time-dependent behaviour of RC beams (Cruz 1994; Ferraz 2010). The experimental tests were composed by simple supported beams with 8.0m of span and rectangular cross-sections, differing on the quantity of passive reinforcement, prestressing forces applied and load history. The beams had no transversal reinforcement. The tests were performed with constant load during 4.5 years.

From the experimental campaign two beams (LT05Q and LT08Q) with phased load levels were simulated with the proposed model, in order to determine their deflections along time. The geometric characteristics and reinforcement of the beams are reproduced in Figure 5.2, and the material properties are indicated in Table 5.1. A prestress force of 1228kN per tendon was applied by post-tension at the age of 14 days in one of the extremities. The prestress tendons of beam LT05Q have a linear variation with an inclination of 3.2º with the horizontal between the load points and the supports, and the ones of beam LT08Q have constant eccentricities. Besides the dead load, the beams were submitted to two concentred loads Q at different time stages, as presented in the Table 5.2.

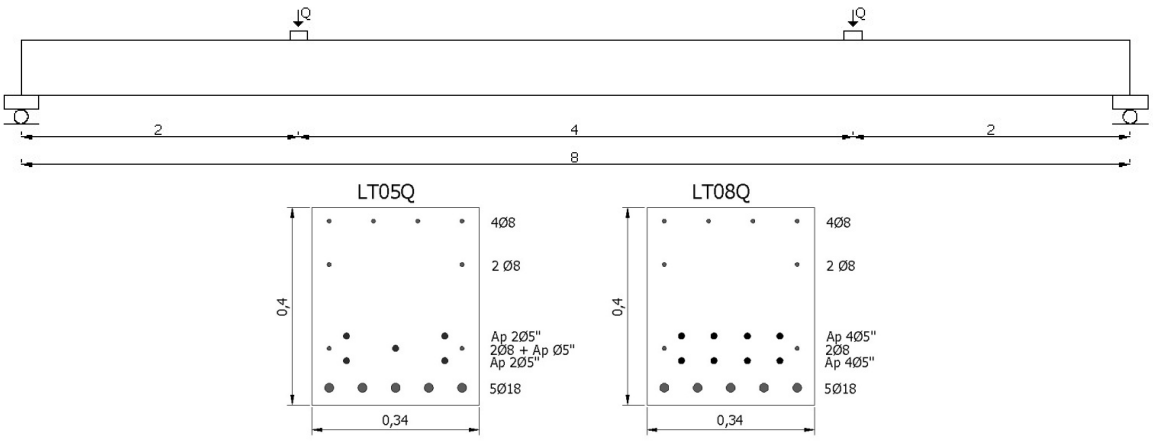

Figure 5.2 – Characteristics of the experimental test of Espion and Halleux: structural scheme, geometry and reinforcement

Table 5.1 Material properties of the Espion and Halleux beams

Tests	Concrete	Steel Active reinforcement	Steel Passive reinforcement
LT05Q	f_c = 33.9 MPa f_{ct} = 3.0 MPa E_c = 30.75 GPa ε_{cu} = 3.5×10^{-3}	f_{sy} = 1715 MPa f_{su}= 1892MPa E_s = 200 GPa	f_{sy} = 500 MPa E_s = 200 GPa
LT08Q	f_c= 34.9 MPa f_{ct} = 3.0 MPa E_c = 31.04 GPa ε_{cu} = 3.5×10^{-3}		

Table 5.2 Loading history of the Espion and Halleux beam tests

Tests	Time (days)	Dead weight (kN/m)	Q (kN)
LT05Q	0 < *t* < 14	0	0
	14 < *t* < 28	3.332	0
	28 < *t* < 84	0	16.5
	84 < *t* < 1642	0	63.75
LT08Q	0 < *t* < 14	0	0
	14 < *t* < 28	3.332	0
	28 < *t* < 85	0	16.5
	85 < *t* < 1642	0	63.75

Pertaining to the numerical model, the FE mesh used for the simulation of these beams are presented in Figure 5.3. A simulation with the basic model CONS was also carried out with the same mesh.

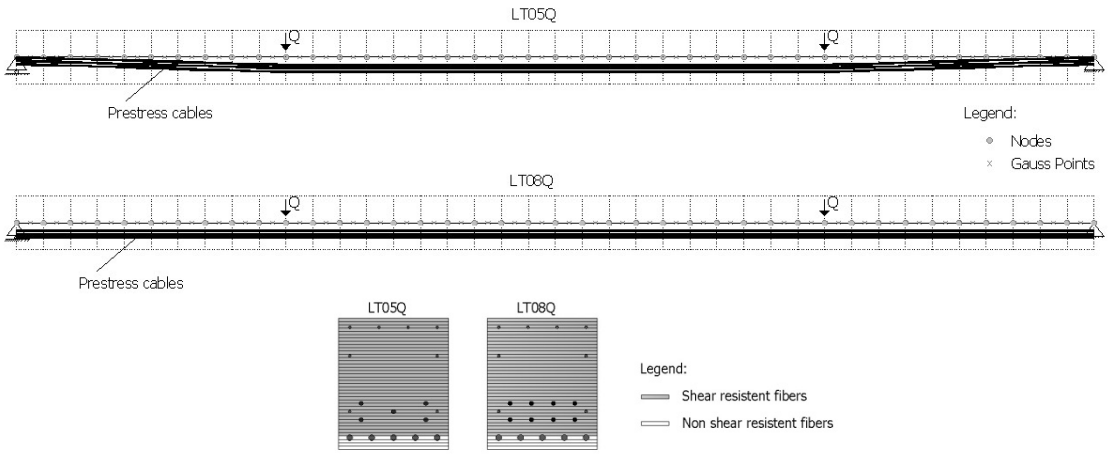

Figure 5.3 – Model of the beam tests by Espion and Halleux

Appearance of cracking on both beams when submitted to 63.75kN was reported (Espion 1993). The crack patterns predicted by the proposed model after the application of the second load phase are represented in Figure 5.4, in which only vertical flexural cracks

appear, being consistent with the experimental observation. Also, as expected, the lesser prestressed beam LT5Q presents more extensive cracking than beam LT8Q.

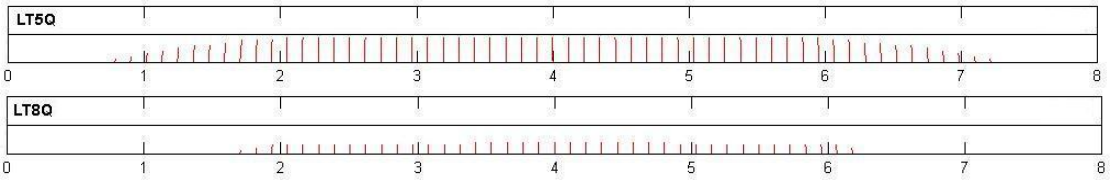

Figure 5.4 – Predicted crack patterns for the Espion beams after application of Q=63.75kN

The time-dependent responses of the beams under the two-phase load levels are depicted in Figure 5.5, along with the numerical predictions of the proposed shear model and the flexural basic model (CONS). The results computed by other flexural fibre beam models (Cruz 1994; Ferraz 2010) are also included. For both beams, and before the application of the second load increment at the age of 85 days, the proposed model predicts the experimentally observed behaviours quite accurately. Afterwards, the difference between the experimental and the computed results increases, as also observed with the other numerical model predictions. Even though, as the beams presented cracking at this stage, the smeared crack approach and the nonlinear constitutive equations for concrete allow the proposed model to provide good predictions of the experimental observations, in comparison to the other models. The computation based on the linear constitutive equations (Ferraz 2010) is the one that deviates more from the measured response.

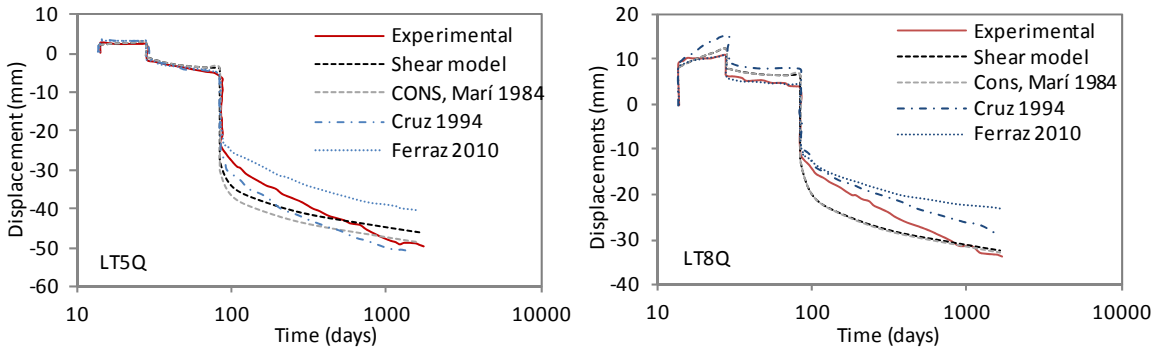

Figure 5.5 – Time-dependent deflection of the Espion and Halleux beams: a) LT5Q and b) LT8Q

Unsurprisingly, shear effects are of small importance in these creep tests, as the predictions computed by the shear model are similar to the ones from the flexural model. It can be noticed that the larger differences between the two numerical models are observed in the less prestressed beam LT05Q, which presented earlier and more extensive cracking. In this case, less creep deflection is predicted by the shear model in comparison with the flexural

model. This is due to the fact that the presence of shear forces diminishes the compression stresses in the uncracked top area of the cross section for the same applied bending moment. As the creep deflection of the beam is mainly dependent on the compression stresses, the shear model predicts less time-dependent displacements for cracked cross-sections than the flexural model. This aspect will be addressed latter in this chapter (in Section 5.4.2).

5.3.3 Beams with diagonal cracking

Experimental creep tests on diagonally pre-cracked beams under sustained load were performed by (Nie and Cai 2000). The goal of this experimental campaign was to assess the contribution of shear to the long-term deflection of RC beams. For this reason, the specimens were designed to develop both flexural and diagonal cracking. Also, in order to determine the load level to apply in the creep tests that ensured significant diagonal cracking, previous short-term loading tests on analogous beams were carried out. By these means, the sustained load was chosen so as to cause diagonal cracking with widths of circa 0.2-0.3mm in the specimens. The geometry, reinforcement and other details of the simple supported beams are presented in Figure 5.6. The beams were tested under two-point loading with a shear span ratio of 2.5. From all the specimens tested, the ones with vertical transversal reinforcement were considered for simulation, whose characteristics are detailed in Table 5.3. The analyzed beams distinguished from each other in the ratios of longitudinal ρ_{sl} and transversal ρ_{st} reinforcement and in the concrete strength $f_c^{'}$. The duration of the long-term tests were of 3 months, and only mid-span deflection data is available. The general information about the applied loads, correspondent diagonal crack widths and deflections are resumed in Table 5.4.

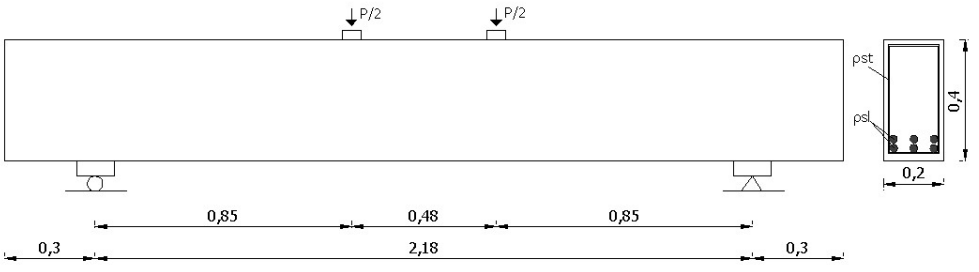

Figure 5.6 – Geometry and scheme of the beam tests by Nie and Cai

Table 5.3 Reinforcement and material characteristics of the Nie and Cai beam tests

Beam	Longitudinal reinforcement ratio ρ_{sl} (%)	Transversal reinforcement	Stirrups ratio ρ_{st} (%)	Longitudinal steel f_{sy} (MPa)	Transversal steel f_{sy} (MPa)	Concrete f'_c (MPa)
B1	2.5	Ø8//200	0.25	462	293	38
B2	3.4	Ø8//200	0.25	462	293	38
B3	2.5	Ø8//100	0.50	462	293	38
B5	2.5	Ø8//100	0.50	462	293	41
B6	2.5	Ø8//100	0.50	462	293	41

Table 5.4 Experimental information on the Nie and Cai beam tests

Beam	Sustained load (kN)	Initial diagonal crack width (mm)	Initial deflection at mid-span (mm)	Deflection increment after 90 days (mm)
B1	220	0.2	2.9	2.0
B2	210	0.2	3.0	1.7
B3	220	0.2	2.4	2.1
B5	220	0.2	2.5	1.8
B6	260	0.3	3.1	1.5

The experimental tests were simulated with the proposed shear model and with the flexural basic model. The mesh used in both numerical models is presented in Figure 5.7, and the reinforcement ratios and material properties considered are presented in Table 5.3. Firstly, the predicted crack patterns by the shear model after the application of the instantaneous load are represented in Figure 5.8 for the specimens B1 and B6. Despite of the unavailability of experimental observations of the crack patterns, the predictions agree with reported evidence of significant diagonal cracking.

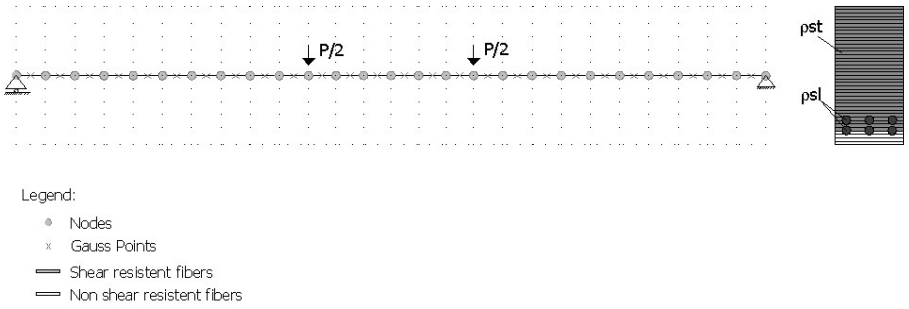

Figure 5.7 – Model of the beam tests by Nie and Cai

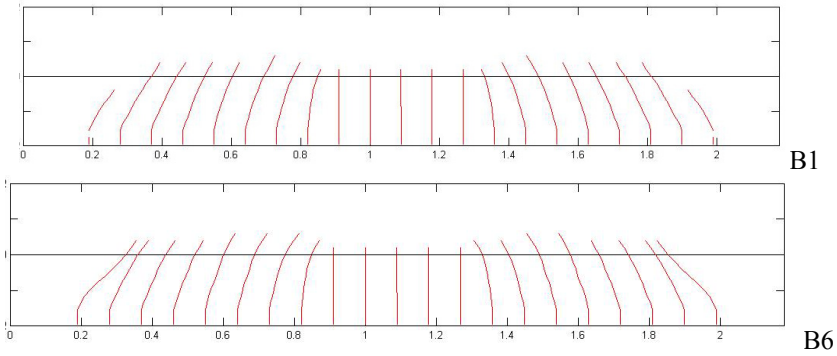

Figure 5.8 – Predicted cracking patterns of beams B1 and B6 after application of the sustained loads

The experimental deflections at mid-span with time for all the analysed beams are depicted in Figure 5.9*a*, along with the predictions from the shear and the flexural models. In a general view, the instantaneous deflection is well predicted by the shear model, in contrast to the systematic lesser deflection computed by the flexural model. This difference evidences the significant importance of shear in the behaviour of these specimens. The exception to these remarks is beam B2, were the predictions of the proposed model differ significantly from the measured response. In fact, this specimen presented rather unexpected results, as it can be straightforwardly observed in Table 5.4: it has more longitudinal reinforcement, the same material properties and less sustained load than specimen B1, however the instantaneous deflection is comparatively higher. Diversely, and as expected, the numerical models predict lesser instantaneous deflection for beam B2 than for beam B1.

Regarding the long-term response, even though the numerical analyses systematically predict lower deflection in comparison to the experimental data, in a general manner the proposed model gave acceptable predictions, as it can be observed in Figure 5.9*a*. Pertaining to the shear model, the contributions of bending and shear to the total long-term deflection of the beam are represented in the graphics of Figure 5.9*b*. In general, it is observed that distortion only plays a significant role in the instantaneous deflection, being almost insignificant in the long-term phase.

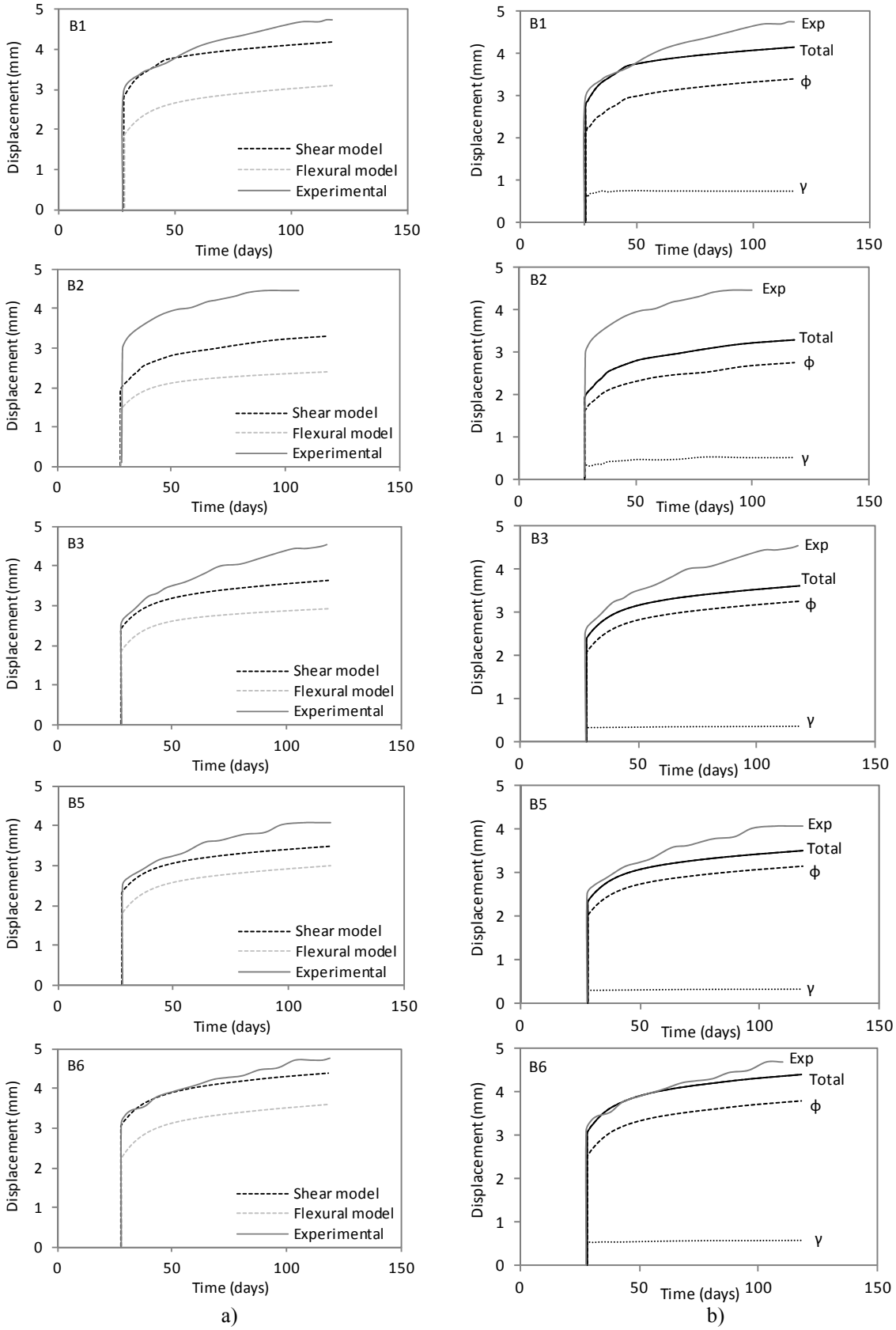

Figure 5.9 – Deflection at mid span vs. time: a) computed results and experimental data and b) predicted contributions of shear and bending by the proposed shear model

As the magnitude of shear effects was not explicitly measured in this experimental campaign, key aspects of the validation of the model are left incomplete. In fact, measuring the time-dependent development of transversal strains in concrete and axial strains in the stirrups in RC elements with significant diagonal crack is aimed to be accomplished in future works. Despite of the limitations of this shear related validation, the capacity of the proposed model to perform numerical analysis on time-dependent response on shear critical elements was demonstrated and will be further explored in the parametric studies to be presented in the following.

Pertaining to the linear creep assumption, the stress levels for which this approximation is considered to lose validity (for 1D cases) were not achieved. The distribution of principal compression stresses in concrete after the application of the instantaneous load in beams B1 and B6 is presented in Figure 5.10. It can be observed that the stresses in the concrete struts do not exceed 45% of the compressive strength (the threshold for validity of the linear creep assumption), which corresponds to 17MPa for the specimen B1 and 19MPa for the specimen B6.

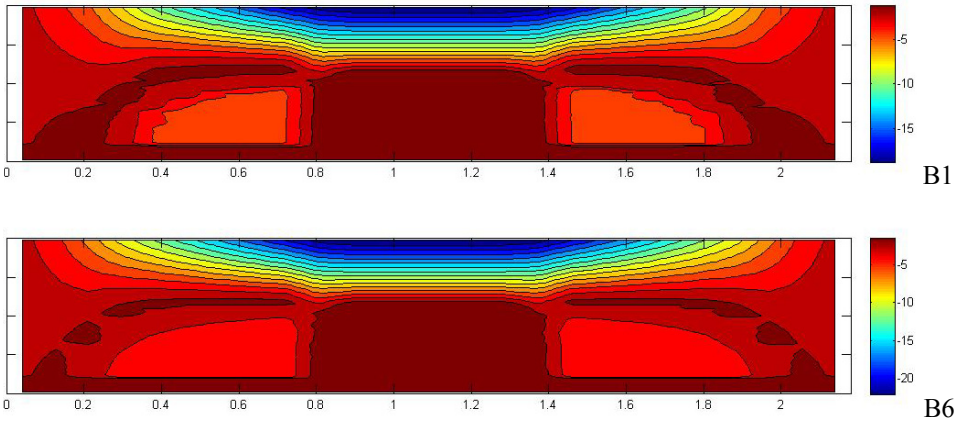

Figure 5.10 – Computed principal compression stresses in concrete for beams B1 and B6 after application of the instantaneous load (MPa)

5.4 Parametric studies

5.4.1 Overview

The analyses to be presented henceforward, which aim to check the influence of shear-related characteristics on the time-dependent performance of RC frames, are purely

numerical. By these means, the classical shear beam test VSA1 (Vecchio and Shim 2004), submitted to an instantaneous incremental load until failure at the age of 38 days - simulated with the proposed model in Section 3.3.3 - is used as the reference example in this section.

These numerical studies include two different approaches: (*i*) to determine the influence of shear in the late deflection and load capacity of a beam after long-time creep deformation, and (*ii*) to evaluate the effects of restrained shrinkage in the ultimate resistance of a shear critical beam. This study is a continuation of the one presented in the Section 4.3 (concerning the influence of restraint in the shear capacity of a beam in a frame) by including the effects of a previous stress state due to shrinkage.

The modelling strategy used in Chapter 3 for validation of the fibre beam formulation with inclusion of shear effects is considered in the present numerical studies, assuming the same geometry and reinforcement characteristics (Figure 3.23), material properties (Table 3.2) and mesh discretization (Figure 3.24).

5.4.2 Time-dependent performance of shear-critical beams

The simple supported beam VSA1 was loaded at 40% of the ultimate load (P_u=460kN) at the age of 38 days, and this load remained until the age of 10000 days, as summarily presented in Table 5.5. The response of the beam under sustained load was determined with both the basic and the proposed models, in order to determine the importance of considering shear effects in this type of analysis.

The global responses predicted by both fibre beam models are presented in Figure 5.11*a*, through the deflections computed along the beam for the ages of 38 and 10000 days. By comparing the results of the two models it is noticed that the shear model predicts higher instantaneous and long-term deflections after creep deformation. According to Figure 5.11*b*, which reproduces only the time-dependent deflections, both models give fairly similar predictions of the beam vertical displacements due to creep. Even though the final long-term deflection takes higher values in the prediction by the shear model, this is only due to the higher instantaneous deflection. In fact, in the long-term the shear model gives a slight less deflection due to creep than the flexural model. This is better observed in the force-displacement curves of Figure 5.12, where the instantaneous deflection predicted by the shear model is much higher, and the time-dependent deformation slightly decreases.

The same conclusions can be drawn from the graphics of Figure 5.13, where the mid-span deflections are represented as function of time. The shear model predicts higher deflections in comparison with the flexural model (Figure 5.13*a*), however, the time-dependent deflection due to creep are similarly predicted by both models (Figure 5.13*b*), with slight lesser values attributed to the shear model.

Table 5.5 Loading history

Time (days)	P (kN)
t<38	0
38<t<10000	185 (0.4P_u)

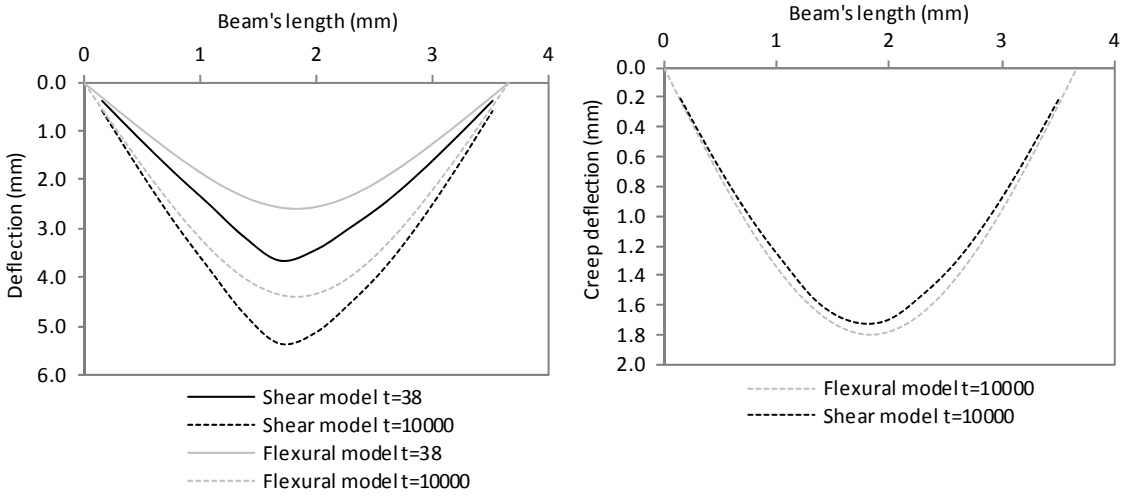

a) b)

Figure 5.11 – Vertical deflections along the beam under sustained load: a) total deflection for t=38 and t=10000 days and b) time-dependent deflection after t=10000days

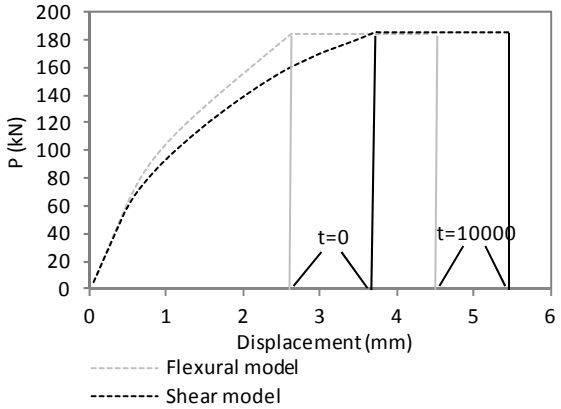

Figure 5.12 – Load vs. mid-span displacements

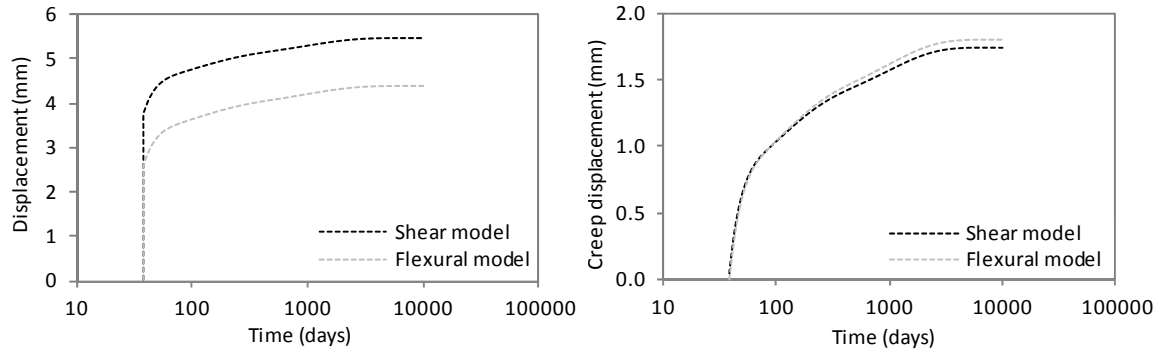

Figure 5.13 – Displacements at mid-span vs. time: a) total displacement and b) time-dependent portion of creep deflection

The instantaneous and long-term deflections of the beams predicted by the shear and flexural models are compared in Table 5.6. Although the instantaneous deflection computed by the shear model is higher than the one computed by the flexural model, the time-dependent deflection is reduced when shear effects accounted for. The lesser deflection due to creep predicted by the shear model is related to the decrease of the compression stresses in the uncracked top are of the cross section in the presence of shear forces. This aspect can be observed in Figure 5.14, in which the longitudinal stresses in concrete along the quarter-span section after the application of load (t=38days) are depicted for the shear and flexural models.

Table 5.6 Deflections at mid-span (mm)

Deflections	Shear model	Flexural model
Total instantaneous t=38	3.70	2.61
Total Long-term t=10000	5.45	4.41
Increment due to creep	1.75	1.80

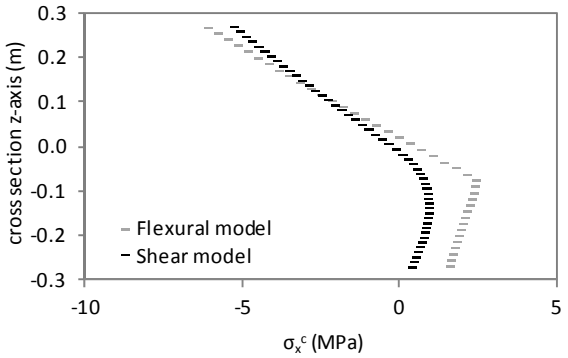

Figure 5.14 – Stresses in concrete computed in the quarter-span section after application of the load (t=38days)

Subsequently, it is intended to determine the magnitude of the contributions of bending and shear related strains on the time-dependent response of the beam due to creep. To accomplish this, in Figure 5.15 the total displacement of the beam predicted by the proposed shear model is depicted along with the fractions of displacements due to the bending curvature ϕ and to the deformation due to shear distortion γ. The prediction of the pure flexural model is also included in these graphics for comparison. In Figure 5.15*a* the total long-term deflection is represented, whilst in Figure 5.15*b* only the time-dependent creep part of the displacement is depicted. The few influence of the distortion on the long-term deflection of the beam is observed, as the creep deflection of the beam is highly dominated by the flexure mechanism. It is also remarkable that the fraction of total displacement due to bending curvature predicted by the shear model is very similar to the results provided by the flexural model. Again in Figure 5.15b it is observed the decrease of creep displacement when shear is taken into account.

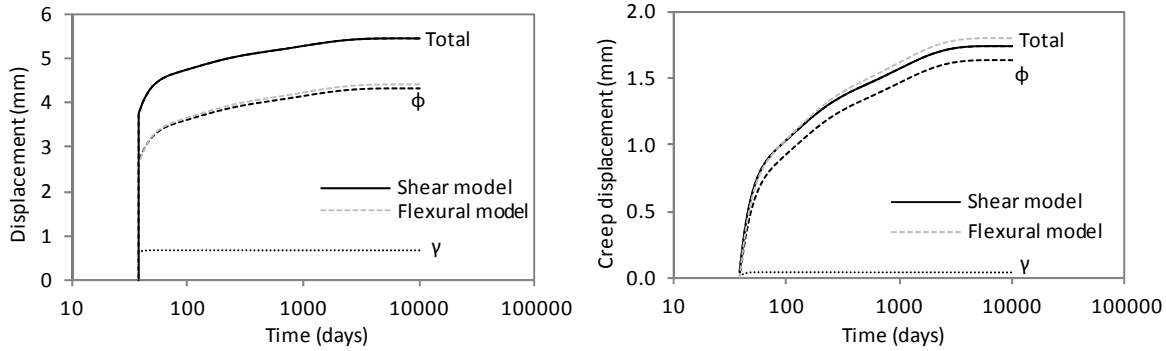

a) b)

Figure 5.15 – Displacements at mid-span vs time (contributions of bending and shear curvatures): a) total displacement and b) time-dependent deflection

Regarding the stress state in the longitudinal reinforcement, the development of stresses under the applied load computed by both models is depicted in Figure 5.16. The increment of stresses in the longitudinal reinforcement due to the consideration of the "tension-shift" effect in the proposed model, which was already discussed in Chapter 3, is extensively observed with the application of the instantaneous load. Furthermore, as time goes by the effects of creep in the increment of stresses in the longitudinal reinforcement are less pronounced when shear effects are considered, than when they are not. By these means, as it is perfectly observable in Figure 5.17*a*, the predicted long-term total stress in the longitudinal reinforcement with the shear model is higher than with the flexural one. However, according to Figure 5.17*b* this difference is only due to the instantaneous load,

as its time-dependent response gives less increment of stresses in steel due to creep than the flexural model.

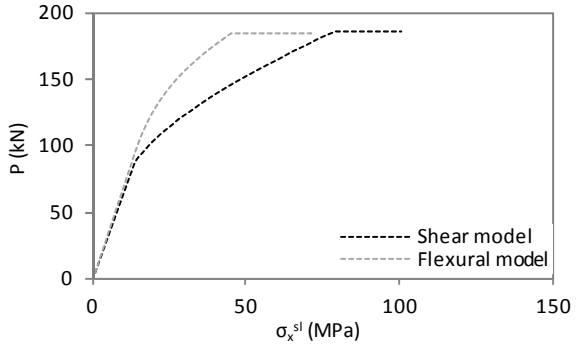

Figure 5.16 – Applied load vs. stresses in the longitudinal reinforcement at the shear-span

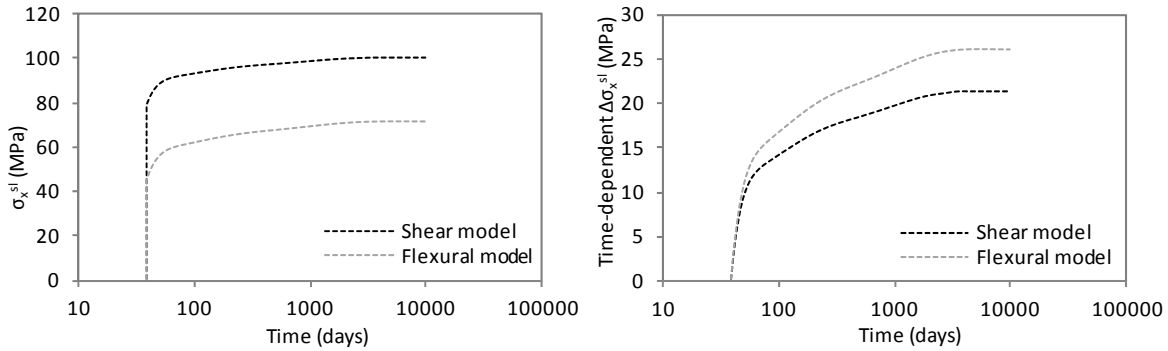

a) b)

Figure 5.17 – Axial stresses in the longitudinal reinforcement at shear-span vs. time: a) total stresses and b) increment of stresses due to creep

The stresses in the transversal reinforcement computed by the proposed shear model are depicted in Figure 5.18 for a fibre in the bottom part of the cross-section located in the shear span. It is observed that for the applied load the stirrups were activated but reached very low stress levels (approximately 7MPa). Afterwards, the stresses in the stirrups presented a slight diminution with time (approximately 1MPa). The paradigmatic issue in these results is that at the fibre level, due to equilibrium requirements in the vertical direction, the vertical strains in concrete and reinforcement are of tensile nature, but the stresses in concrete are of compression. In this manner, when a crack appears the transversal reinforcement has strains and stresses applied with the same signal (tension), but concrete has strains and stresses with opposite signs. So, if relaxation of the concrete fibre occurs due to compressive creep, owing to the equilibrium requirements the stirrups in the fibre also experience relaxation. The validity of these results lacks experimental validation, which is, an interesting object for future work.

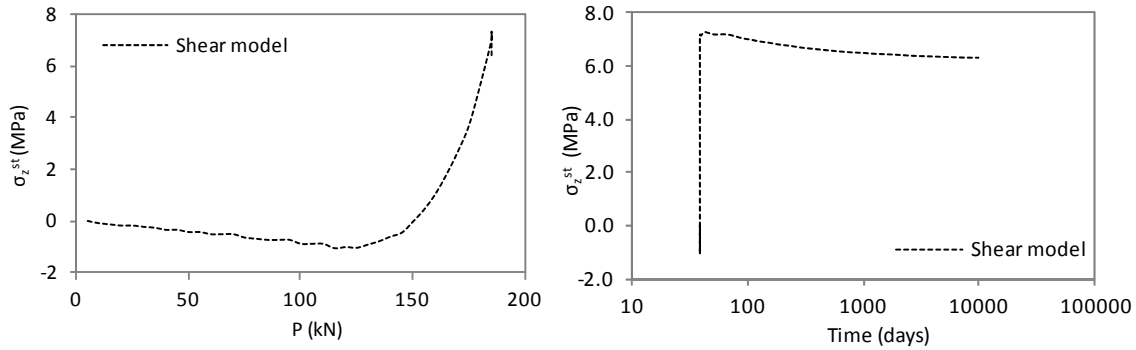

a) b)

Figure 5.18 – Axial stresses in the transversal reinforcement on the shear-span: a) with load and b) with time

After being under sustained load for 10000 days, the beam is now loaded incrementally until failure. By these means, it is aimed to determine the effects of shear in the ultimate resistance of the beam after long-term deformation due to creep. The loading history of this analysis is presented in Table 5.7. The responses of the beam after creep deformation computed by the flexural and shear models are represented in Figure 5.19. Regarding these graphics, as expected, no relevant difference in the ultimate load capacity of the beam after long-term creep was predicted to occur, which must be related to the low influence of the second-order effects in this element.

Table 5.7 Loading history

Time (days)	P (kN)
t<38	0
38<t<10000	185
t>10000	Load until failure P_u

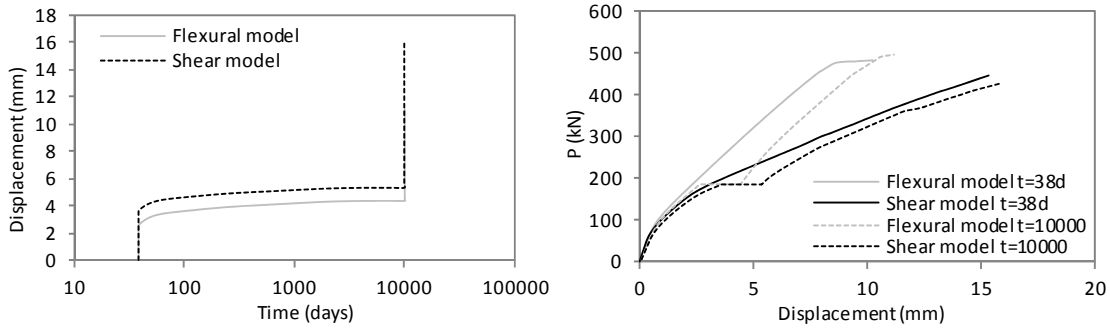

a) b)

Figure 5.19 – Results of the beam loaded until failure after creep deformation: a) displacement-time curves and b) force-displacement curves

5.4.3 Response of shear critical beams after restraint shrinkage

The stress state resultant from the restraint of shrinkage strains in concrete can influence the later response of beams. In this manner, as the proposed model is able to perform time-dependent analysis with the influence of shear effects in the resistant mechanism of RC elements, this section aims to evaluate the effects of shrinkage restrained strains on the ultimate resistance of shear critical beams.

The parametric study considered in the Section 4.3 for the instantaneous analysis of the load carrying capacity of shear critical beams belonging to frames is analysed again, but now including the effects of long-term concrete shrinkage and creep, prior to applying the external load until failure. By comparing both analyses for different restraint levels - the instantaneous short-term test and the tests after long-term shrinkage - it is possible to assess the influence of the offset time-dependent strains in the later response of shear critical beams belonging to frames.

Accordingly, the same mesh and material properties of the numerical model presented in the Section 3.3.3 (Figure 3.24 and Table 3.2, respectively) are assumed for the present study. Moreover, the same frame scheme and restraint levels brought by the elastic supports that represent the columns previously considered in Figure 4.8 are also assumed here. The single variation in the present analysis is that, before the application of load until reaching failure, the beam is considered under the effects of shrinkage and creep for 10000 days. During this time the beam is only subjected to dead load and creep is related to the stress state generate by shrinkage. By these means, the time step-by-step procedure available in the proposed model computes the time-dependent strain and stress states in the beam before the application of the external load. As the flexural basis model was already concluded to be inappropriate for the analysis of beams with important shear stresses, this parametric study will be carried out only by the proposed shear model. Thus, after the 10000 days of shrinkage and creep acting on the frame, the beam is incrementally loaded until failure.

The variables considered in the parametric study are presented in Table 5.8 along with the results of the load tests: the short-term one at the age 38 days and the late age load test performed at 10000 days. The ultimate failure load (P_u) computed by both analyses (short-term and late age load test) are depicted in Figure 5.20*a* as function of the axial restraint stiffness K_x and in Figure 5.20*b* as function of the rotational restraint stiffness $K_{\theta y}$ of the columns. It is observed that the offset strains brought by the long-term restraint shrinkage

affect the ultimate shear resistance of the beam, decreasing the failure load. This decrease is noticed in the Figure 5.21, where the ratio between the ultimate loads of the late age (long-term $P_{u,\infty}$) and the early age (short-term $P_{u,0}$) tests are depicted as function of the axial (Figure 5.21*a*) and rotational (Figure 5.21*b*) restraints. In fact, in a general way the long-term load carrying capacity of the beam decreased an average of 11.3% in relation to the short-term load test. A tendency for larger decreases of the ultimate load under higher levels of restraint is observed. In fact, for the limit situation of double end-fixed beam (VSA1_0) the decrease on the ultimate load was of 135kN, which corresponds to a 21.1% loss in the load carrying capacity of the late age test in relation to the correspondent test performed at early age.

Table 5.8 Summary of the variables considered in the parametric study and the results correspondent to the ultimate response of the shear-critical beam VSA1

Beam in frame	Columns				Supports		Short-term failure t=28 days			Long-term failure t=10000 days		
	L (m)	h (m)	*b* (m)	*E* (MPa)	K_x (kN/m)	$K_{\theta y}$ (kNm)	Failure mode	$P_{u,0}$ (kN)	$\delta_{u,0}$ (mm)	Failure mode	$P_{u,\infty}$ (kN)	$\delta_{u,\infty}$ (mm)
VSA1	0	0	0	0	0	0	Shear	444.8	15.3	Shear	464.0	16.1
VSA1_0	∞	∞	∞	∞	∞	∞	Shear	653.0	3.7	Shear	515.0	3.7
VSA1_1	3	0.3	0.3	30	13500	27000	Shear	470.0	7.9	Shear	442.0	8.3
VSA1_2	3	0.4	0.3	30	32000	64000	Shear	552.4	9.0	Shear	490.0	8.5
VSA1_3	3	0.5	0.3	30	62500	125000	Shear	580.7	8.8	Shear	540.0	8.8
VSA1_4	4	0.3	0.3	30	7594	20250	Shear	490.7	8.6	Shear	442.0	8.2
VSA1_5	4	0.4	0.3	30	18000	48000	Shear	577.6	10.0	Shear	450.0	8.1
VSA1_6	4	0.5	0.3	30	35156	93750	Shear	575.7	9.1	Shear	510.0	8.7
VSA1_7	3	0.3	0.3	35	15750	31500	Shear	481.9	7.8	Shear	470.0	8.4
VSA1_8	3	0.4	0.3	35	37333	74667	Shear	581.3	9.3	Shear	505.0	8.7
VSA1_9	3	0.5	0.3	35	72917	145833	Shear	580.0	8.5	Shear	548.0	8.8
VSA1_10	4	0.3	0.3	35	8859	23625	Shear	532.4	9.4	Shear	387.0	7.4
VSA1_11	4	0.4	0.3	35	21000	56000	Shear	456.9	7.2	Shear	441.0	7.7
VSA1_12	4	0.5	0.3	35	41016	109375	Shear	561.7	8.7	Shear	530.0	8.9

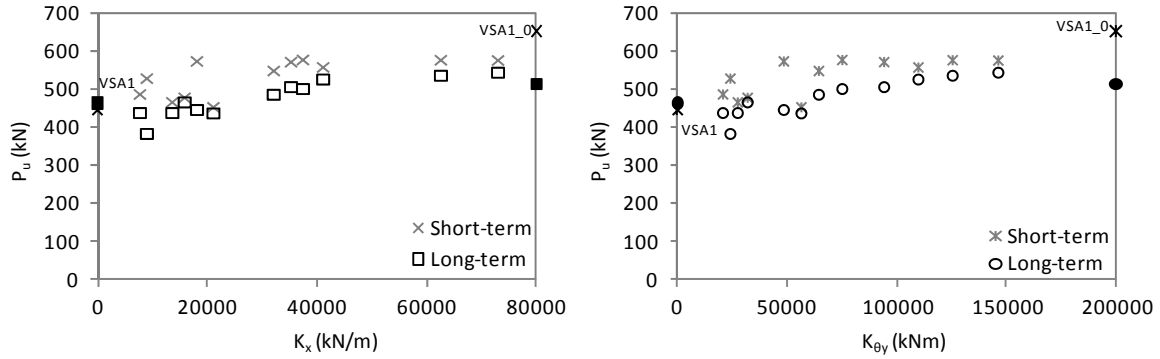

Figure 5.20 – Ultimate load of the beam vs. level of restraint of the columns for the long-term and short-term analysis: a) longitudinal stiffness and b) rotational stiffness

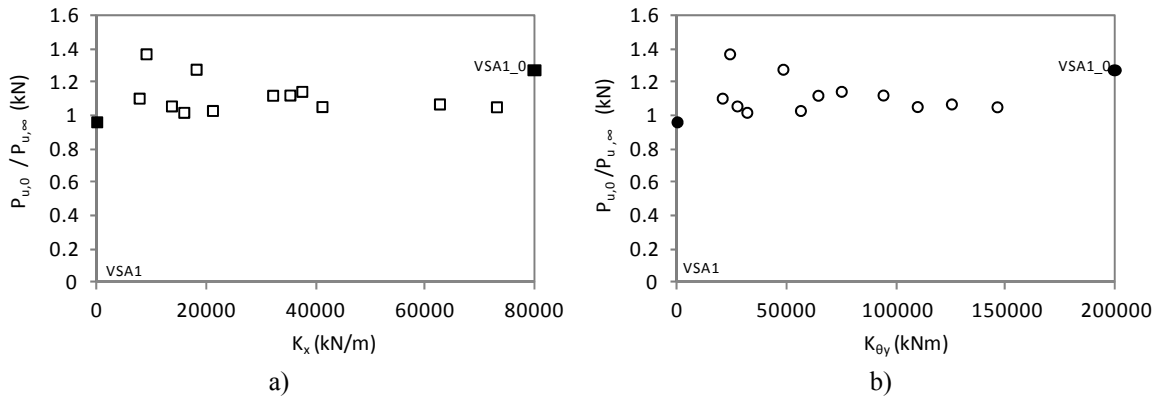

Figure 5.21 – Ratio of the ultimate load of the beam for the long-term and short-term analysis vs. level of restraint of the columns: a) longitudinal stiffness and b) rotational stiffness

Concerning the prediction of the level of damage in the beams caused by the time dependent shrinkage, the crack patterns computed by the model at the age of 10000 days are depicted in Figure 5.22 for two extreme situations: the simple supported beam (VSA1) and double end-fixed beam (VSA1_0). The restraint strains caused by the effects of shrinkage were enough to cause vast cracking to beam VSA1_0. Nevertheless, vast cracking was only predicted in this extreme situation; in the intermediate levels of restraint no relevant cracking was predicted. Even tough, the restraint of the shrinkage strains induces initial stresses in the beam that influence its later load carrying capacity, which was captured by the numerical model.

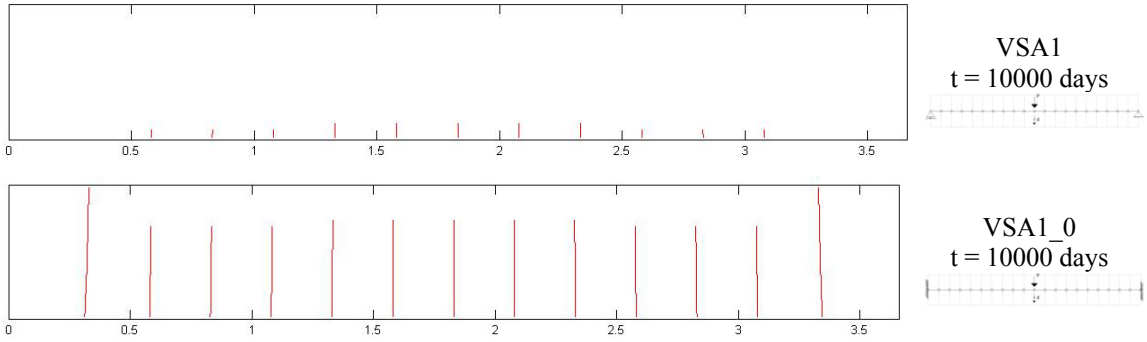

Figure 5.22 – Crack patterns after 10000 days of shrinkage and creep

The initial tensile strain caused by the restraint shrinkage diminishes the concrete contribution to the shear resistance and causes a sooner activation of the transversal reinforcement. This can be observed in Figure 5.23 for the simple supported (VSA1) and double end-fixed (VSA1_0) beams, were the stresses in the transversal reinforcement σ_z^{st} at the mid-shear span are depicted as function of the applied shear force V for the cases of short-term and late age (long-term) test. As the beams fail in shear by failure of the transversal reinforcement, when stirrups start to be loaded for lower shear forces they also reach a lower ultimate load. In this manner, the initial stresses caused by restrained shrinkage strains influence the shear resistance of beams with tensile shear failure. This effect of the previous cracking or tensile strain state in concrete on the concrete contribution to shear resistance and on the ultimate shear resistance of beams was experimentally found in (Sato and Kawakane 2008) for the case of the early age shrinkage and in (Fernandez 2011) for the case of shear-critical beams under tensile stresses.

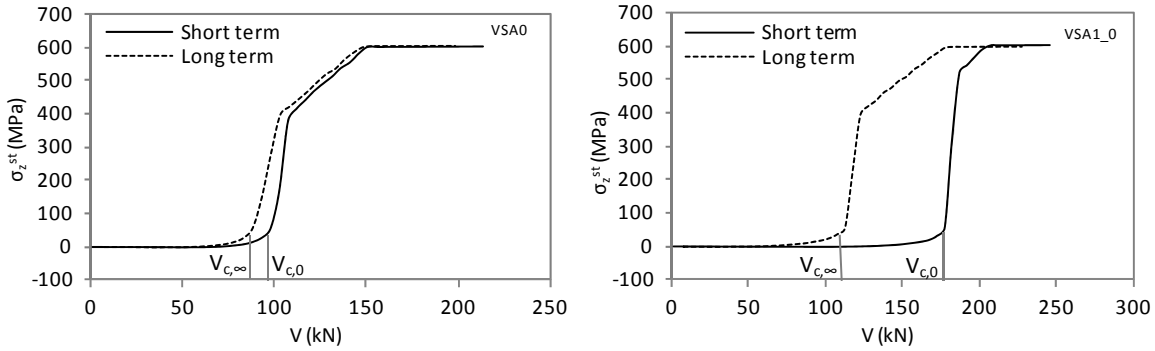

Figure 5.23 – Stresses in the transversal reinforcement in the mid-shear span vs. shear force: a) simple supported beam and b) double end-fixed beam

In Figure 5.24 the concrete contribution to shear resistance V_c, determined approximately as the load correspondent to the activation of the stirrups at the mid-shear span section (see

Figure 5.23) is depicted for the various levels of restrain and for the short-term ($V_{c,0}$) and long-term ($V_{c,\infty}$) cases. In Figure 5.25, the ratio between the concrete contribution to shear resistance for the short-term and long-term test ($V_{c,}0/Vc_{,\infty}$) are presented. Later age tests after restrained shrinkage present lower values for the contribution of concrete to shear resistance, and the ratio between the values correspondent to the short and long-term tests presents a tendency to increase for higher restraint levels.

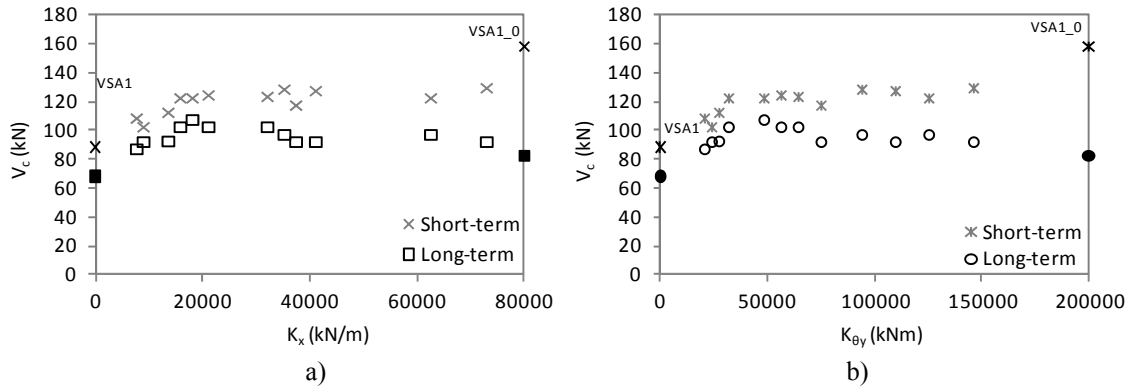

Figure 5.24 – Concrete contribution to shear resistance vs. level of restraint of the columns for the long-term and short-term analysis: a) longitudinal stiffness and b) rotational stiffness

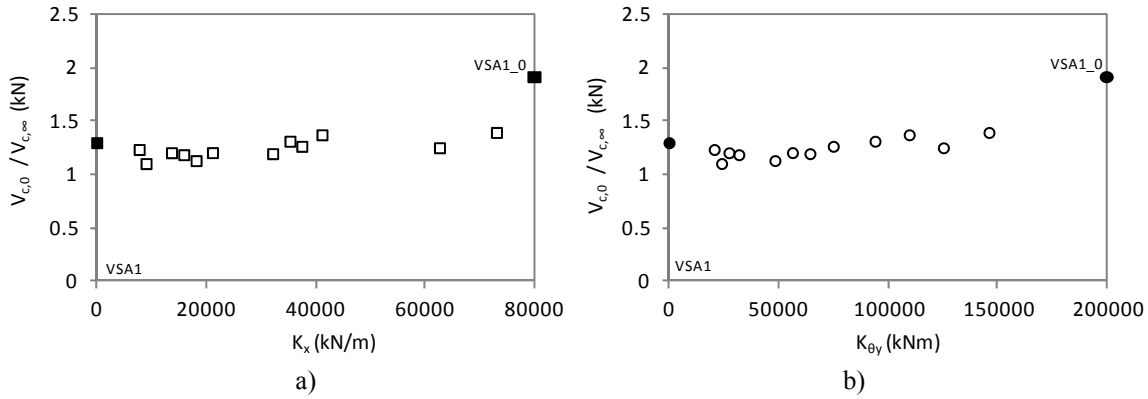

Figure 5.25 – Ratio of the concrete contribution to shear resistance of the beam for the long-term and short-term analysis vs. level of restraint of the columns: a) longitudinal stiffness and b) rotational stiffness

5.5 Conclusions

In this chapter the time-dependent features available in the basic flexural model were extended to the biaxial case in order to be integrated into the proposed shear-flexural model. Therefore, starting from the original numerical solution procedures, the uniaxial

models for the time-dependent response of concrete were extended in order to maintain the consistency with the 2D stress-strain state present in the shear resistant fibres. By these means, an existent time-dependent analysis procedure for plane elements was adapted to the case of the 1D fibre beam element model with inclusion of shear effects.

The validation of the model was performed with two experimental tests available in the literature: (*i*) a typical flexural benchmark on partially prestressed beams, in which the influence of shear was not important; (*ii*) a set of diagonally pre-cracked RC beams under sustained load, in which shear effects were relevant. The first example was chosen to ensure that the extension of the time-dependent model from the 1D to the 2D strain state was performed correctly, and that for the shear negligible cases the model was also performing accurately. Pertaining to the creep experimental tests on diagonally cracked beams, the shear effects were important and the proposed shear model achieved a better fitting with the experimental data, in comparison to the pure flexural model. However, the difference between the results of the two models was mostly observed in the instantaneous deflections. The influence of shear in the long-term deflection was not straightforwardly evaluated from these experimental tests. Actually, the scarcity of experimental tests focused on the shear related parameters on the time-dependent behaviour of RC frame structures inhibited a proper validation.

Subsequently a series of numerical studies on the time-dependent performance of shear-critical RC beams were carried out. Starting from a previously studied case – the VSA1 beam presented in Chapter 3 - the beam was submitted to a sustained load correspondent to 40% of its ultimate resistance, and the correspondent time-dependent response was computed by the numerical model. By these means, it was observed that the deflection of the beam was predicted to achieve significantly higher values with the consideration of shear effects. However, the differences between the results of the shear and flexural models are essentially due to the instantaneous portion of the total deflection. In fact, the time-dependent deflection due to distortion was rather insignificant. Moreover, the relaxation of the stresses in the stirrups with time, due to the decrease of compressive stresses in concrete in the vertical direction, was predicted by the shear model. After the time-dependent analysis, the beam was incrementally loaded until failure. No influence of the sustained load and creep phenomena on the ultimate resistance of the beam was observed, as expected.

Afterwards, as a continuation of the parametric study on the influence of restraint effects on shear critical beams belonging to frames presented in Chapter 4, an analogous study

was carried out by considering long-term shrinkage before loading. By these means, it was observed that the presence of restraint strains due to shrinkage had an effect on the ultimate response of the beam. A considerable decrease of the ultimate load was predicted by the numerical model (5-20%), as consequence of the previous damage and stress states brought by the time-dependent effects of shrinkage. This effect is due to decrease of the concrete contribution to shear resistance when previous tensile strain states are applied to the beam, leading to the activation of the transversal reinforcement for lower loading levels. It was observed that, for higher levels of restraint, the decrease on the shear resistance of the beam was higher in relation to the short-term analysis.

Chapter 6

NUMERICAL ASSESSMENT AND STRENGTHENING INTERVENTIONS ON SHEAR CRITICAL CONCRETE STRUCTURES

6.1 Introduction

In this chapter, the proposed nonlinear and time-dependent fibre beam model is enhanced in order to simulate the response of existent RC and prestressed structures subjected to repair and strengthening interventions. The proposed shear model was implemented in the existing flexural fibre beam model for the time-dependent analysis of segmental constructed RC frames (Marí 2000). By these means, along with the possibility of simulating shear critical problems, the model is able to reproduce evolutionary construction phases, such as repair or strengthening interventions. In fact, modelling strengthening procedures as phases of an evolutionary construction is a suitable way to predict the behaviour of strengthened elements, as the previous damage can influence their final responses.

The proposed model is validated with experimental results concerning a shear damaged and subsequently strengthened RC beam, available in the literature. Relevance of considering the shear-bending interaction and the previous damages in the numerical assessment of strengthened RC beams is highlighted. An alternative strengthening solution

for the same damaged beam, based on using post-tensioned steel stirrups, is numerically analysed as well.

Afterwards the numerical model is used to assess the beams of the girders of the Wassnerwald bridge, put into service in Swiss in 1969 and dismantled in 1996, because the shear resistance requirement was no longer satisfied according to actual design codes. The beams were fully prestressed, and only a minimum reinforcement quantity was used as stirrups. The dismantled beams were used to perform full-scale tests up of to failure by the Institute of Structural Engineering IBK of the Swiss Federal Institute ETH in Zurich. The goal of these tests was to assess the 'real' load carrying capacity of the bridge, and in this manner infer the structural safety and strengthening needs of other existent bridges of the same type. These *in situ* full-scale experimental tests are reproduced by the proposed numerical model. Afterwards, different strengthening proposals for the beams regarding prestress solutions are analysed.

The proposed fibre beam model, with inclusion of shear effects, can be specially appropriate and useful for this kind of analysis, which includes the assessment of existent and strengthened structures. By these means, this chapter aims to demonstrate the original and essential contribution of this thesis, which consists in the development of a numerical tool to perform numerical assessment of damaged frame structures and predict the response of strengthening interventions.

6.2 Enhancement of the proposed model for simulation of strengthening interventions

Regarding that the proposed formulation for the consideration of shear-bending interaction in a fibre beam model was implemented on the numerical model CONS (Marí 2000), its time-dependent and sequential analysis features are exploited by extending its application to the case of RC structures under important shear stresses. By these means, the time step-by-step analysis allows the simulation of segmental construction procedures and subsequent later changes, in which repair and strengthening interventions are included. The required adaptations in the proposed model in order to allow for the simulation of strengthening procedures within a step-by-step time integration domain are detailed presented in the following.

6.2.1 Segmental construction analysis

The flowchart of the algorithm that implements the proposed model with segmentation construction capabilities is presented in Figure 6.1. It includes three global loops, which run through: (*i*) the constructive phases, (*ii*) the time steps and (*iii*) the load steps. It is noteworthy that the algorithm is a continuation of the one related to the load steps presented in Chapter 3 for the proposed shear-bending fibre beam model (see Figure 3.8), and of the one related to the time-steps for the time-dependent analysis in Chapter 5 (Figure 5.1), adding a loop for the construction phases.

Most modifications that may take place during the construction process and along the service life of a structure - such as changes in the cross-sectional and longitudinal geometry, structural scheme, material properties and applied loads - can be simulated by the proposed model, through the available step-by-step solution scheme for the nonlinear problem. Deterioration and repair procedures may also be modelled due to the possibility to consider different concrete and steel types, with different activation and removal timings, for each fibre and each filament in a cross-section. Hence, the following operations related to retrofitting and strengthening of existing structures can be simulated: substitution of damaged concrete parts, enlargement of the concrete cross-section, introduction of new reinforcement bars (longitudinal and transversal), placement or removal of temporary shores, imposed movements and application of external prestressing.

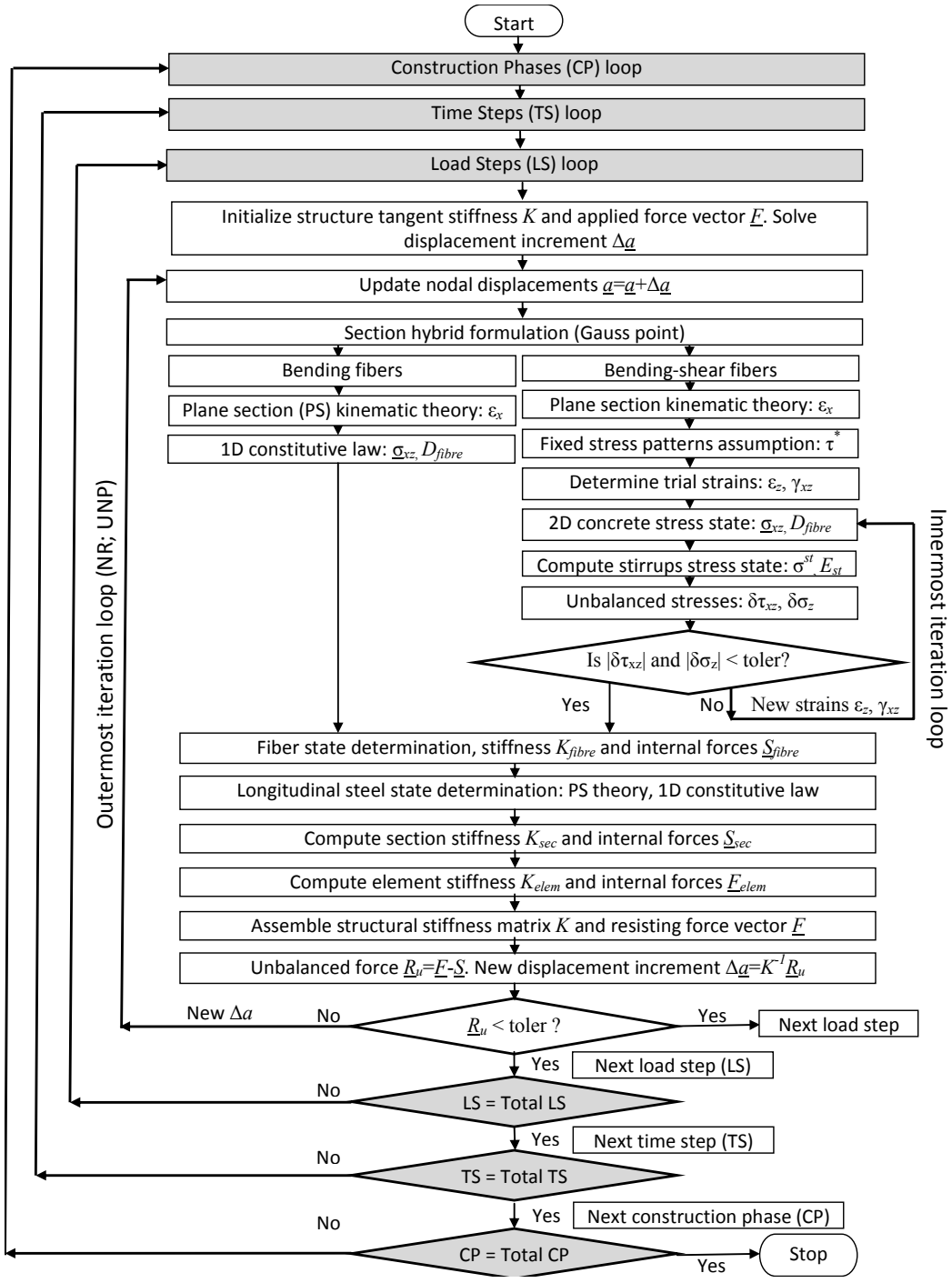

Figure 6.1 – Flowchart of the global model

6.2.2 Evolutive section assumption for shear

Pertaining to the simulation of the evolutionary section response, the mixed kinematic/force-based assumptions are represented in Figure 6.2: both the original and the added fibres for strengthening are assumed to comply with the plane section theory. Before strengthening procedures the constant shear force V is carried by the area A^* of the shear resistant fibres; after strengthening the constant increment of shear stress ΔV along the cross-section is equally distributed between the original and the added fibres, and the effective shear area increases of A^*_{stren} (the area of the strengthening shear resistant fibres).

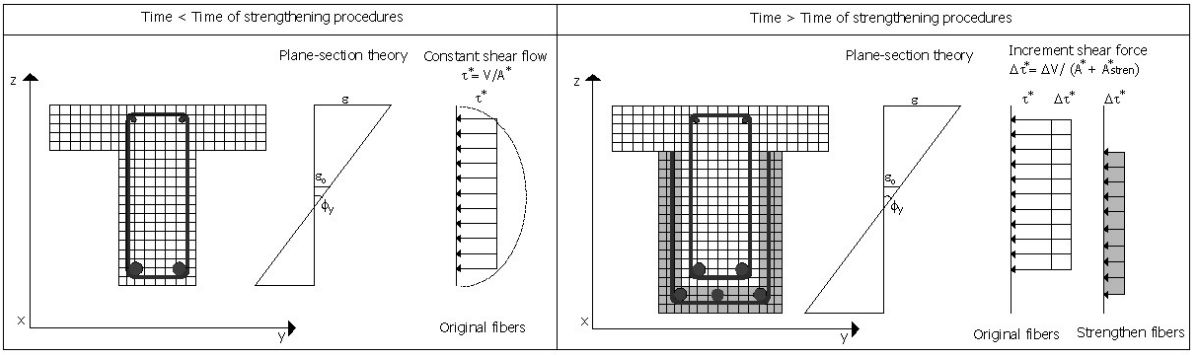

Figure 6.2 – Assumptions of the evolutionary sectional model

By assuming this hypothesis of identical stress distribution in the shear effective area of the strengthened section, possible differences between the distribution of shear stresses of the original and repair materials/fibres are neglected.

Furthermore, the historical plasticity and damage variables of the original fibres are kept memorized (unchanged) when the new strengthening fibres are activated. Hence, influence of previous damages in the structure, which can be particularly relevant, is accounted for in the model.

6.2.3 Simulation of post-tensioned stirrups

Strengthening of RC elements to shear with post-tensioned stirrups is an efficient method to increase the shear capacity of the structure, allowing for the development of its full flexural capacity. Transversal reinforcement is considered smeared in the shear resistant fibres, as described in Section 3.2.2. If vertical prestress is applied at a given time-step, the prestressed stirrups are activated with a given stress as schematically represented in Figure 6.3.

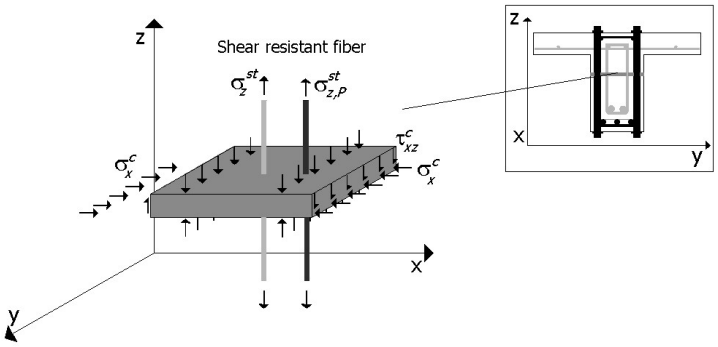

Figure 6.3 – Simulation of post-tensioned stirrups

By these means, the equilibrium of stresses in concrete and transversal steel in the vertical direction at the fibre level, originally stated in Eq. (3.21), is rewritten in order to account for this extra increment of tensile force

$$\Delta\sigma_z^c + \rho_{st}\Delta\sigma_z^{st} + \rho_{sp}\Delta\sigma_z^{sp} = 0 \tag{6.1}$$

where ρ_{sp} is the volumetric ratio and $\Delta\sigma_z^{sp}$ is the increment of axial stresses (along direction z) of the prestressed stirrups. The prestress is considered in the model as an offset strain ε_z^p as

$$\Delta\sigma_z^c + \rho_{st}E_s\varepsilon_z + \rho_{sp}E_{sp}\left(\varepsilon_z + \varepsilon_z^p\right) = 0 \tag{6.2}$$

where E_{sp} is the elasticity modulus of the prestressing steel. Through this equilibrium requirement the concrete fibre is submitted to an active confinement when the vertical prestress is applied, and existing stirrups made with ordinary reinforcement will be pre-compressed.

The 1D constitutive law for ordinary reinforcing steel presented in Figure 3.4 is also used for the simulation of prestressing steel.

6.3 Experimental validation: Souza and Appleton beam tests

6.3.1 Description

The experimental tests of shear damaged and subsequently strengthened RC beams carried out by (Souza 1990; Souza and Appleton 1997a) were simulated with the proposed model. With this example it is aimed to validate the capacity of the model to numerically assess

the behaviour of existent damaged and strengthened RC elements under high shear forces. Among the several specimens with different strengthening techniques tested in the experimental campaign, the selected ones relate to the beams repaired with shotcrete and additional closed stirrups. The geometry characteristics, loading conditions, reinforcement details and material properties of the experimental tests are indicated in Figure 6.4: the specimen after strengthening is represented in black line, whereas the original beam before strengthening is represented in grey colour. The specimens are 2.07m long, having T-shaped cross-sections with heights of 0.20m for the original beams and of 0.245m after strengthening, and web thicknesses of 0.08m and 0.13m, prior and after strengthening, respectively. The original beam has a very low shear reinforcement ratio (0.2%), with the purpose of simulating a design error; an extra stirrups ratio of 0.246% was added to the strengthened beam. The beams are heavily reinforced for bending, in order to guarantee high shear damages and failure after strengthening.

The original beam (WPB1) was loaded incrementally until appearance of considerable damage at the load level near the shear resistance. Afterwards the beam was completely unloaded and the strengthening work was carried out: the concrete cover of the web was removed; vertical holes were opened in the flanges in order to fix the additional transversal reinforcement and then filled with cement past; the extra longitudinal reinforcement was placed and shotcrete was added until the desired cross-section dimensions were reached. No treatment was applied to the cracks caused by the first loading tests. After the strengthening procedures, the beam (WPB1R) was submitted to increasing load until failure in a second test.

In addition to the WPB1 and WPB1R tests two reference tests were also considered: (*i*) one specimen with the same characteristics of the non-strengthened beam (DW) and (*ii*) one specimen with the same characteristics of the strengthened beam (RW2). Both reference specimens were not submitted to any previous damage or strengthening intervention and were loaded until failure. The non-strengthened reference beam test (DW) allows determining the level of damage applied to WPB1 specimen, *i.e.* how near it was to failure load before strengthening interventions. By comparing specimens WPB1R with the reference RW2 the influence of the previous damage on the response of the strengthened beam is induced. The names of the tests were maintained as in the original data (Souza 1990). The recorded experimental data consisted on displacements (by means of displacement transducers), localized strains in reinforcement (using electric gauges),

strains and crack widths in concrete (through extensometers) and observed cracking patterns.

In total, three shear beam tests were simulated with the proposed model: (*i*) the reference original beam DW, (*ii*) the reference strengthened beam RW2 and (*iii*) the previously damaged and then strengthened beam (WBP1-WPB1R). The FE model and the cross-section idealization by means of concrete fibres and steel filaments is represented in Figure 6.5.

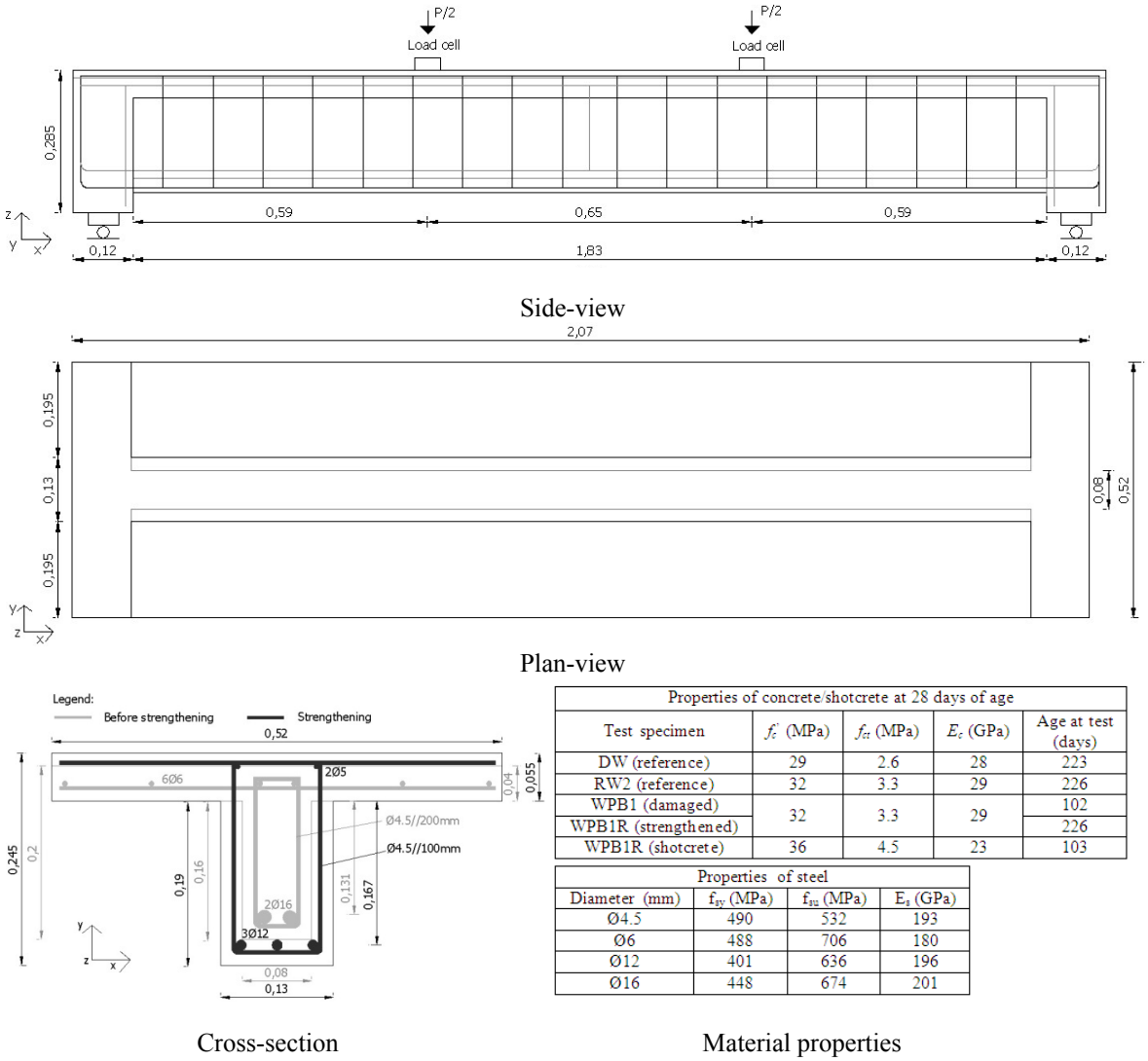

Properties of concrete/shotcrete at 28 days of age				
Test specimen	f_c' (MPa)	f_{ct} (MPa)	E_c (GPa)	Age at test (days)
DW (reference)	29	2.6	28	223
RW2 (reference)	32	3.3	29	226
WPB1 (damaged)	32	3.3	29	102
WPB1R (strengthened)				226
WPB1R (shotcrete)	36	4.5	23	103

Properties of steel			
Diameter (mm)	f_{sy} (MPa)	f_{su} (MPa)	E_s (GPa)
Ø4.5	490	532	193
Ø6	488	706	180
Ø12	401	636	196
Ø16	448	674	201

Material properties

Figure 6.4 – Geometry, reinforcement and material properties of the shear beam tests by Souza and Appleton

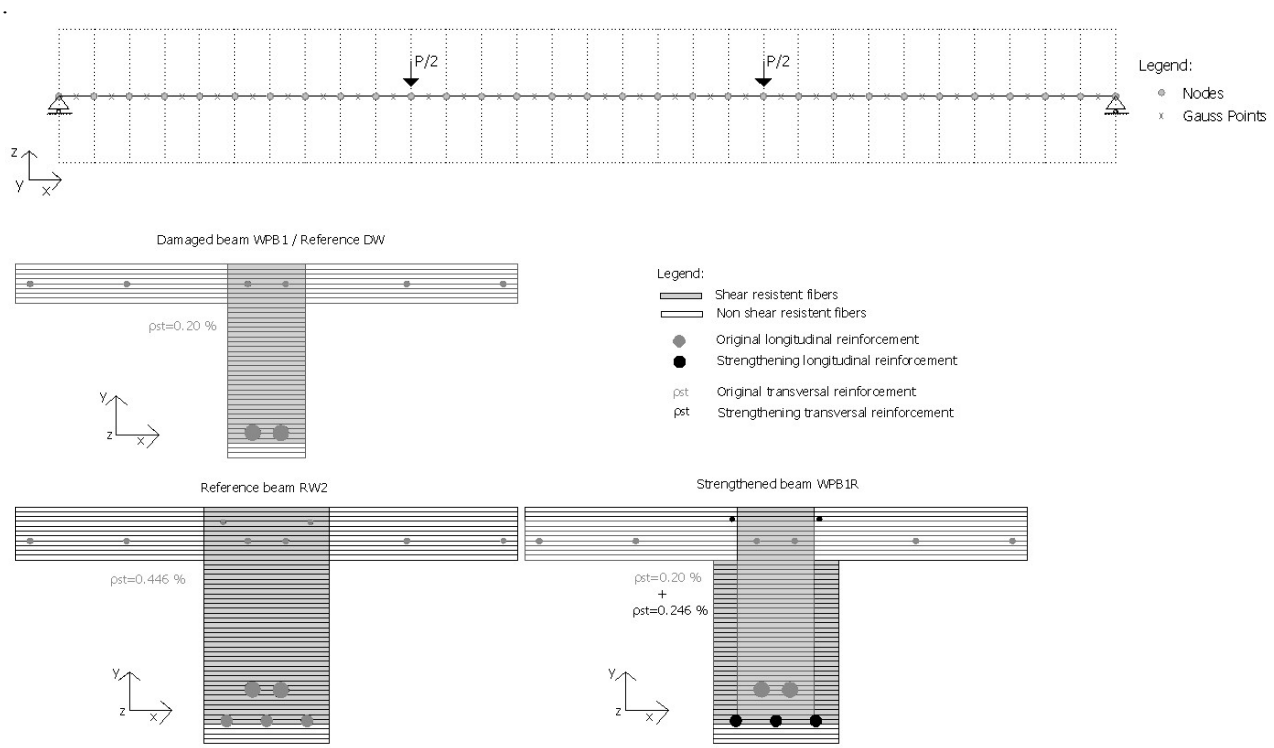

Figure 6.5 – - Numerical model adopted for the Souza and Appleton's shear beam tests

Concerning to the load application, in the case of the reference beams (DW and RW2) the vertical load was incrementally imposed until failure. In the case of the damaged and subsequently strengthened beam, firstly the vertical load P was applied incrementally to the original beam (WPB1) until reaching 54kN, and then was unloaded until $P \cong 0$. Afterwards strengthening concrete and reinforcement were activated (WPB1R), and the load was again incrementally applied until failure. An identical simulation was performed with the pure flexural fibre beam model CONS (Marí 2000), to evaluate the importance of taking into account the nonlinear shear effects in this analysis.

6.3.2 Results and discussion

6.3.2.1. Failure loads and collapse modes

According to the experimental observations (Souza 1990), the three beam specimens loaded until failure in laboratory failed in shear. In the case of beam WPB1R the strengthening intervention proved to be very successful, allowing for a correct transference of load between old and added materials, as the stirrups remained well anchored and the

bond between the repair and original concrete was achieved. Collapse was caused by failure of the external stirrups and compressive crushing of the concrete web. The reference beam RW2 showed a similar performance to that of beam WPB1R, with a shear failure induced by the rupture of the internal and external stirrups, in correspondence to the location of a diagonal crack. In Table 6.1 a summary of the experimental and computed results at failure for the three analyzed beams is presented. Good predictions of the ultimate shear force and failure mode were given by the proposed model. In contrast, and as expected, the basic flexural model CONS showed to be inadequate for the simulation of these shear influenced beam tests, providing unsafe estimations of the failure loads.

Table 6.1 Summary of experimental and computed results at failure

Beam	Experimental		Proposed model (shear-bending model)		Basic model (pure bending model)	
	Vu (kN)	Failure mode	Vu (kN)	Failure mode	Vu (kN)	Failure mode
DW	38	Shear [a]	39	Shear[*]	47	Bending[**]
RW2	88	Shear [b]	91	Shear[*]	116	Bending[**]
WPB1R	91	Shear [c]	90	Shear[*]	101	Bending[**]

[a] Web failure due to a main diagonal crack.
[b] Stirrups failure in the position of a main diagonal crack.
[c] Stirrups failure and crushing of the concrete compression flange.
[*] Stirrups failure and crushing of the concrete web.
[**] Failure of longitudinal reinforcement.

6.3.2.2. Global response

Experimentally observed mid-span beam deflections are compared with the numerically computed ones in Figure 6.6. Relating to the damaged and strengthened specimen (WPB1 – WPB1R) and for a better interpretation of the graphics, the results related to the test performed before strengthening (WPB1) and to the test performed after strengthening (WPB1R) are represented separately. As it can be seen, very good agreement between the experimental results and the numerical predictions with the shear-bending model has been obtained for all the studied cases. This occurs even in the strengthened beam WPB1R, in which the shear stress distribution cannot be uniform in all the section due to the previous damage. By analysing Figure 6.6 it is also clear that the pure flexural model is not suitable to simulate these shear-critical beams, as their predictions are very different from the experimental observations in terms of deflections and ultimate loads.

By comparing the strengthened beam WPB1R with its reference 'twin' RW2 a quite similar behaviour is perceived. The residual damage of the beam WPB1 (such as plastic strains in concrete and cracking) had few influence on its final response (WPB1R). No yielding of the reinforcement was observed during the previous damage test. The same aspects were found in the numerical simulation, as no relevant decrease in the stiffness and in the ultimate load were predicted for the previously damaged beam WPB1R when compared with the reference specimen RW2.

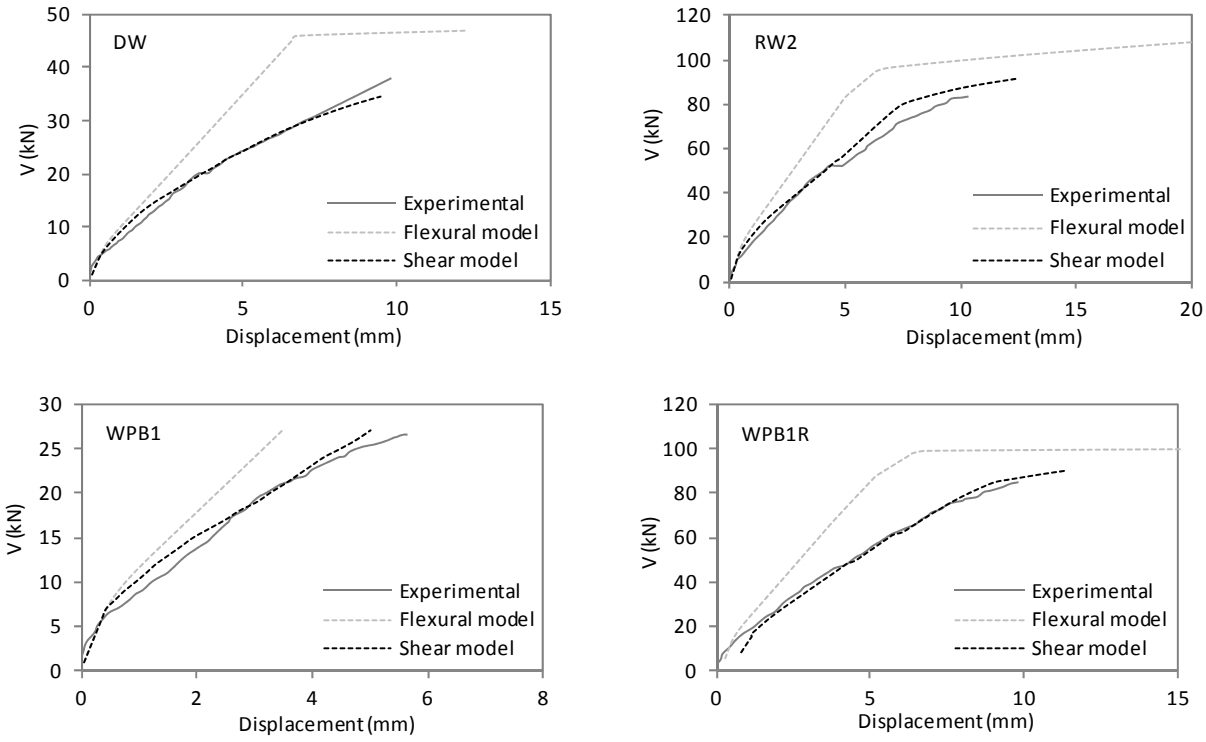

Figure 6.6 – Displacements at mid-span

Average curvatures ϕ_y measured at mid-span are depicted in Figure 6.7, along with the numerical predictions for the strengthened beams RW2 and WPB1R. In these graphics a more ductile experimental response of the reference beam RW2 is observed, in comparison to the one from beam WPB1R. In relation to the results computed by the proposed shear model, they fit better to the experimental observations for beam WPB1R, although relevance of shear is evident in both beams.

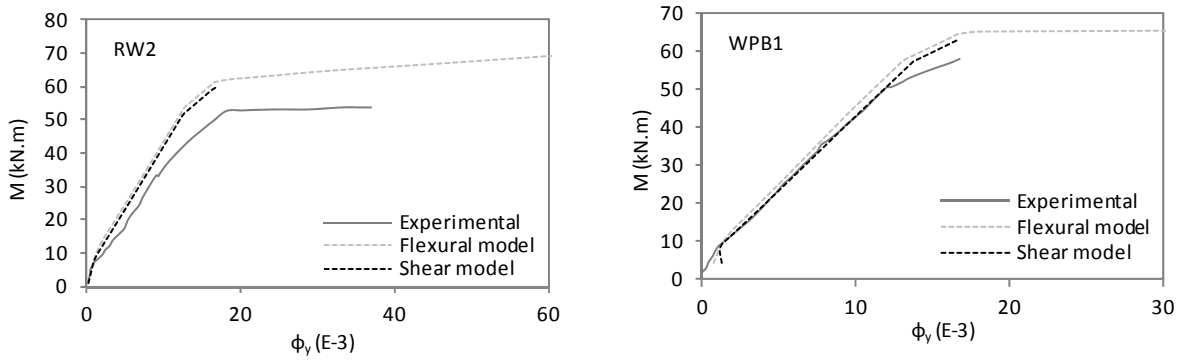

Figure 6.7 – Curvatures at mid-span for the strengthened beams

6.3.2.3. Stress-strain state in the longitudinal reinforcement

The strain measurements at the bottom longitudinal reinforcement, mid shear span, are compared in Figure 6.8 with the model predictions for ε_x^{sl}. For the case of the strengthened beams (WPB1R and RW2) the presented results correspond to the reinforcement added in the strengthening intervention. The importance of considering shear effects in the numerical simulations is, in this case, particularly evident.

The increment of axial strain in the tensile longitudinal reinforcement in the presence of shear forces (the 'tension-shift' effect) is a consequence of the shear-bending interaction mechanism. This effect, observable in Figure 6.8 in the higher strains computed by the shear model in contrast with the ones of the pure flexural model, is well captured by the proposed model and allows a good fitting with the experimental data. In the case of the strengthened beam WPB1R, the residual damage does not play an important role in the development of the stresses in the longitudinal reinforcement, as experimental and computed results are quite similar to the respective reference specimen RW2. This is due to fact that there was no previous yielding of the longitudinal reinforcement during the first loading stage.

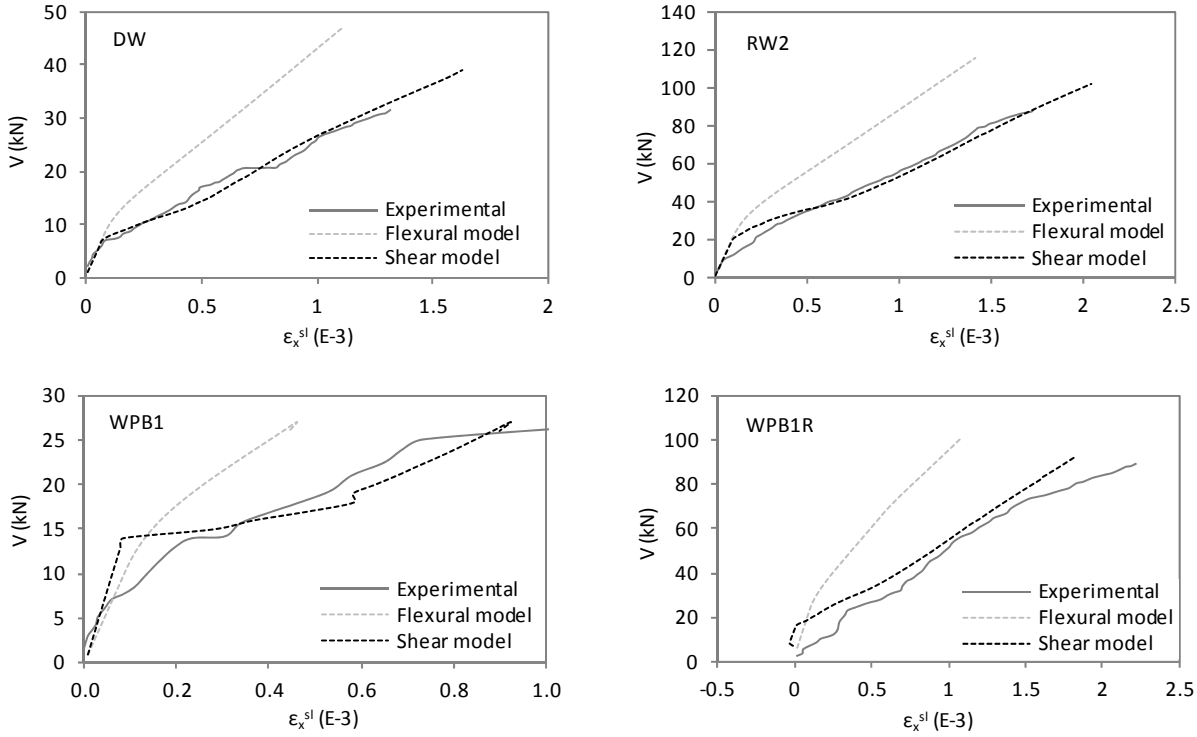

Figure 6.8 – Strains in the longitudinal reinforcement at the shear span (x=0.36m)

The strain ε_x^{sl} in the bottom longitudinal reinforcement along the beam's length, predicted by the shear and flexural models, is presented in Figure 6.9 for different load levels. In relation to the strengthened beams (RW2 and WPB1R), the reinforcement added in the strengthening intervention is the one considered in the graphics. The available experimental data are also included (Souza 1990). It is noteworthy that the experimental data correspond to average values, which depend on the crack location. It can be observed that the 'tension-shift' effect in the shear span is only reproduced by the proposed shear model. The peaks of ε_x^{sl} in the curves of the shear model when passing from the area of null shear force between applied loads to the shear spans represent this 'tension-shift' effect of increment of strains due to the presence of shear. Pertaining to the strengthened beams (Figure 6.9b), greater experimental strains in the pure bending region and lower strains in the shear span are found for the reference beam RW2, in comparison to WPB1R. In relation to numerical predictions, no significant differences between the beams RW2 and WPB1R are found.

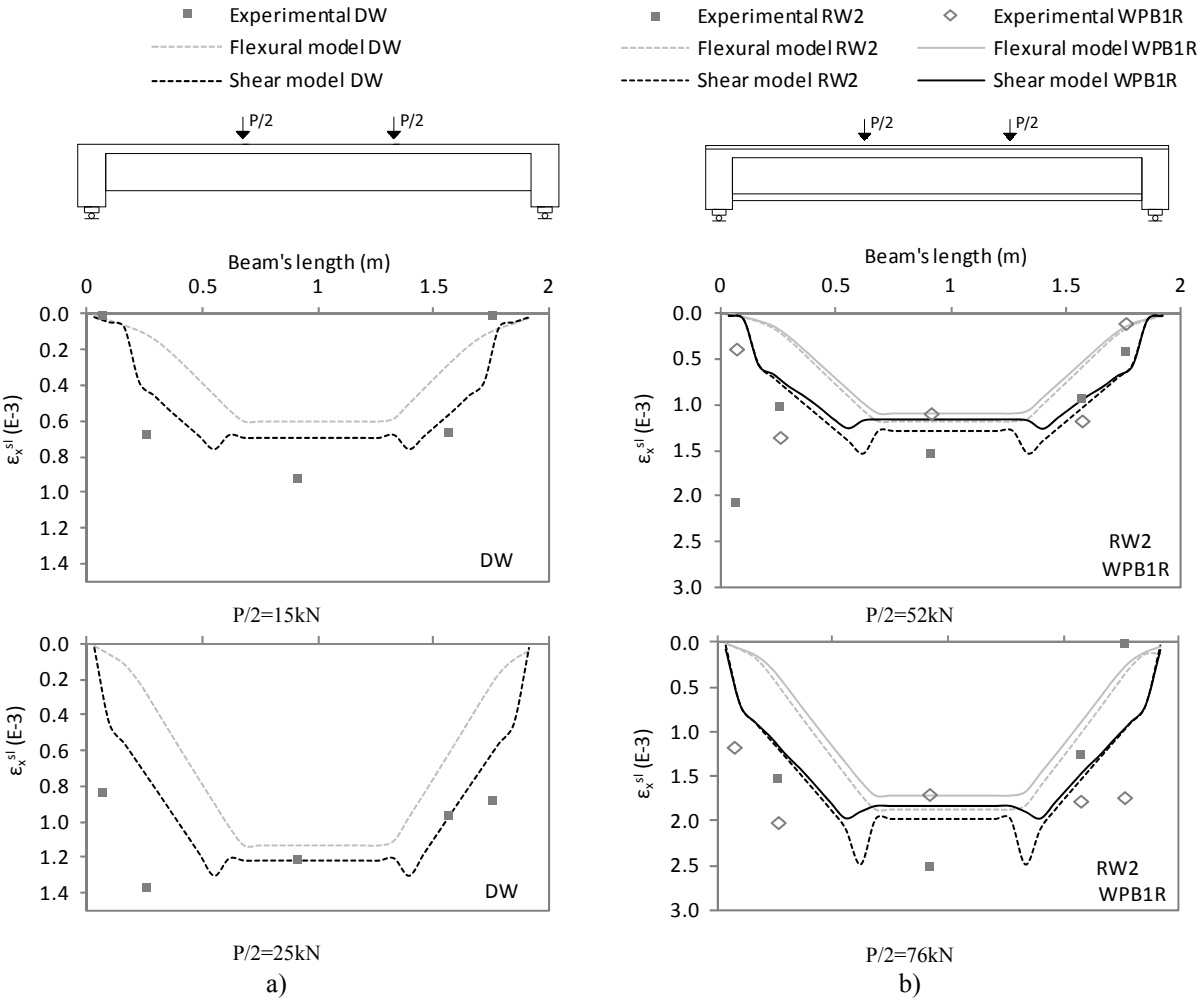

Figure 6.9 – Strains in the tensile longitudinal reinforcement along the beam: a) non-strengthened reference beam DW; b) strengthened beams RW2 and WPB1R

The axial stresses σ_x^{sl} on the original bottom reinforcement at the mid-shear span predicted by the proposed shear model for both strengthened beams RW2 and WPB1R are compared in Figure 6.10. A slight increase of σ_x^{sl} is noticed for beam WPB1R in relation to RW2 for earlier load stages; the curve of the previously damaged beam WPB1R presented no bulge (related with the tension-stiffening effect) in contrast with the curve of the reference beam RW2. This is due to the fact that the original reinforcement of the strengthened beam is immediately loaded, as concrete in that area is already cracked by the previous damage (as will be presented next in Section 6.3.2.6). The observation of this fact was also mentioned in the discussion of the experimental results of the strengthened beams tested (Souza 1990). For later load stages, axial stresses in the longitudinal reinforcements are identical for both beams.

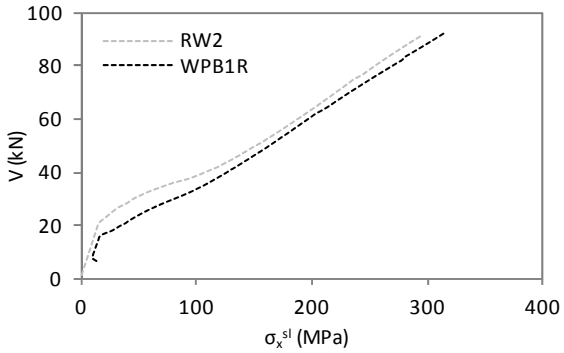

Figure 6.10 – Axial stresses in the original bottom longitudinal steel at the mid-shear span (x=0.36m), for the strengthened beams (shear model predictions)

6.3.2.4. Stress-strain state in the transversal reinforcement

Numerical predictions and experimental measurements of the strains ε_z^{st} in the stirrups are presented in Figure 6.11 for all the analysed beams. The strain sensors are located in a cross-section at the mid-shear span (x=0.36m), and 5.5cm above the bottom of the closed stirrups. The presented measurements concern to the original transversal reinforcement, for both the non-strengthened and strengthened beams. According to Figure 6.11, the visible change in the inclination of the numerical and experimental curves coincides with the start of the diagonal cracking, when the concrete contribution to shear resistance (*i. e.* the contribution of concrete to the tension ties of the shear resistant mechanism of a beam) is over and the stirrups start to carry the tensile stresses generated by the shear mechanism. It is important to underline that these experimental measurements are very much dependent on the position of the cracks. This influence is more important for the cases of widely spaced stirrups, when few diagonal cracks appear and failure occurs through a major crack. As a consequence, the comparison of the numerical predictions with the experimental data is not straightforward, due to the discrete nature of cracking and to the position of the strain sensors with respect to the closest crack. Even though, by analysing the experimental and the shear model graphics an overestimation of the strains by the numerical model is perceived. However, for the case of the beams with lesser spaced stirrups (RW2 and WPB1R) the fitting is better. In this case there are no predictions from the flexural model, as the transversal reinforcement is not taken into account.

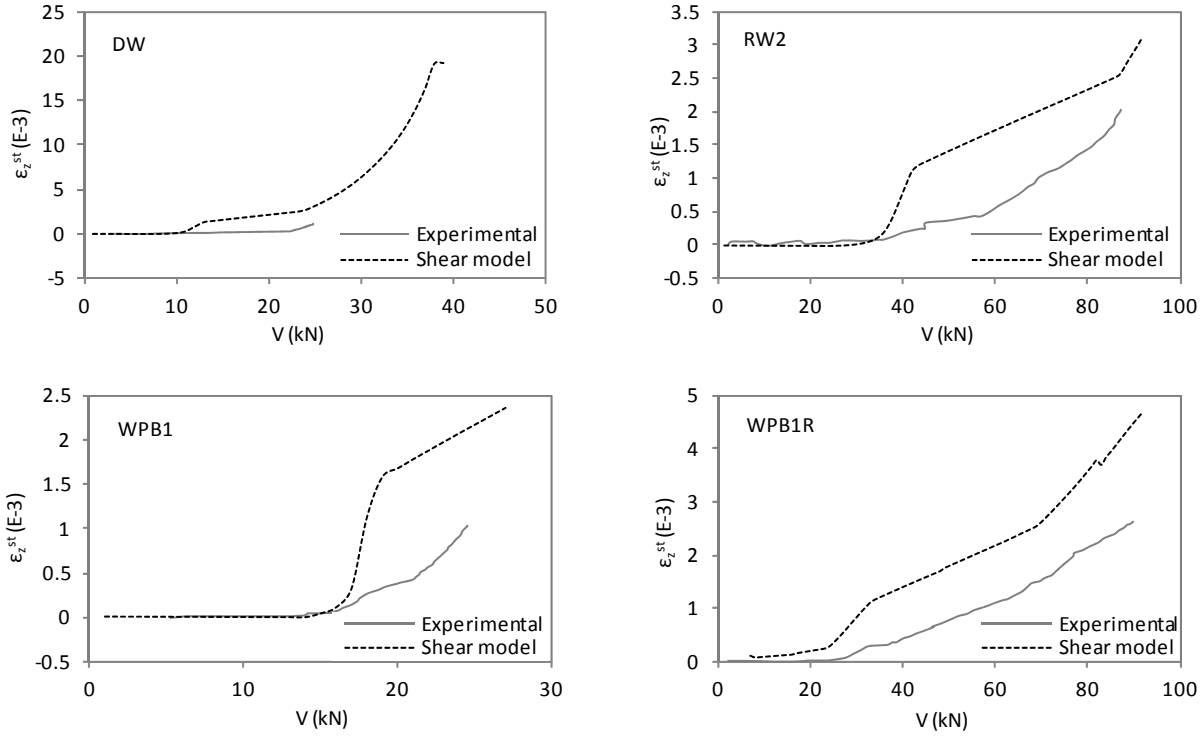

Figure 6.11 – Axial strains in transversal reinforcement at the mid-shear span (x=0.36m)

The axial stresses σ_z^{st} in the transversal reinforcement, at the same location of the measurements presented in Figure 6.11, are depicted in Figure 6.12 for the strengthened beams. The influence of the previous damage brought by the first loading test in their later responses after strengthening is noticed: a sooner ending of the concrete contribution and the consequent earlier activation of the stirrups is observed for beam WPB1R in comparison with beam RW2. Regarding the beam WPB1R (original and strengthening reinforcements), and during the first loading stages, the original transversal reinforcement is activated sooner and reached higher stresses σ_z^{st} than the strengthening shear reinforcement; for a later stage an identical behaviour is however observed. In the case of the reference beam RW2, the original and strengthening stirrups presented identical responses, so only the stresses σ_z^{st} in the original reinforcement are presented in Figure 6.12.

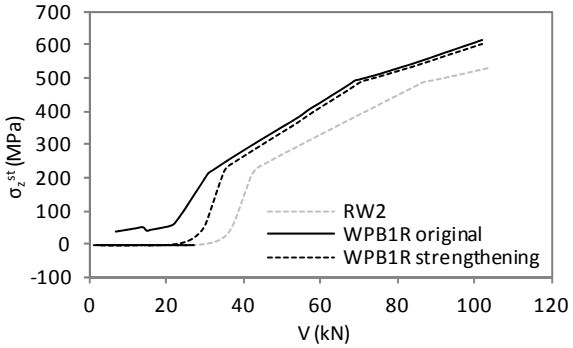

Figure 6.12 – Axial stresses in the transversal steel at the mid-shear span (x=0.36m) for the strengthened beams

Still concerning to the strengthened beams, distributions of stresses σ_z^{st} along direction z at the mid-shear span cross-section (x=0.36m) are depicted in Figure 6.13 for a loading stage near failure (P/2=90kN). Higher stresses appear in the cracked part of the cross-section, and nearly null stresses occur in the compressed top region. At this load stage, steel yielding at the bottommost part is observed, being more pronounced for the WPB1R beam. Original and strengthening reinforcement of both beams presents a quite similar behaviour.

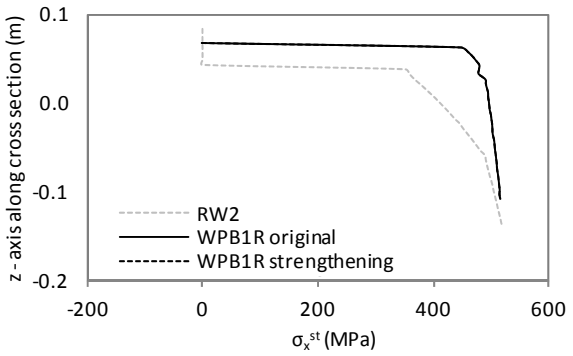

Figure 6.13 – Axial stresses in transversal reinforcement along the mid-shear span cross-section (x=0.36m) for P/2=90kN

6.3.2.5. Stress-strain states in concrete

Concrete shear stresses τ_{xz} and distortions γ_{xz} at the mid-shear span cross-section, and at the location of the strain sensor adopted for the transversal reinforcement in Figure 6.11, are presented in Figure 6.14 for the strengthened beams. Regarding the WPB1R beam, both original and strengthening concrete fibres are presented, in which an identical behaviour is observed. In comparison with the reference beam RW2, higher concrete shear stresses and

strains are observed. In fact, along with the effects of the previous damage, this difference is due to the lesser shear resistant area that is considered in the model of WPB1R beam, in comparison to the model of beam RW2 (see Figure 6.5). The plastic shear strain of the original fibre in the previously damaged beam WPB1R is perceived by the offset of the curve in Figure 6.14*b*.

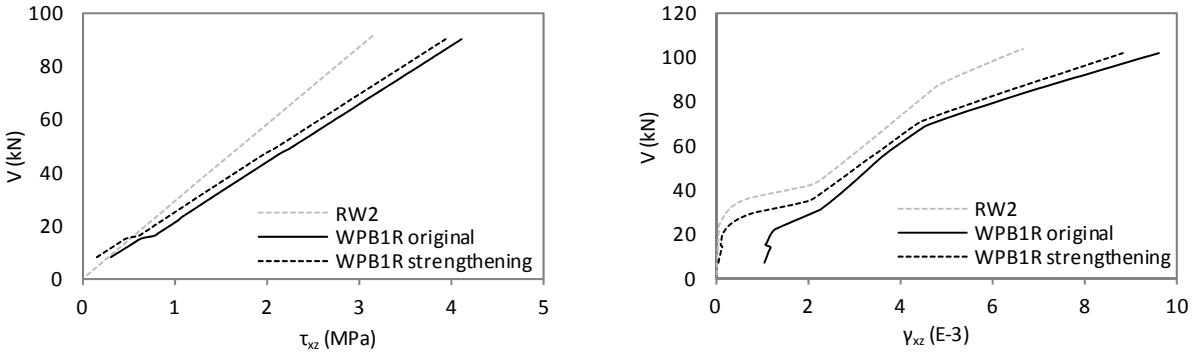

Figure 6.14 – Concrete shear stresses a) and strains b) at the mid-shear span (x=0.36m) for the strengthened beams

The concrete normal stress distributions σ_x^c along the vertical direction in the web of the shear critical cross-section of the strengthened beam WPB1R are depicted in Figure 6.15, for a loading stage near failure (P/2=90kN). Results computed by both the proposed shear and the flexural models are presented. The absolute different predictions from the two models, especially in the area below the neutral axis, are noteworthy. In the case of the pure flexural model tensile stresses due to tension stiffening appear in this zone. Conversely, compressive stresses are computed by the shear model, which correspond to the longitudinal component of the diagonal compressive struts. Identical results were found for the reference beam RW2.

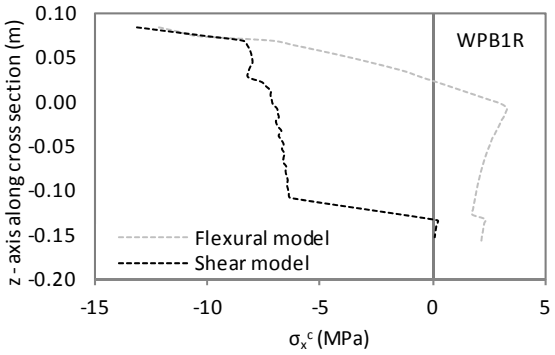

Figure 6.15 – Longitudinal stresses in concrete along the web of the shear critical cross-section at x=0.36m for the WPB1R beam (P/2=90kN)

6.3.2.6. Cracking

An illustration of the observed cracking patterns for the maximum load stage is presented in Figure 6.16, along with the predictions from the proposed shear model. A general good representation of the observed cracking is achieved, with vertical cracks at the bending span and diagonal cracks in the shear span. In comparison to the reference test RW2, it is clear on the crack representations provided by the numerical model the more extensive cracking, as well as the greater inclinations of the diagonal cracks, of the previously damaged and subsequently strengthened beam WPB1R.

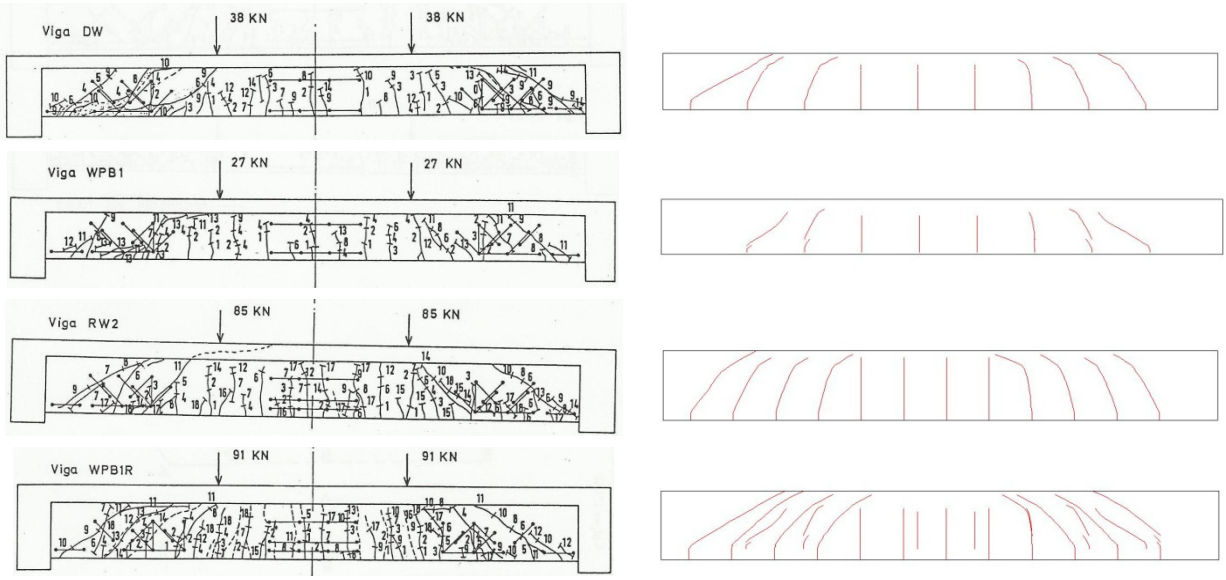

a) b)

Figure 6.16 – Cracking patterns

6.3.3 Alternative shear strengthening technique

In the following, an alternative strengthening solution for the shear beam test WPB1R (Souza 1990) is analysed numerically. Thus, starting from the numerical shear model of the previously damaged beam, the extra stirrups of the original strengthening were replaced by vertical prestressing rebars.

6.3.3.1. Description

The characteristics of the alternative strengthening solution are presented in Figure 6.17: 16mm diameter rebars were used as stirrups at a spacing of 200mm; post-tensioning was applied vertically; the prestressed bars were tensioned to 53% of its yielding strength at an initial pre-elongation of 0.002; the rebars were anchored to the beam top and bottom faces. Properties of the prestressing steel are (according to the notation of Figure 3.4): f_{sy}=1050MPa, E_s=200GPa, f_{su}=750MPa and ε_{su}=0.07.

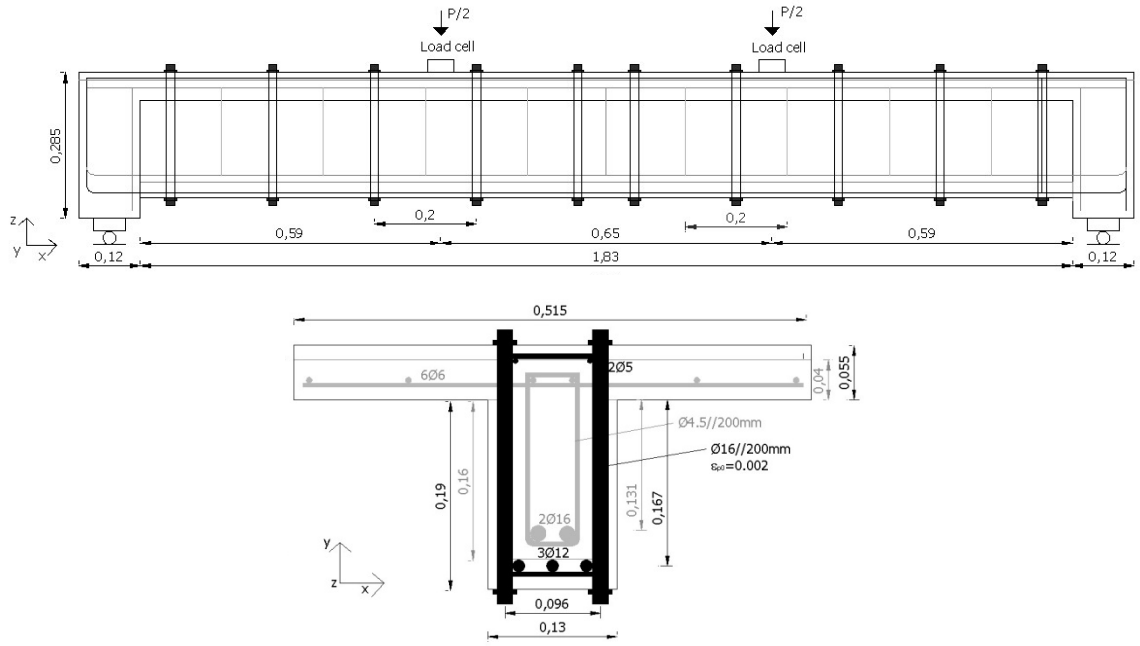

Figure 6.17 – Alternative strengthening solution by using prestressed vertical stirrups (beam WPB1R-VP)

Material properties of the concrete and ordinary steel, as well as the geometry and reinforcement of the damaged non-strengthened beam WPB1, are the same of the original test (see Figure 6.4). The enlargement of the concrete cross-section is also the same as for the experimental test WPB1R, in terms of geometry and material properties. The numerical model is analogous to the case of the simulation of the experimental test WPB1R (Figure 6.5), the only difference being in the definition of the transversal prestressing steel. Similarly to the WPB1R beam test, the original beam was firstly loaded until P=54kN to induce an initial cracking. Then it was unloaded until approximately null load, and afterwards the strengthening concrete, the longitudinal reinforcement and the prestressed stirrups were activated, and the load was incrementally applied until failure.

6.3.3.2. Numerical results and discussion

Deflections at mid-span for the strengthened beam with prestressed stirrups (WPB1R-VP) are depicted in Figure 6.18, along with the numerical results of the original beam WPB1R. Post-tensioned stirrups produce a considerable increase in the stiffness and in the shear resistance of the damaged beam, allowing for the full development of its flexural strength. Therefore, the brittle shear failure of the original strengthened beam changed to a ductile flexural mechanism. Relating to other shear-related aspects of the behaviour of the beam, it was observed that the use of the prestressed stirrups caused a decrease of the average concrete distortion γ_{xz} (see Figure 6.19), as well as an increase of the angle of the compressive concrete struts θ at the shear span (see Figure 6.20).

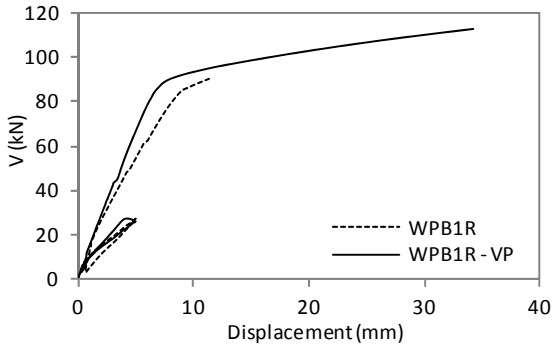

Figure 6.18 – Displacements at mid-span for WBPB1R and WPB1R-VP beams

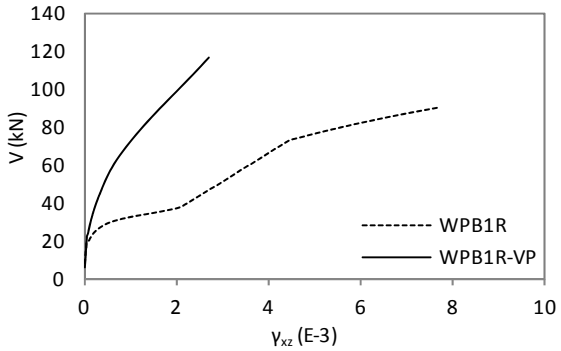

Figure 6.19 –Average concrete distortion at the shear span for WPB1R and WPB1R-VP beams

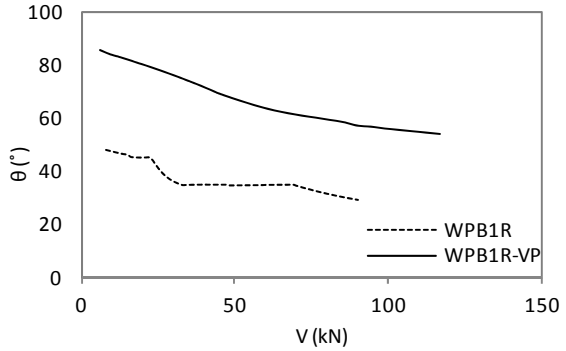

Figure 6.20 – Average angle of the compressive concrete struts with the beam axis at the shear span for WPB1R and WPB1R-VP beams

Numerical strains in the ordinary (passive) and pre-stressed (active) transversal reinforcement at the mid-shear span of WPB1R-VP beam are presented in Figure 6.21. It can be observed that the stress growth in the stirrups progresses very slowly with the external load increase, and only happens for a load level much higher than in the WPB1R beam (see Figure 6.11). This load stage corresponds to the start of the diagonal cracking (when the strains in the stirrups start to increase): at the beginning the passive stirrups were under compression due to the imposed transversal compression, and only started to be in tension after V=50kN; active pre-stressed stirrups had nearly constant tensile stresses until this load stage, and afterwards there was a smooth stress increment. Both types of stirrups remained elastic until the beam failure.

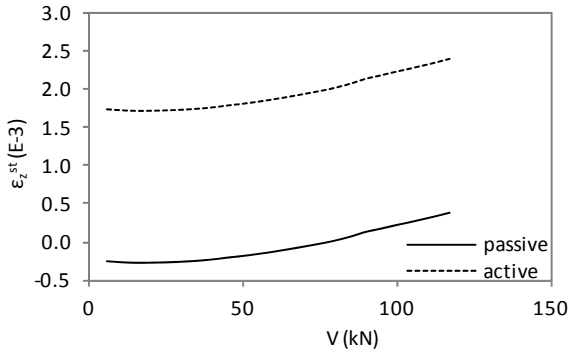

Figure 6.21 –Strains in the transversal reinforcement in the shear span of WPB1R-VP beam

Figure 6.22 reproduces the development of strains and stresses in the shear reinforcement of beam WPB1R-VP (both in the original (inner) and in the strengthening pre-stressed rebars), which are compared to the passive stirrups of beam WPB1R (both the original and strengthening passive rebars). In Figure 6.22*a* (for the inner reinforcement) and in the Figure 6.22*c* (for the strengthening reinforcement, active for WPB1R-VP and passive for

WPB1R) it can be observed that for beam WPB1R-VP post-tensioning allow for a later strain development and no yielding is predicted, in contrast to what is foreseeable for beam WPB1R. The offset of strains and stresses in the prestressed stirrups in the WPB1R-VP beam is noticed in curves of Figure 6.22*c* and Figure 6.22*d*, respectively, through the initial values of strains and stresses at the start of loading that correspond to the post-tensioning. The resulting pre-compression of the inner stirrups when transversal prestress is applied is also observable in Figure 6.22*b*.

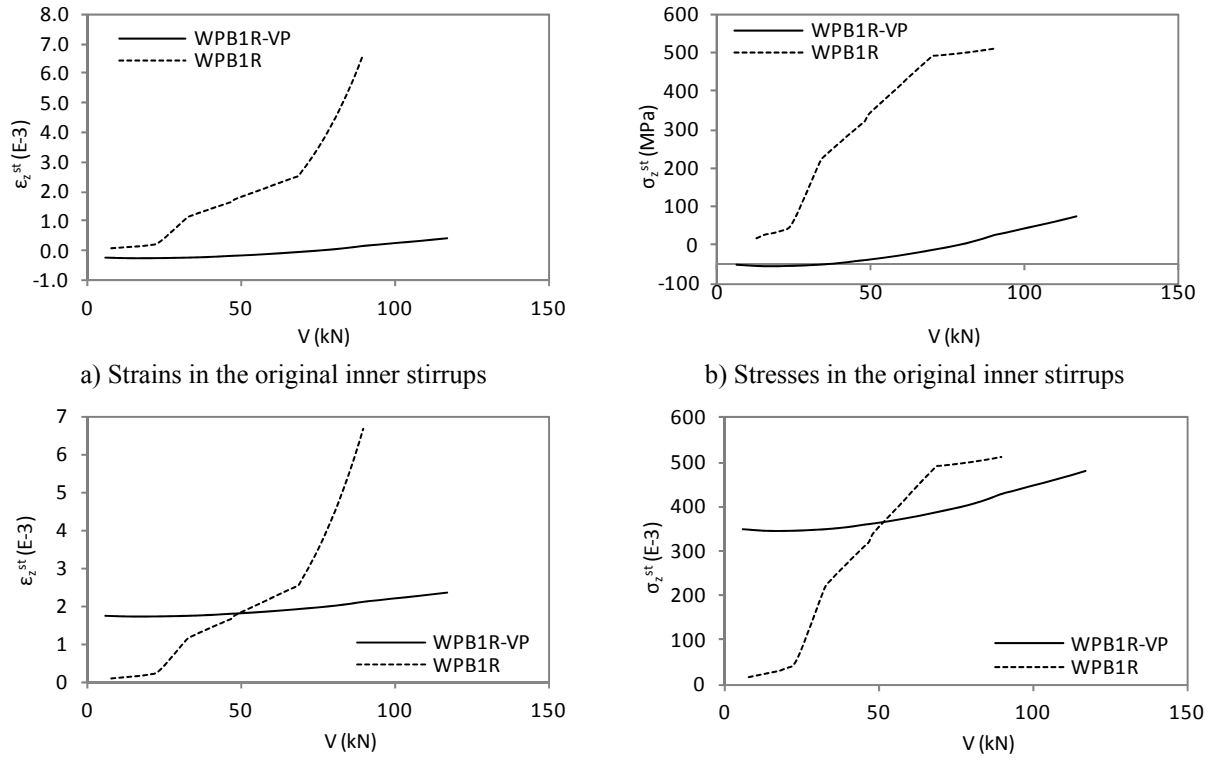

a) Strains in the original inner stirrups

b) Stresses in the original inner stirrups

c) Strains in the strengthening stirrups

d) Stresses in the strengthening stirrups

Figure 6.22 – Strains and stresses in the strengthening transversal reinforcement in the shear span of beams WPB1R (passive) and WPB1R-VP (active)

Strains in the longitudinal reinforcement ε_x^{sl} at the mid-shear span of WPB1R-VP beam are reproduced in Figure 6.23, where post-yielding of steel is perceived, almost reaching the ultimate plastic strain. In contrast, the longitudinal steel in beam WPB1R remains elastic until shear failure (see Figure 6.8).

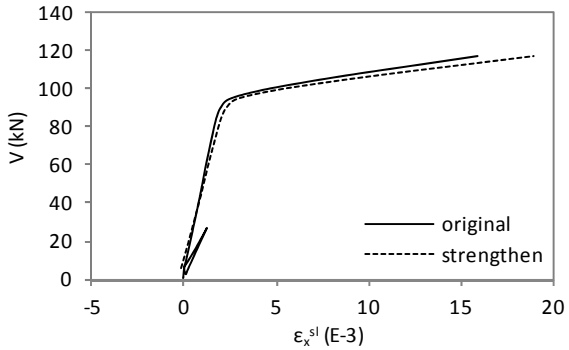

Figure 6.23 – Strains in the longitudinal reinforcement at the mid-shear span of WPB1R-VP beam

Concerning the prediction of cracking, as the non-strengthened initial beams are the same for the cases of WPB1R and WPB1R-VP, the initial damage is equal. However, the propagation of the diagonal cracking of the strengthened beam with prestressed stirrups happens at later load stages, and with higher inclinations in relation to the beam's longitudinal axis as illustrated in Figure 6.24.

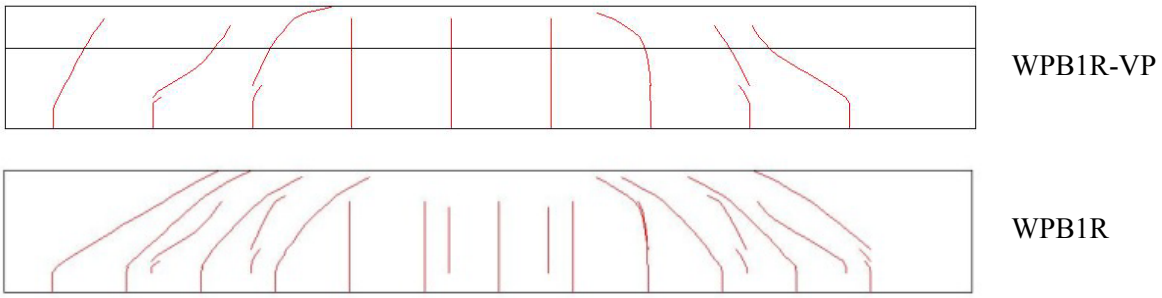

Figure 6.24 – Cracking pattern of beams WPB1R-VP and VPB1R at failure load

6.4 Full-scale application: numerical assessment and strengthening of the Wassnerwald bridge

6.4.1 Overview

An experimental campaign consisting of *in situ* tests performed on full-scale bridge girders was carried out by the Swiss Federal Institute of Technology ETH. These tests were part of a research project to assess the strength of beams provided with minimum shear reinforcement (Zwicky and Vogel 2000).

The beams came from a dismantled bridge (Lehnenviadukt Wassnerwald), built in 1969. The cross-section of the bridge consisted of four prefabricated prestressed concrete girders, and a road deck of *in situ* cast concrete, as illustrated in Figure 6.25.

Insufficient structural safety for bending and shear according to design codes at that time was reported. As the beams were highly prestressed and had a low shear reinforcement ratio (0.25%) a special attention was paid to shear strength. In fact, the initial goals of the research project were to assess the shear strength of the beams and to study strengthening solutions. However, even applying different test set-ups, shear failure was not reached before bending failure. Extra shear resistance was found to exist in this structure, even against the predictions of the actual codes.

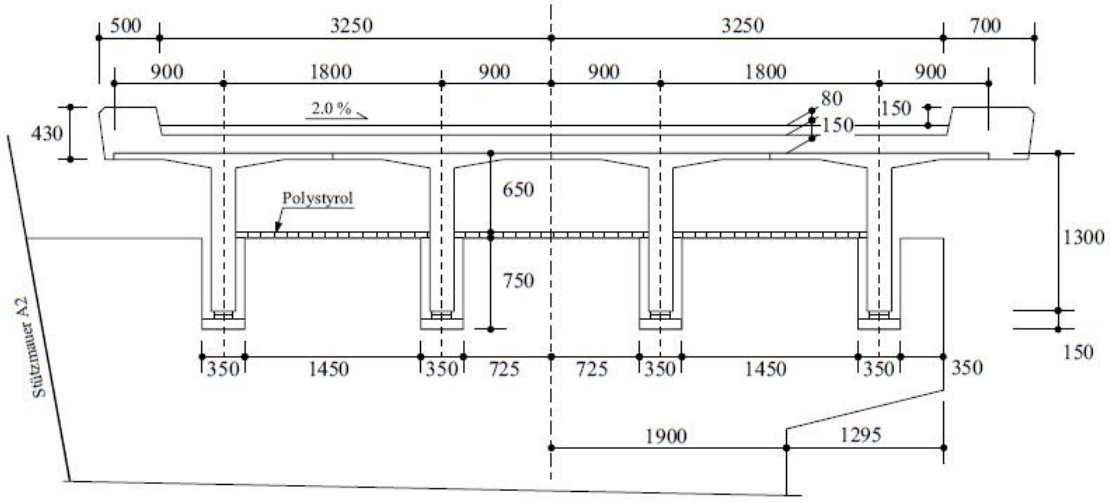

Figure 6.25 – Geometry of the cross-section of the Wassnerwald bridge (Zwicky and Vogel 2000)

The experimental full-scale tests were simulated with the proposed shear model with the objective of evaluating its capacity to reproduce the overall response of the beams. Also, it was aimed to verify if the model is able to predict the effective shear strength of prestressed beams with very low shear reinforcement.

Simulations with the pure flexural fibre beam model CONS are also included, to determinate the importance of including shear effects in the analysis. Also, the results of the numerical simulation using the FE code DIANA with 3D FE, carried out by (Pimentel, Figueiras and Bruhwiler 2007), is included. The comparison of the proposed 1D shear model with fibre beam elements with the 3D FE model of DIANA aims to demonstrate

that, the former can be a good alternative to analyse entire existent structures, with the evident advantages of simplicity and promptness.

Afterwards, in order to demonstrate the capabilities of the proposed numerical model to study dissimilar strengthening solutions of existing structures, two different solutions are to be presented: (*i*) a shear strengthening technique using vertical prestress and (*ii*) a bending strengthening through external longitudinal prestress. The resistance capacity of the strengthened beams is assessed through the proposed model. As the beams are shear-critical according to actual design codes, the consideration of shear effects in the nonlinear model is of paramount importance. Although the failure mechanism of the beams was bending dominant, it is essential to diagnose safety towards shear forces after strengthening.

6.4.2 Full-scale *in situ* tests

6.4.2.1. Description

The geometry and reinforcement characteristics of the dismantled beams are presented in Figure 6.26. Prestress consisted of pre-tensioned wires, mainly concentrated at the bottom of the web, and a post-tensioned tendon with a parabolic shape. The ordinary (passive) longitudinal and transversal reinforcement consisted of welded steel meshes. Extra reinforcement was placed near the supports. The beams were tested up to failure, and measurements included the monitoring of vertical deflections, strains in the concrete surface, cracking inclinations and crack-widths.

Two experimental tests with different load configurations (PV1 and PV4) were considered for simulation. The FE mesh of the adopted numerical model is presented in Figure 6.27, which is the same for both tests: 65 FE with approximately 0.32m of length and fibres with width from 0.13m to 0.17m. Shear resistant fibres were considered only in the cross-section web. The material properties used in the numerical model are indicated in Table 6.2, which correspond to the average results of the experimental tests on concrete and steel specimens extracted from the bridge. Pertaining to prestress, the following stress values in steel are referred (Zwicky and Vogel 2000): 1160MPa of initial prestress of the wires after immediate losses, and 1300MPa of initial post-tension of the parabolic tendon. Long term prestress losses were considered in the numerical model as 25% for the tension wires and 30% for the post-tension tendon (Pimentel, Figueiras and Bruhwiler 2007).

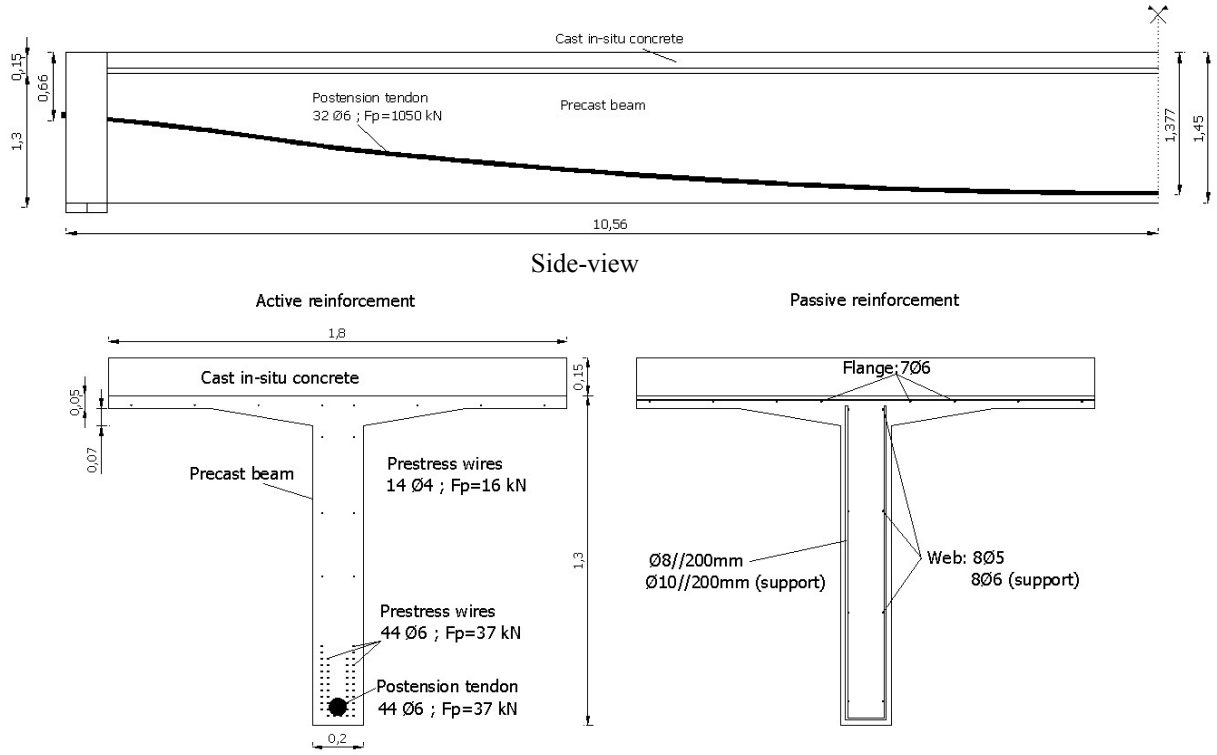

Figure 6.26 – Geometry and reinforcement of the beams of the Wassnerwald bridge

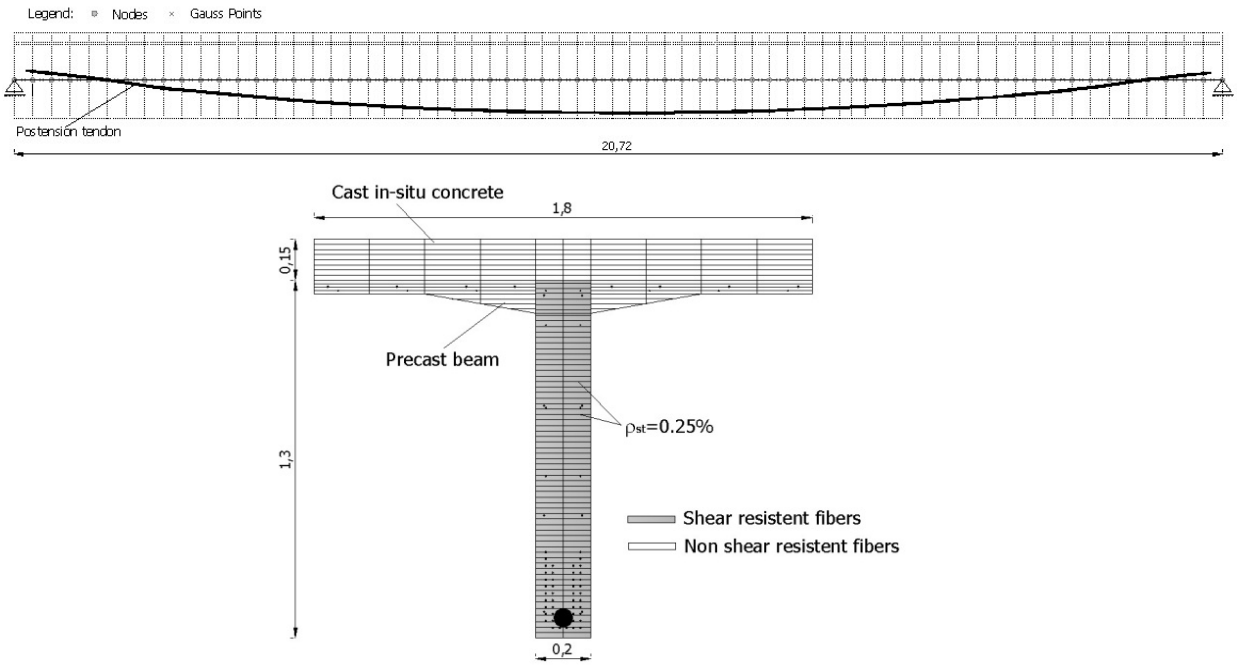

Figure 6.27 – Model of the beams of the Wassnerwald bridge

Table 6.2 Material properties of the beams of the Wassnerwald bridge (Zwicky and Vogel 2000)

Tests	Concrete (cast *in situ*)	Concrete (precast beam)	Pre-stress steel	Ordinary steel
PV1	f_c = 56.5 MPa f_{ct} = 2.41 MPa E_c = 37.0 GPa $\varepsilon_{cu} = 3.6\times10^{-3}$	f_c = 73.6 MPa f_{ct} = 2.64 MPa E_c = 34.5 GPa $\varepsilon_{cu} = 2.17\times10^{-3}$	f_{sy} = 1500 MPa f_{su}= 1700 MPa E_s = 210 GPa $\varepsilon_{su} = 26.2\times10^{-3}$	f_{sy} = 515 MPa f_{su}= 625 MPa E_s = 200 GPa
PV4	f_c= 74.3 MPa f_{ct} = 1.73 MPa E_c = 40.15 GPa $\varepsilon_{cu} = 2.89\times10^{-3}$	f_c= 83.3 MPa f_{ct} = 3.02 MPa E_c = 37.7 GPa $\varepsilon_{cu} = 2.12\times10^{-3}$		

The prestress and the self-weight of the beams were applied simultaneously in the first load step. Pre-stress with values of 910MPa were applied in the wires and 870MPa in the post-tension tendon. Afterwards, vertical load was incrementally applied until failure.

6.4.2.2. PV1 test

The set-up of the test is represented in Figure 6.28, which includes a 4-point loading configuration, a span of 20.7m (equivalent to the one in the original structure) and a shear span of 6.36m. The girder failed in bending in the middle region. Shear strength exceeded the theoretical predictions and no sign of shear failure was observed.

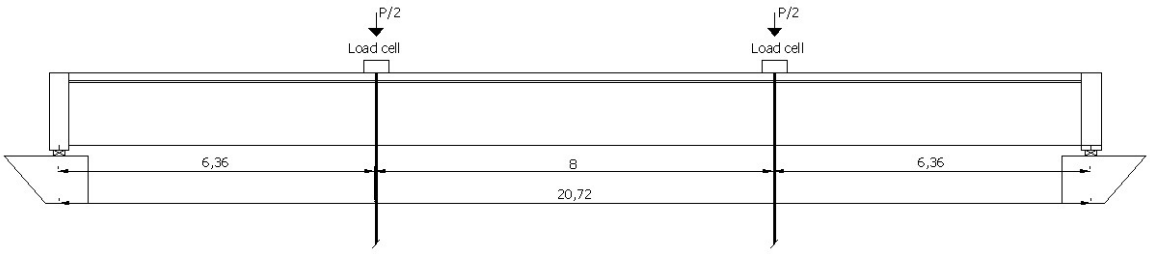

Figure 6.28 – *In situ* test PV1

Force-deflection curves for the PV1 test are depicted in Figure 6.29. An overall good prediction was achieved by all the numerical models, including the cracking and ultimate load stages. In fact, due to the flexural dominant behaviour of the beam the difference between the responses given by the flexural and the shear models are rather small. Even though, the proposed shear model approximates better the experimental curve. It is particularly relevant to observe the similar responses of the 1D proposed model and the Pimentel *et al.* 3D model. Only the ultimate strain is rather differently predicted: the 3D model estimation is much more ductile than in the experimental test (almost the double of

the ultimate experimental displacement is achieved), in contrast to the lesser ultimate displacement predicted by the proposed shear model. A summary of the experimental and numerical results at failure is presented in Table 6.3. Bending failure was predicted by all the numerical simulations, with failure of the pretension wires at the web, in the middle of the beam.

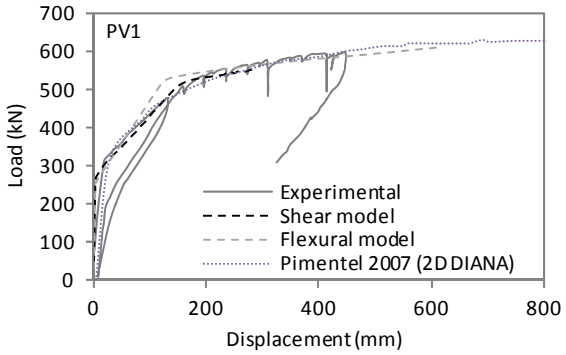

Figure 6.29 – Force-displacement at mid-span for beam PV1

Table 6.3 Summary of the experimental and numerical results for test PV1

PV1	Experimental	Shear model	Flexural model	3D DIANA (Pimentel *et al.* 2007)
P_u (kN)	597	555	612	637
Failure mode	Bending	Bending	Bending	Bending

The crack pattern at failure experimentally observed and the one predicted by the proposed shear model are presented in Figure 6.30. A generally good representation of the development and inclination of the cracks is achieved with the shear model. It is noteworthy that the separation of the diagonal cracks in the web of the beam (due to shear) is much greater than the vertical ones at the bottom due to bending; aspect that the model is not able to represent.

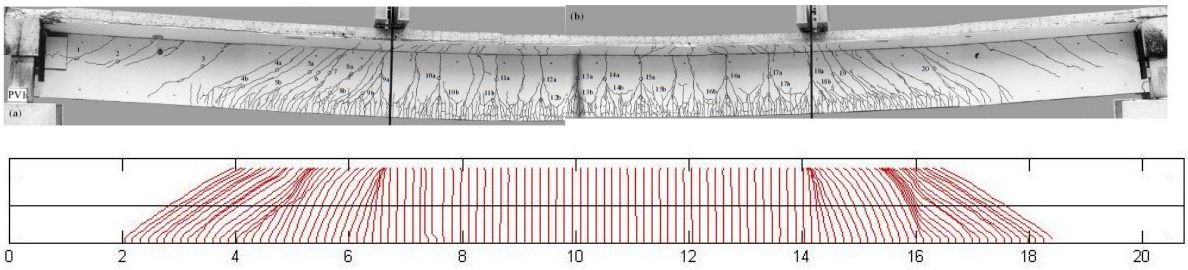

Figure 6.30 – Experimental and predicted crack patterns at failure for the PV1 test

Activation of the transversal web reinforcement was reported in a region at a 4.0m distance from the loading points, exceeding the yielding strain of the web reinforcement but without reaching the failure strain. The proposed shear model also predicted an extensive yielding of shear reinforcement in the shear spans, as demonstrated by the distribution of the vertical strain in the stirrups for the load P=505kN, presented in Figure 6.31. It is observed that the yielding strain, which takes the value of 2.575×10^{-3}, is exceeded in the shear spans near the loading point.

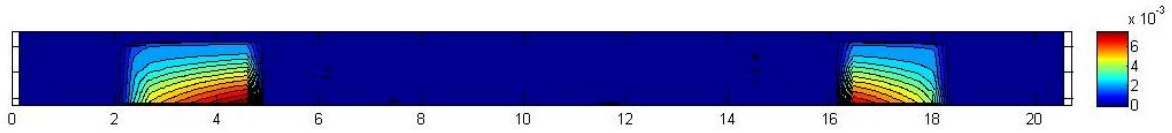

Figure 6.31 – Vertical strains at PV1 test for P=505kN

6.4.2.3. PV4 test

The set-up of the experimental *in situ* test PV4 is represented in Figure 6.32. The aim of this test was to obtain a shear failure through the crushing of the web concrete, which did not happened. The main span was reduced to 18.6m and a 3-point loading configuration was considered, with a distance of 3.8m between the left support and the load application point. The position of a vertical strain gauge T_Z measuring strains in concrete is also represented in this Figure.

The beam also failed in bending at the loading point, however, an abrupt failure with no strain-softening behaviour was reported. It was also mentioned that the shear resistance determined according to the codes at that time was exceeded in 93% (Zwicky and Vogel 2000).

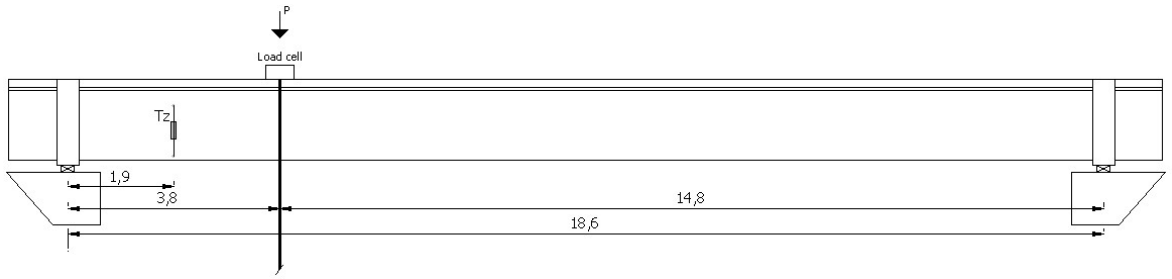

Figure 6.32 – *In situ* test PV4

The experimental force-deflection curve is depicted in Figure 6.33, along with the predictions from the numerical models. In this case, as shear stresses are more significant, the difference between the shear and the flexural model curves is more accentuated in comparison to the PV1 test. Even predicting a lower ultimate load, an acceptable fitting between the proposed shear model and the experimental data is perceived. In turn, the 3D model gives a better prediction of the failure load, but the ultimate displacement is much higher than the experimental one. A summary of the experimental and computed responses of the beam test at failure is given in Table 6.4. Bending failure was predicted by all the models. In the proposed shear model, along with the failure of the longitudinal bottom web reinforcement, an extensive yielding of stirrups was predicted in the shear span.

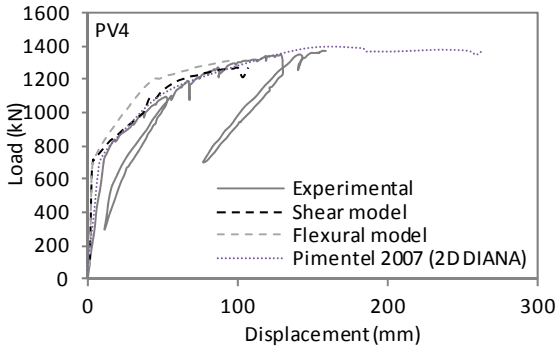

Figure 6.33 – Force-displacement under load for beam PV4

Table 6.4 Summary of the experimental and numerical results for test PV4

PV4	Experimental	Shear model	Flexural model	3D DIANA (Pimentel *et al.* 2007)
P_u (kN)	1345	1265	1323	1367
δ_u (mm)	142	101	98	264
Failure mode	Bending	Bending	Bending	Bending

Average strains in the vertical direction (correspondent to concrete and the stirrups) in the shear span are depicted in Figure 6.34, where is observed that the load correspondent to the activation of the transversal reinforcement is well reproduced by the shear model. In turn, the 3D model predicts a sooner activation of the stirrups, but fits better the following development of the strains.

It is reported that the transversal reinforcement reached yielding in a region from 2.5m of the left support towards the loading point, but stirrup failure was not achieved. Similar predictions were given by the proposed shear model, as it can be observed in the

distribution of the stirrup strains along the beam in Figure 6.36 for a load P = 1200kN. The yielding stirrup strain is 0.002575, value that is extensively exceeded in the shear span near the loading point.

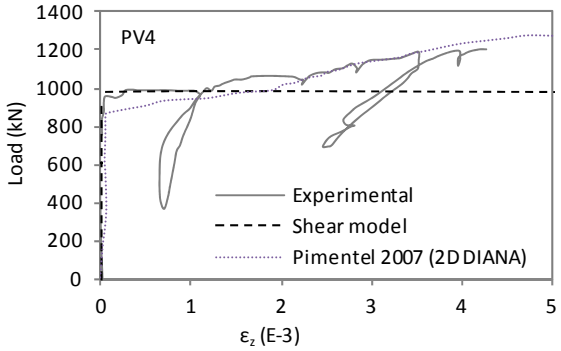

Figure 6.34 –Strains in the vertical direction in the shear span for beam PV4

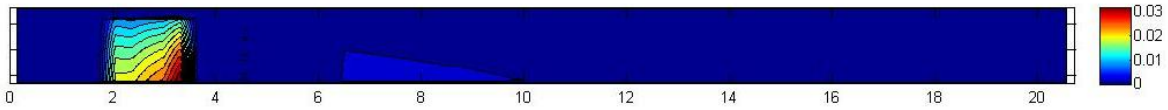

Figure 6.35 – Vertical strains at PV1 test for P=1200kN

Observed crack pattern at failure and the correspondent prediction from the shear model are presented in Figure 6.36. A high concentration of cracks in the shear span near the point of load application is indicated by the proposed model, corresponding to the region of extensive yielding of the stirrups. Generally speaking, the damage of the beam at failure is well reproduced by the numerical model.

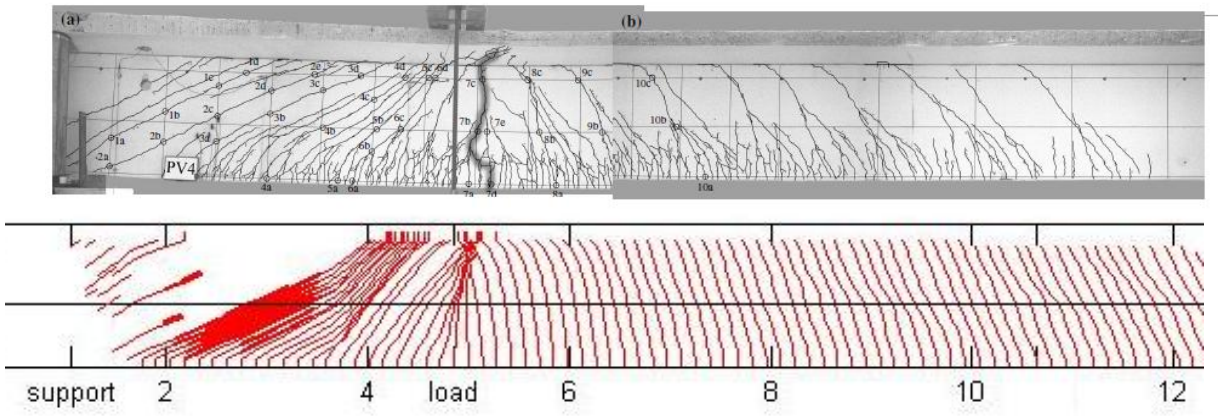

Figure 6.36 – Experimental and predicted crack patterns at failure for the PV4 test

6.4.3 Strengthening solutions

6.4.3.1. Preamble

The decision of dismantling the Wassnerwald bridge was based on the lack of safety found according to the standards at that time. Two possible strengthening solutions are analysed with the proposed shear model.

As the beams had minimum transversal reinforcement, shear resistance was originally the main concern. Consequently, a strengthening solution towards increasing shear resistance by means of extra stirrups vertically prestressed is initially presented. As the beams actually failed in bending, a shear strengthening measure can be inefficient to increase the load capacity of the bridge.

Hence, a flexural strengthening solution applying extra longitudinal external prestress was studied afterwards. Even with a bending dominant failure, the consideration of the shear effects in the nonlinear analysis is of paramount importance in order to reach a realistic prediction of the behaviour. Also, it is essential for verifying shear safety when the structure is strengthened to bending.

The strengthened beams were simulated considering the PV4 test configuration and the same meshes and material properties were used in the simulations.

6.4.3.2. Addition of vertical prestress

The shear strengthening solution presented in the following consists of adding vertical prestress bars with 36mm of diameter, with a 400mm spacing. The properties of the prestressing steel bars were considered as: f_{sy}=970MPa, E_s=205GPa, f_{su}=1070MPa and ε_{su}=0.07. A post-tension of 690MPa (based on 90% of the yielding strength, and assuming 20% for the total prestress losses) is assumed to be applied vertically. The prestress rebars were anchored to the top and bottom faces of the beam and the web was enlarged as represented in Figure 6.37.

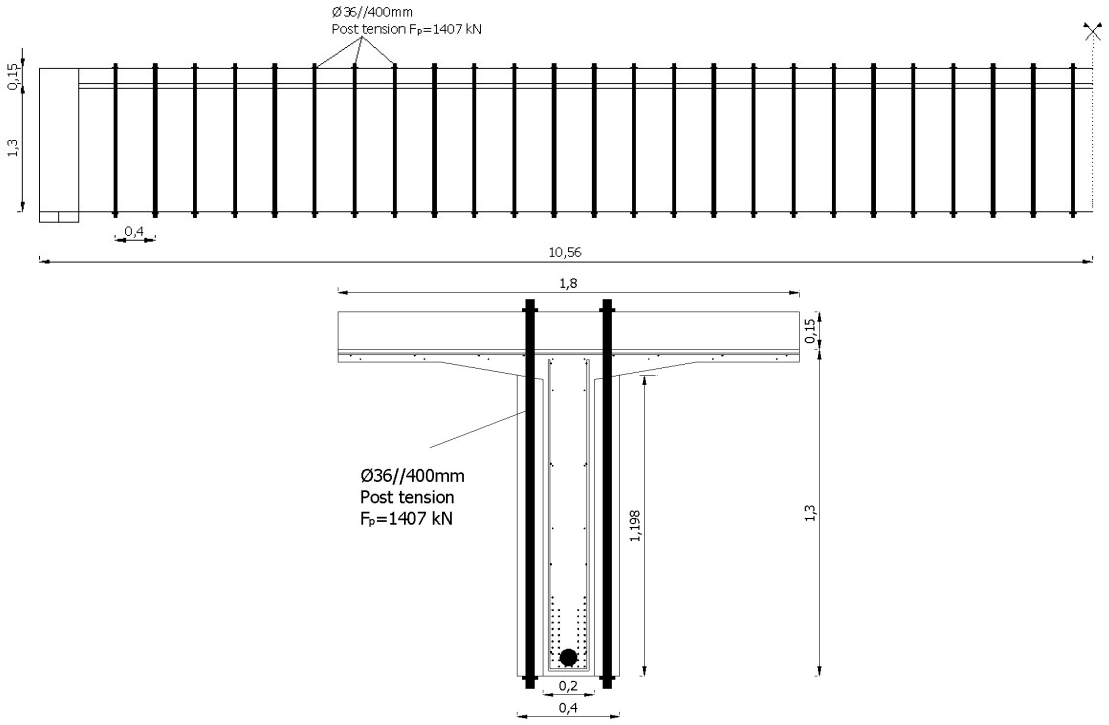

Figure 6.37 – Shear strengthening proposal for the Wassnerwald bridge

The global behaviour of the strengthened beam is expressed by the force-deflection curve depicted in Figure 6.38, together with the experimental and numerical ones of the original beam. As the failure mechanism, against the expectations, ended up to be flexural critical, the increment of shear resistance made no difference in the failure load of the strengthened beam. A later cracking load and a stiffer response of the strengthened beam are also observed, in comparison with the original one.

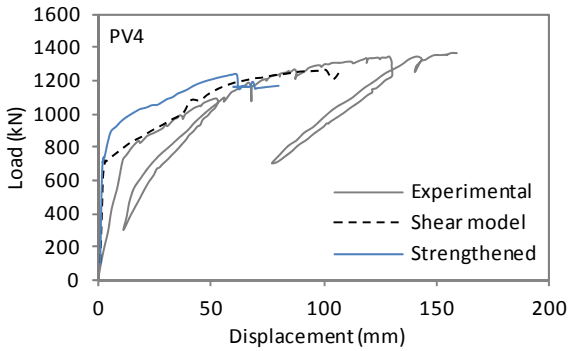

Figure 6.38 – Displacement under load for the test PV4: original and shear strengthened beams

6.4.3.3. Longitudinal external prestress

The strengthening solution with longitudinal external post-tensioned tendons is presented in Figure 6.39. It consisted of two external rebars with a 36mm diameter, with a linear configuration. The properties of the prestressing steel bars were considered as: f_{sy}=1500MPa, E_s=210 GPa, f_{su}=1700MPa and ε_{su}=0.0262. A post-tension stress of 870MPa was applied at each external tendon.

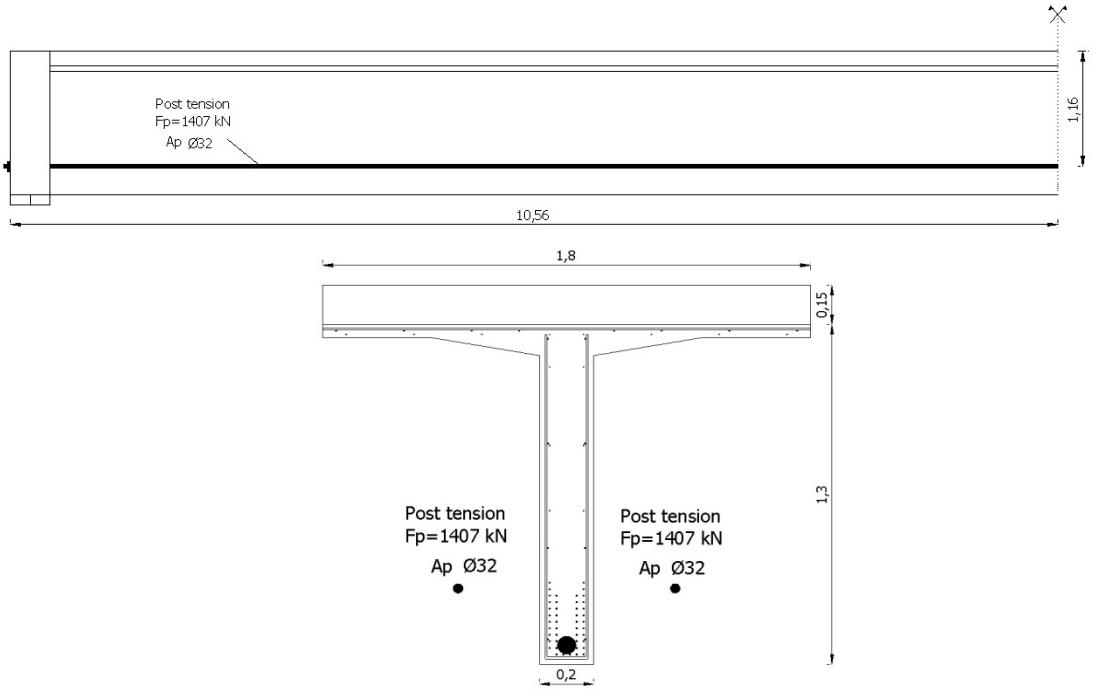

Figure 6.39 – Strengthening proposal of the Wassnerwald bridge by post-tensioned longitudinal reinforcement

The response of the strengthened beam is represented by the force-deflection curve depicted in Figure 6.40, where the numerical and experimental curves of the original beam are included as well. A greatly improved performance, both in terms of the cracking and of the failure loads, was attained with this strengthening solution. In fact, the strengthened beam almost doubled its load carrying capacity, reaching a flexural failure for an total external force of 2184kN. As a result of with this preliminary analysis, this proposal could be a possibility for a strengthening intervention to the existent bridge.

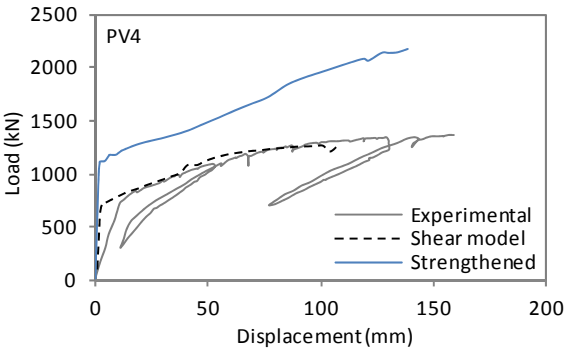

Figure 6.40 – Force-displacement under load for the test PV4: original and flexural strengthened beams

6.5 Conclusions

In this chapter, the proposed model was enhanced in order to analyse existent RC structures subjected to repair and strengthening interventions. In this ambit, the relevant attributes of the proposed formulation are: (*i*) its capability for considering shear effects in both service and ultimate levels and (*ii*) the step-by-step nonlinear sequential type of analysis, which allows capturing the strengthening effects, accounting for the state of the structure prior and after the interventions.

In order to validate the proposed model, an experimental test available in the literature, with previously shear damaged beams and subsequently repaired and loaded until failure, was simulated. The entire loading history and repair procedures of the test were modelled, along with the reference beams (without previous damage or strengthening interventions). An acceptable fitting of the model predictions to the experimental results was observed, namely relating to the ultimate shear strength, the shear failure mechanism, the deflections, the strains in the longitudinal and transversal reinforcement and the diagonal cracking patterns. Importance of the shear-bending interaction in the numerical analysis was underlined by comparing the results of the shear model with the ones provided by the pure flexural FE model.

Also, an alternative strengthening solution for the damaged beam based on post-tensioned stirrups was numerically analysed. This technique showed to be effective to avoid brittle shear failure, allowing for the development of all the flexural capacity of the repaired

beam. Consequently, the original shear brittle failure mode changed to the ductile flexural one.

Afterwards, the numerical assessment of an existent bridge was presented. The experimental full scale *in situ* tests carried out on the beams of a dismantled bridge in Swiss (Wassnerwald Viaduct) were analysed with the proposed shear model. As the beams were heavily prestressed and had a minimum reinforcement as stirrups, shear resistance was the main concern. At the end, only bending failures were achieved and loading capacities were substantially higher than the ones determined through the standard codes. The general response of the beam tests, both in cracked and ultimate stages, was reasonably well reproduced by the proposed shear model.

Afterwards, two strengthening solutions for the bridge were analysed with the proposed model: one towards increasing the shear capacity of the beam by applying vertical prestressed stirrups, which proved to be inefficient as the failure mechanism was flexural dominant; and other with external longitudinal post-tensioned tendons that allowed a significant increase of the load carrying of the beams.

Therefore, the strengthening solutions analysed with the proposed model demonstrate its most relevant significance: the ability to predict the response and the load capacity of existent shear-critical RC structures and supporting the design of feasible strengthening interventions.

Actually, existent structures may not be assessed according to actual standard norms in the same way as new structures. This is a very complex topic that has special urgency to be developed. In fact, accurate assessment of existence structures can actually prevent expensive strengthening, or premature dismantling of whole structures. Nonlinear FE models, as the one proposed in this thesis, can be a tool in the assessment of aging structures.

Chapter 7

CONCLUSIONS

7.1 General results and conclusions

The model presented in this thesis aims to extend the capabilities of a pure bending displacement-based fibre beam approach for the time-dependent analysis of segmentally constructed RC structures with relevant shear forces. Shear effects are introduced by means of a mixed kinematic/force-based sectional approach, in which the plane section's theory is used to determine the normal strains in each fibre, along with the assumption of a fixed shear stress flow along the section. At the element level, the Timoshenko beam's theory accounts for the shear deformation. The non-orthogonal and full-rotating smeared crack concept is used to simulate the response of cracked concrete under multiaxial stress states. A discrete crack representation is performed by means of an external algorithm that prints the development of the crack patterns in the finite elements.

The time-dependent structural response under phenomena such as concrete creep and shrinkage, temperature variations and relaxation of prestressing steel under multiaxial stress states is available within a time-step analytical procedure. In addition, the model is able to simulate the response of existing RC frame structures subjected to repair and strengthening interventions through a step-by-step nonlinear sequential analysis.

The goals listed in Section 1.2 are considered fulfilled, having been successfully accomplished the following aims of this research work:

- An enhanced shear-sensitive fibre beam element model, suitable for the numerical simulation of the nonlinear response along the service life of existing RC frame structures, was developed and implemented. The model considers the interaction of normal and shear forces at service and ultimate limit stages.
- Along with the possibility of simulating shear-critical problems, the model is able to reproduce evolutive construction, such as repair procedures, by means of time-dependent and segmental construction modelling features.
- Time-dependent effects such as concrete creep and shrinkage, as well as prestress relaxation, are taken into account, regarding the multiaxial stress and strain states generated by the presence of shear forces.
- The step-by-step nonlinear sequential type of analysis allows capturing the strengthening effects, accounting for the state of the structure prior to the retrofitting and upgrading interventions.
- Fulfilling the rising need for repair or strengthening of existing structures, the model can be used to accurately assess the structural behaviour of existing RC frames, in order to evaluate the needs of intervention and also to design a safe repair or retrofit intervention.
- Due to its computational efficiency the model is feasible for engineering practice applications, being a suitable alternative tool to complex nonlinear higher-order FE analyses.

From the results attained in the several numerical simulations performed, the general conclusions drawn from this research work can be pointed out as it follows:

- Shear critical RC frame structures cannot be correctly simulated by means of flexural fibre beam models.
- Shear effects influence the overall performance of the structures, and affect the deflections and the development of cracking at the service-life load stages. They also influence the load carrying capacities and structural failure modes at the ultimate stages.
- The simplified approach of constant shear stress throughout the height of the cross-section, along with the smeared crack approach, proved to be adequate for

efficiently predicting the development of diagonal concrete cracking, the yielding of transversal reinforcement and the shear failure modes.

- The proposed fibre beam model reproduced accurately the structural response of shear critical beams and frames.
- The inclusion of shear effects is essential for the numerical assessment of existent and strengthened structures, as the strengthening measures can change the failure mode from flexural- to shear-based.
- Existent damaged structures may also lack of shear resistance and require shear strengthening interventions. Their responses can only be accurately determined by numerical formulations that include the shear-bending interaction and are capable of predicting shear failure modes.
- Consideration of the damages previous to the interventions is essential to achieve an adequate accuracy in the analysis of strengthened beams and frames.
- Pertaining to numerical efficiency, the model is robust enough to treat problems with vast cracking patterns and fragile failures, such as the typical shear-critical cases.

In the ensuing section the specific conclusions related to each part of the research work developed in this thesis are presented.

7.2 Specific conclusions

7.2.1 Inclusion of shear effects in a fibre beam model

In order to validate the proposed model, various experimental tests on shear-critical RC beams and frames, both available in the literature and carried out by the author, were simulated. From these numerical analyses and comparisons with the experimental data, the following conclusions can be set:

- The numerical model was able to reproduce the failure loads and mechanisms of shear critical beams (shear-tension and shear-compression).
- Importance of including the shear-bending interaction in the numerical analysis was underlined by comparing the results of the shear- and of the pure flexural–based FE models. In the former case, only bending failures are possible and the strain

increments in the longitudinal reinforcement due to the shear resistant mechanism are neglected.

- Fairly good predictions of the overall experimental behaviour were provided by the proposed shear model. Experimental measurements were compared with the computed results - displacements, principal strains and directions in concrete, distortion in concrete webs, strains in the longitudinal and transversal reinforcement - and a good fitting was generally obtained.
- The fundamental hypothesis of the sectional model – constant shear stress flow along the height of the cross-section – allowed to achieve good predictions of the response of RC elements without the need of great computational resources.
- Regarding that the proposed shear model is based on simplified assumptions, its capacity to properly account for the contribution of the stirrups in the shear resistance of the beams was remarkable.
- The validity of the model for analysing shear critical elements is also verified for the case of beams without transversal reinforcement.
- Cracking patterns of RC beams with transversal reinforcement were accurately predicted by the numerical model, in terms of direction and propagation of cracking during the loading history.

7.2.2 Shear effects and time-dependent analyses

The influence of shear on the long-time response due to concrete creep and shrinkage of diagonally cracked RC elements was analysed with the numerical model, based on experimental tests available in literature. Also, parametric studies on the influence of restraint strains due to shrinkage on the ultimate response of shear critical beams were carried out. From this research, the following conclusions are set:

- Considering shear effects in the numerical simulation of the time-dependent response of diagonally cracked beams is required in shear dominated situations, to ensure a correct prediction of the total deflections.
- Shear effects had a strong influence on the instantaneous behaviour of shear-dominated RC applications, but a much lesser impact in the long-term deformation.
- The consideration of shear effects slightly reduces the computed increment of deflection due to creep as, for a cracked cross-section, the presence of shear

stresses leads to lower longitudinal stresses in concrete in the uncracked area, for the same applied bending moment.

- Relaxation of the stresses in the stirrups with time due to the decrease of compressive stresses in concrete in the vertical direction was predicted by the numerical model. However, this effect did not present a relevant significance in the analysis.
- Restraints to shrinkage-induced strains affected the long-term response of shear critical beams. The damage and initial tensile strain caused by the restrained shrinkage strains diminish the load carrying capacity of the beams (circa 5-20% of the ultimate load) as it reduces the concrete contribution to shear resistance and causes the activation of the transversal reinforcement for lower loading levels.

7.2.3 Modelling damaged and shear strengthened concrete elements

An experimental test available in the literature with previously damaged shear critical beams, and subsequently strengthened and loaded until failure, was simulated with the model. The entire loading history and repairing procedures of the test were modelled, along with the reference beams (without previous damage or strengthening interventions). After being validation with the experimental data and based on the former experimental test, an alternative strengthening technique based on using external post-tensioned stirrups was numerically analysed.

Lastly, the model was applied to the assessment of a real bridge that was dismantled and submitted to full-scale tests. The bridge was deficient in shear resistance, in light of the current design codes. Different strengthening solutions based on external prestress were numerically studied.

From these numerical analyses on shear damaged and strengthened structures the following conclusions are derived:

- The proposed model is accurate for simulating shear damaged and strengthened RC beams.
- An acceptable fitting of the model predictions to the experimental observations was observed for the shear strengthened beams, namely in what concerns to the ultimate shear strength, the failure mode, the deflections, the strains in the longitudinal and transversal reinforcement and the diagonal cracking patterns.

- Modelling strengthening procedures through phased-analysis is essential to attain good predictions of the behaviour of strengthened beams, as the previous damage can influence its final response.
- The transversal post-tension strengthening technique, which is a rather efficient method towards increasing the shear capacity of RC beams, was accurately simulated by the proposed model.
- Post-tensioned tendons showed to be effective to avoid brittle shear failures, by allowing the development of all the flexural capacity of the repaired beams. Consequently, the original shear brittle failure mode changed to the ductile flexural one.
- The model predicted the response of an existent prestressed concrete bridge with good accuracy, and demonstrated efficiency for checking the performance of different strengthening solutions.
- The failure of the beams of bridge was dominated by bending and the shear strengthening solution by means of vertical prestressed stirrups was not efficient in increasing its load carrying capacity, as failure was predicted to occur by crushing of the concrete strut in the web.
- Strengthening of the beams of the bridge regarding longitudinal external post-tensioning was predicted to be efficient in increasing significantly its ultimate loading.

7.3 Original contributions

The main contribution of the research work developed in this thesis was centred on the implementation of a nonlinear shear-bending interaction formulation, based on the fixed stress approach into a fibre beam model. Also, the enlargement to shear-critical cases of the basic flexural model capabilities to simulate the time-dependent and segmental construction features generated a fibre beam model with unique characteristics, resulting into a powerful and functional computational tool.

Hence, the original contributions of the model developed in this thesis are:

- Consideration of normal-shear force interaction in the resistance mechanism, as well as, shear contribution to deflection during all the nonlinear path of the

structure under loading by means of a computationally efficient nonlinear fibre beam model.

- Correctly simulate the load carrying capacity and failure mechanisms of shear-critical RC frame structures, with or without transversal reinforcement.
- Consideration of time-dependent analysis, such as, creep, shrinkage, ageing, prestress loss, regarding the multiaxial strain-stress state generated by the presence of shear forces.
- Performing life-time analysis, that accounts for any changes in the structural layout and strengthening/retrofit interventions, through a segmental constructive analysis procedure. The state of the structure previous to change or intervention is accounted for in the subsequent analysis.
- Simulates shear-strengthening interventions, including the application of extra stirrups and concrete section and transversal post-tensioned tendons.

7.4 Future developments

As a consequence of the numerous analyses that are possible to be undertaken with the enhanced shear-bending fibre beam model, many research subjects are left opened. Some topics need experimental tests in order to validate some model's assumptions; others require further numerical improvements to increase the accuracy and computational stability. As the model is written in a modular scheme, the incorporation of new formulations can be accomplished in a direct and straightforward manner.

The future work proposals are related with the enhancement of the nonlinear numerical model for life-time analysis of strengthened structures presented in this thesis. In this manner, it is aimed to attain better numerical approaches for the assessment of existing structures and to check the performance of strengthening procedures. All the developments in the ambit of computational models require suitable experimental tests for its proper validation. Hence the main proposals for future research works are briefly described as follows:

- *Experimental tests on the time-dependent response of diagonally cracked RC concrete beams.*

  The shear effects on the time-dependent response of cracked RC beams are still considerably unknown. In fact, experimental tests and numerical analyses focused

on this ambit are scarce. Also, the effects of creep and restrained shrinkage in the behaviour of shear critical elements, both in service and ultimate stages, are not clearly defined. In this thesis a brief insight into this topic has been made; however, it needs further development. Shear-focused experimental tests on diagonally cracked beams under sustained loading are needed, in order to better understand this phenomenon. The experimental work is also essential for the development of more accurate numerical models in this field.

– *Shear sectional assumption for evolutive and strengthened cross-sections.*
Research on the stress distribution between old and new parts in RC strengthened elements is required. The simplification hypothesis assumed in this thesis, of identical stress distribution in the shear effective area of the whole strengthened section, neglects possible differences on the distributions of the shear stresses among the original and the repairing materials. The shear stress distribution along a cross-section can be more accurately studied through advanced models (e.g., model TINSA (Bairán and Marí 2006; Bairán and Marí 2006)). An improved solution for the assumption taken in the proposed model can be based on a phased-analysis version of this advanced model.

– *Shear stress assumption for complex geometries.*
The constant shear stress distribution along the height of the beam web assumed in the proposed model showed to be accurate for the cases of rectangular and T-shaped cross-sections. For other complex cross-sectional geometries a more sophisticated analysis with the model TINSA (Bairán and Marí 2006; Bairán and Marí 2006) is required, in order to determine the portion of section that is preponderant for resisting to shear forces. This subject deserves further developments, in order to provide the criteria for the definition of fixed shear stress patterns for beams with complex cross-section configurations.

– *Enhanced shear stress patterns.*
Development of enhanced patterns for the distribution of shear stresses in the cross section associated with key stages of damage – e.g. linear, cracked, advanced shear cracking and yielding of transversal reinforcement and near failure – based on the assumption that damaged fibres carry less shear stresses than undamaged ones. In this manner, the shape of the shear stress flow would change during the analysis, in some key strategic pre-defined points, by concentrating the shear stresses in the less

damaged cross-section zones. This would increase the accuracy of the model by approximating it to the actual shear resistance mechanisms. This could also enhance the numerical performance of the model for post-peak analyses, by assisting the innermost iteration procedure at the fibre level to continue the computation beyond material failure.

- *Experimental tests on the time-dependent response of strengthened elements.*
  Development of experimental tests on shear critical RC elements submitted to previous mechanical and environmental damages, and subsequently strengthened via different solutions, is commendable. The experimental observation would also support the development of more accurate numerical formulations in this ambit. Influence of the time-dependent phenomena on the mechanical response of the strengthened RC elements could also be studied.

- *Constitutive and bond-slip models for strengthening materials.*
  The simulation of fibre reinforced polymers (FRP) can be included in the numerical model by means of a new constitutive law. Also, implementation of a suitable bond-slip model at the new-old concrete and concrete-FRP interfaces would be advantageous. In this manner, the model would be able to simulate strengthened shear-critical RC frame structures with higher accuracy and enlarging its application to the use of FRP.

- *Account for fibre reinforced concrete.*
  Implementation of a constitutive equation for fibre reinforced concrete is proposed in order to be able to simulate shear-critical elements made with this material. Also, by these means, it will be possible to simulate strengthening interventions towards increasing shear capacity by means of enlarging the cross-section with fibre reinforced concrete.

- *Flexibility-stiffness mixed finite element*
  Capturing the contribution of shear to the deflection of the elements is not an easy task to accomplish by means of fibre beam models. In fact, the proposed model considers shear flexibility at the element level as a constant additional rotation of the cross-section, resulting into an important simplification of the sectional behaviour. For this reason, the element shear rotation is corrected through residual forces, by means of the average sectional distortion determined from the sectional

model. This correction of shear distortion at the element level is needed because of the characteristics of the model: displacements are used to approximate flexural-based strains and forces are used to approximate shear strains and stiffnesses; and they are both linked to a displacement-based FE model.

In fact, as the sectional model developed in this thesis is based on a mixed formulation (force and strains as inputs and outputs), the natural way to passing it to the element level should be by means of a mixed FE formulation. A flexibility-stiffness mixed element, in which the nodal displacements would be used to approximate the normal strains and curvatures (bending-related variables), and a force node in the element would be used to determine stresses, would be the ideal formulation format. This is a conceptual proposal for an element explicitly devised for the mixed sectional model developed in this thesis. By this means, the numerical model could increase its accuracy and numerical stability.

- *Seismic actions*

  Given its relative simplicity and computational efficiency, beam filament models are a powerful tool for design purposes, namely for applications where seismic actions are involved. For this reason, the proposed model could be extended for seismic loading cases. In this manner, shear influence on the structural response and shear failure mechanisms could be intrinsically detected in the analysis of damaged and strengthened structures.

- *Partially prestressed concrete elements*

  The model developed in this thesis can be used to study partially prestressed concrete elements, including its redistribution capacity and overall structural response in service and ultimate stages. In this manner the model can act as a key tool for the development of a performance-based design methodology for the consideration of non-linear structural behaviour in the design stage.

- *Reliability analyses*

  The deterministic nonlinear numerical model developed in this thesis could be introduced to a probabilistic framework, in order to perform reliability analysis of bending and shear critical structures. In this ambit, due to its inherent computational efficiency, the proposed nonlinear fibre beam model with shear-bending interaction could determinate the structural capacity with few computational and processing-time demands. Also, time-dependent deterministic

analyses can be broadened to probabilistic analyses for each point in time. Service-life modelling and the determination of the efficiency of strengthening measures were performed in a deterministic manner by the proposed nonlinear fibre beam model. But by taking into account the probabilistic life-time approach, the structural reliability could be evaluated concerning different strengthening alternatives.

REFERENCES

Abdollahi, A. (1996). "Investigation of objectivity in the application of the FEM to RC structures - II." *Computers & Structures*, Vol. 58(6), p. 1183-1211.

Aboutaha, R. and N. Burns (1994). "Strengthening of prestressed concrete composite beams using external prestressed stirrups." *PCI Journal*, July-August, p. 65-74.

ACI Committee 318 (1995). *Building code requirements for reinforced concrete*. Detroit.

Adhikay, B. and H. Mutusuyoshi (2006). "Shear strengthening of reinforced concrete beams using various techniques." *Construction and Building Materials*, Vol. 20, p. 366-373.

Bairán, J. (2005). *A non-linear coupled model for the analysis of reinforced concrete sections under bending, shear, torsion and axial forces*. PhD Thesis, Departament D'Enginyeria de la Construcció, Universitat Politècnica de Catalunya, Barcelona.

Bairán, J. and A. Marí (2006a). "Coupled model for the non-linear analysis of anisotropic sections subjected to general 3D loading. Part 1: Theoretical formulation." *Computers & Structures*, Vol. 84, p. 2254-2263.

Bairán, J. and A. Marí (2006b). "Coupled model for the non-linear analysis of anisotropic sections subjected to general 3D loading. Part 2: Implementation and validation." *Computers & Structures*, Vol. 84, p. 2264-2276.

Bairán, J. and A. Marí (2007a). "Shear-bending-torsion interaction in structural concrete members: a nonlinear coupled sectional approach." *Arch Comput Methods Eng*, Vol. 14(3), p. 249-278.

Bairán, J. and A. Marí (2007b). "Multiaxial-coupled analysis of RC cross-sections subjected to combined forces." *Engineering Structures*, Vol. 29, p. 1722-1738.

Bairán, J. M., A. R. Marí and S. Mohr (2010). "Estudio del comportamiento del hormigón armado ante esfuerzos normales y tangentes mediante modelos seccionales de interacción

completa (Study of the behaviour of RC under normal and tangential stresses through total interaction sectional models)". *Informes de la Construcción*, Vol. 62(518), p. 65-77.

Bakis, C. E., L. C. Bank, V. L. Brown, E. Cosenza, J. F. Davalos, J. J. Lesko, A. Machida, S. H. Rizkalla and T. C. Triantafillou (2002). "Fibre-reinforced polymer composites for construction - state-of-the-art review." *Journal of Composites for Construction*, Vol. 6(2), p. 73-87.

Balázs, G. L. (2010). "A historical review of shear. Shear and punching shear in RC and FRC elements. " *FIB - Technical Report*, Proceedings of a workshop on 15-16 October 2010, Lake Garda, Italy.

Bazant, Z. (1983). "Comment on orthotropic models for concrete and geomaterials." *Journal of Eng Mechanics*, Vol. 109(3), p. 849-865.

Bazant, Z. (1988). *Mathematical modeling of creep and shrinkage of concrete*, John Wiley and Sons.

Bazant, Z. and S. Wu (1973). "Dirichlet series creep function for ageing concrete." *Journal of Eng Mechanics Division*, Vol. 99, p. 367-87.

Bazant, Z. P. and I. Carol (1993). "Fifth RILEM International Symposium on Creep and Shrinkage of Concrete (ConCreep-5). Barcelona, Spain 6-9 September 1993." *Materials and Structures*, Vol. 27(6), p. 370-372.

Bazant, Z. P. and J. Guang-Hua (2008). *Comprehensive database on concrete creep and shrinkage. (S. E. R. N. 08-3/A210c)*, Infrastructure Technology Institute, McCormick School of Engineering and Applied Science, Northwestern University, Evanston, Illinois, USA.

Bazant, Z. P. and B. H. Oh (1985). "Microplane model for progressive fracture of concrete and rock." *Journal of Eng Mechanics*, Vol. 111(4), p. 559-582.

Bazant, Z. P. and J. Ozbolt (1990). "Nonlocal microplane model for fracture, damage, and size effect in concrete structures." *Journal of Eng Mechanics*, Vol. 114(10), p 1672-1702.

Bazant, Z. P. and S. T. Wu (1973). "Dirichlet series creep function for aging concrete." *Journal of Eng Mechanics*, Vol. 99(2), p. 367-387.

Bentz, E. (2000). *Sectional analysis of reinforced concrete members*. PhD Thesis, University of Toronto, Toronto

Borst, R. (1987). "Computation of post-bifurcation and post-failure behavior of strain-softening solids." *Computers & Structures*, Vol. 25(2), p. 211-224.

Borst, R. and P. Nauta (1985). "Non-orthogonal cracks in a smeared finite element model." *Eng. Comput*., Vol. 2, p. 35-46.

Bresler, B. and A. C. Scordelis (1963). "Shear strength of reinforced concrete beams." *Journal American Concrete Institute*, Vol. 60(1), p. 51-72.

Broo, H. (2008). *Shear and torsion in concrete structures*. PhD Thesis, Department of Civil and Environmental Engineering, Chalmers University of Technology, Goteborg.

Buckle, I. and A. Jackson (1981). *A filamented beam element for the non-linear analysis of reinforced concrete shells with edge beams*, Departament of Civil Engineering, University of Auckland, New Zeland.

Bukhari, I. A., R. L. Vollum, S. Ahmad and J. Sagaseta (2010). "Shear strengthening of reinforced concrete beams with CFRP." *Magazine of Concrete Research*, Vol. 62(1), p. 65-77.

Carol, I. and Z. P. Bazant (1997). "Damage and plasticity in microplane theory." *International Journal of Solids and Structures*, Vol. 34(29), p. 3807-3835.

Carol, I., P. C. Prat and Z. P. Bazant (1992). "New explicit microplane model for concrete: Theoretical aspects and numerical implementation." *International Journal of Solids and Structures*, Vol. 29(9), p. 1173-1191.

CEB-FIP (1992). *Model Code 1990*, London.

CEB (1996). *RC elements under cyclic loading: State of the art report*. London.

CEN (2004). *Eurocode 2. Design of Concrete Structures. Part 1-1: General rules and rules for buildings.*

Ceresa, P., L. Petrini and R. Pinho (2010). "Flexure-shear fiber beam-column elements for modeling frame structures under seismic loading - State of the Art." *Journal of Earthquake Engineering*, Vol. 11(1), p. 46-88.

Ceresa, P., L. Petrini, R. Pinho and R. Sousa (2009). "A fibre flexure-shear model for seismic analysis of RC-framed structures." *Earthquake engineering and structural dynamics*, Vol. 38, p. 565-586.

Cervenka, V. (1985). "Constitutive model for cracked reinforced concrete." *ACI Journal*, Vol. 82(6), p. 877-882.

Cervenka, V., L. Jendele and J. L. & Cervenka (2005). *ATENA Program documentation, Part 1: Theory*, Prague.

Collins, F. and H. Roper (1990). "Laboratory investigation of shear repair of reinforced concrete beams loaded in flexure." *ACI Materials Journal*, Vol. 97(2), p. 149-159.

Collins, M. P., E. Bentz and E. Sherwood (2008). "Where is shear reinforcement required? Review of research results and design procedures." *ACI Structural Journal*, Vol. 105(5), p. 590-600.

Collins, M. P. and D. Mitchell (1987). "Prestress concrete basics." Canadian Prestressed Concrete Institute.

Collins, M. P., F. J. Vecchio and R. G. Selby (1997). "The failure of an offshore platform." *Concrete International*, Vol. 19(8), p. 28-35.

CPH (2008). *Instrucción de Hormigón Estructural- EHE-08 (Spanish Concrete Structures Code)*. Ministério del Fomento, Spain

Crisfield, M. A. (1996). *Non-linear finite element analysis of solids and structures Vol.1*, John Wiley & Sons.

Cruz, P. (1994). *Un modelo para el análisis no lineal y diferido de estructuras de hormigón y acero construidas evolutivamente (A model for the nonlinear and time-dependent analysis of segmentally constructed structures of concrete and steel)*. PhD Thesis, Departament D'Enginyeria de la Construcció, Universitat Politècnica de Catalunya, Barcelona.

Chan, E. (1982). *Nonlinear geometric, material and time dependent analysis of reinforced concrete shells with edge beams*. Structural Engineering and Structural Mechanics, Department of Civil Engineering. University of California, Berkeley, California.

Chen, E. C.-Y. (1982). *Plasticity in reinforced concrete*. New York.

Chong, K. T. C., S. J. Foster and R. I. Gilbert (2008). "Time-dependent modelling of RC structures using the cracked membrane model and solidification theory." *Computers & Structures*, Vol. 86, p. 1305-1317.

Espion, B. (1993). *Benchmark examples for creep and shrinkage analysis computer programs. Creep and shrinkage of concrete*. RILEM, Barcelona, E&FN Spon.

Espion, B. and P. Halleux (1991). "Long term behavior of prestressed and partially prestressed concrete beams: experimental and numerical results." *ACI Special Publication* , Vol. 129, p. 19-38.

Fernandez, D. (2011). *Influencia de las solicitaciones axiles de tracción en la resistencia a cortante de las viguetas de forjado sin armadura transversal (Influence of the tensile stress loads in the shear resistance of beams without transversal reinforcement)*. PhD Thesis, Universidad Politecnica de Madrid, Madrid.

Ferraz, M. (2010). *Modelo de avaliação do comportamento estrutural de obras de arte (Model for the evaluation of the structural behaviour of bridges)*. PhD Thesis, Faculdade de Engenharia, Universidade do Porto, Porto.

FIB (2006). *Retrofitting of concrete structures by externally bonded FRPs*.

FIB (2010). *Model Code 2010*.

Godat, A., P. Labossière and K. W. Neale (2012). "Numerical investigation of the parameters influencing the behaviour of FRP shear-strengthened beams." *Construction and Building Materials*, Vol. 32, p. 90-68.

Godat, A., P. Labossière, K. W. Neale and O. Chaallal (2012). "Behavior of RC members strengthened in shear with EB FRP: assessment of models and FE simulation approaches." *Computers and Structures*, Vol. 92-93, p. 269-282.

Gopalakrishnan, K. S., A. Neville and A. Ghali (1969). "Creep poisson's ratio of concrete under multiaxial compression." *ACI Journal*, Vol. 66(90), p. 1008-1020.

Gopalakrishnan, K. S., A. Neville and A. Ghali (1970). "A hypothesis on mechanism of creep of concrete with reference to multiaxial compression." *ACI Journal*, Vol. 67(3), p. 29-35.

Governement du Québec (2007). *Commission of inquiry into the collapse of a portion of the de la Concorde overpass.* Canada.

Guedes, J. and A. V. Pinto (1997). *A numerical model for shear dominated bridge piers*. Seconde Italy-Japan Workshop on Seismic Design and Retrofit of Bridges, Rome, Italy.

Güner (2008). *Performance assessment of shear-critical reinforced concrete plane frames.* PhD Thesis, Department of Civil Engineering. Toronto, University of Toronto.

Hadi, M. N. S. (2003). "Retrofitting of shear failed reinforced concrete beams." *Composite Structures*, Vol. 62, p. 1-6.

Hernández, H. D. and W. L. Gamble (1975). *Time-dependent prestress lossess in pre-tensioned concrete construction.* Structural Research Series No 417, Civil Engineering Studies, University of Illinois, Urbana (IL).

Hognestad, E., N. W. Hanson and D. McHenry (1955). "Concrete stress distribution in ultimate strength design." *ACI*, Vol. 52(12), p. 455-480.

Hoque, M., N. Rattanawangcharoen and A. H. Shah (2007). "3D nonlinear mixed finite-element analysis of RC beams and plates with and without FRP reinforcement." *Computers and Concrete*, Vol. 4(2), p. 135-156.

Hsu, T. (1988). "Softened truss model theory for shear and torsion." *ACI Structural Journal*, Vol. 85(6), p. 624-635.

Illston, J. M. and I. J. Jordaan (1972). "Creep prediction for concrete under multiaxial stress." *ACI Journal*, Vol. 69(14), p. 158-164.

Kabir, A. F. (1976). *Nonlinear analysis of reinforced concrete panels, slabs and shells for time dependent effects*. PhD Thesis, Division of Structural Engineering and Structural Mechanics, University of California, Berkeley.

Kachlakev, D. and D. D. McCurry (2000). "Behavior of full-scale reinforced concrete beams retrofitted for shear and flexural with FRP laminates." *Composites Part B: Engineering*, Vol. 31, p. 445-452.

Kang, Y. (1977). *Nonlinear geometric, material and time dependent analysis of reinforced and prestressed concrete frames*. UC-SESM Report, No 77-1, Division of Structural Engineering and Structural Mechanics, University of California, Berkeley.

Kang, Y. and A. Scordelis (1980). "Nonlinear analysis of prestressed concrete frames." *Journal of Structural Division*, Vol. 106, p. 445-462.

Kani, M. (1977). *An experimental investigation of reinforced and prestressed beams in shear*. M.Sc. Thesis, University of Toronto.

Kaufmann, W. (1998). *Strength and deformations of structural concrete subjected to in-plane shear and normal forces*. PhD Thesis, Institute of Structural Engineering, Swiss Federal Institute of Technology Zurich.

Kaufmann, W. and P. Marti (1996). *Tests on structural concrete girders subjected to shear and normal forces (in German)*. IBK Bericht Nr. 226, Birkhauser Verlag, Basel, Institut fur Baustatik und Konstryktion, ETH Zurich.

Khalifa, A. and A. Nanni (2002). "Rehabilitation of rectangular simply supported RC beams with shear deficiencies using CFRP composites." *Construction and Building Materials*, Vol. 16, p. 135-146.

Kim, J. K., S. H. Kwon and Y. Y. Kim (2005). "Experimental studies on creep of sealed concrete under multiaxial stresses." *Magazine of Concrete Research*, Vol. 57(10), p. 623-634.

Kim, J. K., S. H. Kwon and Y. Y. Kim (2006). "Analytical studies on creep of sealed concrete under multiaxial stresses using a microplane model." *Magazine of Concrete Research*, Vol. 58(1), p. 9-20.

Kim, S.-W. and F. J. Vecchio (2008). "Modeling of shear-critical reinforced concrete structures repaired with fiber-reinforced polymer composites." *Journal of Structural Engineering*, Vol. 134(8), p. 1288-1299.

Kupfer, H., H. K. Hilsdorf and H. Rusch (1969). "Behavior of concrete under biaxial stresses." *ACI Journal*, Vol. 66(8), p. 656-666.

Lee, H. K., S. K. Ha and M. Afzal (2008). "Finite element analysis of shear-deficient RC beams strengthened with CFRP strips/sheets." *Structural Engineering and Mechanics*, Vol. 30(2), p. 247-261.

Leonhardt, F. (1988). *Estructuras de Hormigon Armado. Tomo I (Reinforced Concrete Structures. Part I)*. El Ateneo, Buenos Aires.

Leonhardt, F. and R. Walther (1961). *The Stuttgart shear tests, 1961. Contributions to the treatment of the problems of shear in reinforced concrete construction. (A translation of the papers theat appeared in "Beton-und Stahlbetonbau": Vol 56, No. 12. 1967; Vol 57, Nos. 2,3,6,7 and 8, 1962*). Cement and Concrete Association, London.

Magura, D. D., M. A. Sozen and S. C.P (1964). "A study of stress relaxation in prestressing reinforcement." *PCI Journal*, Vol. 9(2).

Marí, A. (2003). "Proyecto de estructuras de hormigón basado en sus prestaciones." Revista International Construlink, Vol. 1(2), p. 1-16.

Marí, A. R. (1984). *Nonlinear geometric, material and time dependent analysis of three dimensional reinforced and prestressed concrete frames*. Division of Structural Engineering and Structural Mechanics, Department of Civil Engineering, University of California, Berkeley.

Marí, A. R. and M. Valdés (2000). "Long-term behavior of continuous precast concrete girder bridge model." *Journal of Bridge Engineering*, Vol. 5(1), p. 22-30.

Marí, A. R. B. (2000). "Numerical simulation of the segmental construction of three dimensional concrete frames." *Engineering Structures*, Vol. 22, p. 585-596.

Marí, A. R. B. and J. Bairán (2008). *Evaluation of the response of concrete structures along their service life by nonlinear evolutive analysis methods*. IALCCE 08 - First International Symposium on Life-Cycle Civil Engineering Varenna, Lake Como, Italy, Taylor & Francis.

Marí, A. R. B. and J. Bairán (2009). "Evaluación de los efectos estructurales del deterioro, reparación y refuerzo, mediante análisis no lineal evolutivo (Evaluation of the structural effects of deterioration, repair and strengthening through an evolutive nonlinear analysis)" *Hormigón y Acero*, Vol. 60(252).

Marini, A. and E. Scapone (2006). "Analysis of reinforced concrete elements including shear effects." *ACI Structural Journal*, Vol. 103(5), p. 645-655.

Mohr, S. (2011). *Nonlinear static and dynamic model for the analysis of reinforced concrete frames under high shear forces*. PhD Thesis, Department d'Enginyeria de la Construcció, Universitat Politècnica de Catalunya, Barcelona.

Mohr, S., J. Bairán and A. R. Marí (2010). "A frame element model for the analysis of reinforced concrete structures under shear and bending." *Engineering Structures*, Vol. 32(12), p. 3936-3954.

Mohr, S., J. M. Bairán and A. R. Marí (2010). "A frame element model for the analysis of reinforced concrete structures under shear and bending." *Engineering Structures*, Vol. 32(12), p. 3936-3954.

Mosallam, A. S. and S. Banerjee (2007). "Shear enhancement of reinforced concrete beams strengthened with FRP composite laminates." *Composites Part B: Engineering*, Vol. 38, p. 781-793.

Mullapudi, R. and A. Ayoub (2010). "Modeling of the seismic behaviour of shear-critical reinforced concrete columns." *Engineering Structures*, Vol. 32, p. 3601-3615.

Navarro, J. G. (2009). *Modelización de elementos lineales de hormigón armado incluyendo el efecto del esfuerzo cortante (Model for linear elements of reinforced concrete including the effects of shear)*. PhD Thesis, Departamento de Ingeniería de la Construcción y de Proyectos de Ingeniería Civil, Universidad Politécnica de Valencia, Valencia.

Nie, J. and C. S. Cai (2000). "Deflection of cracked RC beams under sustained loading." *Journal of Structural Engineering*, Vol. 126(6), p. 708-716.

Nitereka, C. and K. W. Neale (1999). "Analysis of reinforced concrete beams strengthened in flexure with composite laminates." *Canadian Journal of Civil Engineering*, Vol. 26, p. 646-654.

Oñate, E. (1995). Cálculo *de estructuras por el método de los elementos finitos. Análisis estático lineal (Analysis of structures by means of the finite element method. Linear static analysis)*. CIMNE, Barcelona.

Osorio, E., J. Bairán and A. Marí (2012). "Lateral behavior of concrete under uniaxial compressive cyclic loading." *Materials and Structures*, p. 1-16, DOI 10.1617/s11527-012-9928-9.

Ozbolt, J. and Z. P. Bazant (1992). "Microplane model for cyclic triaxial behaviour of concrete." *Journal of Eng Mechanics*, Vol. 118(7), p. 1365-1386.

Pang, X.-B. and T. Hsu (1996). "Fixed angle softened truss model for reinforced concrete." *ACI Structural Journal*, Vol. 93(2), p. 196-208.

Park, H., R. Klingner and D. Wheat (1995). "Numerical techniques for predicting brittle failure of reinforced concrete planar structures." *Journal of Structural Engineering*, Vol. 121(10), p. 1507-1513.

Park, R. and T. Paulay (1994). *Estructuras de concreto reforzado (Reinforced concrete structures)*. Mexico.

Petrangeli, M. and J. Ozbolt (1996). "Smeared crack approaches - material modelling." *Journal of Engineering Mechanics*, Vol. 122(6), p. 545-554.

Petrangeli, M., P. E. Pinto and V. Ciampi (1999). "Fiber element for cyclic bending and shear of RC structures. I:Theory." *Journal of Eng Mechanics*, Vol. 125(9), p. 994-1009.

Pimentel, P., J. Figueiras and E. Bruhwiler (2007). *Numerical modelling of prestressed beams for structural examination of existing bridges*. CMNE/CILAMCE, APMTAC Porto.

Plos, M. and K. Gylltoft (2006). *Evaluation of shear capacity of a prestressed concrete box girder bridge using non-linear FEM*. Structural Engineering International, SEI Editorial Board. 3, p. 213-221.

Póvoas, R. (1991). *Modelos não-lineares de análise e dimensionamento de estruturas laminares de betão incluindo efeitos diferidos (Nonlinear models for analysis and design of reinforced concrete laminar structures including difered effects)*. PhD Thesis, Departamento de Engenharia Civil, Faculdade de Engenharia da Universidade do Porto, Porto.

Ranzo, G. (2000). *Experimental and numerical studies on the seismic performance of beam-column RC structural members subjected to high shear*. PhD Thesis, University of Rome "La Sapienza", Rome.

Reddy, J. N. and C. M. Wang (1997). "Relationships between bending solutions of classical and shear deformation beam theories." *International Journal of Solids and Structures*, Vol. 34(26), p. 3373-3384.

Saether, I., T. Kantad, J. A. Overli and M. Bergstrom (2010). "Phased time-dependent FE analysis of reinforced concrete beams." *Magazine of Concrete Research*, Vol. 62(8), p. 543-556.

Saritas, A. and F. C. Filippou (2009). "Inelastic axial-flexural-shear coupling in a mixed formulation beam finite element." *International Journal of Non-Linear Mechanics*, Vol. 44, p. 913-922.

Sato, R. and H. Kawakane (2008). "A new concept for the early age shrinkage effect on diagonal cracking strength of reinforced HSC beams." *Journal of Advanced Concrete Technology*, Vol. 6(1), p. 45-67.

Scapone, E., F. C. Filippou and F. Taucer (1996). "Fibre beam-column model for non-linear analysis of R/C frames: part I. Formulation." *Earthquake engineering and structural dynamics*, Vol. 25, p. 711-725.

Souza, H. R. (1990). *Análise do comportamento de vigas de betão armado reforçadas à flexão e ao esforço transverso* (*Analysis of the behavior of reinforced concrete beams to bending and shear)*. PhD Thesis, Civil Engineering, Instituto Superior Técnico, Universidade Técnica de Lisboa, Lisbon.

Souza, H. R. and J. Appleton (1997a). "Behaviour of shear-strengthened reinforced concrete beams." *Materials and Structures*, Vol. 30, p. 81-90.

Souza, H. R. and J. Appleton (1997b). "Flexural behaviour of strengthened reinforced concrete beams." *Materials and Structures*, Vol. 30, p. 154-159.

Stramandinoli, R. S. B. and H. L. La Rovere (2012). "FE model for nonlinear analysis of reinforced concrete beams considering shear deformation." *Engineering Structures*, Vol. 35, p. 244-253.

Taljsten, B. (2003). "Strengthening concrete beams for shear with CFRP sheets." *Construction and Building Materials*, Vol. 17, p. 15-26.

Ulm, F., J. Clement and J. Guggenberger (1994). *Recent advances in 3-D nonlinear FE-analysis of R/C and P/C beam structures*. ASCE Structures Congress XII, Atlanta (GA), New York, ASCE.

Valipour, H. R. and S. J. Foster (2007). *A novel flexibility based beam-column element for nonlinear analysis of reinforced concrete frames* (U. R. N. R-447), School of Civil and Environmental Engineering, The University of New South Wales, Australia.

Van Greunen, J. (1979). *Nonlinear geometric, material and time dependent analysis of reinforced and prestressed concrete slabs and panels*. Division of Structures and Materials

Research, Department of Civil Engineering, College of Engineering. University of California, Berkeley, California.

Vecchio, F. J. (1999). "Towards cyclic load modeling of reinforced concrete." ACI *Structural Journal*, Vol. 96(2), p. 1070-1077.

Vecchio, F. J. (2000). "Distributed stress field model for reinforced concrete." *ACI Journal of Structural Eng*, Vol. 126(9), p. 1070-1077.

Vecchio, F. J. and M. P. Collins (1986). "The modified compression-field theory for reinforced concrete elements subjected to shear." *ACI Journal*, Vol. 83(2), p. 1357-1417.

Vecchio, F. J. and M. P. Collins (1988). "Predicting the response of reinforced concrete beams subjected to shear using the modified compression field theory." *ACI Journal*, Vol. 85(3), p. 258-268.

Vecchio, F. J. and M. B. Emara (1992). "Shear deformations in reinforced concrete frames." *ACI Structural Journal*, Vol. 89(1), p. 46-56.

Vecchio, F. J. and W. Shim (2004). "Experimental and analytical reexaminations of classic concrete beam tests." *Journal of Structural Engineering*, Vol. 130(3), p. 460-469.

Walraven, J. C. (1981). "Fundamental analysis of aggregate interlock." *Journal of Structural Division*, Vol. 108, p. 2254-2270.

Wong, P. S. and F. J. Vecchio (2002). *Vector2 & Formworks user's manual*. University of Toronto.

Zararis, I. P., M. K. Karaveziroglou and P. D. Zararis (2006). "Shear strength of reinforced concrete T-beams." *ACI Journal*, Vol. 103(5), p. 693-700.

Zienkiewicz, O. C. (1977). *The finite element method*. McCraw-Hill, London.

Zienkiewicz, O. C. and R. L. Taylor (2004*). El método de los elementos finitos. Las bases (The finite element method. The basis)*. CIMNE, Barcelona.

Zwicky, D. and T. Vogel (2000). *Failure tests on dismantled prestressed concrete bridge girders (in German)*. Institute of Structural Engineering IBK, Swiss Federal Institute of Technology ETH Zurich.

Annex A

The mathematic operations related to the fibre state determination, presented in Chapter 3 - A hybrid fibre beam-column model including shear effects – are detailed described in the following.

Derivation of Eq. (3.26) and Eq. (3.27) presented in the Section 3.2.2: increment of vertical strain $\Delta\varepsilon_z$ and shear strain $\Delta\gamma_{xz}$, respectively correspondent to the equations (A13) and (A15) of this Annex.

The incremental strain and stress state of a fibre is related through the stiffness matrix D_{fibre} as

$$\begin{pmatrix} \Delta\sigma_x \\ \Delta\sigma_z \\ \Delta\tau_{xz} \end{pmatrix} = \begin{pmatrix} D_{11} & D_{12} & D_{13} \\ D_{21} & \overline{D}_{22} & D_{23} \\ D_{31} & D_{32} & D_{33} \end{pmatrix} \begin{pmatrix} \Delta\varepsilon_x \\ \Delta\varepsilon_z \\ \Delta\gamma_{xz} \end{pmatrix}; \ \overline{D}_{22} = D_{22} + \rho_{st} E_{st} \tag{A1}$$

from which the increment of stress in the z-direction $\Delta\sigma_z^c$ and the increment of shear stress $\Delta\tau_{xz}$ can be, respectively written as

$$\Delta\sigma_z^c = D_{21}\Delta\varepsilon_x + D_{22}\Delta\varepsilon_z + D_{23}\Delta\gamma_{xz} \tag{A2}$$

$$\Delta\tau_{xz} = D_{31}\Delta\varepsilon_x + D_{32}\Delta\varepsilon_z + D_{33}\Delta\gamma_{xz} \tag{A3}$$

Equilibrium along z-direction imposes that the sum of the increment of stresses in transversal steel $\Delta\sigma_z^{st}$ and in concrete $\Delta\sigma_z^c$ is null:

$$\Delta\sigma_z^c + \rho_{st}\Delta\sigma_z^{st} = 0 \tag{A4}$$

Replacing Eq. (A2) into Eq. (A4), the equilibrium in the vertical direction can be written as

$$D_{21}\Delta\varepsilon_x + D_{22}\Delta\varepsilon_z + D_{23}\Delta\gamma_{xz} + \rho_{st}E_{st}\Delta\varepsilon_z = 0 \tag{A5}$$

The computed increment of shear stress $\Delta\tau_{xz}$ must equal the imposed increment of shear stress given by the fixed stress constraint $\Delta\tau^*$, imposing that:

$$\Delta\tau^* - \Delta\tau_{xz} = 0 \tag{A6}$$

By replacing Eq. (A3) into Eq. (A6), the former equation comes as

$$D_{31}\Delta\varepsilon_x + D_{32}\Delta\varepsilon_z + D_{33}\Delta\gamma_{xz} = \Delta\tau^* \tag{A7}$$

In this manner, a system of two equations can be solved in order to determine the increment of vertical $\Delta\varepsilon_z$ and shear $\Delta\gamma_{xz}$ strains:

(*i*) Equilibrium in the vertical direction:

$$D_{21}\Delta\varepsilon_x + D_{22}\Delta\varepsilon_z + D_{23}\Delta\gamma_{xz} + \rho_{st}E_{st}\Delta\varepsilon_z = 0 \tag{A8a}$$

$$D_{21}\Delta\varepsilon_x + \Delta\varepsilon_z\left(D_{22} + \rho_{st}E_{st}\right) + D_{23}\Delta\gamma_{xz} = 0 \tag{A8b}$$

$$D_{21}\Delta\varepsilon_x + \Delta\varepsilon_z\left(\overline{D_{22}}\right) + D_{23}\Delta\gamma_{xz} = 0 \tag{A8c}$$

(*ii*) Constitutive relation of shear stresses:

$$D_{31}\Delta\varepsilon_x + D_{32}\Delta\varepsilon_z + D_{33}\Delta\gamma_{xz} = \Delta\tau^* \tag{A9}$$

Hence, the former system of the two equations is written as

$$\begin{cases} D_{21}\Delta\varepsilon_x + \Delta\varepsilon_z\left(\overline{D_{22}}\right) + D_{23}\Delta\gamma_{xz} = 0 & \text{(A10a)} \\ D_{31}\Delta\varepsilon_x + D_{32}\Delta\varepsilon_z + D_{33}\Delta\gamma_{xz} = \Delta\tau^* & \text{(A10b)} \end{cases}$$

and can be reorganized as

$$\begin{cases} D_{21}\Delta\varepsilon_x + \Delta\varepsilon_z\left(\overline{D_{22}}\right) + D_{23}\Delta\gamma_{xz} = 0 & \text{(A11a)} \\ \Delta\gamma_{xz} = \dfrac{\left(\Delta\tau^* - D_{31}\Delta\varepsilon_x - D_{32}\Delta\varepsilon_z\right)}{D_{33}} & \text{(A11b)} \end{cases}$$

Replacing $\Delta\gamma_{xz}$ of Eq (A11b) into equation (A10a) and reorganizing, results in:

$$D_{21}\Delta\varepsilon_x + \Delta\varepsilon_z\left(\overline{D_{22}}\right) + \frac{D_{23}}{D_{33}}\left(\Delta\tau^* - D_{31}\Delta\varepsilon_x - D_{32}\Delta\varepsilon_z\right) = 0 \tag{A12a}$$

$$\left(D_{21} - \frac{D_{23}D_{31}}{D_{33}}\right)\Delta\varepsilon_x + \frac{D_{23}}{D_{33}}\Delta\tau^* + \left(\overline{D_{22}} - \frac{D_{23}D_{32}}{D_{33}}\right)\Delta\varepsilon_z = 0 \tag{A12b}$$

$$\left(D_{33}D_{21} - D_{23}D_{31}\right)\Delta\varepsilon_x + D_{23}\Delta\tau^* + \left(D_{33}\overline{D_{22}} - D_{23}D_{32}\right)\Delta\varepsilon_z = 0 \tag{A12c}$$

Consequently, the increment of vertical strain $\Delta\varepsilon_z$ can be written as

$$\Delta\varepsilon_z = \frac{\left(D_{23}D_{31} - D_{33}D_{21}\right)\Delta\varepsilon_x - D_{23}\Delta\tau^*}{D_{33}\overline{D_{22}} - D_{23}D_{32}} \tag{A13}$$

Replacing $\Delta\varepsilon_z$ given by Eq. (A13) into Eq. (A11b) and rearranging the ensuing equation, results in the following expressions:

$$\Delta\gamma_{xz} = \frac{\Delta\tau^* - D_{31}\Delta\varepsilon_x}{D_{33}} - \left(\frac{D_{32}}{D_{33}}\right)\frac{\left(D_{23}D_{31} - D_{33}D_{21}\right)\Delta\varepsilon_x - D_{23}\Delta\tau^*}{\left(D_{33}\overline{D_{22}} - D_{23}D_{32}\right)} \tag{A14a}$$

$$\Delta\gamma_{xz} = \frac{\Delta\tau^*}{D_{33}} - \frac{D_{31}\Delta\varepsilon_x}{D_{33}} - \left(\frac{D_{32}}{D_{33}}\right)\frac{\left(D_{23}D_{31} - D_{33}D_{21}\right)\Delta\varepsilon_x - D_{23}\Delta\tau^*}{\left(D_{33}\overline{D_{22}} - D_{23}D_{32}\right)} \tag{A14b}$$

$$D_{33}\Delta\gamma_{xz} = \frac{\left(D_{33}\overline{D_{22}} - D_{23}D_{32}\right)\Delta\tau^* - \left(D_{33}\overline{D_{22}} - D_{23}D_{32}\right)D_{31}\Delta\varepsilon_x}{\left(D_{33}\overline{D_{22}} - D_{23}D_{32}\right)} - \frac{D_{32}\left(\left(D_{23}D_{31} - D_{33}D_{21}\right)\Delta\varepsilon_x - D_{23}\Delta\tau^*\right)}{\left(D_{33}\overline{D_{22}} - D_{23}D_{32}\right)} \tag{A14c}$$

$$D_{33}\Delta\gamma_{xz} = \frac{\left(D_{33}\overline{D_{22}} - D_{23}D_{32} + D_{23}D_{32}\right)\Delta\tau^*}{\left(D_{33}\overline{D_{22}} - D_{23}D_{32}\right)} - \frac{\left(D_{31}D_{33}\overline{D_{22}} - D_{31}D_{23}D_{32} + D_{32}D_{23}D_{31} - D_{32}D_{33}D_{21}\right)\Delta\varepsilon_x}{\left(D_{33}\overline{D_{22}} - D_{23}D_{32}\right)} \tag{A14d}$$

$$D_{33}\Delta\gamma_{xz} = \frac{\left(D_{33}\overline{D_{22}}\right)\Delta\tau^* - \left(D_{31}D_{33}\overline{D_{22}} - D_{32}D_{33}D_{21}\right)\Delta\varepsilon_x}{\left(D_{33}\overline{D_{22}} - D_{23}D_{32}\right)} \tag{A14e}$$

From the previous deduction, the increment of shear strain $\Delta\gamma_{xz}$ can be written as

$$\Delta\gamma_{xz} = \frac{\overline{D_{22}}\Delta\tau^* + \left(D_{32}D_{21} - D_{31}\overline{D_{22}}\right)\Delta\varepsilon_x}{\left(D_{33}\overline{D_{22}} - D_{23}D_{32}\right)} \tag{A15}$$

Derivation of Eq. (3.30) and Eq. (3.31) presented in the Section 3.2.2.1: unbalanced vertical $\delta\varepsilon_z$ and tangential $\delta\gamma_{xz}$ strains at the innermost iterative procedure at the fibre level, respectively given by equations (A23) and (A25) of this Annex.

Regarding the equilibrium condition at the vertical direction (Eq. A4), the unbalanced vertical stresses can be determined as

$$\delta\sigma_z = -\rho_{st}\Delta\sigma_z^{st} + \Delta\sigma_z^c \tag{A16}$$

Due to the imposed shear constraint, the unbalanced shear stress is determined as

$$\delta\tau_{xz} = \Delta\tau^* - \Delta\tau_{xz} \tag{A17}$$

Within the innermost iteration at the fibre level, the increment of longitudinal axial strain $\Delta\varepsilon_x$ (determined through the plane section theory) is kept fixed. So, the remaining unbalanced strains and stresses can be written as follows, making use of the reduced form of the stiffness matrix D_{fibre} as

$$\begin{pmatrix}\delta\sigma_z\\ \delta\tau_{xz}\end{pmatrix} = \begin{pmatrix}\overline{D}_{22} & D_{23}\\ D_{32} & D_{33}\end{pmatrix}\begin{pmatrix}\delta\varepsilon_z\\ \delta\gamma_{xz}\end{pmatrix};\ \overline{D}_{22} = D_{22} + \rho_{st}E_{st} \tag{A18}$$

Accordingly, the unbalanced stress in the vertical direction $\delta\sigma_z$ is given by:

$$\delta\sigma_z = \overline{D}_{22}\delta\varepsilon_z + D_{23}\delta\gamma_{xz} \tag{A19}$$

and the unbalanced shear stress $\delta\tau_z$ is written as

$$\delta\tau_{xz} = D_{32}\delta\varepsilon_z + D_{33}\delta\gamma_{xz} \tag{A20}$$

Hence, the system the two former equations can be rewritten in order to determine the unbalanced increment of vertical strain $\delta\varepsilon_z$ and shear strain $\delta\gamma_{xz}$ as

$$\begin{cases}\delta\varepsilon_z = \dfrac{\delta\sigma_z - D_{23}\delta\gamma_{xz}}{\overline{D}_{22}} & \text{(A21a)}\\ \delta\gamma_{xz} = \dfrac{\delta\tau_{xz} - D_{32}\delta\varepsilon_z}{D_{33}} & \text{(A21b)}\end{cases}$$

By replacing Eq. (A21b) into Eq. (A21a) and rearranging, the following expressions come out:

$$\delta\varepsilon_z = \frac{D_{33}\delta\sigma_z - D_{23}\left(\delta\tau_{xz} - D_{32}\delta\varepsilon_z\right)}{\overline{D}_{22}D_{33}} \tag{A22a}$$

$$\delta\varepsilon_z = \frac{D_{33}\delta\sigma_z - D_{23}\delta\tau_{xz} + D_{23}D_{32}\delta\varepsilon_z}{\overline{D}_{22}D_{33}} \tag{A22b}$$

$$\overline{D}_{22}D_{33}\delta\varepsilon_z - D_{23}D_{32}\delta\varepsilon_z = D_{33}\delta\sigma_z - D_{23}\delta\tau_{xz} \tag{A22c}$$

$$\delta\varepsilon_z\left(\overline{D}_{22}D_{33} - D_{23}D_{32}\right) = D_{33}\delta\sigma_z - D_{23}\delta\tau_{xz} \tag{A22d}$$

Hence, the unbalanced increment of vertical strain $\delta\varepsilon_z$ can be written as

$$\delta\varepsilon_z = \frac{D_{33}\delta\sigma_z - D_{23}\delta\tau_{xz}}{\overline{D}_{22}D_{33} - D_{23}D_{32}} \tag{A23}$$

Subsequently, by replacing Eq. (A23) into Eq. (A21b) and rearranging it, the following expressions appear:

$$D_{33}\delta\gamma_{xz} = \delta\tau_{xz} - D_{32}\frac{D_{33}\delta\sigma_z - D_{23}\delta\tau_{xz}}{\overline{D}_{22}D_{33} - D_{23}D_{32}} \tag{A24a}$$

$$D_{33}\delta\gamma_{xz} = \frac{\delta\tau_{xz}\left(\overline{D}_{22}D_{33} - D_{23}D_{32}\right) - D_{32}\left(D_{33}\delta\sigma_z - D_{23}\delta\tau_{xz}\right)}{\overline{D}_{22}D_{33} - D_{23}D_{32}} \tag{A24b}$$

$$D_{33}\left(\overline{D}_{22}D_{33} - D_{23}D_{32}\right)\delta\gamma_{xz} = \delta\tau_{xz}\overline{D}_{22}D_{33} - \delta\tau_{xz}D_{23}D_{32} - D_{32}D_{33}\delta\sigma_z + D_{32}D_{23}\delta\tau_{xz} \tag{A24c}$$

$$D_{33}\left(\overline{D}_{22}D_{33} - D_{23}D_{32}\right)\delta\gamma_{xz} = \delta\tau_{xz}\overline{D}_{22}D_{33} - D_{32}D_{33}\delta\sigma_z \tag{A24d}$$

$$\left(\overline{D}_{22}D_{33} - D_{23}D_{32}\right)\delta\gamma_{xz} = \delta\tau_{xz}\overline{D}_{22} - D_{32}\delta\sigma_z \tag{A24e}$$

Therefore, the unbalanced increment of shear strain $\delta\gamma_{xz}$ is determined as

$$\delta\gamma_{xz} = \frac{\delta\tau_{xz}\overline{D}_{22} - D_{32}\delta\sigma_z}{\overline{D}_{22}D_{33} - D_{23}D_{32}} \tag{A25}$$